ADVANCED STEEL CONSTRUCTION

An International Journal

Volume 18 Number 4

December 2022

CONTENTS

Technical Papers

Website: *http://www.hkisc.org*
ISSN 1816-112X
Science Citation Index Expanded, Materials Science Citation Index and ISI Alerting
Cover: A Steel Structure in Hong Kong Science Park. Photo @LIU Yao-Peng

ADVANCED STEEL CONSTRUCTION

VOL.18, NO.4 (2022)

ADVANCED STEEL CONSTRUCTION

an International Journal

ISSN 1816-112X

Volume 18 Number 4

December 2022

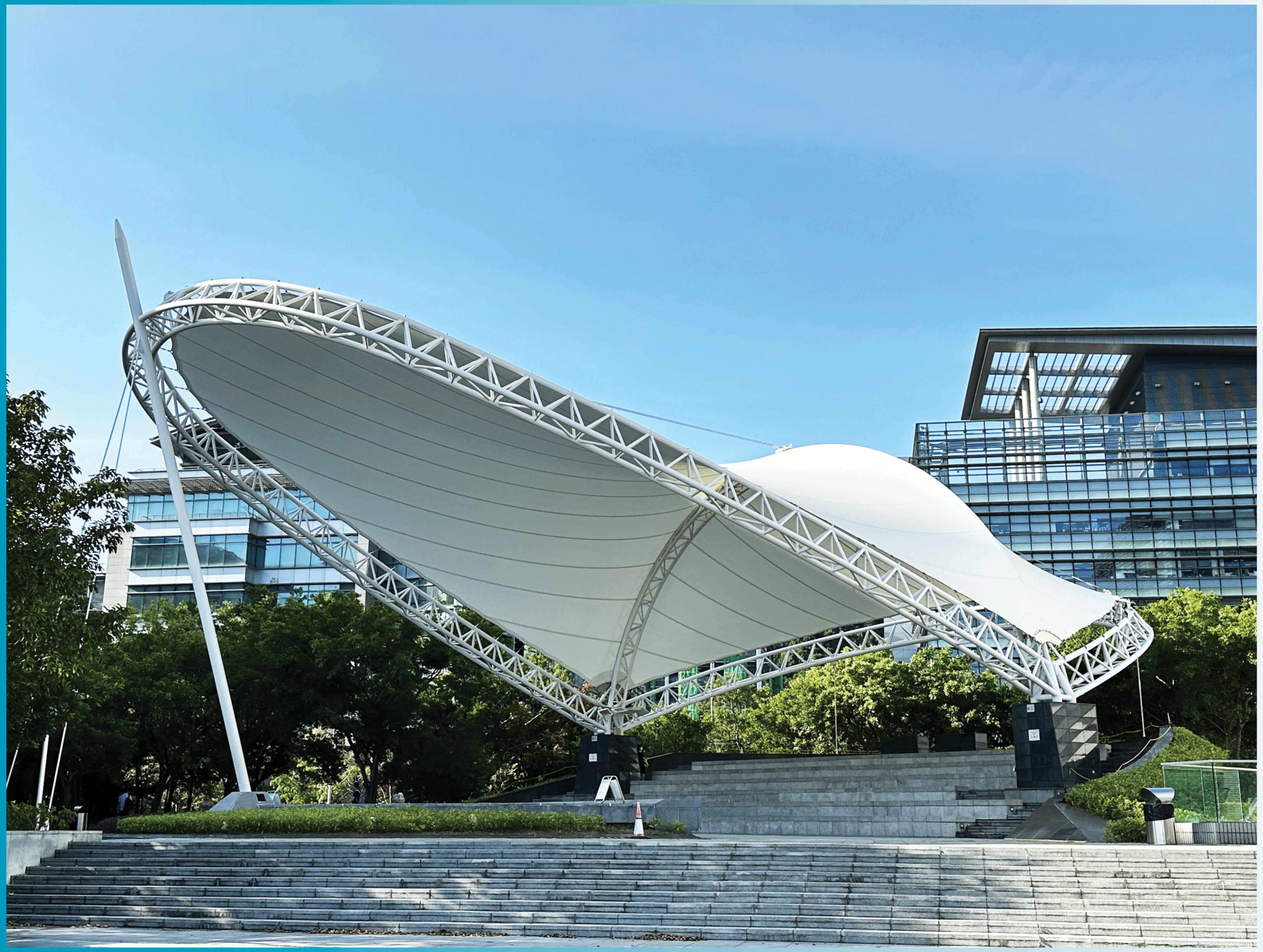

ISSN 1816-112X

Science Citation Index Expanded, Materials Science Citation Index and ISI Alerting

Advanced Steel Construction

an international journal

EDITORS-IN-CHIEF

Asian Pacific, African and organizing Editor
S.L. Chan
The Hong Kong Polyt. Univ., Hong Kong, China

American Editor
W.F. Chen
Univ. of Hawaii at Manoa, USA

European Editor
R. Zandonini
Trento Univ., Italy

ASSOCIATE EDITORS

Y.P. Liu
The Hong Kong Polyt. Univ., Hong Kong, China

S.W. Liu
The Hong Kong Polyt. Univ., Hong Kong, China

INTERNATIONAL EDITORIAL BOARD

F.G. Albermani
Central Queensland Univ., Australia

I. Burgess
Univ. of Sheffield, UK

F.S.K. Bijlaard
Delft Univ. of Technology, The Netherlands

R. Bjorhovde
The Bjorhovde Group, USA

M.A. Bradford
The Univ. of New South Wales, Australia

D. Camotim
Technical Univ. of Lisbon, Portugal

C.M. Chan
Hong Kong Univ. of Science & Technology, Hong Kong, China

T.H.T. Chan
Queensland Univ. of Technology, Australia

T.M. Chan
The Hong Kong Polyt. Univ., Hong Kong, China

Z.H. Chen
Tianjin Univ., China

S.P. Chiew
Nanyang Technological Univ., Singapore

W.K. Chow
The Hong Kong Polyt. Univ., Hong Kong, China

G.G. Deierlein
Stanford Univ., California, USA

L. Dezi
Univ. of Ancona, Italy

D. Dubina
The Politehnica Univ. of Timosoara, Romania

R. Greiner
Technical Univ. of Graz, Austria

L. Gardner
Imperial College of Science, Technology and Medicine, UK

Y. Goto
Nagoya Institute of Technology, Japan

L.H. Han
Tsinghua Univ. China

S. Herion
University of Karlsruhe, Germany

G.W.M. Ho
Ove Arup & Partners Hong Kong Ltd., Hong Kong, China

B.A. Izzuddin
Imperial College of Science, Technology and Medicine, UK

J.P. Jaspart
Univ. of Liege, Belgium

S. A. Jayachandran
IIT Madras, Chennai, India

S.E. Kim
Sejong Univ., South Korea

S. Kitipornchai
The Univ., of Queensland, Australia

D. Lam
Univ. of Bradford, UK

H.F. Lam
City Univ. of Hong Kong, Hong Kong, China

G.C Li
Shenyang Jianzhu Univ., China

G.Q. Li
Tongji Univ., China

J.Y.R. Liew
National Univ. of Singapore, Singapore

E.M. Lui
Syracuse Univ., USA

Y.L. Mo
Univ. of Houston, USA

J.P. Muzeau
CUST, Clermont Ferrand, France

D.A. Nethercot
Imperial College of Science, Technology and Medicine, UK

Y.Q. Ni
The Hong Kong Polyt. Univ., Hong Kong, China

D.J. Oehlers
The Univ. of Adelaide, Australia

J.L. Peng
Yunlin Uni. of Science & Technology, Taiwan, China

K. Rasmussen
The Univ. of Sydney, Australia

J.M. Rotter
The Univ. of Edinburgh, UK

C. Scawthorn
Scawthorn Porter Associates, USA

P. Schaumann
Univ. of Hannover, Germany

Y.J. Shi
Tsinghua Univ., China

G.P. Shu
Southeast Univ. China

L. Simões da Silva
Department of Civil Engineering, University of Coimbra, Portugal

J.G. Teng
The Hong Kong Polyt. Univ., Hong Kong, China

G.S. Tong
Zhejiang Univ., China

K.C. Tsai
National Taiwan Univ., Taiwan, China

C.M. Uang
Univ. of California, USA

B. Uy
University of Western Sydney, Australia

M. Veljkovic
Univ. of Lulea, Sweden

F. Wald
Czech Technical Univ. in Prague, Czech

Y.C. Wang
The Univ. of Manchester, UK

Y.L. Xu
The Hong Kong Polyt. Univ., Hong Kong, China

D. White
Georgia Institute of Technology, USA

E. Yamaguchi
Kyushu Institute of Technology, Japan

Y.B. Yang
National Taiwan Univ., Taiwan, China

Y.Y. Yang
China Academy of Building Research, Beijing, China

B. Young
The Univ. of Hong Kong, Hong Kong, China

X.L. Zhao
Monash Univ., Australia

X.H. Zhou
Chongqing University, China

Z.H. Zhou
The Hong Kong Polyt. Univ., Hong Kong, China

S.Y. Zhu
The Hong Kong Polyt. Univ., Hong Kong, China

R.D. Ziemian
Bucknell Univ., USA

Cover: A Steel Structure in Hong Kong Science Park. Photo @LIU Yao-Peng

e-copy of IJASC is free to download at "www.ascjournal.com" in internet and mobile apps.

General Information
Advanced Steel Construction, an international journal

Aims and scope

The International Journal of Advanced Steel Construction provides a platform for the publication and rapid dissemination of original and up-to-date research and technological developments in steel construction, design and analysis. Scope of research papers published in this journal includes but is not limited to theoretical and experimental research on elements, assemblages, systems, material, design philosophy and codification, standards, fabrication, projects of innovative nature and computer techniques. The journal is specifically tailored to channel the exchange of technological know-how between researchers and practitioners. Contributions from all aspects related to the recent developments of advanced steel construction are welcome.

Subscription inquiries and change of address. Address all subscription inquiries and correspondence to Member Records, IJASC. Notify an address change as soon as possible. All communications should include both old and new addresses with zip codes and be accompanied by a mailing label from a recent issue. Allow six weeks for all changes to become effective.
The Hong Kong Institute of Steel Construction
HKISC
c/o Department of Civil and Environmental Engineering,
The Hong Kong Polytechnic University,
Hunghom, Kowloon, Hong Kong, China.
Tel: 852- 2766 6047 Fax: 852- 2334 6389
Email: *ceslchan@polyu.edu.hk* Website: *http://www.hkisc.org/*
ISSN 1816-112X
Science Citation Index Expanded, Materials Science Citation Index and ISI Alerting

ISSN 1816-112X

**Science Citation Index Expanded,
Materials Science Citation Index and
ISI Alerting**

Advanced Steel Construction
an international journal

VOLUME 18 NUMBER 4 **December 2022**

Technical Papers

Advanced Steel Construction – Vol. 18 No. 4 (2022) 736–744
DOI:10.18057/IJASC.2022.18.4.1

A MODEL FOR PREDICTING MOMENT-CURVATURE BEHAVIOR OF SELF-STRESSING SSACFST COLUMNS UNDER LOW CYCLIC LOADING

Feng Yu [1], Yue Cao [1], Yuan Fang [1, 2, *], Yuan-Di Qian [1, 3], Chi Yao [1] and Yin Qin [1]

[1] Department of Civil Engineering and Architecture, Anhui University of Technology, Ma'anshan, China
[2] Key Laboratory of Metallurgical Emission Reduction & Resources Recycling (Anhui University of Technology), Ministry of Education
[3] China MCC 17 Group Co., Ltd
**(Corresponding author: Email: fyuan86@126.com)*

ABSTRACT

This paper reports the experimental investigation and theoretical model of self-stressing steel slag aggregate concrete-filled steel tubular (SSACFST) columns under low cyclic loading. Fourteen specimens including ten self-stressing SSACFST columns and four ordinary SSACFST columns (reference columns) are tested, and the effects of four experimental variables, such as axial compression ratio (n), diameter-thickness ratio (D/t_s), shear-span ratio (λ), and expansion rate (P_{ct}) of steel slag aggregate concrete (SSAC) on failure mode, moment-curvature hysteretic curves and skeleton curves are examined. Experimental results demonstrate that the failure mode of columns with high shear-span ratio is bending failure while the bending-shear failure dominates the damage of columns with low shear-span ratio. With the enhancement of axial compression ratio or expansion rate of SSAC, the peak moment of specimens increases. The increase of shear-span ratio or diameter-thickness ratio decreases the peak moment of specimens. The peak curvature of specimens decreases as axial compression ratio increases, while it increases as shear-span ratio increases. The impacts of diameter-thickness ratio and expansion rate of SSAC on peak curvature of specimens are marginal. A simplified calculation method of moment-curvature skeleton curves is suggested and the hysteresis rules of self-stressing SSACFST columns are also proposed by analyzing the features of hysteretic curves. Ultimately, a model for evaluating moment-curvature behavior of self-stressing SSACFST columns under low cyclic loading is established and validated the experimental results with good agreement.

ARTICLE HISTORY

Received: 22 June 2021
Revised: 18 March 2022
Accepted: 27 March 2022

KEYWORDS

Concrete filled steel tube;
Steel slag aggregate concrete;
Self-stressing;
Low cyclic loading;
Moment-curvature

1. Introduction

Steel slag is main industrial waste produced in steel-making process. In developing countries, especially in China, the emissions of steel slag reaches more than 100 million tons per year, while the utilization rate of steel slag is only 29.5% [1]. Numerous accumulated steel slag not only occupies land resources, but also gives rise to environmental pollution. Therefore, the reasonable and scientific treatment of these steel slag wastes has attracted the attention of researchers.

Currently, an increasing number of scholars use steel slag as fine aggregate[2], coarse aggregate [3-4] or both fine and coarse aggregates [5] to prepare SSAC, and a large number of investigations have been conducted [6-8]. These investigations prove that the steel slag can meet the requirements of concrete aggregate and SSAC will be a potential treatment method of steel slag wastes, which will bring satisfactory environmental and economic effects. The benefits of using SSAC are listed in Table 1.

Table 1
The benefits of using SSAC

	SSAC
Benefits	Reduce land occupation, alleviate environmental pollution, significant environmental benefits
	Recycle solid waste, reduce natural aggregate consumption, considerable economic benefits
	Excellent mechanical properties
	Favorable durability
	Low hydration heat

Qasrawi et al. [9] used steel slag as fine aggregate in the concrete mix and found that the 28-day compressive and and tensile strength was improved by 1.1~1.3 and 1.4~2.4 times, respectively, depending on concrete grade and sand replacement ratio. Maslehuddin et al. [10] conducted the experimental study on durability of SSAC and demonstrated that the durability of SSAC was superior than that of crushed limestone aggregate concrete. However, SSAC is not widely used in structural engineering. This results arises because SSAC potentially contains high contents of free CaO and MgO, which expand when hydrated, the generated internal pressure causes surface cracks and protrusion [11]. To this end, scholars have proposed some stabilization measures to inhibit the volume expansion of SSAC, such as carbonation of steel slag [12], phosphoric acid modification [13] and reduction of MgO and free CaO contents [14].

Concrete-filled steel tubular (CFST) column has been extensively applied in bridge engineering, power transmission towers, and high-rise buildings due to its significant merits of high load capacity, favorable ductility and convenient construction. Numerous experimental and theoretical investigations on CFST columns have been performed and fruitful research results have been achieved [15-17]. However, the hardening shrinkage of core concrete may reduce the durability and affect the safety of structure. To solve this problem, a self-stressing CFST column formed by pouring expansive concrete into steel tube has been proposed and a lot of experimental studies have been conducted [18-19]. Li et al. [20] tested the self-stressing CFST columns under axial compression and demonstrated that the ultimate bearing capacity increased by 9.8%-27.6% compared with ordinary CFST columns. Chang et al. [21] studied the mechanical performances of self-stressing CFST columns under eccentric load and revealed that the bearing capacity of self-stressing CFST columns was generally higher than that of ordinary CFST columns and it decreased with the increase of eccentricity.

As mentioned above, the existence of the self-stressing alleviates the impact of shrinkage on the mechanical behavior of CFST column and improves its co-operative working ability. At present, the expansive concrete prepared by adding additives can compensate volume shrinkage and form self-stressing in steel tubes. However, the incorporation of additives increases the construction cost and complicates the hydration and hardening process of concrete.

In recent years, scholars have poured expanded SSAC into steel tubes to prepare self-stressing SSACFST members and conducted the relevant theoretical and experimental investigations [22-23]. Considering the impact of the diameter-thickness ratio, expansion rate of SSAC and eccentricity, Yu et al. [24] experimentally investigated the static performances of self-stressing SSACFST columns, revealed the failure mode of the axially or eccentrically loaded self-stressing SSACFST columns, and proposed the corresponding prediction formulas of ultimate bearing capacity. Fang et al. [25] reported the axial compressive behavior of self-stressing SSACFST short and medium long columns, and proposed the calculation formulas of bearing capacity. Yu et al. [26] investigated the axial compressive behavior of self-stressing SSACFST columns with different loading modes and evaluated the rationality of existing CFST design formulas to estimate their bearing capacity. These investigations confirmed that the self-stressing SSACFST columns not only alleviates the shrinkage of core concrete in steel tubes, but also effectively recycles steel slag wastes. In addition, to capitalize on the volume expansion of SSAC, a SSAC filled-FRP tube column was proposed in recent research [27] and its physical and mechanical properties were systematically tested.

Obviously, a series of studies on the static performances of self-stressing SSACFST columns have been conducted and considerable results have been obtained. However, research on seismic performance of self-stressing

SSACFST columns is rarely reported. To further reveal the seismic response of this novel composite column, fourteen specimens including ten self-stressing SSACFST columns and four ordinary SSACFST columns (reference columns) are tested. The effects of the axial compression ratio (n), diameter-thickness ratio (D/t_s), shear-span ratio (λ), and expansion rate (P_{ct}) on failure modes, moment-curvature hysteretic curves and skeleton curves are examined. Additionally, an analytical model for predicting moment-curvature behavior of self-stressing SSACFST columns under low cyclic loading is established and validated the experimental results with good agreement.

2. Experimental program

2.1. Specimen design

In this study, ten self-stressing SSACFST columns and four ordinary SSACFST columns (reference columns) are designed and fabricated. To reveal the impacts of P_{ct} on seismic response of self-stressing SSACFST columns under low cyclic loading, an expansive SSAC with P_{ct}=11.1×10^{-4} and a reference SSAC with P_{ct}=-3.4×10^{-4} are designed and used in the experiments. The detailed composition of two types of SSAC are listed in Table 2. The particle size range of steel slag sand and coarse steel sand are 0~4.75mm, and 4.75~26.5 mm, respectively. The photos of steel slag aggregates are shown in Fig .1.

Three other tested variables are also considered, such as axial compression ratio (i.e., n = 0.2 and 0.4), diameter-thickness ratio (i.e., D/t_s= 44.88, 58.71 and 76.84), and shear-span ratio (i.e., λ = 0.91, 1.37 and 1.83). The expansion rate of SSAC is measured in accordance with the method suggested in Chinese code GB/T50082-2009 [28], 100 mm×100 mm×300 mm prismatic specimens are selected. The first group length is measured after 3 days of curing and counted as the initial length of specimens L_0, and thereafter the lengths of the specimens are measured daily and counted as length L_t. The free expansion rate of SSAC can be calculated by Eq (1).

$$P_{ct} = (L_t - L_0)/L_b \tag{1}$$

where, P_{ct} is the free expansion rate of SSAC on day t, L_b is the standard distance of the specimens.

The mineral composition of steel slag are measured by X-ray diffraction and X-ray fluorescence spectrometry, as listed in Table 3. All the specimens are designed to be I-shaped with a total height of 1600 mm. The appearance, dimension and configuration of reinforcement are shown in Fig. 2. Specimen manufacturing process is depicted in Fig. 3. The detailed design parameters of specimens are listed in Table 4.

Table 2
Detailed mechanical properties of SSAC

Type of concrete	Water cement ratio	Material usage / kg.m^{-3}				
		Water	Cement	Steel slag sand	Gravel	Coarse steel slag
Self-stressing SSAC	0.5	189.8	396.3	779.6	777.8	261.1
Reference SSAC	0.58	189.8	326.9	780.6	0	1038.9

Table 3
Mineral composition of steel slag

Mineral composition	CaO (%)	SiO_2 (%)	Al_2O_3 (%)	Fe_2O_3 (%)	MgO (%)	SO_3 (%)	TiO_2 (%)	MnO (%)
Steel slag	52.71	12.97	2.12	19.53	4.31	0.3	1.59	2.21


(a) Steel slag sand (b) Coarse steel slag

Fig. 1 Photos of steel slag aggregates

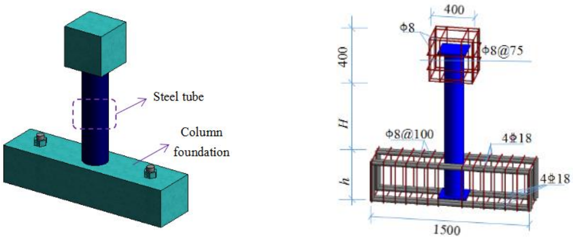

Fig. 2 The dimension of the columns and reinforcement skeleton (unit: mm)


(a) Binding of steel skeleton (b) Template installation


(c) Pouring of concrete (d) Curing of specimen

Fig. 3 Specimen manufacturing process

Table 4
Experimental parameters of the specimens

Specimen	H /mm	D /mm	t_s /mm	n	D/t_s	λ	P_{ct} /10^{-4}
S1-1	800	219	2.85	0.2	76.84	1.83	11.1
S1-2	800	219	3.73	0.2	58.71	1.83	11.1
S1-3	800	219	4.88	0.2	44.88	1.83	11.1
S1-4	600	219	2.85	0.2	76.84	1.37	11.1
S1-5	400	219	2.85	0.2	76.84	0.91	11.1
S1-6	800	219	2.85	0.4	76.84	1.83	11.1
S1-7	800	219	3.73	0.4	58.71	1.83	11.1
S1-8	800	219	4.88	0.4	44.88	1.83	11.1
S1-9	600	219	2.85	0.4	76.84	1.37	11.1
S1-10	400	219	2.85	0.4	76.84	0.91	11.1
S2-1	800	219	2.85	0.2	76.84	1.83	-3.4
S2-2	600	219	2.85	0.2	76.84	1.37	-3.4
S2-3	400	219	2.85	0.2	76.84	0.91	-3.4
S2-4	800	219	2.85	0.4	76.84	1.83	-3.4

Note: H is column length, D denotes outer diameter of steel tube, t_s represents thickness of steel tube.

2.2. Mechanical properties of the materials

The mechanical properties of steel tube and SSAC are measured based on the suggested test methods in Chinese code GB/T228.1-2010 [29] and GB/T 50081-2019 [30], respectively. The measured average yield tensile strength of steel tubes with thickness of 2.85 mm, 3.73 mm and 4.88 mm are 336 MPa, 314 MPa, 308 MPa, and the corresponding ultimate tensile strength are 561 MPa, 532 MPa and 504 MPa, respectively. Fig. 4 depicts the measured stress-strain curves of steel tubes with three different thickness. In this figure, σ_s is the compressive stress of steel tube, ε_z and ε_h represent the circumferential and axial strains, respectively. The compressive strength of the reference SSAC and self-stressing SSAC are 38.27 MPa, 38.40 MPa, and the corresponding elastic modulus are 2.953×10^4 MPa and 2.958×10^4 MPa, respectively.

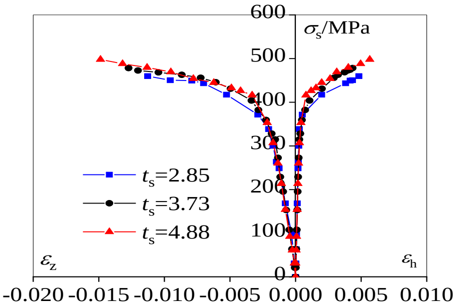

Fig. 4 Stress-strain curves of steel tubes

2.3. Test setup and loading scheme

The constant axial load and the horizontal cyclic load are respectively applied by a 2000 kN hydraulic jack and a 500 kN MTS electro-hydraulic servo actuator on the top of specimens. Initially, single-stage cyclic displacement loading scheme is adopted and the displacement increment is 1 mm. After yielding, single-stage cyclic displacement loading scheme is switched to three-stage cyclic displacement loading, and the displacement of each stage is an integral multiple of the yield displacement. When the horizontal bearing capacity drops to 85% of the ultimate strength, the test is terminated.

3. Experimental results analysis

3.1. Failure modes

According to the test results, the failure modes of columns with low shear-span ratios (i.e., λ=0.91 and 1.37) were basically similar, which were manifested as bending-shear failure, whereas the bending failure dominated the damage of columns with high shear-span ratio (i.e., λ=1.83). The impacts of other three experimental variables (n, D/t_s, and P_{ct}) on the final failure mode were marginal.

In the present study, specimen S1-4 was taken as an example to specify the failure characteristics of the low shear-span ratio specimens. As shown in Fig. 5, the steel tube yielded within 150 mm from the bottom of column. The local buckling appeared about 21 mm away from the bottom of column, where the steel tube formed a two-way drum wave and a horizontal crack was developed at the crest of wave. After experiment, the outer steel tube was stripped, and it was found that the core SSAC was crushed within 40 mm from the bottom of column and presented obvious granular slag. The fracture degree of core SSAC decreased as the n or P_{ct} increased. Besides, a few circumferential and oblique cracks appeared at the bottom of the column, and the width and depth of the cracks were small. No obvious cracks appeared in other parts of the column.

Compared with low shear-span ratio specimens, the steel tube yield range of columns with high shear-span ratio was larger, the local buckling of steel tube was more distinct and the concrete crushing range was larger. Taking the specimen S1-1 as an example, the steel tube yielded within 200 mm from the bottom of column. The yield range of steel tube in specimen S1-1 was approximately 1.33 times than that of in specimen S1-4. The local buckling appeared about 120 mm away from the bottom of column, where the steel tube formed a two-way drum wave and a horizontal crack was developed at the crest of wave. With the increase of the n or P_{ct}, the buckling degree of steel tube decreased, while the influence of the D/t_s on it was insignificant. Similarly, the outer steel tube was peeled off and it was found that the core SSAC was crushed within 50 mm from the bottom of column and presented distinct powder slag. In contrast, the concrete crushing degree of the high shear-span ratio columns was less serious than that of the low shear-span ratio specimens. A small number of circumferential cracks appeared at the bottom of columns, while no distinct cracks appeared in other parts of the columns. The integrity of the core SSAC columns was favorable. The typical failure mode of column with high shear-span ratio is shown in Fig. 6.

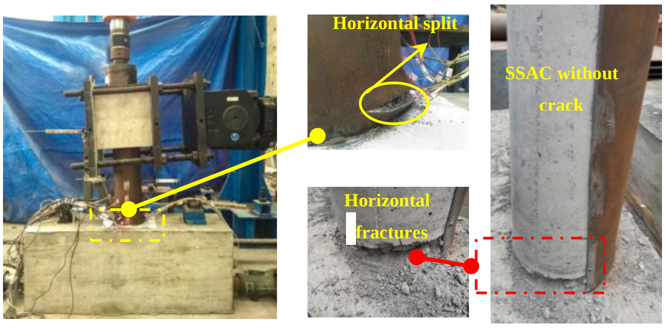

(a) Overall failure mode (b) Local failure mode

Fig. 5 The typical failure mode of column with low shear-span ratio (S1-4)

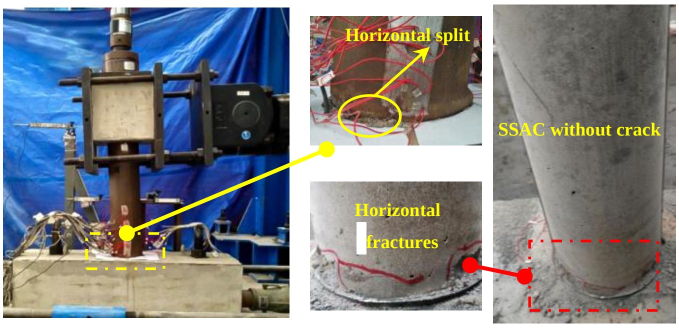

(a) Overall failure mode (b) Local failure mode

Fig. 6 The typical failure mode of column with high shear-span ratio (S1-1)

3.2. Moment-curvature hysteretic curves

The moment-curvature hysteretic curves $M-\phi$ of the specimens are shown in Fig. 7. Initially, all specimens show elastic response, moment and curvature increase linearly, and stiffness degradation is not apparent. Meanwhile, the hysteretic loop area is relatively small. As the load increases, the $M-\phi$ hysteretic curves gradually deviate from the linearity, and the columns come into elastic-plastic stage. At this stage, the hysteretic curves exhibit remarkable fusiform shape, and the hysteretic loop area significantly increases. In plastic stage, the $M-\phi$ hysteretic curves present slight pinch phenomenon when the columns reach the ultimate bearing capacity. The hysteretic loop shape is still similar to fusiform, indicating that the columns show satisfactory energy dissipation capacity.

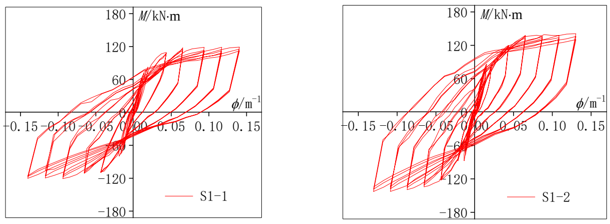

(a) S1-1 (b) S1-2

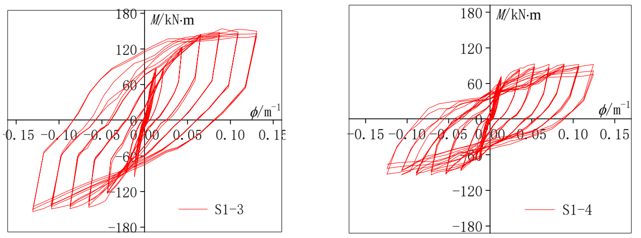

(c) S1-3 (d) S1-4

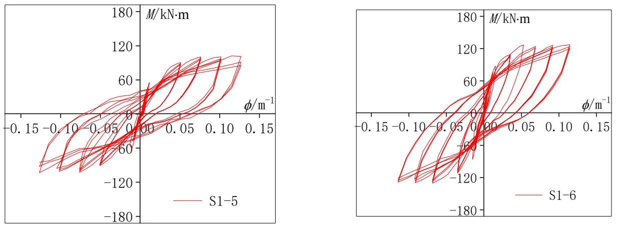

(e) S1-5 (f) S1-6

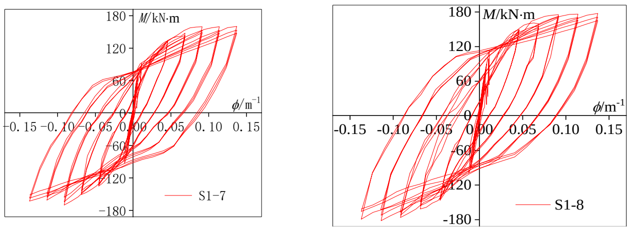

(g) S1-7 (h) S1-8

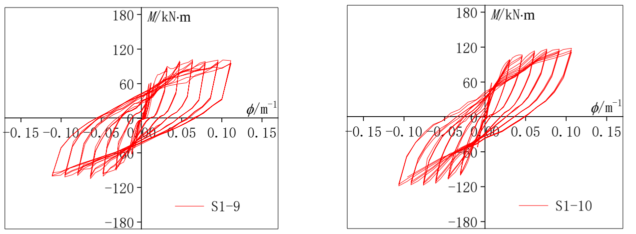

(i) S1-9 (g) S1-10

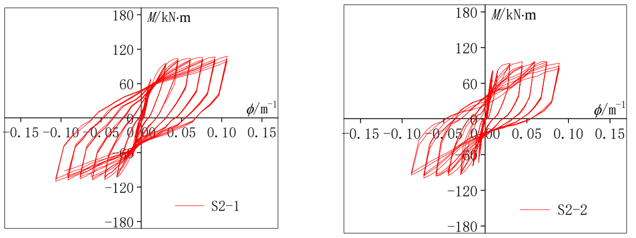

(k) S2-1 (l) S2-2

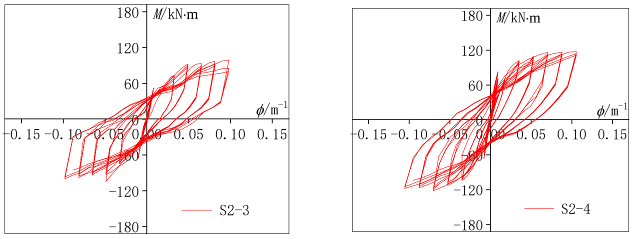

(m) S2-3 (n) S2-4

Fig. 7 The $M-\phi$ hysteresis curves

3.3. Moment-curvature skeleton curves analysis

The $M-\phi$ skeleton curves of self-stressing SSACFST columns are approximately divide into rising and stable stages. In the rising stage, the $M-\phi$ skeleton curves of the specimens increase linearly. As the moment reaches 61%~73% of the ultimate moment, the $M-\phi$ skeleton curves deviate from the linear growth and the turning points appear. As load further increases, the slope of $M-\phi$ skeleton curves decreases gradually and eventually the moment nearly remains constant.

3.3.1. Effect of axial compression ratio

As can be seen from Fig. 8(a), with the enhancement of *n*, the initial stiffness of columns increases, the peak moment increases while the peak curvature decreases. For example, the peak moment of specimen S1-6 increases by 12.7% compared with that of specimen S1-1. This is because increasing the *n*, the lateral stiffness of the column increases, and the ability to resist deformation is strengthened. After reaching the peak moment, the slope of $M-\phi$ skeleton curves of columns with an axial compression ratio of 0.2 decreases relatively slowly compared with those with an axial compression ratio of 0.4, indicating that columns with lower axial compression ratio have better ductility. With the increase of the *n*, the stiffness degradation accelerates and the ductility decreases.

3.3.2. Effect of the shear-span ratio

Fig. 8(b**)** depicts the effect of the λ on $M-\phi$ skeleton curves of the columns. The initial $M-\phi$ skeleton curves are approximately coincident, indicating that the λ has little impact on the initial stiffness. As the λ decreases, the peak moment of columns increases. Compared with specimen S1-1, the peak moment of specimen S1-5 increases by 30.1%. After reaching the peak moment, for the columns with low λ, the descending section of skeleton curves is steeper. The columns with high λ shows favorable ductility and their peak moment decreases slowly. With the decrease of the λ, the effective height of columns decreases, the horizontal shear stress of the column section increases, and the ultimate curvature decreases.

3.3.3. Effect of the diameter-thickness ratio

As illustrated in Fig. 8(c), the initial stiffness of columns with different D/t_s is basically the same. With the decrease of the D/t_s, the peak moment of columns increases, whereas, the impact of D/t_s on the peak curvature is marginal. When the D/t_s decreases from 76.84 (S1-1) to 44.88 (S1-3), the peak moment and peak curvature increase by 58.1% and 5.1%, respectively. The reason is that decreasing the D/t_s increases the steel ratio of specimen, the confinement effect of the outer steel tube on core SSAC is strengthened, the moment resistance of the columns is enhanced.

3.3.4. Effect of the expansion rate of SSAC

As shown in Fig. 8(d), at the initial of loading, specimen with larger P_{ct} shows higher stiffness. This result proves that the existence of self-stressing is beneficial to improve the lateral stiffness of the columns. With the increase of the P_{ct}, the peak moment increases. In contrast, the impact of the P_{ct} on the peak curvature is marginal. For instance, the peak moment and peak curvature of specimen S1-2 increases by 13.6% and 2.4% compared with those of specimen S2-2. This may be due to the fact that with the increase of the P_{ct}, the core SSAC is always in a tri-axial stress state, and the self-stressing makes the outer steel tube have a stronger confinement on core SSAC.

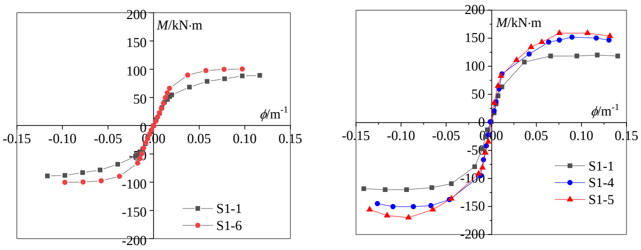

(a) Axial compression ratio (b) Shear-span ratio

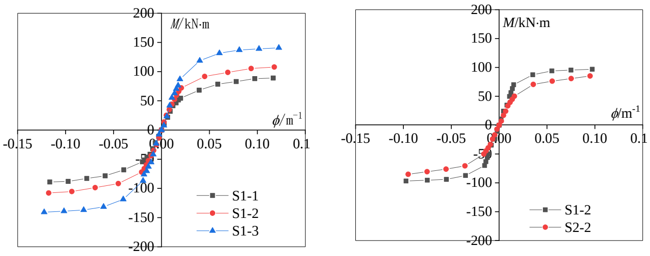

(c) Diameter-thickness ratio (d) Expansion rate of SSAC

Fig. 8 Effect of variable parameters on $M-\phi$ skeleton curves

4. Analytical modeling of moment-curvature

4.1. A model for predicting the $M-\phi$ skeleton curves

In this section, a model for conveniently predicting the $M-\phi$ skeleton curves is proposed based on tri-linear skeleton model of CFST members. The calculated yield peak and ultimate points are connected to form a simplified $M-\phi$ skeleton curve, as shown in Fig. 9.

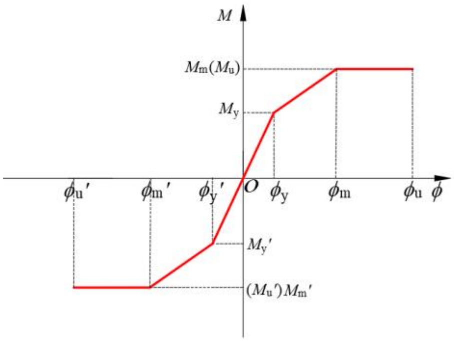

Fig. 9 Simplified $M-\phi$ skeleton curve

4.1.1. Basic assumptions

To develop the simplified $M-\phi$ skeleton curve model, the following assumptions are made.

(1) The self-stressing SSACFST column section conforms to the plane-section hypothesis.

(2) The tensile action of core SSAC is neglected.

(3) The relative slip between steel tube and SSAC is ignored.

(4) The constitutive relationship models of steel tube and self-stressing SSAC are respectively adopted in references [31-32].

4.1.2. Parameters determination

To accurately establish the above simplified $M-\phi$ skeleton model, several key characteristic points, such as yield moment (M_{y}), yield curvature (ϕ_{y}), peak moment (M_{m}), peak curvature (ϕ_{m}), ultimate moment (M_{u}) and ultimate curvature (ϕ_{u}), are needed to be determined.

(1) Yield moment (M_{y})

According to the measured strain values, the circumferential stress of steel tube can be calculated, as shown below.

$$\sigma_{\mathrm{h}}=\frac{E_{\mathrm{s}}}{1+\nu^2}(\varepsilon_{\mathrm{h}}+\nu\varepsilon_{\mathrm{z}}) \tag{2}$$

where, σ_{h} is circumferential stress of steel tube, ε_{h} and ε_{z} are measured circumferential strain and longitudinal strain of steel tube, respectively, ν is Poisson's ratio.

The initial self-stressing of core SSAC can be determined as follows.

$$\sigma_0=\frac{t_{\mathrm{s}}}{R_{\mathrm{c}}}\sigma_{\mathrm{h}} \tag{3}$$

In which, σ_0 is self-stressing of core SSAC and R_{c} is inner radius of core SSAC.

The yield moment of self-stressing SSACFST columns can be determined by the following formula.

$$M_{\mathrm{y}}=\frac{f_{\mathrm{co}}A_{\mathrm{c}}}{\pi}\left(\frac{2}{3}\mu R_{\mathrm{c}}\cos^3\theta_{\mathrm{y}}+(R_{\mathrm{c}}+R_{\mathrm{s}})\ \xi\cos\theta_{\mathrm{y}}\right) \tag{4}$$

where θ_{y} denotes correlation angle of compression zone corresponding to the yield of specimens, $\theta_{\mathrm{y}}=\frac{2.674\mu-2n\pi(\xi+1)}{4\xi+1.849\mu}$, R_{s} is cross-sectional radius of circular steel tube, ξ is constraint effect coefficient, $\xi=f_{\mathrm{y}}A_{\mathrm{s}}/f_{\mathrm{co}}A_{\mathrm{c}}$, $f_{\mathrm{co}}=0.67f_{\mathrm{cu}}$, $\mu=1+4\frac{\sigma_0}{f_{\mathrm{co}}}$, μ represents self-stressing enhancement coefficient.

(2) Yield curvature (ϕ_{y})

In this study, the stiffness of specimens is determined according to EC4 (2004) [33], and the calculation formula can be expressed as follows.

$$K_{\mathrm{e}}=E_{\mathrm{s}}I_{\mathrm{s}}+0.6E_{\mathrm{c}}I_{\mathrm{c}} \tag{5}$$

In which, I_{c} represents the inertia moment of core SSAC section, $I_{\mathrm{c}}=\frac{\pi(D-t_{\mathrm{s}})^4}{64}$, I_{s} denotes the cross-section inertia moment of outer steel tube, $I_{\mathrm{s}}=\frac{\pi D^4}{64}-I_{\mathrm{c}}$.

The calculation formula of yield curvature can be determined as:

$$\phi_{\mathrm{y}}=\frac{M_{\mathrm{y}}}{K_{\mathrm{e}}} \tag{6}$$

(3) Peak moment (M_{m})

The constraint force of axial compression specimens can be determined by the following formula [34] .

$$P_0=\frac{0.067\alpha f_{\mathrm{y}}}{1.2+0.2\alpha} \tag{7}$$

where α is steel ratio, $\alpha=A_{\mathrm{s}}/A_{\mathrm{c}}$.

The non-uniformity coefficient γ is introduced and the relationship between the equivalent constraint force P_{e} and constraint force is established, as shown below.

$$P_{\mathrm{e}}=\gamma P_0 \tag{8}$$

$$\gamma=-942.1\eta^2+146.76\eta+3.62 \tag{9}$$

$$\eta=\sigma_0/f_{\mathrm{co}} \tag{10}$$

In which, η is the self-stressing level of core SSAC.

The calculation formula of the peak moment of self-stressing SSACFST columns is as follows.

$$M_{\mathrm{m}}=\frac{f_{\mathrm{co}}A_{\mathrm{c}}}{\pi}G(\theta,\xi,\mu,\psi) \tag{11}$$

$$G(\theta,\xi,\mu,\psi)=\frac{2}{3}\mu' R_{\mathrm{c}}\cos^3\theta+\psi\xi(R_{\mathrm{c}}+R_{\mathrm{s}})\cos\theta \tag{12}$$

$$\psi=0.737n+1.376\eta-0.00067D/t_{\mathrm{s}}+1.166 \tag{13}$$

$$\mu'=\mu+4P_{\mathrm{e}}/f_{\mathrm{co}} \tag{14}$$

(4) Peak moment (ϕ_{m})

The stiffness of the elastic-plastic section of moment-curvature curves is shown in the following formula.

$$K_{\mathrm{s}}=2792-42.1D/t_{\mathrm{s}}+2034\eta+4223n \tag{15}$$

where, K_{s} is linear elastic-plastic segment stiffness.

The peak curvature of self-stressing SSACFST columns is determined as follows.

$$\phi_{\mathrm{m}}=\frac{M_{\mathrm{m}}-M_{\mathrm{y}}}{K_{\mathrm{s}}}+\phi_{\mathrm{y}} \tag{16}$$

(5) Ultimate moment (M_{u})

In this analysis, to simplify the calculation, it is considered that the peak moment of the columns is equal to the ultimate moment, $M_{\mathrm{u}}=M_{\mathrm{m}}$.

(6) Ultimate curvature (ϕ_{u})

According to the test results, the self-stressing SSACFST column section meets the assumption of plane-section during the loading process. The ultimate curvature can be calculated by the following formula.

$$\phi_{\mathrm{u}} = \frac{\varepsilon_{\mathrm{cu}}}{R_{\mathrm{c}}\left(1-\sin\theta\right)} \tag{17}$$

where, $\varepsilon_{\mathrm{cu}}$ is the ultimate strain of core SSAC, $\varepsilon_{\mathrm{cu}}=110\alpha+0.015\sqrt{f_{\mathrm{cp}}}$, $f_{\mathrm{cp}} = \mu f_{\mathrm{co}} + 4P_{\mathrm{e}}$, $\theta=\frac{\left|2.674\mu' - 2n\pi\left(\xi+1\right)\right|}{4\psi\xi+1.849\mu'}$.

4.1.3. Evaluation of the proposed model

The comparisons between the experimental $M-\phi$ skeleton curves and theoretical $M-\phi$ skeleton curves are shown in Fig. 10. Clearly, the theoretical $M-\phi$ skeleton curves are close to the experimental results, demonstrating that the above proposed model has an acceptable precision.

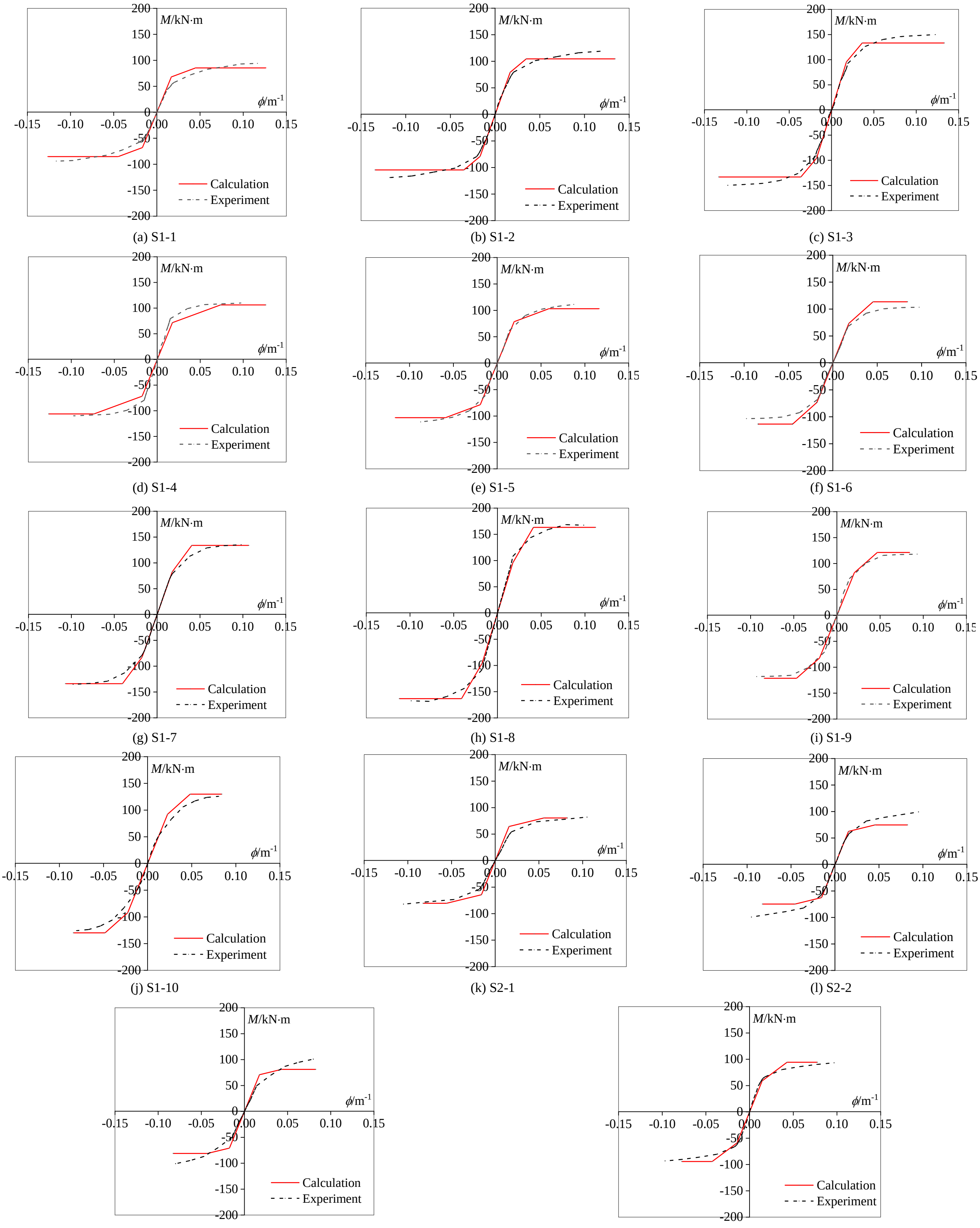

(a) S1-1 (b) S1-2 (c) S1-3

(d) S1-4 (e) S1-5 (f) S1-6

(g) S1-7 (h) S1-8 (i) S1-9

(j) S1-10 (k) S2-1 (l) S2-2

(m) S2-3 (n) S2-4

Fig. 10 The comparisons between the experimental $M-\phi$ skeleton curves and theoretical $M-\phi$ skeleton curves

4.2. Hysteresis rules

To establish a complete model for estimating moment-curvature behavior of self-stressing SSACFST columns, the hysteresis rules are required to be analyzed. As shown in Fig. 11, according to the degradation three-line model, five key parameters, such as elastic stiffness (K_e), moment at point A (M_1), yield moment (M_y), yield curvature (ϕ_y), and stiffness corresponding to the third stage (K_p), needed to be further determined. The specific calculation results are shown in Table 5.

(1) Elastic stiffness

To simplify the analysis, the elastic stiffness (K_e) is calculated according to EC4 (2004) [33] in this study, as shown in Eq (5).

(2) Moment at point A

The moment at point A can be determined by the following equation [32].

$$M_1 = 0.6M_y \tag{18}$$

(3) Yield moment and yield curvature

In this analysis, the yield moment M_y and the yield curvature ϕ_y can be calculated by Eq (4) and Eq (6).

(4) Stiffness corresponding to the third stage

Stiffness corresponding to the third stage K_p is the slope of connecting line segment between the yield point (M_y, ϕ_y) and ultimate point (M_u, ϕ_u) on skeleton curves, which can be calculated by the following formula.

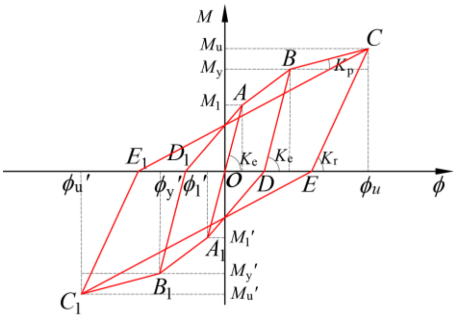

Fig. 11 Loading and unloading rules of the self-stressing SSACFST columns under low cyclic loading

$$K_p = \frac{M_u - M_y}{\phi_u - \phi_y} \tag{19}$$

(5) Softening stage

When the specimen is in elastic stage, the influences of stiffness degradation and residual deformation are ignored, the unloading curve is taken as an oblique line. At this stage, the unloading stiffness is equal to the elastic stiffness, $K_r = K_e$. When the specimen exceeds the elastic stage, the following unloading stiffness calculation formula K_r can be used to consider the degradation of component stiffness.

$$K_r = a_1 K_e \left(\frac{\phi_1}{\phi_y}\right)^{b_1} \tag{20}$$

where K_r is unloading stiffness, ϕ_1 is curvature corresponding to the unloading point of the i-th cyclic stiffness, a_1 and b_1 are the calculated parameters, which are related to n, λ and initial self-stressing σ_0.

$$a_1 = -2.34n + 0.93\lambda + 0.013D/t_s + 0.614\sigma_0 - 1.75 \tag{21}$$

$$b_1 = 0.27n - 0.11\lambda - 0.01D/t_s - 0.37\sigma_0 + 1.74 \tag{22}$$

4.3. Verification of the proposed model

On the basis of the skeleton curve prediction model and hysteresis rules, a model for predicting the $M-\phi$ hysteresis curves of self-stressing SSACFST columns is established. The comparisons between the experimental and theoretical $M-\phi$ hysteresis curves are shown in Fig. 12. It can be seen that the theoretical curves agree well with the experimental curves.

Table 5
Unloading stiffness of the specimens

ID		Variations of unloading stiffness of specimens											
S1-1	ϕ_1/ϕ_y	1.07	2.46	3.96	5.03	6.58	8.48	9.32	11.19				
	K_r/K_e	1.63	1.63	1.57	1.51	1.44	1.35	1.16	0.96				
S1-2	ϕ_1/ϕ_y	1.06	2.33	2.99	3.66	4.32	5.19	6.05	6.91	7.77	8.64	9.66	10.33
	K_r/K_e	1.77	1.78	1.78	1.69	1.61	1.61	1.56	1.57	1.57	1.46	1.37	1.18
S1-3	ϕ_1/ϕ_y	1.01	2.57	3.36	4.14	4.93	5.91	6.90	7.89	8.87	9.86	10.79	12.57
	K_r/K_e	1.96	2.01	1.99	1.94	1.88	1.83	1.81	1.84	1.77	1.76	1.76	1.68
S1-4	ϕ_1/ϕ_y	1.04	1.27	2.91	3.54	4.18	4.81	5.44	6.06	6.69	7.32		
	K_r/K_e	1.14	1.14	1.09	0.98	1.00	1.03	0.98	0.88	0.8	0.77		
S1-5	ϕ_1/ϕ_y	1.13	3.26	4.39	5.52	6.65	7.54	8.42	9.30	10.19	11.07		
	K_r/K_e	1.09	1.00	0.96	1.00	0.90	0.89	0.82	0.86	0.84	0.83		
S1-6	ϕ_1/ϕ_y	1.10	2.4	3.09	3.79	4.49	5.09	5.68	6.28	6.87	7.47	9.10	11.4
	K_r/K_e	1.61	1.64	1.55	1.51	1.47	1.51	1.45	1.38	1.33	1.31	1.31	1.34
S1-7	ϕ_1/ϕ_y	1.12	3.84	5.26	6.68	8.10	8.91	9.72	10.53	11.34	12.16	12.42	13.84
	K_r/K_e	1.63	1.65	1.58	1.52	1.56	1.41	1.42	1.43	1.24	1.21	1.23	1.15
S1-8	ϕ_1/ϕ_y	1.25	3.5	4.75	6.00	7.25	7.98	8.70	9.42	10.15	10.87	12.25	13.5
	K_r/K_e	1.86	1.54	1.35	1.17	1.10	1.11	1.17	1.19	1.20	1.42	1.22	1.24
S1-9	ϕ_1/ϕ_y	1.04	2.28	2.93	3.57	4.21	4.84	5.47	6.11	6.74	7.37		
	K_r/K_e	1.21	1.21	1.18	1.18	1.17	1.05	1.06	1.06	1.06	1.00		
S1-10	ϕ_1/ϕ_y	1.12	5.24	7.35	9.47	10.42	11.36	12.31	13.26	14.26			
	K_r/K_e	1.04	0.95	0.85	0.79	0.79	0.80	0.89	0.85	0.82			
S2-1	ϕ_1/ϕ_y	1.08	2.15	2.73	3.30	3.88	4.92	5.95	6.99	8.03	9.06		
	K_r/K_e	2.28	2.38	2.21	2.57	2.51	1.61	1.41	1.37	1.13	0.97		
S2-2	ϕ_1/ϕ_y	1.02	3.84	5.26	6.68	7.52	8.35	9.18	10.02				
	K_r/K_e	1.72	1.55	1.46	1.44	1.39	1.31	1.35	1.33				
S2-3	ϕ_1/ϕ_y	1.01	4.22	5.83	7.44	8.37	9.30	10.23	11.16				
	K_r/K_e	1.58	1.31	1.11	0.94	1.00	1.07	1.05	1.03				
S2-4	ϕ_1/ϕ_y	1.11	4.33	5.99	7.65	8.63	9.60	10.58	11.55				
	K_r/K_e	1.13	1.14	0.96	0.89	0.86	0.83	0.77	0.78				

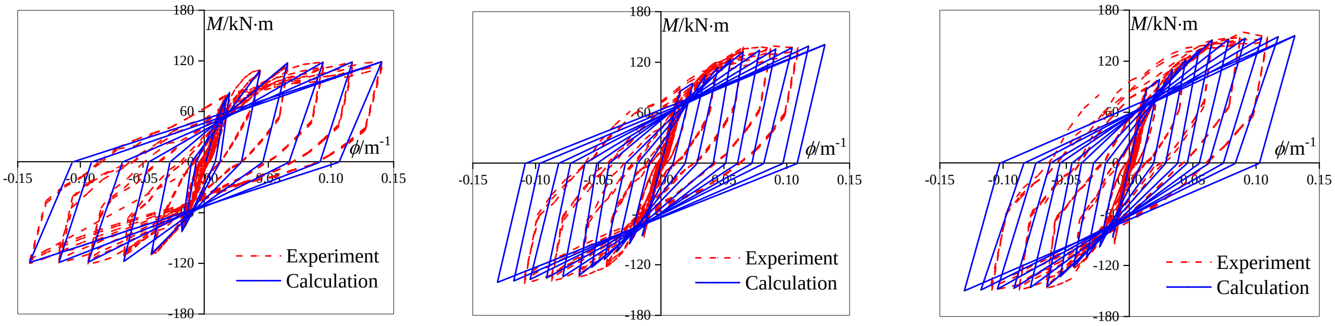

(a) S1-1 (b) S1-2 (c) S1-3

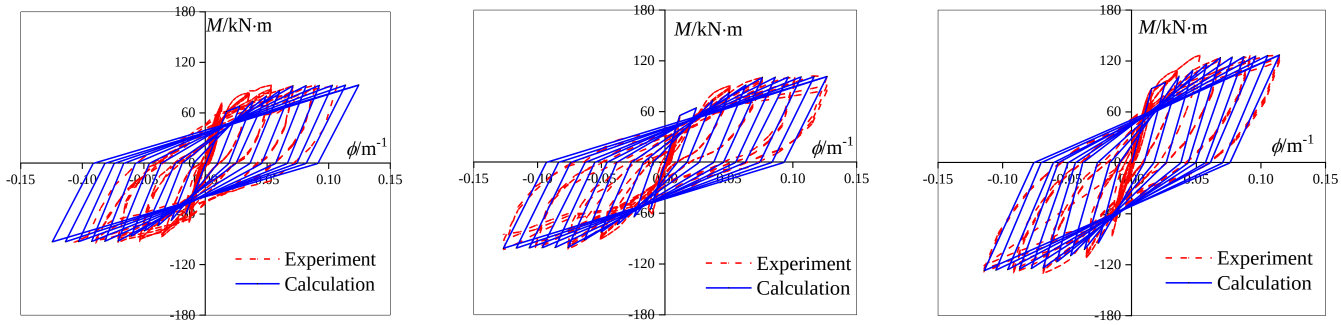

(d) S1-4 (e) S1-5 (f) S1-6

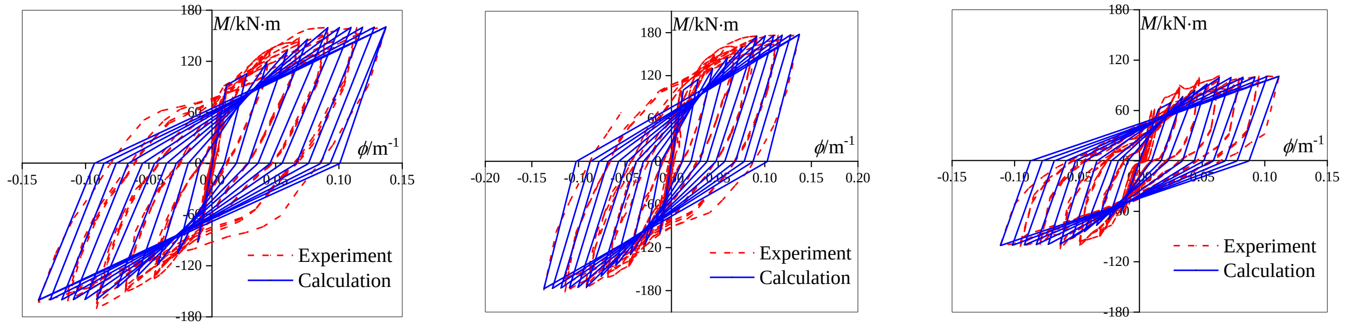

(g) S1-7 (h) S1-8 (i) S1-9

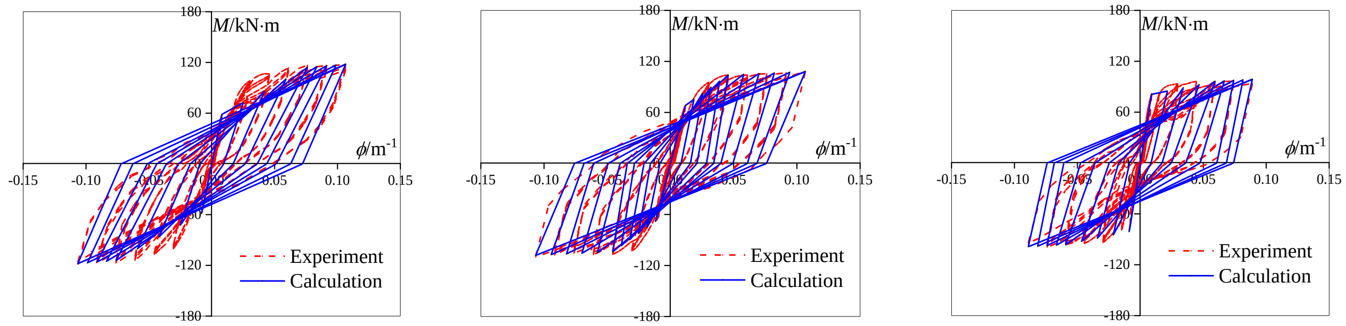

(j) S1-10 (k) S2-1 (l) S2-2

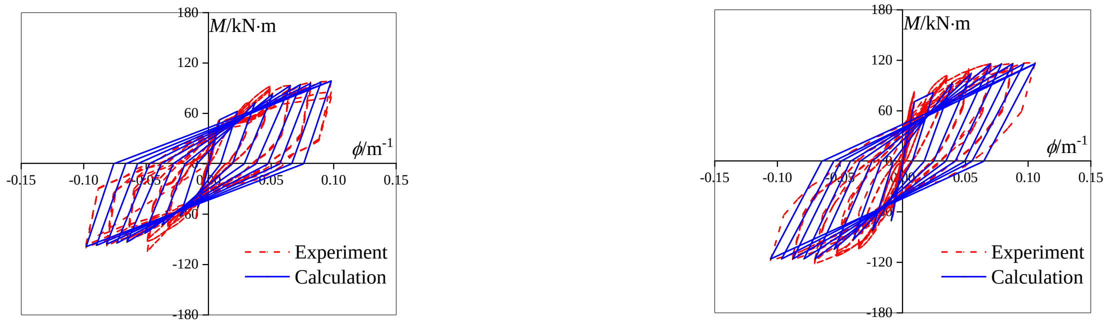

(m) S2-3 (n) S2-4

Fig. 12 Comparisons between the experimental $M-\phi$ hysteresis curves and theoretical $M-\phi$ hysteresis curves

5. Conclusions

In this paper, ten self-stressing SSACFST columns and four ordinary SSACFST columns (reference columns) under low cyclic loading are tested. The effects of axial compression ratio, diameter-thickness ratio, shear-span ratio and expansion rate of SSAC on seismic performances are analyzed.

(1) Under the cyclic loading, the failure mode of self-stressing SSACFST columns with high shear-span ratio exhibits bending failure, while that of the columns with low shear span ratio is bending-shear failure. The other three experimental parameters have insignificant influence on final failure mode.

(2) All specimens initially show elastic response, moment and curvature increase linearly. The $M-\phi$ hysteretic curves gradually deviate from the linearity, the hysteretic curves exhibit remarkable fusiform shape and show satisfactory energy dissipation capacity. The $M-\phi$ hysteretic curves present slight pinch phenomenon at the late loading stage.

(3) With the enhancement of axial compression ratio or expansion rate of SSAC, the peak moment of specimens increases. The increase of shear-span ratio or diameter-thickness ratio decreases the peak moment. The peak curvature of specimens decreases as axial compression ratio increases, while it increases as shear-span ratio increases. The impacts of diameter-thickness ratio and expansion rate of SSAC on the peak curvature are marginal.

(4) A simplified model for predicting the $M-\phi$ skeleton curves of self-stressing SSACFST columns is suggested based on tri-linear skeleton model of CFST members. The hysteretic rules of the specimens are also proposed by analyzing the features of the hysteretic curves. A model for evaluating the moment-curvature behavior of self-stressing SSACFST columns under low cyclic loading is established and validated the experimental results with good agreement.

Acknowledgements

This study was sponsored by the National Natural Science Foundation of China (No.52078001), Outstanding Youth Fund of Anhui Province (No. 2008085J29), Key Research and Development Project of Anhui Province (No. 2022i01020005), Major Science and Technology Project of Anhui Province (No. 202203a07020005), Key Laboratory of Metallurgical Emission Reduction & Resources Recycling (Anhui University of Technology), Ministry of Education (No. JKF22-08).

References

[1] Guo, J. L., Bao, Y. P. and Wang, M., "Steel slag in China: Treatment, recycling, and management", Waste Manage, 2018, Vol. 78, No. 8, pp. 318-330.
[2] Guo, Y., Xie, J., and Zhao, J., "Utilization of unprocessed steel slag as fine aggregate in normal- and high-strength concrete", Constr Build Mater, 2019, Vol. 204, No. 20, pp. 41-49.
[3] Palankar, N., Ravi Shankar, A.U., and Mithun, B.M., "Durability studies on eco-friendly concrete mixes incorporating steel slag as coarse aggregates", Clean Prod, 2016, Vol. 129, No. 15, pp. 437-448.
[4] Saxena, S., Tembhurkar, A.R., "Impact of use of steel slag as coarse aggregate and wastewater on fresh and hardened properties of concrete", Constr Build Mater, 2018, Vol. 165, pp. 126-137.
[5] Lai, M. H., Zou, J., Yao, B., Ho, J.C.M., Zhuang, X., and Wang, Q., "Improving mechanical behavior and microstructure of concrete by using BOF steel slag aggregate", Constr Build Mater, 2021. Vol. 277, 122269.
[6] Netinger, I., Bjegović, D. and Vrhovac, G., "Utilization of steel slag as an aggregate in concrete", Fatigue Fract Eng M, 2011, Vol. 44, No. 9, pp. 1565-1575.
[7] Anastasiou, E., Filikas, K.G. and Stefanidou, M., "Utilization of fine recycled aggregates in concrete with fly ash and steel slag", Constr Build Mater, Vol. 50, No. 1, pp. 154-161.
[8] Gencel, O., Karadag, O., and Oren, O. H., "Steel slag and its applications in cement and concrete technology: A review", Constr Build Mater, 2021, Vol. 283, 122783.
[9] Qasrawi, H., Shalabi, F. and Asi, I., "Use of low CaO unprocessed steel slag in concrete as fine aggregate", Constr Build Mater, 2009, Vol. 23, No. 2, pp. 1118-1125.
[10] Maslehuddin, M., Sharif, A.M., Shameem, M., Ibrahim, M. and Barry, M. S., "Comparison of properties of steel slag and crushed limestone aggregate concretes", Constr Build Mater, 2003, Vol. 17, No. 2, pp. 105-112.
[11] Wang, Q., Yan, P., "Hydration properties of basic oxygen furnace steel slag", Constr. Build. Mater, 2010, Vol. 24, No. 7, pp. 1134-1140.
[12] Wang, X., Ni, W., Li, J.J. and Zhang, S. Q., Michael, H. and Rodrigo. P., "Carbonation of steel slag and gypsum for building materials and associated reaction mechanisms", Cement Concrete Res, 2019, Vol. 125, No. 11, 105893.
[13] Huo, B. B., Li, B. L., Huang, S. Y., Chen, C., Zhang, Y. M. and Banthia, N., "Hydration and soundness properties of phosphoric acid modified steel slag powder", Constr Build Mater, 2020, Vol. 254, No. 11, 119319.
[14] Wang, Q. Wang,, D.Q. and Zhuang, S.Y., "The soundness of steel slag with different free CaO and MgO contents", Constr Build Mater, 2017, Vol. 151, pp. 138-146.
[15] Ukanwa, K.U., Clifton, C.G., Lim, J. B. P., Hicks, S. and Sharma, U. K., "Numerical analysis of plain and steel fiber reinforced concrete filled steel tubular slender column", Adv Steel Constr, 2018, Vol. 14, No. 2, pp. 308-323.
[16] Wang, Q. L., Qu S. E., Shao, Y. B. and Feng, L. M., "Static behavior of axially compressed circular concrete filled cfrp-steel tubular (c-cf-cfrp-st) columns with moderate slenderness ratio", Adv Steel Constr, 2016, Vol. 12, No. 3, pp. 263-295.
[17] Ji, B., Fu, Z., Qu, T. and Wang, M., "Stability behavior of lightweight aggregate concrete filled steel tubular columns under axial compression". Adv Steel Constr, 2013, Vol. 9, No. 1, pp. 1-13.
[18] Xu, L.H., Zhou, P. H., Huang, L., Ye, J. Q. and Yu, M., "Performance of the high-strength self-stressing and self-compacting concrete-filled steel tube columns subjected to the uniaxial compression", Int J Civ Eng, 2018, Vol. 16, No. 9, pp. 1069-1083.
[19] Zhou, S. X., Ma, Y. and Sun, D. S., "The influence of bearing capacity of self-stressed cfst members for different strength grades and self-stressed magnitudes of concrete", Appl. Mech. Mater, 2012, No. 5, pp. 1546-1551.
[20] Li, N., Lu, Y. Y., Li, S. and Gao, D. Y., "Axial compressive behaviour of steel fibre reinforced self-stressing and self-compacting concrete-filled steel tube columns", Eng Struct, 2020, Vol. 222, No. 11, 111108.
[21] Chang, X., Huang, C. K. and Chen, Y. J., "Mechanical performance of eccentrically loaded pre-stressing concrete filled circular steel tube columns by means of expansive cement", Eng Struct, 2009, Vol. 31, No. 11, pp. 2588-2597.
[22] Yu, F., Yao, C., Hu, Y., Fang, Y., Niu, K., and Xiang, G. S., "Axial compressive behavior of self-stressing steel slag aggregate concrete filled steel tubular columns with bond-slip damage", Adv Steel Constr, 2020, Vol. 16, No.1, pp. 13–19.
[23] Shen, Q. H., Gao, H. B., Wang, J. F., and Wang, C. G., "Experimental study on performance of steel slag concrete filled elliptical steel tubular stub columns under axial load", J. Build Struct, 2021, Vol. 42, No.2, pp. 197-203 (in Chinese).
[24] Yu, F., Fang, Y., Zhang, Y. and Xu. L., "Mechanical behavior of self-stressing steel slag aggregate concrete filled steel tubular stub columns", Struct. Concr, 2020, Vol. 4, No. 20. pp. 1597-1611.
[25] Fang, Y., Yu, F., Zhang, Y. Xu, L. and Wang, X. L., "Mechanical behavior and bearing capacity calculation of self-stressing steel slag aggregate reinforced concrete filled circular steel tube columns", Acta Materiae compositae sinica, 2020, Vol. 37, No. 5, pp. 1211-1220 (in Chinese).
[26] Yu, F., Cao, Y., and Fang, Y.,"Mechanical behavior of self-stressing steel slag aggregate concrete filled steel tubular short columns with different loading modes", Struct, 2020, Vol. 26, pp. 947-957.
[27] Feng, P., Li, Z. Y., Zhang, S. B., and Yang, J. Q.,"Steel slag aggregate concrete filled-in FRP tubes: Volume expansion effect and axial compressive behaviour", Constr Build Mater, 2022, Vol. 318, 125961.
[28] GB/T50082-2009, Standard for test methods of long-term performance and durability of ordinary concrete, National Standards of People's Republic of China, Beijing, China, 2009.
[29] GB/T228.1-2010, Metallic materials-Tensile testing-Part 1: Method of test at room temperature, National Standards of People's Republic of China, Beijing, China, 2010.
[30] GB/T 50081-2019, Standard for test method of mechanical properties on ordinary the concrete strength of the concrete, National Standards of People's Republic of China, Beijing, China, 2019.
[31] Han, L.H., Concrete Filled Steel Tube Structure-Theory and Practice, Science Press, Bejing, China, 2016.
[32] Yao, C., Experimental study and theoretical analysis on seismic behavior of self-stressing steel slag aggregate concrete filled steel tubular columns, Master Thesis, Anhui University of Technology, 2020.
[33] Euro code 4, Design of Composite Steel and Concrete Structures, European Committee for Standardization, European, 2004.
[34] Zhong, S. T.,"Theoretical study on limit state of concrete filled steel tubular members under axial compression", Journal of Harbin Institute of Architectural Engineering, 1981, Vol. 1, No. 31, pp. 1-9 (in Chinese).

Advanced Steel Construction – Vol. 18 No. 4 (2022) 745–752
DOI:10.18057/IJASC.2022.18.4.2

SHEAR BEHAVIOR OF NOVEL DEMOUNTABLE BOLTED SHEAR CONNECTOR FOR PREFABRICATED COMPOSITE BEAM

Yun-Biao Luo [1, 2], Shuo-Ke Sun [2], Jia-Bao Yan [1, 2, *], Yu-Cai Zhao [2] and Dennis Lam [3]

[1] *Key Laboratory of Earthquake Engineering and Engineering Vibration, Institute of Engineering Mechanics, China Earthquake Administration, Harbin, 150080, China*
Key Laboratory of Earthquake Disaster Mitigation, Ministry of Emergency Management, Harbin,150080, China
[2] *School of Civil Engineering, Tianjin University, Tianjin 300350, China*
[3] *Department of Civil and Structural Engineering, University of Bradford, Bradford, West Yorkshire, BD7 1DP, UK*
** (Corresponding author: E-mail: yanj@tju.edu.cn)*

ABSTRACT

Bolted shear connectors offer alternatives to achieve steel-concrete composite action instead of conventional welded headed studs especially for prefabricated constructions and demountable composite structures. This paper firstly proposed a new type of demountable steel-concrete bolted shear connectors based on the double-nut friction-grip high strength bolted connector, which modify the upper nut into conical locking nut. This paper performed ten full scale push-out tests to study shear behaviors of the developed new type of connectors. Testing parameters included bolt configuration, strength, diameter of bolts and strength of infilled grout. Test results indicate that shear behaviors and slip capacity of the conventional bolted connectors are significantly improved when the bolted connector incorporating with conical locking nut. The influences of these studied parameters on shear behaviour of novel bolted shear connectors are revealed and discussed. The developed novel demountable connector exhibits an average 25% improvement in ultimate shear resistance over conventional bolted connectors. Moreover, the shear stiffness of the developed bolted connectors is about six times of the conventional bolted connector through eliminating the clearance between steel flange hole and bolt shank.

ARTICLE HISTORY

Received:	23 October 2021
Revised:	25 April 2022
Accepted:	2 May 2022

KEYWORDS

Bolted connector;
Demountable shear connector;
Push-out test;
Composite structures

1. Introduction

Owing to the combined advantages of steel tension and concrete compression, steel-concrete composite structures (SCCSs) becomes popular and put into use in civil engineering constructions. The steel-concrete composite action in SCCSs is usually achieved using shear connectors. Various kinds of connectors have been proposed for SCCCs among which welded headed studs may be the most widely used type of connector due to easy installation, high capacity and low cost. However, considering the sustainability of steel-concrete composite structures such as steel frame with decking floor slab and bridges with steel-concrete composite girders, replacement, rehabilitation or strengthening needs to exerting to extend their service life. The composite structural components with embedded welded headed stud shear connectors will face challenge due to their difficult removal and recycle use in the reconstruction process.

In comparisons with traditional welded headed studs, post-installed high strength bolts exhibit more advantages of easy disassembling and rapid replacement of the concrete parts. Such bolted connectors can extend the life cycle and improves the sustainability of SCCSs. Moreover, bolted connectors exhibit more significant advantages of shortened construction period, reduced labor force for casting on site, improved construction quality, and savings on constructional costing for prefabricated constructions. Therefore, researches on shear performance of bolted connectors are important for in-depth understanding on structural behavior of prefabricated steel-concrete composite members.

Dedic and Klaiber [1] carried out push-off tests to study mechanical behavior of high strength bolts. Kwon et al. [2] conducted push-out tests on post-installed bolt connectors (PIBCs), and found that they exhibit higher fatigue resistance than welded headed studs. Kwon et al. [3] proposed a strengthening strategy for non-composite bridge girder using PIBCs, and their strengthening effectiveness was confirmed through five full-scale beam tests. Pavlović et al. [4] proposed high-strength friction-grip (HSFG hereafter) bolts for prefabricated composite structures and examined the shear performance of M16 and M24 HSFG bolts by push-out tests. Moynihan and Allwood [5] conducted static loading test for composite beam using M20 HSFG bolts, to investigate their mechanical performance. Dai and Lam [6] developed a novel type of bolted connectors through machining headed studs that achieved about 84% ultimate shear resistance of welded headed studs. Moreover, it achieved a slip capacity of more than 6 mm as observed in the corresponding push-out tests. Liu et al. [7] studied the mechanical behavior of HSFG bolts in composite beam with precast slabs. The load-slip behavior of bolted connector showed identified three distinct stages with excellent shear behaviors. Ataei et al. [8] further investigated structural performances of composite beam using bolted connectors developed by Liu et al. [7]. Ban et al. [9], Henderson et al. [10,11] and Pathirana et al.[12] contributed to structural behaviors of composite beams using blind-bolt type of connectors. They observed that compared with welded headed studs, blind bolts offered comparable composite actions to SCCSs. Yang et al.[13] performed push-out tests to investigate shear behaviors of novel demountable bolted connectors. Their test results showed that the shear stiffness of their novel bolted connectors was significantly affected by the shank-hole clearance of bolts.

2. The development of locking nut shear connectors

Nonetheless, it should be noticed that all the previous tests on HSFG bolted connectors exhibit an unfavorable large early stage slip. Such bolts sliding occurs inside the bolt holes as the acting shear load exceeds the slab-steel beam interfacial friction resistance. Therefore, although Eurocode 4 [14] includes HSFG bolts type of connectors, restrictions are imposed to prevent the fully exploitation of their shear resistance. Johnson and Buckby [15] suggested that for friction-grip bolts, their shear resistances should be limited by the friction resistance if they are used as shear connectors. To overcome such problem of the friction-grip bolts as shear connector, Suwaed et al. [16] proposed a locking nut shear connector (LNSC hereafter) as shown in Fig.1. In the proposed LNSC, a special conical locking nut configuration, restricting the slipping of bolts within the holes, is adopted to connect the bolts to beam flange. In addition, in the locking nut shear connectors, the two ends threaded bolts with conical locking nut work with precast concrete plugs and plate washers. Pretension load is applied to the bolts shank between the lower No. 1 nut and the upper conical locking No. 2 nut to fasten the bolt as shown in Fig.1, and also applied to the bolts shank between Nut 3 and Nut 2 to produce friction resistance between the steel beam flange and the precast concrete plugs.

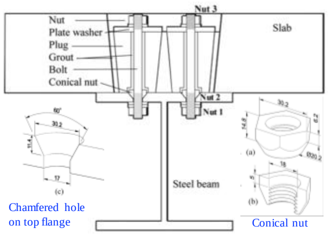

Fig. 1 Cross section of composite beam using locking nut shear connectors [17]

Suwaed et al. [17] carried out push-out tests to investigate the shear behavior of novel LNSC. Their test results showed that the shear resistance, shear stiffness, and slip capacity are much higher than welded headed studs. However, although the shear performance is proved to be satisfactory, yet the configurations, which includes too many components and are rather complicated for on-site assembly.

This paper proposed a simplified application of the LNSC for steel-precast concrete composite beam as shown in Fig. 2. In such application, the configurations of grout plug, slab pockets and plate washer are not included, only the bolted connector with conical locking nut and the chamfered countersunk seat on beam flange remains. Briefly speaking, the LNSCs are proposed to substitute HSFG bolted connectors in the steel-precast concrete composite structure.

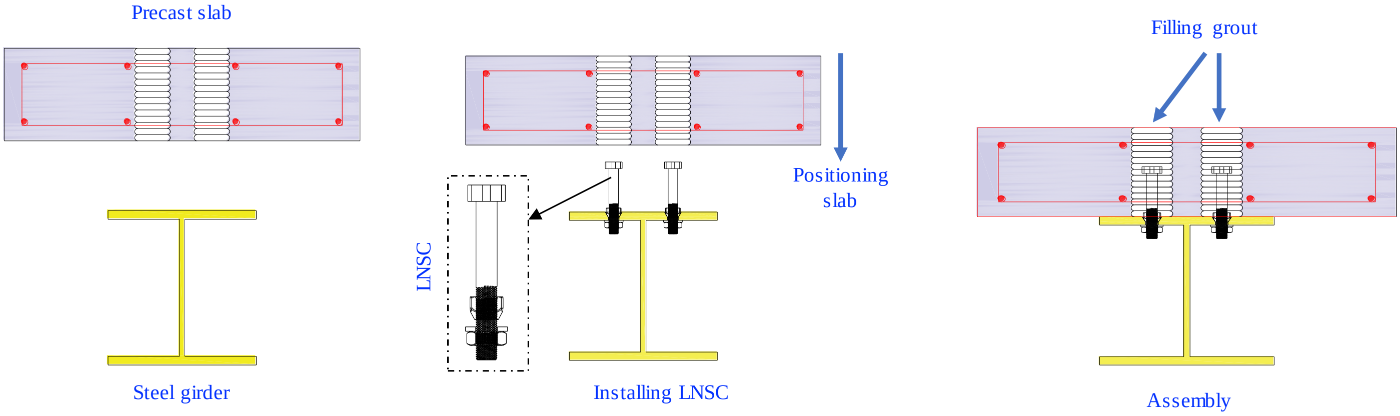

(a) (b) (c)

Fig. 2 Assembly of steel-precast concrete composite beam using LNSC

The LNSC is expected have several advantages against conventional HSFG bolt connector, which are: (1) larger shear stiffness due to the elimination of bolt slip between bolt shank and bolt hole; (2) larger shear capacity due to the shear contribution from the conical nut; (3) more favorable shear-slip behavior as shear connector; (4) require lower pretension load to fasten the bolted due to its locking nut mechanism.

Nonetheless, the mechanical behavior of LNSC connects steel beam and precast slab, with embedding in preformed hole filled with grout, has not been investigated through experimental study. The main purposes of this study are to check the shear performance of bolted connector post-installed in steel-precast concrete composite beam, with the configurations of locking conical nut and chamfered countersunk seat.

3. Details of push-out test specimens

3.1. Bolt configuration

Fig. 3 shows the configuration for the conventional HSFG bolt and the novel demountable LNSC, and geometric details of novel bolted connectors installed to the steel beam flange in the test specimens.

As shown in Fig.3a, the conventional HSFG bolted connection consist of a bolt shank with thread and an upper hexagonal nut, an upper washer, a lower washer, and a lower hexagonal nut. Between the upper and lower nut, preloading was applied to fasten the bolted connectors to underneath steel beam.

The novel demountable LNSC bolted connector is proposed on the basis of the HSFG bolts, with the root of upper nut in the conical shape. The bolts are with threads in a length of 70 mm at in one end. The bolts are installed to the flange of steel beam through the two clapping nuts as shown in Fig.3(b). The upper part of bolt hole is a countersunk seat with chamfered sides in 60-degree to horizontal direction, as shown in Fig.3(b). The upper conical nut is modified on the basis of a standard hexagonal nut, with the lower part machined in to conical shape following the same 60-degree angle to fit the bottom countersunk seat in the flange of beam. Thus, the upper conical nut restrains the bolt within the countersunk seat. While the lower part of conical nut fits into the chamfered hole, the upper part of conical nut appears above the top surface of the beam flange with a height of a few millimeters. Such upper part of conical nut appeared above the flange-slab interface is expected to play a role similar to welded collar of headed stud shear connectors, the positive effect of which on shear resistance have been reported by many experimental and numerical studies. The lower hexagonal nut is used along with a hardened washer [see Fig.3(b)]. Pretension is applied to bolts between the upper conical nut and the lower hexagonal nut by fastening the lower nut using a torque wrench.

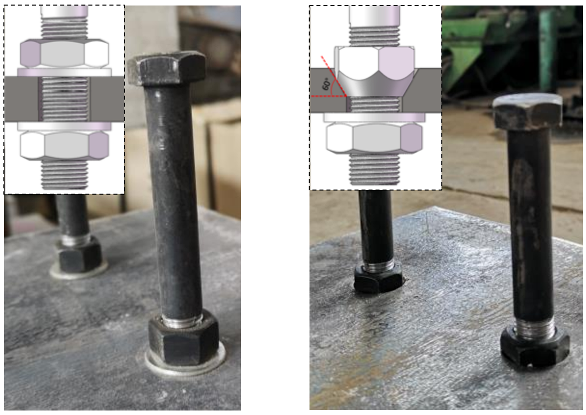

(a) Configurations of HSFG bolt (b) Configurations of LNSC bolt

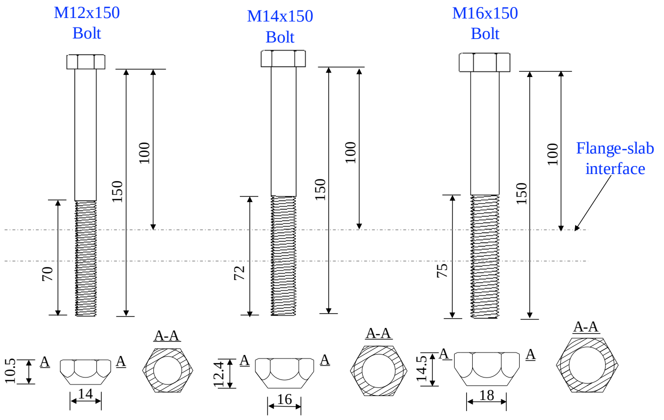

(c) Dimensions and details of the bolted connectors

Fig. 3 Configurations and dimension of bolted connectors

Bolts with nominal diameter of M12, M14 and M16 were selected as bolted connectors for the push-out tests as depicted in Fig.3(c). The height of bolted connector is 150 mm with varying length of threads of 70 mm, 72 mm and 75 mm. All the embedded length of bolts in the concrete slab is 100 mm. The dimensions of nut vary when the corresponding nominal diameter of bolts changes from 12 to 16 mm. The height of M12, M14 and M16 bolt nuts are 10.5, 12.4, and 14.5 mm, respectively. The inclined angle of the conical part of the upper nut is a 60-degree angle. The lower part of the conical nut is grinded following such 60-degree angle till the external diameter of the lower end of nut is 2 mm larger than the nominal diameter of the corresponding bolt.

The pretension load, which represents 20% of its ultimate tensile resistance is applied between the upper conical nut and the lower hexagonal nut using a torque wrench. By applying such pretension load, a robust locking configuration is ensured, and bolts from slipping within the bolt hole can be prevented. It should be noticed that, the applied pretension load is relatively low when compared to that of 70% of its ultimate tensile capacity, which was adopted in LNSC application suggested by Suwaed and Karavasilis[17]. Such relatively low pretension load is determined based on the following consideration. According to experimental study and numerical analysis by Pavlović et al. [4], it was not found any influence on shear resistance for pretension load up to 100% of the ultimate tensile capacity. Therefore, bolt preload does not have significant influence on the shear resistance when the failure mode is shear-off of bolt shank.

The ultimate tensile strength of bolted connectors was obtained from uniaxial tensile tests. The ISO bolt grades, ultimate tensile resistance, the gross diameter for bolt shank and effective diameter for bolt thread part, for each group of high strength bolts are summarized in Table 1. It reflects that, the gross diameter is slightly smaller than nominal diameter of bolts, and effective sectional area in thread region of bolts to its sectional area out of thread region equals to about 0.8. The tensile strength is calculated by dividing the tensile force to the effective area.

Table 1
Tensile strength and dimension of bolts

Bolts group	Tensial resistance （kN）	Gross diameter (mm)	Effective diameter (mm)	Effective area/Gross area	Tensile strength (MPa)
M12 (8.8)	91.0	11.86	10.08	0.83	1140.3
M14 (8.8)	124.4	13.88	12.12	0.76	1078.3
M14 (10.9)	146.2	13.88	12.08	0.76	1308.8
M16 (8.8)	169.7	15.78	14.14	0.80	1012.5

3.2. Specimen details

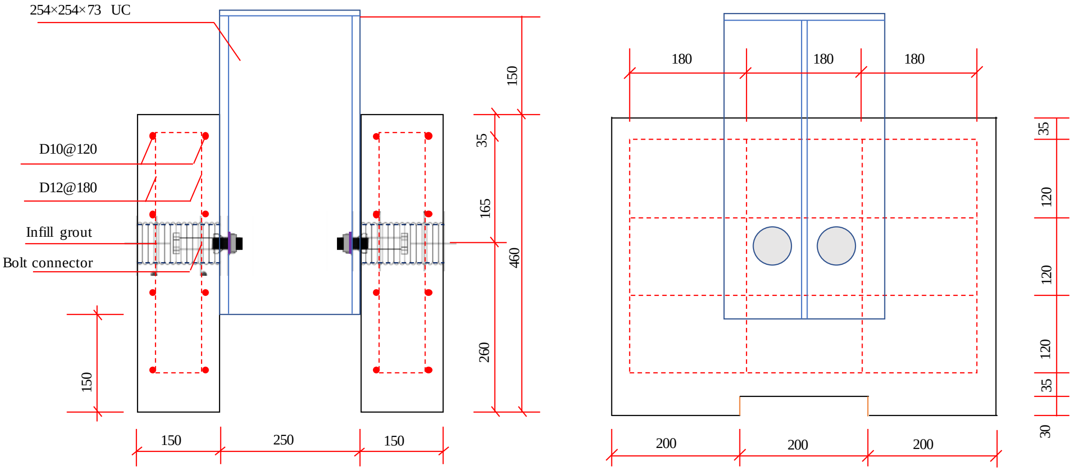

Fig. 4 Geometric configuration of push-out test specimens (unit: mm)

3.2. Specimen details

Totally ten push-out specimens were fabricated with different parameters and divided into five groups as summarized in Table 2. The tested parameters are diameter of bolts (M12, M14 and M16), bolt configuration (conventional HSFG bolts and novel demountable bolts), steel grade of bolt (grade 8.8 and grade 10.9), and the strength of infilled grout. Each push-out specimen consists of a steel beam segment with 254 × 254 × 73 UC section and two precast concrete slabs (see Fig. 4). The dimensions of all the test specimens are the same following EN 1994-1-1. The length, width and thickness of the precast concrete slab are 460, 600, and 150 mm, respectively. Each precast concrete slab was cast with two preformed holes using PVC corrugated tube, which is 50 mm in diameter and 1.5 mm in thickness. Steel reinforcements for concrete slabs were designed accordingly to Eurocode 4. The precast concrete slabs were all cast in a horizontal position.

Table 2
Parameters of push-out specimens

Group	Specimen	Diameter of bolt (mm)	Strength grade	Bolt configuration	Grade of infilled group
SP1	SP1-1	14	Grade 8.8	Conical nut	C50
	SP1-2				C90
SP2	SP2-1	12			C50
	SP2-2				C90
SP3	SP3-1	16			C50
	SP3-2				C90
SP4	SP4-1	14	Grade 10.9		C50
	SP4-2				C90
SP5	SP5-1	14	Grade 8.8	HSFG bolt	C50
	SP5-2				C90

Fig. 5 illustrates key steps of the prefabrication of specimens, which includes machining of conical nuts on the basis of the standard hexagonal nut, drilling chamfered holes on beam flange, positioning and fastening the bolts by the locking nut configuration, as well as casting concrete slabs with performed holes, were performed in the workshop. After fabrication of all these components, the assembly of the steel beam and precast concrete slabs was performed. First, a pair of bolts were installed on the top flange of beam. Each precast slab is installed on the top of steel beam to make sure its opening geometric center coincide with the center of two installed bolts. Fast-hardening infilled grout is then poured into the preformed holes in precast slab. After seven-days hardening of the grout, the specimens was turned up-side-down, and the same assembly procedures were implemented between the precast concrete slab and the steel beam at opposite side. Hardening of infilled grout completes the whole fabrication process of the push-out specimen.

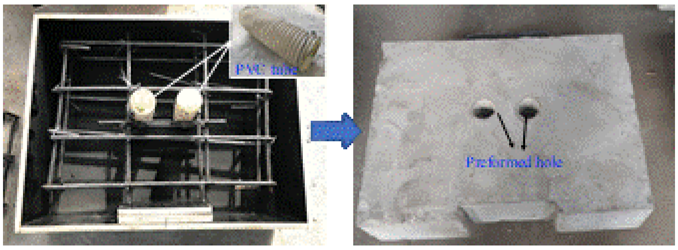

(a) Casting of precast concrete slab with preformed hole

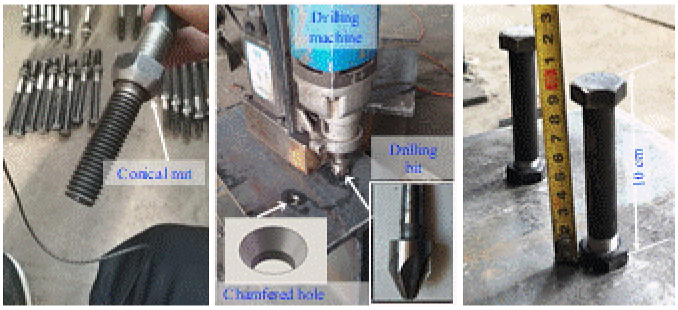

(b) Machining of conical nut, drilling chamfered hole and bolt positioning

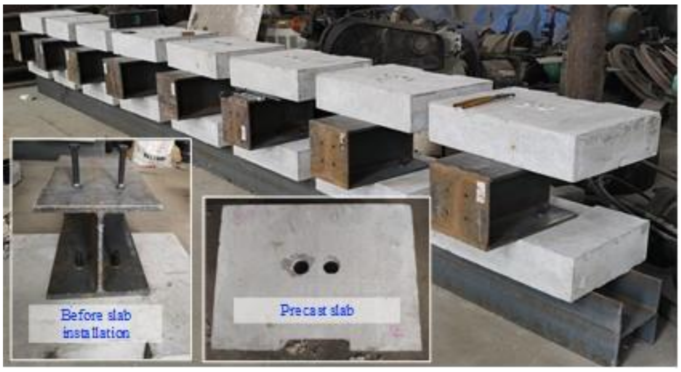

(c) Assembling of specimens

Fig. 5 Fabrication of specimens

The design mixes for the concrete slabs and the grout are given in Table 3. The grout used to fill the preformed holes are commercial cementitious grout with nominal strength of C50 and C90. The material properties of the concrete slab, infilled grout and steel beam were evaluated. Cylinder specimens for concrete and grout, with a 100-mm diameter and 200-mm height, were used to obtain the respective compressive strength. The elastic modulus, tensile strength and characteristic compressive strength were calculated based on ACI 318-08 [18].

Table 3
Typical Mix proportions and material strength for slab and grout

Material	Slabs	Grout C50	Grout C90
Cement (kg/m3)	432	-	-
Water (kg/m3)	168	-	-
Sand (kg/m3)	558	-	-
Gravel (kg/m3)	1242	-	-
Compressive strength (MPa)	42.3	49.8	95.1
Tensile strength (MPa)	3.2	2.6	4.5

3.3. Test setup and measurement

Fig. 6 shows the setup and instrumentations of push-out tests. The specimen was installed on a rigid base and tested by a loading machine with a capacity of 5,000 kN. The displacement load was applied to the top end of I-beam. Vertical displacements of loading end of specimens were measured by two linear variable displacement transducers (LVDTs) as shown in Fig. 6. Four LVDTs attached to the concrete slab, with two LVDTs in the front and back, measured concrete slab-steel beam interfacial slips. The precision of the LVDTs is 1/1000 mm.

During the test, the uniaxial displacement-controlled load was applied to the specimen with a speed of 1/10 mm/min. The load-slip behavior was measured until the applied load was reduced to 20% of the obtained maximum load.

Fig. 6 Test setup and instrumentation

4. Test results

4.1. Failure mode

Failure modes of all the five groups of push-out specimens were shearing of bolts directly from the I-beam at the threaded portion of bolts. As shown in Fig.7(a), the specimens with LNSC all exhibit bolt shear off at the section right above the upper conical nut; meanwhile, in the specimens with conventional high strength friction grip bolts the shear off section locates at right below the upper hexagonal nut, aligning to the interface between the top flange and the concrete slab.

Fig. 7(b) illustrates the damage on concrete slab of tested specimens. It can be noted that only minor spalling occurred to slabs without global cracking or splitting. The local spalling of concrete occurred mainly within the region of infilled grout surrounding the bolt. The chamfered hole on steel flange sustained the shear force transferred through the conical nut during the push-out loading.

Fig. 7(c) illustrates the local deformation of chamfered hole after removing the fractured bolted connector. It shows that no obvious deformation occurred to the steel around the chamfered hole in the specimens SP1-1 with M14 bolts (grade 8.8), while slight local deformation in front of chamfered hole can be found in the specimen SP3-1 with M16 bolts (grade 8.8), which had developed the largest shear capacity among all the tested specimens.

SP1-1M14 (8.8) SP2-1M12 (8.8) SP3-2 M16 (8.8) SP4-2 M14 (10.9) SP5-1M14 (8.8)

(a) Bolted connector after shearing off

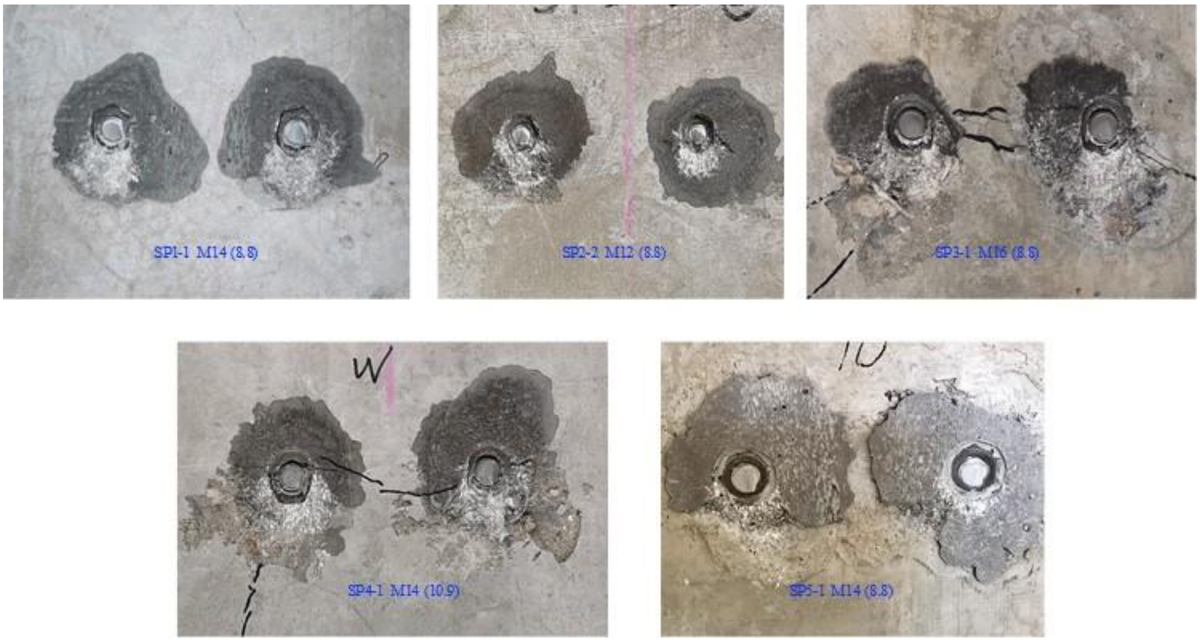

(b) Damage on concrete slab

(c) Steel beam flange after removing failure bolts

Fig. 7 Failure modes and damages of specimens

4.2. Shear-slip relationship curves

Fig. 8(a)~(e) plots the load-slip curves of tested specimens. The curves in each sub-figure are obtained from the test results of specimens varied only in strength of infilled grout, grade C50 for the first series (denoted with '-1'in the nomination of specimen) and grade C90 for the second series (denoted with '-2'in the nomination of specimen). The load of single connector was obtained through dividing the total measured force over total number of connectors, while the relative slip between the slab and steel flange was obtained by taking average of the measured values from the four LVTDs.

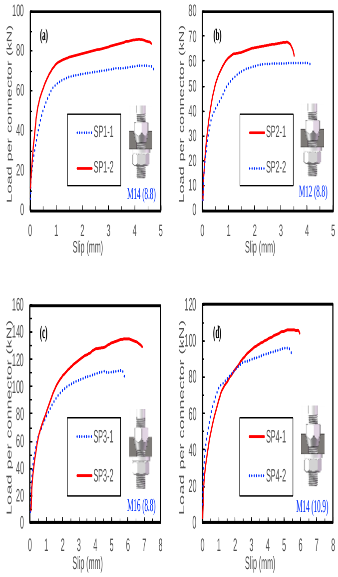

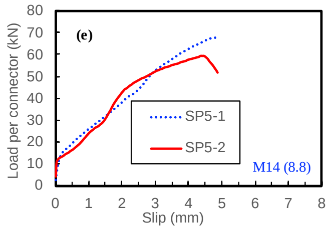

Fig. 8 Shear-slip curves for push-out specimens

Test results including the shear resistance, the ultimate slip capacity, and the shear stiffness are summarized in Table 4. The shear stiffness (*K*) for each bolted connector is defined as the ratio of 70% of the shear resistance (Vu) to its corresponding slip value sk [19] as specified in Clause A.3(3) of EN 1994-1-1.The shear resistance V_u and the slippage corresponding to $0.7V_u$ are obtained from the tested shear-slip relationship curves. The results are discussed in the following sections.

Table 4

Summary of push-out test results

Spec.	V_u(kN)	T_u(kN)	V_u/T_u	s_u(mm)	$0.7V_u$(kN)	s_k(mm)	K(kN/mm)
SP1-1	72.8	124.4	0.585	4.73	50.94	0.521	97.9
SP1-2	86.1		0.692	4.64	60.26	0.473	127.5
SP2-1	59.2	91	0.651	4.17	41.41	0.413	114.3
SP2-2	67.4		0.741	3.50	47.19	0.546	75.8
SP3-1	111.6	169.7	0.658	5.78	78.09	1.006	77.6
SP3-2	135.7		0.800	6.89	94.98	1.386	68.5
SP4-1	96.4	146.2	0.659	5.44	67.47	1.286	57.6
SP4-2	105.9		0.724	5.96	74.12	0.737	91.5
SP5-1	67.6	124.4	0.543	4.92	47.3	2.692	17.6
SP5-2	59.5		0.478	4.88	41.65	1.952	21.3

5. Discussions

The main test parameter included configuration of bolted connector (with/without conical nut), diameter, strength of bolts, and compressive strength of infilled grout. The effects of these parameters are discussed below.

5.1. Effect of the strength of infilled grout

For the specimens using bolted connector with conical locking nut, as shown in Fig.8(a)~(d), it can be noticed that the specimens with higher strength of infilled grout developed larger shear resistance, it may owe to the fact that stronger grout around the bolted connector provided larger confining effect to the connector, thus increased the ultimate shear capacity. Fig.8(e) compares the shear-slip curves of specimens SP5-1 and SP5-2, in which the conventional HSFG bolts were used, it can be found that using stronger infilled grout did not increase the ultimate shear capacity. Nonetheless, the ultimate relative slip does not seem to be relative with the strength of the infilled grout.

5.2. Effect of the bolt configuration

Two types of configuration of bolted connector, conventional bolt with single nut embedded in slab and novel bolt with conical locking nut embedded in slab and chamfered hole on steel flange, are used in specimen group SP1 and SP5, respectively. The bolt shear off locations for different shear connectors are compared in Fig.9. The shank of HSFG bolt shear off at the cross-section along the beam flange-concrete slab interface, while the shank of LNSC bolt shear off at the cross-section right above the conical locking nut. As show in Fig.7, after the shank shear off, the end part of the HSFG bolt and the lower nut detach from the concrete slab and steel beam flange; while in the LNSC bolt, after the shank shear off, the conical locking nut and the lower nut still fasten to the beam flange, and crushed infilled grout remain in front the of conical locking nut, which indicates that the conical locking nut have sustained large load from the surrounding infilled grout.

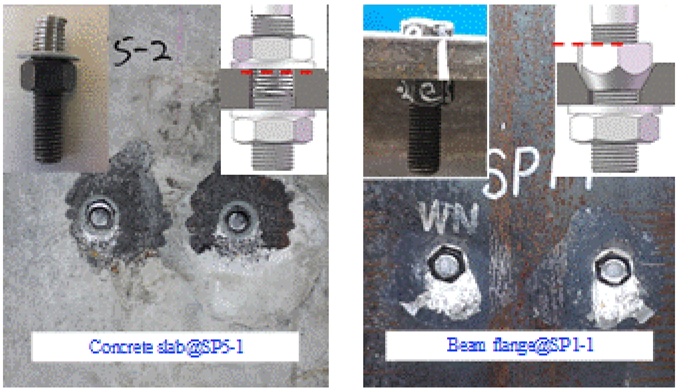

(a) HSFG bolt specimen (b) LNSC bolt specimen

Fig. 9 Comparison on bolt shear off locations

The load-slip curves are compared in Fig.10. The curves for the two configurations are significantly different. The specimens with conical locking nut exhibit a shear-slip relationship with much larger initial stiffness and more than 25% larger shear resistance than the specimens with conventional bolt configuration. This is a favorable mechanical property for shear connector used in composite structural element, since it avoids the drawbacks of the conventional bolted connector that its shear stiffness is very sensitive to the clearance between bolt shank and flange hole [13].

As shown in Table.4, the average shear stiffness of specimens SP1-1 and SP1-2 is 112.7 kN/mm, while the average shear stiffness of specimens SP5-1 and SP5-2 is 19.4 kN/mm. The shear stiffness of specimens with the developed novel demountable bolted connectors is about 600% of that of specimens with conventional HSFG bolted connectors.

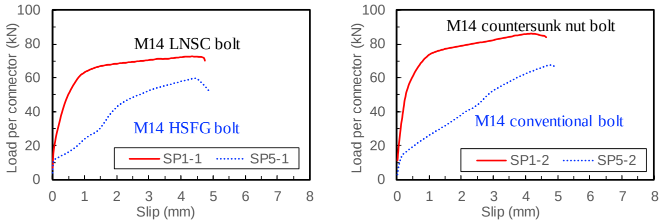

Fig. 10 Specimens with different bolt configurations

5.3. Effect of the diameter of bolt

Shank diameter is a critical parameter for shear capacity of shear connector. Specimens with different nominal bolt diameters, 12 mm, 14 mm and 16 mm, are compared in Fig.11. The shear capacity as well as the ultimate slip increase as the bolt diameter increases. The effective cross section area of M16 bolt and M14 bolt are 1.71 and 1.26 times of that for M12 bolt, and 1.86 times and 1.36 times of shear capacity were developed in the M16 bolt and M14 bolt.

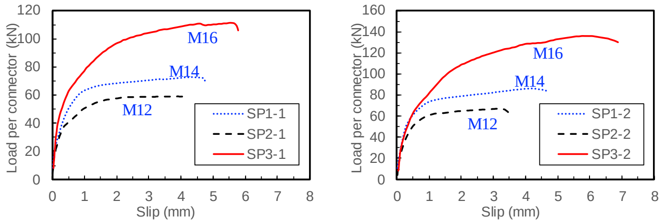

Fig. 11 Specimens with different bolt diameter

5.4. Effect of the strength of bolt

The effect of bolt strength is verified by adopting different grades of bolts for the bolted connector, which are grade 8.8 and grade 10.9. Specimens with grade 10.9 bolted connector developed about 25% larger shear capacity than those with grade 8.8, as shown in Fig.12. It can be also found that specimens with higher bolt strength shown larger ultimate slip, this is because of the reason that bolted connector with higher strength caused larger plastic deformation to the surrounding grout thus the connector can deform more before its final sheared off.

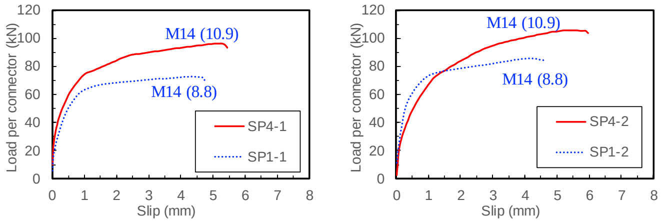

Fig. 12 Specimens with different bolt strength grades

6. Analysis on shear behavior of novel bolted connectors

6.1. Shear resistance

The test results showed that for novel bolted connectors, their shear resistances relate to their diameter, strength of bolt, and strength of surrounded grout/concrete. The specific design equation for the shear resistance of bolted connector is not yet available, and design guidance for shear resistance of welded headed studs is used to predict the shear resistance of bolt. The design equations for shear resistance of welded headed shear connector are available in Eurocode 4 [20] and other design specifications such as ANSI/AISC 360[21], AASHTO [22].

The shear resistance of single welded headed stud in Eurocode 4 is given as below.

$$V_u = \min\left(V_{u,s}, V_{u,c}\right) \tag{1}$$

$$V_{u,s}=0.8f_u(\pi d^2/4)=0.8T_u \tag{2a}$$

$$V_{u,c}=0.29d^2\sqrt{E_c f_{ck}} \tag{2b}$$

where f_u is ultimate strength of the stud, MPa; f_{ck} is characteristic cylinder strength of the concrete, MPa; d is diameter of stud, mm.

A number of design engineers used the Equ. (1) and (2) to predicting the shear resistance of bolted connectors. Kwon et al. [3] conducted several experimental studies on high strength friction grip bolts in steel-concrete composite structures. According to their test results, it is found that the ultimate strength of HSFG bolts is dominated by shear fracture of the bolt shank. The ultimate strength is given as:

$$V_{u,s}=0.5T_u \tag{3}$$

where T_u is the tensile resistance of the bolted connector, the corresponding values for the tested specimens in this paper are summarized in Table.1.

The predicted results calculated using the aforementioned Equ. (1) and (3), are compared to the tested results on shear capacity in Fig.13(a) and Fig.13(b). As shown in Fig.13(a), when the ratio of V_u/T_u is 0.8 (Equ.(1), for welded headed stud), the predicted results is generally overestimating the shear capacity and the maximum relative error is 36%; while the ratio of V_u/T_u is 0.5 (Equ.(3), for HSFG bolts), the predicted results is underestimating the tested results by a maximum relative error of 32%.

Since the none of two ratio of V_u/T_u, 0.8 and 0.5, is capable to provide satisfactory prediction for the shear capacity. A compromise is made by modifying the ratio of V_u/T_u to 0.65, which is the average of 0.5 and 0.8. The shear capacity is given as followings:

$$V_u=0.65T_u \tag{4}$$

The comparison is shown in Fig.13(c), the coefficient of variation is reduced to 0.08 and the maximum relative error is reduced to 19%. It should be noted that the maximum relative errors for nine out of ten specimens are smaller than 10%.

According to the test results, the strength of infilled grout has siginificant effect on the shear resistance of the novel demountable bolted connector, even though all of the specimens failed in bolt-shank shear off. Equation (4) can provide acceptable predictions on shear capacity for practical design with certain conservation; however, the formula is determined only by the tensile strength and the dimensions of the bolt shear connector, while the effect of strength of the infilled grout can not be considered. To provide a more reasonable prediction formula for the novel bolted connector, the shear resistance is assumed to be the sum of shear capacity of the bolt shank and the bearing force sustained by the conical locking nut portion embedded in the infilled grout.

Luo et al. [23] proposed an empirical equation to evaluate the shear resistance of welded headed stud embedded in ultra-high performance concrete (UHPC) by considering the contribution of welded collar portion at the root of the headed stud. The ultimate shear capacity is given as:

$$V_{u,s}=0.5T_u+\eta f_c^{'}Dh_c \tag{5}$$

where $0.5T_u$ is the shear capacity of high strength friction grip bolts when the failure mode is bolt shank shear off; $\eta f_c^{'}Dh_c$, represents the contribution of the bearing force imposed to the collar portion, from surrounding concrete; η is empirical coefficient considering the tri-directional confining effect that increase the concrete strength, η=2.5 for high strength concrete is suggested by Luo et al.[23]; $f_c^{'}$ is the compressive strength of concrete in the vicinity of the shear connector, for the tested specimens in this paper, $f_c^{'}$ is the compressive strength of the infilled grout; D is the equivalent diameter of the collar portion for the hexagonal nut; h_c is the height of the conical nut referring to the top flange upper surface.

The comparisons between predicetd and tested results are shown in Fig.13(d). When the contribution of the conical locking nut is considered, the predicted result match well with the tested results, with the maximum relative error within 10% and the coefficient of variation (COV) of 0.06.

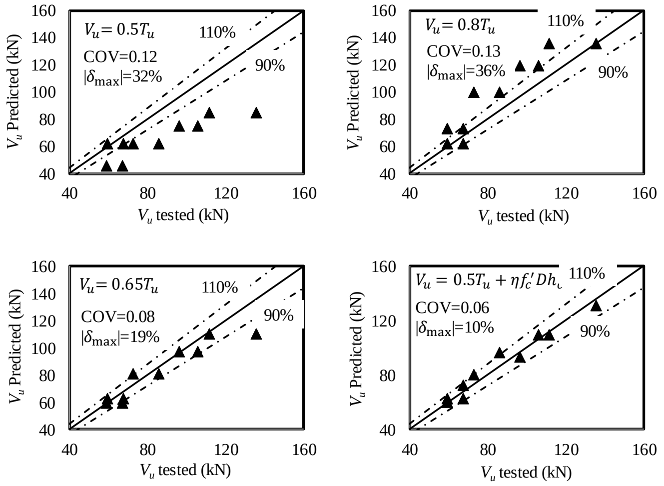

Fig. 13 Comparisons between tested and predicted results on shear capacity

6.2. Characteristic load-slip response

The novel bolted connectors exhibit similar shear-slip relationship curves to that of conventional welded headed stud. One of the most widely used empirical formulas to simulate the shear-slip relationship curves of welded headed studs were proposed by An and Cederwall [24]. The expressions are given by Equ.(6) for welded headed stud embedded in normal strength concrete (NSC), and given by Equ.(7) for those embedded in high strength concrete (HSC), respectively.

$$\frac{V}{V_u}=\frac{2.24(s-0.058)}{1+1.98(s-0.058)} \quad \text{（NSC）} \tag{6}$$

$$\frac{V}{V_u}=\frac{4.44(s-0.031)}{1+4.24(s-0.031)} \quad \text{(HSC)} \tag{7}$$

where s in mm, is slip of the welded headed stud. The measured shear-slip relationship curves obtained from the tests are compared to the above two empirical curves in Fig.14.

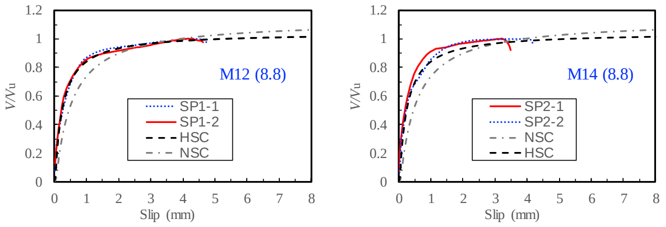

(a) M14 (8.8)   (b) M12 (8.8)

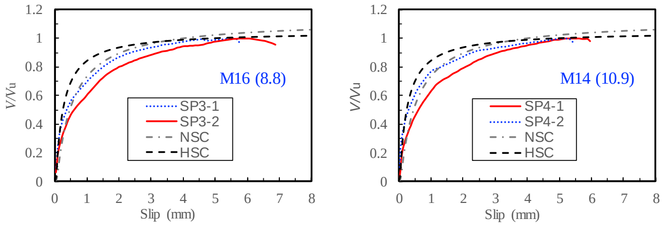

(c) M16 (8.8)   (d) M14 (10.9)

Fig. 14 Shear-slip relationship curves from empirical formula and test

It can be found that the empirical formulae for high strength concrete (HSC) can simulate the shear-relationship curves pretty well for the specimens with M14 (8.8) and M12 (8.8) bolted connectors. However, for the specimens with M16 (8.8) and M14 (10.9) bolts, which had developed relatively larger shear resistance, the shear-slip relationship curves are better simulated by empirical formula for normal strength concrete (NSC). Apparently, a preliminary conclusion can be drawn as following: smaller bolted connectors are more likely to develop shear-slip relationship similar to conventional welded headed stud.

7. Conclusions

In this paper, a new type of demountable steel-precast concrete bolted connector, employing the conical nut and chamfered hole on steel beam flange, was proposed to improve the shear performance of conventional bolted connector with double nut embedded. In order to investigate the shear performance of this novel bolted connector, ten push-out specimens in total for bolted connector have been implemented, with parameters including two types of bolt configuration, three bolt diameters, two bolt strength grades and two strength grades of the in-filled grout. The following conclusions can be drawn from the static push-out tests.

1) The failure mode of the push-out specimens with novel demountable bolted connectors is that the direct sheared off at the bolt cross-section right above the upper face of the conical nut. Few fine cracks and limited local concrete crushing can be observed in the vicinity of bolt and basically within the in-filled grout region.

2) The modified configurations of the bolted connectors, taking advantage of conical locking nut and chamfered flange hole to eliminate the initial clearance between bolt shank and bolt hole on flange, can achieve much better shear performance such as 25% larger shear resistance and much larger shear stiffness up to 600%, compared to the respective performance for specimens with conventional bolted connector.

3) The shear resistance of the novel demountable bolted connector increases with the increase of the bolt diameter, the bolt strength grade as well as the strength of infill grout. The shear resistance of the novel demountable bolted connector can be predicted as 0.65 times of the bolt characteristic tensile resistance. When considering the shear contribution of conical locking nut, a formula including effect of conical locking nut is found to agree well with the tested results.

The parameters investigated in the current experimental studies in still limited. Comprehensive parametric investigation should be carried out through validated numerical models cooperating experimental work in the future studies.

Acknowledgement

This research was financially supported by Scientific Research Fund of Institute of Engineering Mechanics, China Earthquake Administration（Grant No. 2019EEEVL0302，No.2019EEEVL0504）, the National Natural Science Foundation of China (No. 51508381) and Tianjin Science and Technology Program Support (17YFZCSF01140).

Nomenclature

A_{sc}	area of cross section for bolt shank
d	diameter of bolted connector
D	equivalent diameter of hexagonal nut
f'_c	concrete/grout compressive strength
f_u	ultimate tensile strength
h_c	height of the conical nut referring to the top flange upper surface
K	connector shear stiffness
s_k	slippage of shear connector at 70% maximum shear resistance
s_u	slippage of shear connector at maximum shear resistance
s	slippage of shear connector
T_u	ultimate tensile resistance of shear connector
V_u	connector ultimate shear resistance
V	shear force

References

[1] Dedic D.J. and Klaiber F.W., “High-Strength Bolts as Shear Connectors in Rehabilitation Work”, 6, 41-46, 1984.

[2] Kwon G., Engelhardt M.D. and Klingner R.E., “Behavior of post-installed shear connectors under static and fatigue loading”, Journal of Constructional Steel Research, 66, 532-541, 2010.

[3] Kwon G., Engelhardt M.D. and Klingner R.E., “Experimental Behavior of Bridge Beams Retrofitted with Postinstalled Shear Connectors”, Journal of Bridge Engineering, 16, 536-545, 2011.

[4] Pavlović M., Marković Z., Veljković M. and Buđevac D., “Bolted connectors vs. headed studs behaviour in push-out tests”, Journal of Constructional Steel Research, 88, 134-149, 2013.

[5] Moynihan M.C. and Allwood J.M., “Viability and performance of demountable composite connectors”, Journal of Constructional Steel Research, 99, 47-56, 2014.

[6] Dai X.H., Lam D. and Saveri E., “Effect of Concrete Strength and Stud Collar Size to Shear Capacity of Demountable Shear Connectors”, Journal of Structural Engineering, 141, 04015025, 2015.

[7] Liu X., Bradford Mark A. and Lee Michael S.S., “Behavior of High-Strength Friction-Grip Bolted connectors in Sustainable Composite Beams”, Journal of Structural Engineering, 141, 04014149, 2015.

[8] Ataei A., Bradford M.A. and Liu X., “Experimental study of composite beams having a precast geopolymer concrete slab and deconstructable bolted connectors”, Engineering Structures, 114, 1-13, 2016.

[9] Ban H., Uy B., Pathirana S.W., Henderson I., Mirza O. and Zhu X., “Composite beams with blind bolts under sustained loads”, Journal of Constructional Steel Research, 112, 196-207, 2015.

[10] Henderson I.E.J., Zhu X.Q., Uy B. and Mirza O., “Dynamic behaviour of steel–concrete composite beams with different types of shear connectors. Part I: Experimental study”, Engineering Structures, 103, 298-307, 2015.

[11] Henderson I.E.J., Zhu X.Q., Uy B. and Mirza O., “Dynamic behaviour of steel–concrete composite beams with different types of shear connectors. Part II: Modelling and comparison”, Engineering Structures, 103, 308-317, 2015.

[12] Pathirana S.W., Uy B., Mirza O. and Zhu X., “Bolted and welded connectors for the rehabilitation of composite beams”, Journal of Constructional Steel Research, 125, 61-73, 2016.

[13] Yang F., Liu Y., Jiang Z. and Xin H., “Shear performance of a novel demountable steel-concrete bolted connector under static push-out tests”, Engineering Structures, 160, 133-146, 2018.

[14] C. Eurocode 4, “Design of composite steel and concrete structures”, Part, 2004.

[15] Johnson R.P. and Buckby R.J., “Composite structures of steel and concrete”, Wiley Online Library, 1975.

[16] Suwaed Ahmed S. H. and Karavasilis Theodore L., “Novel Demountable Shear Connector for Accelerated Disassembly, Repair, or Replacement of Precast Steel-Concrete Composite Bridges”, Journal of Bridge Engineering, 22, 04017052, 2017.

[17] Suwaed A.S. and Karavasilis T.L., “Removable shear connector for steel-concrete composite bridges”, Steel and Composite Structures, 29, 107-123, 2018.

[18] ACI Committee, American Concrete Institute, International Organization for Standardization, “Building Code Requirements for Structural Concrete (ACI 318-08) and Commentary”, 2008.

[19] Rehman N., Lam D., Dai X. and Ashour A.F., “Experimental study on demountable shear connectors in composite slabs with profiled decking”, Journal of Constructional Steel Research, 122, 178-189, 2016.

[20] Eurocode 4. EN 1994, “Design of composite steel and concrete structures. Part 1 General rules and rules for buildings”, 2004.

[21] ANSI/AISC 360, “Specification for Structural Steel Buildings”, American Institute of Steel Construction, Chicago, Illinois, 2010.

[22] AASHTO, “AASHTO LRFD Bridge Design Specifications”, 6th Edition, AASHTO, 2012.

[23] Luo Y., Hoki K., Hayashi K. and Nakashima M., “Behavior and Strength of Headed Stud–SFRCC Shear Connection. II: Strength Evaluation”, Journal of Structural Engineering, 04015113, 2016.

[24] An L. and Cederwall K., “Push-Out Tests on Studs in High Strength and Normal Strength Concrete”, Journal of Constructional Steel Research, 36, 15-29, 1996.

Advanced Steel Construction – Vol. 18 No. 4 (2022) 753–762
DOI:10.18057/IJASC.2022.18.4.3

BOND-SLIP TESTING AND PERFORMANCE EVALUATION OF SEMI-RIGID FLANGE FOLDED WEB SHEAR KEYS

Zhen-Shan Wang [1, 2, *], Hua-Qian Qin [2], Yong Yang [2], Yun-He Liu [1], Hong-Chao Guo [2] and Jian-Bo Tian [2]

[1] State Key Laboratory of Eco-hydraulics in Northwest Arid Region of China, Xi'an University of Technology, Xi'an 710048, China
[2] School of Civil Engineering and Architecture, Xi'an University of Technology, Xi'an 710048, China
** (Corresponding author: E-mail: wangdayuwang@126.com)*

ABSTRACT

The shear key is crucial to the overall mechanical performance of the structure. A new type of semi-rigid connector-flange folded web shear key was proposed to determine the effective unity of higher bearing capacity and deformation. A total of five groups of specimens were designed, and the push-out test method was used to evaluate the ultimate bearing capacity, bond-slip process, failure mode, and strain distribution of the new shear key. The results show that before sliding, the embedded effect of the concrete and shear key is significant, and it has a significant sliding stiffness. After sliding, the steel plate in the middle of the opening of the outer folded plate buckles, which shows certain semi-rigid characteristics. Compared with equal-area studs, the bearing capacity of the new shear key is increased by more than 40%, and the deformation capacity exceeds 60 %, indicating good bond-slip performance. The constraint range of the shear key is greatly improved compared with the stud, and a trapezoidal area of constraint centered on the shear key is formed, accounting for more than half of the area of the concrete slab. Based on an experimental study, a practical calculation method of ultimate bearing capacity of the shear key is proposed, which can meet engineering safety requirements. Based on the analysis of bond-slip characteristics of different forms of shear keys, compared with the rigid T-shaped shear key, the slip load and ultimate bearing capacity of the new shear key are found to be increased by 39 % and 74 %, respectively, and the deformation capacity is increased more than 10-fold. Compared with the flexible stud shear connectors, the sliding load is increased by 86 %, the ultimate bearing capacity is increased more two-fold, and the stiffness is increased by nearly five times. The device exhibits good comprehensive performance.

ARTICLE HISTORY

Received:	9 July 2021
Revised:	16 April 2022
Accepted:	2 May 2022

KEYWORDS

Semi-rigid shear key;
Bond slip;
Mode of failure;
Ultimate bearing capacity;
Design approach

1. Introduction

Steel-concrete composite beam-slab structure can give full play to the mechanical properties of steel and concrete, forming complementary advantages, and is increasingly widely applied in structural engineering. The composite structure connects the two materials using shear connectors, and makes them work together through friction, mechanical bite force, and bonding force. As an important component of steel-concrete composite beam and slab, shear connectors have two main functions: resisting horizontal shear force and ensuring cooperative action between steel and concrete, and resisting the upward lift at the interface between steel beam and concrete. There are various forms of shear connectors, and their performance differences are also significant. At present, they are mainly divided into two categories: rigid and flexible shear connectors. The stiffness of a rigid shear connector is far greater than that of the concrete structure, which can produce strong constraints thereon, and the bond-slip deformation between concrete and steel structure is controlled; however, due to the shear bond stiffness being too large, when the load exceeds the ultimate bearing capacity, resulting in contact with the concrete leading to crushing or shear failure, the structural deformation capacity is poor. The stiffness of the flexible shear connector is relatively small, the concrete slab can slip with it, and the structural deformation ability is better; however, the constraint on the slip deformation of the concrete structure is reduced due to the low stiffness of the shear key itself. Under the action of rare earthquakes, excessive slip deformation will cause some damage to the structure, and the second-order effect is more serious, causing a significant reduction in the overall safety of the structure. To improve the overall performance of steel-concrete composite beam-slab structure, the analysis of new shear connector connection form and mechanical performance is a focus of much of the research into composite structures.

The stud is one of the most common shear connectors used at present. As a typical flexible shear key, it is widely applied in steel-concrete composite beams and slabs. At present, the influences of stud length, diameter, and number on bond-slip performance and stiffness were evaluated by push-out tests and numerical simulation [1-3]. On this basis, the calculation methods of bearing capacity and stiffness were analyzed, and suggestions for engineering design were proposed. Chaves Marina *et al*. [4] evaluated the relationship between the mechanical properties of concrete-filled steel tube and the bolt shear bond. The results show that the best matching value between the thickness of steel tube and the diameter of bolt shear bond ranges between 1.3 and 2. Angular steel shear parts exhibit the characteristics of high bearing capacity and convenient processing. Arévalo [5], Qiu [6], and Jiang [7] studied the shear keys of angle steel to reveal the influences of angle steel size and angle, the bearing capacity, and shear stiffness of angle steel through monotonic and cyclic loading, and proposed practical calculation formulae for strength and stiffness. Rigid shear connectors are also used in practice. Maleki [8] and Yan [9] studied the mechanical properties of groove shear connectors under monotonic and low cycle fatigue loads. The results show that the failure modes are mainly shear failure and concrete failure. Compared with the same monotonic load condition, the strength is reduced by 10% to 20% under repeated loading. Vianna [10], Isabel [11], Huang [12] and Li [13] investigated the flange size and opening size of a T-shaped plate and a T-shaped perforated plate, and demonstrated its failure mode with a focus on its ultimate bearing capacity and ductility. On this basis, they established a formula for calculating the bearing capacity of shear connectors of T-shaped plates and T-shaped perforated plates, which were close to measured experimental values.

As a new type of shear connector, the PBL has been gradually applied in steel-concrete composite bridge structure. Yong Yang, Mohammed, Yang [14], Mohammed [15], and Zhang [16] conducted experimental research into the bearing capacity and failure mode of PBL connector to analyze the failure mechanisms. It is found that this type of shear connector has obvious embedded effects when set in concrete, offering good mechanical performance. Rodrigues [17], Chen [18] and Yang [19,20] evaluated the influences of the number and diameter of holes on the bearing capacity of PBL connectors by push-out tests. The results showed that the number of holes had a significant impact on the bearing capacity of PBL connectors, while the diameter of holes exerted little effect on the bearing capacity of PBL connectors. Weiqing [21] explored the main factors influencing shear capacity of single-hole PBL connectors based on existing experimental and theoretical studies and established a formula for the shear capacity. Costa-Neves [22], Xue [23], Zhang [24], and Wang [25] studied the influences of the reinforcement in the hole on the bearing capacity, ductility, and failure mode of PBL connector through the push-out test. It is found that the reinforcement in the hole can improve the ultimate bearing capacity, and the ultimate bearing capacity increases with the increase in the diameter of the reinforcement, but the ductility of the specimen is poor. Di *et al*. [26] assessed the mechanical properties and bearing mechanism of large-size PBL connectors under strong constraint conditions and found that the ductility of connectors increases with the increase in the size of the hole under strong constraint conditions. Based on an experimental study, Zhao [27] and Shi [28] conducted numerical simulation of shear connectors with openings, mainly focusing on their layout and opening diameter. The results indicated that it is feasible to use ABAQUS to analyze the mechanical properties of PBL connectors. Chen *et al*. [29] studied the shear bearing capacity, stiffness, and deformation capacity of PBL shear keys with straight and inclined plates. They found that the bearing capacity of PBL shear keys with straight and inclined plates was equivalent, but the PBL shear keys with inclined plates had higher stiffness and better deformation capacity. Ramasamy *et al*. [30] changed the hole shape of the connector to a triangle for test purposes, and the results showed that the slip capacity of the connector with a triangular hole was significantly improved. Li [31] and Suzuki [32] found that the bearing capacity of PBL connectors was reduced by 55% compared with monotonic loading by testing PBL connectors using cyclic loading. Zhang *et al*. [33] proposed an embedded connector with the flange. Through eight groups of push-out tests, it is found that the bearing capacity of the connector is about 1.5 times that of the embedded connector when the flange is stable.

Based on research into traditional connectors, many scholars have studied special-shaped shear connectors with various waveforms. Chen [34], Ruinian [35] and Su [36] found that the deformation of shear connectors with corrugated openings was obvious and the rate of utilization of materials was high by investigating shear connectors with corrugated openings. Sang-Hyo Kim [37-39] studied the mechanical properties of Y-type shear connectors. The results show that the shear strength, shear stiffness, and ductility of Y-type shear connectors are better than those of traditional shear connectors. Nie [40] and Zhuang [41] conducted experimental research on the new type of T-joints with pull-out and non-shear resistance. The results indicated that the joint can improve the mechanical properties in the zone of negative bending moment of the composite beam, and the anti-slip effect is good under low load. Li *et al*. [42] proposed a type of perforated plate connector; through the push-out testing of six groups of specimens, they found that the initial stiffness and bearing capacity of the connector were large. According to the test results, the calculation formula of bearing capacity was established, which was in good agreement with experimental values. Zhao *et al*. [43] proposed a dumbbell-shaped connector for the shortcomings of traditional stud connectors. Through the finite element software for shear analysis, it was found that the dumbbell-shaped connector can significantly improve the shear bearing capacity, and under the same shear effect, the material consumption can be reduced by more than 40 % compared with the use of a stud.

From the current situation, flexible shear key studs are widely used, with good deformation ability and high ability to work together with concrete, but under the action of greater shear force, especially under the condition of strict requirements for slip, rigid shear keys are needed; however, due to the large stiffness of the rigid shear key, the concrete in contact with it is destroyed, and the structural deformation capacity is low. In order to further balance “stiffness” and “deformation”, the concept of a “semi-rigid” shear key is proposed, which can allow a certain deformation while providing large shear capacity, and can meet the dual requirements of “constraint” and “deformation”. Based on the existing research results pertaining to shear connectors, a “flange folded web shear key” is proposed. The design concept entails a web of folded plate form, reducing the web stiffness. Meanwhile, the stiffness of two principal axes of shear keys is balanced to avoid the formation of strong and weak axes. The web opening treatment can improve the embedded effect of shear keys and concrete, which is beneficial to stress transfer and improving structural integrity thereof. By setting the flange, the stability of the web is improved and the anti-lifting effect of shear keys is enhanced.

Herein, five groups of specimens were designed by a push-out test method. The ultimate bearing capacity and failure mode of the shear key were determined to reveal its failure characteristics and constraint effect, and the bond-slip performance and failure mechanism of the shear key were obtained. On this basis, the ultimate bearing capacity and design method were studied. Finally, practical calculation formulae and design suggestions were provided. The bond-slip performance of “new semi-rigid shear key”, “T-rigid shear key”, and a “stud flexible shear key” was compared and evaluated. This paper can provide an experimental basis and technical support for the engineering application of these modified shear keys.

2. Experimental work

2.1. Shear key design

A total of five groups of specimens were designed, and the parameters of each specimen are listed in Table 1. S−1 and S−3 are shear keys of flange double-folded web design, in which steel bars are inserted in the opening of S−3. S-2 and S-4 are shear keys of flange triple-folded web design, in which steel bars are inserted in the opening of S−4. Except for the different forms of folding plates, the material properties, opening size and folding angle of each group of specimens are the same. S-5 is a stud shear connector. The specific dimensions are as follows: taking studs which are widely used in engineering as design reference, the design idea of one shear key equivalent to two studs was adopted (Fig. 1). According to the specification *Cylindrical Head Studs for Arc Stud Welding (GBT10433-2002)* [44], M22 × 90 mm was selected as the stud, and its cross-sectional area was 760 mm^2. The thickness of the folded plate and the upper cover plate of the double-folded plate shear key was 6 mm. The length of the folded plate was 85 mm, and the height was 90 mm. The double-folded plates were at 90° to each other. The length of the upper cover plate was 120 mm, and the middle part of the folded plate was opened with a long round hole of 25 mm in diameter and 70 mm in height to ensure the penetration of concrete. Triple-folded plate shear key on both sides of the folded plate is 63 mm long and the middle folded plate length was 50 mm. The remaining dimensions were consistent with those of the double-folded plate shear key. Through calculation, the areas of the middle section of the double-folded plate and triple-folded plate shear keys are 720 mm^2 and 606 mm^2, respectively (Fig. 2).

Table 1
Specimen parameters

Number and form of shear keys	Inserted rebar	Filling material
S-1 Double-folded plate shear key	NO	C30 commercial concrete
S-2 Triple- folded plate shear key	NO	C30 commercial concrete
S-3 Double-folded plate shear key	YES	C30 commercial concrete
S-4 Triple-folded plate shear key	YES	C30 commercial concrete
S-5 Stud connector	—	C30 commercial concrete

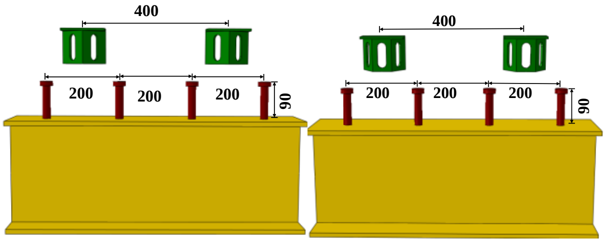

(a) Shear key distribution of flange double-folded web

(b) Shear key distribution of flange triple-folded web

Fig. 1 Distribution of shear keys

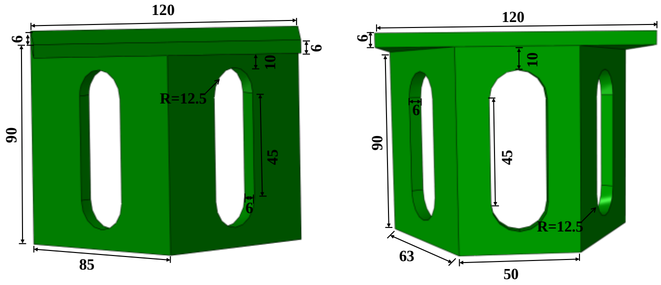

(a) Shear key of flange double-folded web

(b) Shear key of flange triple-folded web

Fig. 2 Form and size of shear keys

2.2. Processing and manufacturing of pushout specimens

The pushout specimen composition and reinforcement arrangement are shown in Fig. 3. The concrete slab measured 580 mm × 550 mm × 130 mm, of which 60 mm was prefabricated and 70 mm was cast-*in-situ*. C30 commercial concrete was used, and the joint was also filled with C30 commercial concrete. The steel beam was fabricated in Q235 grade H steel, the specification of which was HW300×200×8×12 (mm), the shear key was made from Q235 B grade steel, the longitudinal reinforcement of concrete slab was of HRB400Φ8-form, and the rebar at the opening is in an HRB400Φ12 arrangement. The steel and concrete used in the test were tested (Tables 2 and 3). The specimens were formed as follows: a 60-mm thick reinforced concrete slab was prefabricated, cued, and assembled on both sides of the steel beam, the longitudinal reinforcement of the slab was thus broken at the joint. This prefabricated plate was used as the bottom template, and the joint at the shear key was filled before the post-cast laminated layer was constructed. The longitudinal reinforcement was arranged as a whole. After binding, the whole casting was formed (Fig. 3d).

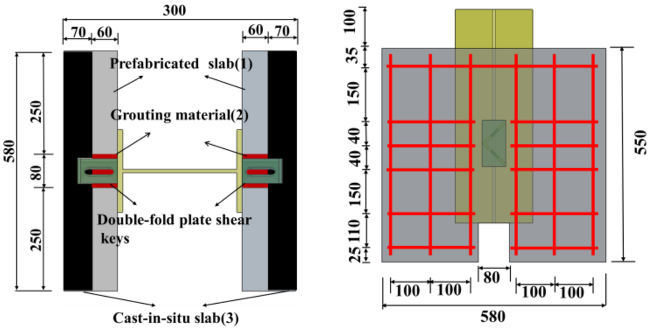

(a) Composition of specimens (b) Steel bar arrangement

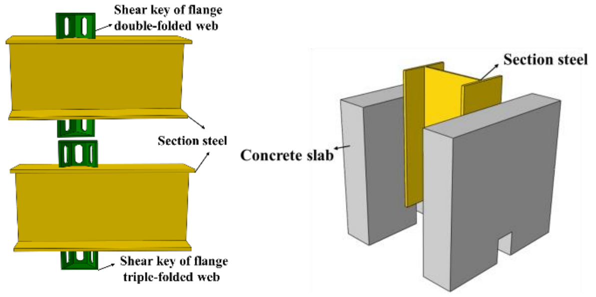

(c) Section steel and shear keys (d) Specimen shaping

Fig. 3 Composition and design of the specimen

Table 2
Measured material properties of concrete

Material type	f_{ck} (MPa)	$f_{cu,k}$ (MPa)	f_c (MPa)	E_c (N/mm^2)
Commercial concrete	27	40.35	19.3	33827

NOTE: $f_{cu,k}$: Standard value of concrete cube compressive strength;
f_{ck}: Axial compression strength of concrete;
f_c: of the designed axial compressive strength of concrete;
E_c: Modulus of elasticity of concrete

Table 3
Test results: steel and reinforcement

Specimen number	f_y (MPa)	f_u (MPa)	ε_y (%)	ε_u (%)	E (GPa)
Reinforcement (Φ6)	572	642	0.5	3.15	189
Reinforcement (Φ8)	472	662	0.47	6.33	183
Reinforcement (Φ12)	509	583	0.34	9.9	187
Steel plate	255	410	0.76	9.49	214

NOTE: f_y: Yield strength; f_u: Tensile strength;
ε_y: Yield strain; ε_u: Tensile strain; E: Elastic modulus of steel

2.3. Loading device and programs

The bond-slip performance of the shear key was studied by push-out tests. The specimen was placed on the long column press, steel plate was placed on the top of the steel, and fine sand was laid on the rigid base and steel plate to avoid stress concentration (Fig. 4).

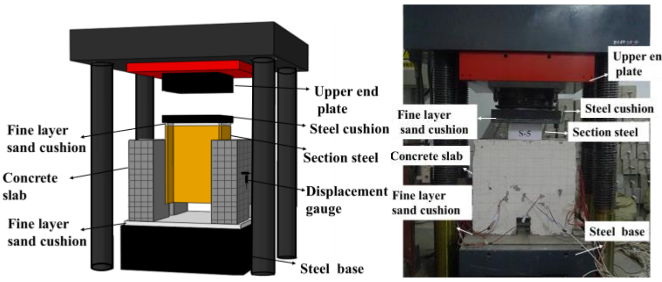

(a) Schematic representation of the loading device (b) Actual loading device

Fig. 4 Test device

The loading scheme adopts load and displacement mixed loading. It first controls force loading, loading to steel beam slip, and then displacement control, until failure (Table 4).

Table 4
Loading scheme

Step	Control mode	Control parameter	Jump options
1	Constant speed force	0.15 kN/s	Before sliding, the force control loading is used, and each loading is 100 kN for two minutes. When the loading is loaded to the specimen sliding, the displacement control is changed.
2	Constant speed displacement	0.03 mm/min	When loading to about 85 % of the ultimate load, stop loading.

3. Experimental results

3.1. Failure process analysis

S-1 is a shear key of flange double-folded web design. At the beginning of loading, there is no obvious failure of the specimen. When the load reaches 210 kN, the steel beam slips, and as the load is increased, small cracks are formed near the shear key (Fig. 5b). With increasing load, the cracks gradually extend and form two main cracks at 45° on both sides of the shear key (Fig. 5b). After reaching the ultimate bearing capacity, multiple inclined cracks are generated around the shear key, resulting in the failure of the concrete slab. The cracks are mainly vertical crack, and the horizontal expansion area is mainly covered by oblique cracks. The maximum horizontal crack range is about two-thirds of the plate width, and the height is about three-fifths of the plate height. The overall crack area is basically trapezoidal (Fig. 5b). When the load is stopped at 80% of the ultimate bearing capacity, the concrete around the shear key is stripped. The failing specimen is shown in Fig. 5c. Along the push-out direction, the overall lateral bending occurs, the outer plate of the folded plate is obviously buckling, and the inner edge of the hole is slightly bent.

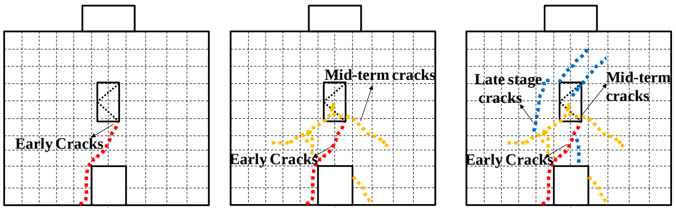

(1) Load: 210 kN (2) Load: 410 kN (3) Displacement: 6 mm

(a) Crack development in Specimen S-1

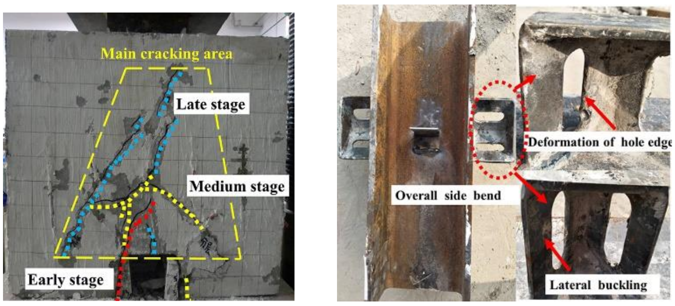

(b) Concrete slab cracks (c) Shear bond damage

Fig. 5 Destruction of Specimen S-1

S-2 is a shear key of flange triple-folded web design; when the load reaches 250 kN, the steel beam begins to slip, and the concrete floor undergoes vertical cracking (Fig. 6b). As the load is increased, the cracks at the bottom of the concrete slab extend upward, and multiple oblique cracks appear (Fig. 6b). After reaching the ultimate load, oblique cracks at 45° to the shear key appear on both sides and at the bottom of the shear key, and the right-hand oblique cracks gradually extend to the bottom of the concrete slab. The maximum crack width is about two-thirds of the slab width, and their height is about four-fifths of the slab height: the overall distribution thereof is trapezoidal (Fig. 6b). Loading to

80% of the ultimate bearing capacity to stop loading, shear bond around the concrete is tripped (Fig. 6c), the web position undergoes bending, along the push-out direction, the lateral buckling of the folded plate is obvious, the edge of the opening suffers little damage, and the middle folded plate remains unbuckled.

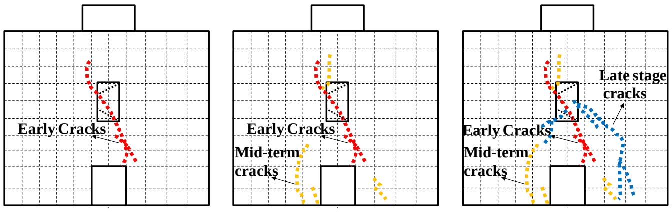

(1) Load: 250 kN (2) Load: 370 kN (3) Displacement: 6 mm

(a) Crack development in Specimen S-2

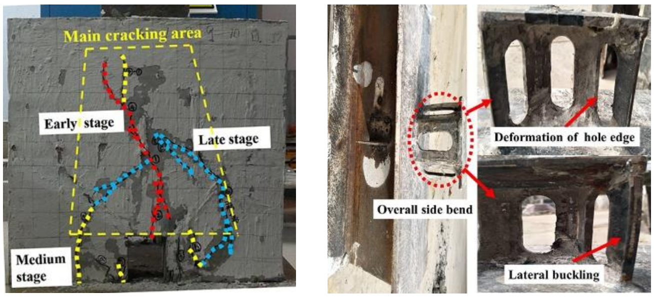

(b) Concrete slab cracks (c) Shear bond damage

Fig. 6 Destruction of Specimen S-2

S-3 is a double-folded plate shear key design with rebar inserted in the hole. At a load of 270 kN, the steel beam slips, vertical cracks appear in the middle of the shear key, and oblique cracks appear in the bottom at 45° direction to the base (Fig. 7b). As the load increases, several cracks appear in the middle and bottom of the concrete slab (Fig. 7b). After reaching the ultimate load, a large crack is formed in the vertical direction of the upper part of the shear bond, and the concrete slab is severely damaged. The bottom crack covers the full width of the section, and vertical cracking area reaches three-quarters of the plate height. The crack form is akin to that in other specimens. Vertical cracks are found to run along the shear bond, and oblique cracks are mainly seen elsewhere (Fig. 7b). When the bearing capacity decreases to 80% of the ultimate bearing capacity, the loading is stopped, and the concrete is stripped. The failure of shear keys and reinforcement is shown in Fig. 7c, which is consistent with the failure of Specimen S-1, and the reinforcement is bent.

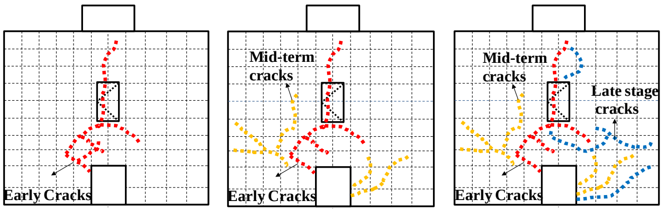

(1) Load: 270 kN (2) Load: 410 kN (3) Displacement: 7 mm

(a) Crack development in Specimen S-3

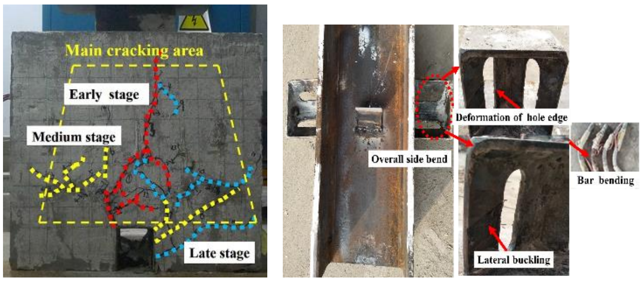

(b) Concrete slab cracks (c) Shear key and steel bar damage

Fig. 7 Destruction of Specimen S-3

S-4 is a triple-folded plate shear key design with rebar inserted in the hole. When the load reaches 270 kN, the steel beam begins to slip, several cracks appear at the bottom of the concrete slab and continue to extend upwards (Fig. 8b). With increasing load, a 45° oblique crack appears near the shear key (Fig. 8b). When reaching the ultimate load, the cracks gradually extend upwards, and several new cracks are generated on the surface of the concrete slab. The biggest crack in the horizontal range covers the slab width, and the vertical crack area also reaches three-quarters of the slab height. The damage to the concrete slab is the most severe, and the main crack area is trapezoidal (Fig. 8b). From 80% of the ultimate bearing capacity to cessation of loading, stripping concrete, shear keys and steel bar damage occur, as shown in Fig. 8c, which is consistent with Specimen S-2, and the steel bar is subject to significant bending.

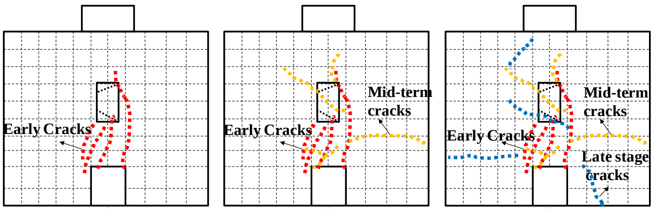

(1) Load: 270 kN (2) Load: 390 kN (3) Displacement: 6 mm

(a) Crack development in Specimen S-4

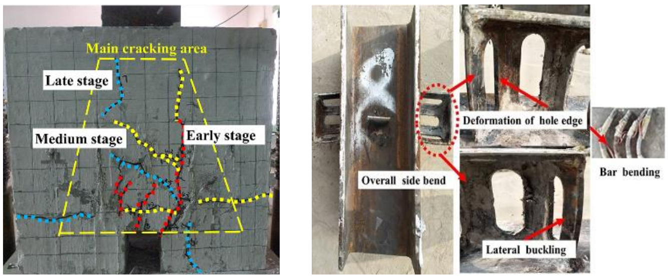

(b) Concrete slab cracks (c) Shear key and steel bar damage

Fig. 8 Destruction of Specimen S-4

S-5 is a stud shear connector; when the load reaches 150 kN, the steel beam slips and cracks appear at the bottom of the stud (Fig. 9b). With increasing load, cracks do not develop rapidly, and no new cracks appear. When the bearing capacity reaches 80% of the ultimate load, cracks appear at the junction of the cast-in-place plate and the prefabricated plate, and oblique cracks appear on the other side of the specimen (Fig. 9c). Under the constraint imposed by the studs, the cracking of concrete slab is slight, and the laminated slab is stratified. Overall, the stud constraint effect is relatively poor, in addition to the point constraint, the integrity of the composite plate is also reduced. Detached concrete and stud failure (Fig. 9e), occurs along with obvious bending along the pushout direction and severe bending in the middle of the web.

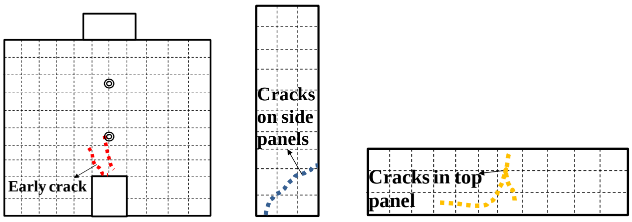

(1) Load: 150 kN (2) Load: 220 kN (3) Load: 240 kN

(a) Crack development in Specimen S-5

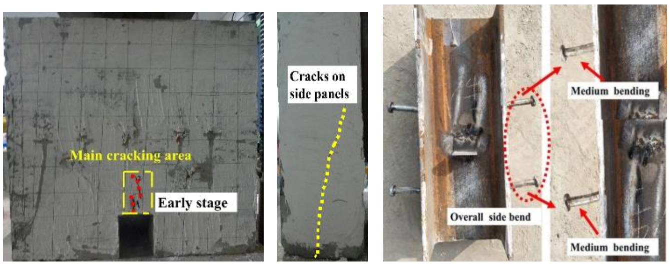

(b) Concrete slab cracks (c) Side cracks (e) Connector damage

Fig. 9 Destruction of Specimen S-5

3.2. Failure mode analysis

Through the push-out tests of five groups of specimens, it is found that the failure process and mode of concrete slabs are similar; firstly, a 45° oblique crack is formed on both sides of the shear key, subsequently, vertical concrete plate cracks propagate along the shear key. Finally, the trapezoidal main cracking area is formed around the shear key. The top cracking reaches one-third of the plate length, the bottom crack reaches about two-thirds of the plate length, and the height is seven-tenths of the plate height (Fig. 10a). The failure modes of shear keys are similar: along the push-out direction, the steel plate on the outer side of the shear keys buckles, and the edge of the hole edge is slightly damaged, among which the damage in the middle of the hole is the most severely damaged. Compared with double-folded plate shear key, the damage at the opening of triple-folded plate shear key is more obvious, and the overall lateral bending is larger (Fig. 10b). From the analysis of the failure mode, it is found that the rigid shear key failure only occurs in concrete, and the shear key does not deform. The flexible shear key deforms significantly, and then the concrete is damaged under the action of the tensile stress. The flange folded web shear key exhibits semi-rigid characteristics. In the early stage of sliding, the shear bond can work well with the concrete. After sliding, the concrete is damaged, and the shear key undergoes yield deformation, and the failure of both materials occurs synchronously. From the perspective of the failure mode of the new shear key, it can better play the cooperative work performance of steel structure and concrete. On the one hand, it can provide significant stiffness and constrain sliding on the concrete. At the ultimate bearing capacity, it can produce a certain deformation with concrete, allowing adjustment of the internal force. Finally, the better implementation of "constraints" and "deformation" are unified.

In summary, the failure mode and working mechanism of the new shear key and stud are quite different. In the early stage of loading, the shear force is mainly borne by the bond to the concrete. When loaded to the sliding load, the stud is separated from the concrete, and the shear force is mainly borne by the stud. Due to its small stiffness, large deformation occurs at the root in the process of pushing, resulting in local damage to the concrete; because of the stiffness of the stud, the bearing capacity does not decrease. After the opening of the new shear keys, this allows a good bond to the concrete, and the bonding form is changed into mechanical occlusion, and the bearing capacity is greatly improved. Since the web lies at a certain angle, the shear force can be transformed into pressure during the pushing process, which is key to its shear bearing capacity. Another advantage of web oblique layout is that it can reduce the stiffness and increase the deformation capacity. From the perspective of failure mode, the constraint range of studs for concrete is small, showing a point-constraint form, and the shear bond constraint range is larger, showing a trapezoidal distribution. After reaching the ultimate load, the bearing capacity of the shear key decreases, albeit slowly, showing obvious semi-rigid characteristics.

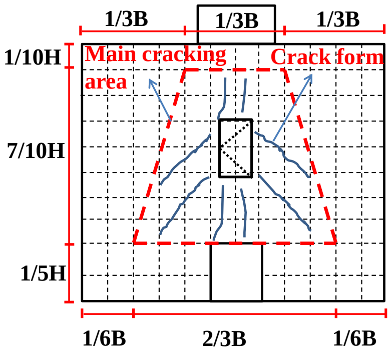

(a) Failure mode of concrete slab

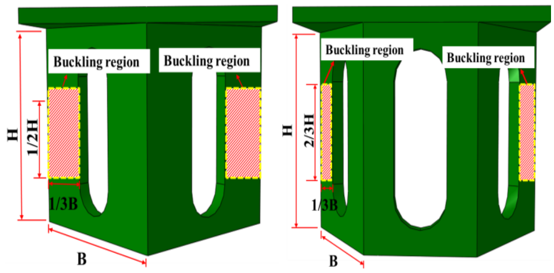

(b) Failure mode of shear key

Fig. 10 Failure mode of a typical specimen

4. Analysis of experimental results

4.1. Load-displacement comparison

The comparison of load-displacement curves of the five groups of specimens is shown in Fig. 11. The failure process is as follows: at the beginning, the bearing capacity increases linearly, and the steel beam does not slip. With increasing load, the steel beam slips and the bearing capacity increases rapidly, while the bearing capacity of the stud increases slowly. After reaching the peak load, the stiffness degrades, the bearing capacity decreases, and the concrete slab is destroyed. The traditional stud shows good deformation ability, and the stiffness and strength degrade slowly. The flange folded web shear key design also exhibits good deformability, and the ultimate bearing capacity and sliding load have been significantly improved. They impose a strong constraint, and provide better integrity, with concrete slabs. Compared with the triple-folded plate shear key design, the double-folded plate shear key has higher ultimate bearing capacity, and the slip load and failure load are similar, indicating that the double-folded plate shear key has good shear performance, and the material strength is fully utilized.

The load-displacement characteristic values of each specimen are illustrated in Table 5, and Fig. 12 depicts the ultimate load and ultimate displacement. Compared with studs, the slip load of the double-folded plate shear key is increased by more than 40 %, and the ultimate bearing capacity is increased by more than 45%. For the triple-folded plate shear key, the sliding load is increased by more than 60%, and the ultimate bearing capacity is increased by more than 30%. The deformation capacity of the two new shear keys reaches more than 61% of the stud. Compared with the triple-folded plate shear key, the ultimate bearing capacity of the double-folded plate shear key is increased by about 11%, and the bearing capacity margin is increased by more than 26%. The double-folded plate shear key and the concrete slab demonstrates better integrity, and the mechanical performance of the shear key is fully developed. Inserting steel bars at the opening has certain effects on the improvement of shear key slip load, deformation capacity, and shear transfer, but the effect is not obvious, which is mainly due to the large difference between steel plate stiffness and steel strength. In summary, compared with studs, the flange folded web shear keys show significantly enhanced bearing capacity, which have a certain deformation capacity. They demonstrate better embedded performance with concrete slabs, and have strong integrity, which can better achieve the design purpose.

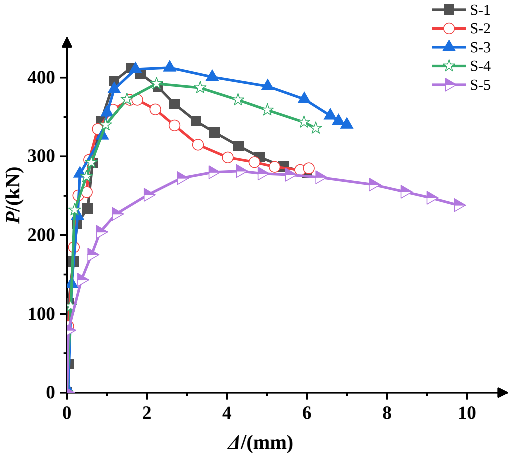

Fig. 11 The comparison of load-displacement curves

Table 5
Eigenvalues of load and displacement

Specimen	Slip load P_y/kN	Ultimate load P_{max}/kN	Displacement of ultimate load Δ_{max}/mm	Failure load P_u/kN	Displacement at failure Δ_u/mm	Bearing capacity margin P_{max}/P_y
S-1	214	412	1.6	280	6.0	1.9
S-2	250	371	1.8	284	6.0	1.5
S-3	277	412	2.2	340	7.0	1.5
S-4	274	392	2.2	335	6.2	1.4
S-5	150	281	4.0	238	9.8	1.9

NOTE: Sliding load P_y is the load corresponding to steel sliding;
Ultimate load P_{max} is the peak load when slipping;
Failure load P_u is the load corresponding to a decrease in peak load to 85 %.

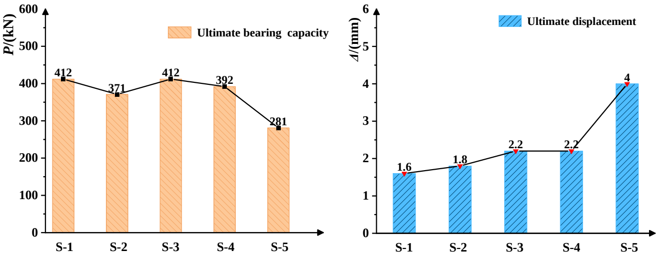

(a) Ultimate bearing capacity (b) Ultimate displacement

Fig. 12 Ultimate load and its corresponding displacement diagram

NOTE: the ultimate displacement is that displacement corresponding to the ultimate load.

4.2. Load-strain analysis

The load-strain relationships of the five groups of specimens are shown in Fig. 13. Flange strain analysis shows that the flange strain of the double-folded plate and the triple-folded plate shear key is small, showing a linear change. Strain analysis in the middle of web openings implies that on the whole, the strain increases with increasing load. Compared with the double-folded plate shear key, the strain in the middle of web openings of the triple-folded plate shear key is larger. A comparative analysis of the left and right-hand folded plate strains shows that the shear key right-hand folded plate (far from the push-out end) strain is less than 10% of left-hand folded plate, in the calculation of bearing capacity, it should be considered as providing a reduction therein. The strain analysis of the inserted steel bar in the hole shows that the strain of the shear key of the inserted steel bar and the uninserted steel bar is the same, and the strain of the shear key of the three-folded plate changes greatly, which is consistent with the failure of the shear key. The strain analysis of the concrete slab indicates that the strain distribution in the concrete slab under the constraint of two new shear keys is more uniform, and the strain therein is larger, indicating that the two new shear keys are better combined with the concrete slab, and the force transmission is more uniform, which agrees with the macroscopic phenomenon found experimentally. Moreover, the concrete under the constraint of the double-folded plate shear key has large ultimate bearing capacity, which fully mobilizes the shear performance of such shear keys.

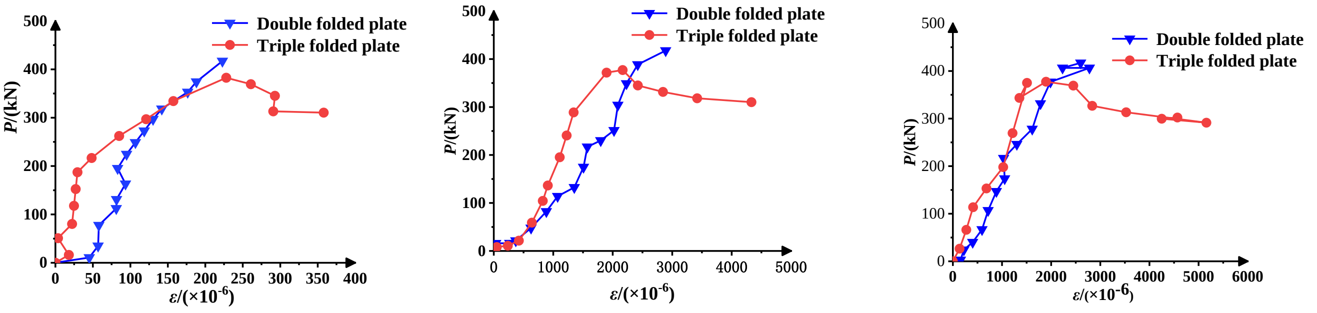

(a) Flange (YB-1) (b) The middle of the opening of the right flap (YB-3) (c) The middle of the opening of the left flap (YB-5, YB-6)

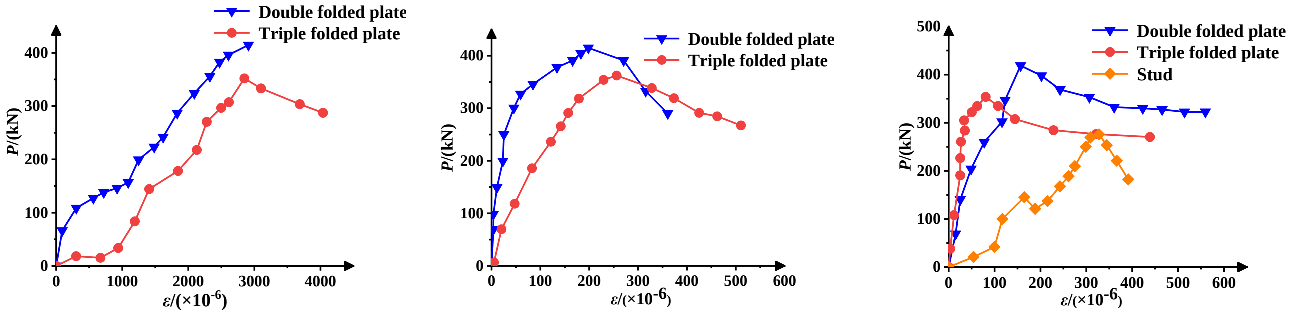

(d) Right fold inserted steel bar (YB-3) (e) Concrete slab on top-left side (H-14) (f) Concrete slab on lower-right side (H-9)

Fig. 13 Comparison of load-strain curves

5. Calculation of bearing capacity and analysis of bond-slip characteristics

5.1. Force model: the shear key

According to the push-out test results and the failure mode of the shear key, the stress on the whole shear key was analyzed. The test pushes the steel beam out along the longitudinal direction of the shear key, the web is subjected to load in two directions (forward and vertical), and the flange is subjected to the same pressure as the push-out direction (Figs. 14a and 14b). On this basis, combined with the test situation, the stress state of each part was simplified and analyzed. The bonding effect between the web and the concrete is negligible when considering the face extrusion between the steel plate and the concrete and the shear effect of the concrete in the hole. The web stress can be divided into three parts: the outer web at the opening, the opening, and the inner web at the opening (corner part); buckling of the lateral web at the opening is the most severe, and the bearing capacity V_1 here mainly depends on the yield strength and the cross-sectional area of the steel plate. The bearing capacity at the opening is V_2. When the specimen is damaged, the concrete in the hole has been destroyed, so the bearing capacity is mainly determined by the compressive strength of the concrete; however, the force distribution is relatively complex here, and the influences of the opening diameter, the angle of the folding plate and the height of the folding plate should be considered at the same time. The bearing capacity of the inner steel plate (corner part) at the opening is V_3, where the stiffness of the steel plate is large, and the bearing capacity is determined by the compressive strength of the concrete. The compressive bearing surface is the transverse projection area of the steel plate. The bearing capacity of flange plate is V_4, which is obtained by the compressive strength of the concrete in the transverse contact part of flange and concrete. According to the strain analysis, the strain in the right-hand steel plate is less than 10% in that in the left-hand steel plate, which is reduced in the calculation of bearing capacity. The triple-folded plate shear key has more intermediate folded plates. Strain analysis shows that the intermediate folded plate strain is small, only considering the shear effect of that concrete in the hole, the bearing capacity is still V_2. The simplified analysis of shear key bearing capacity is shown in Figs. 14c and 14d.

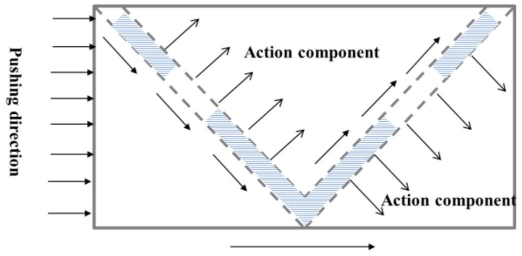

(a) Stress analysis of a shear key in the flange double-folded web

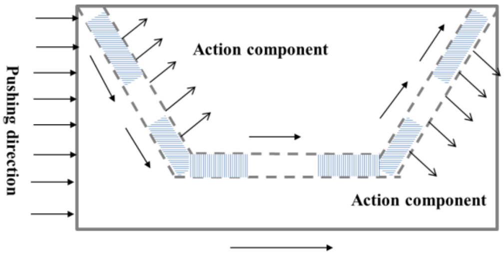

(b) Stress analysis of a shear key in the flange triple-folded web

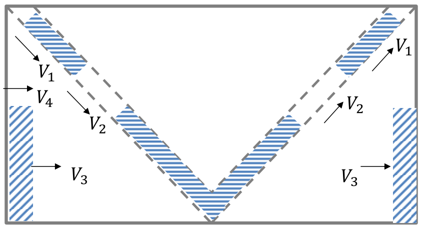

(c) Simplified analysis of the bearing capacity of a shear key in the flange double-folded web

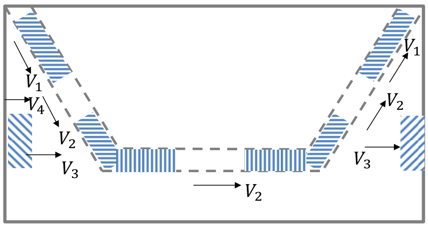

(d) Simplified analysis of the bearing capacity of a shear key in the flange triple-folded web

Fig. 14 Force analysis of a shear key

5.2. Ultimate bearing capacity calculation

Based on the test results, the failure mode of the specimen and the simplified stress model, the calculation formula of the ultimate bearing capacity of the steel plate shear key with the new semi-rigid flange folding web was proposed by considering the factors such as the steel plate strength, the plate height, the hole diameter and the folding angle:

$$V_u = V_1 + V_2 + V_3 + V_4 \tag{1}$$

$$V_1 = b_1 t_1 f_y \alpha_1 \beta \tag{2}$$

where V_u represents ultimate bearing capacity of shear keys; in formula (2), b_1 is width of the plate outside the opening. t_1 denotes web thickness. f_y is yield strength of abdominal plate test. α_1 is the yield strength reduction factor of the whole steel section (usually 0.9). β is the reduction coefficient accounting for the unequal strength of the left and right-hand folded plates (taken as 1.9) according to the difference in strain in the folded plates.

$$V_2 = H_1 t_1 f_{ck} \alpha_2 \beta \cos\theta \tag{3}$$

In formula (3), H_1 is opening height, θ is folding and push-out direction angle and f_{ck} is standard axial compressive strength of concrete. To consider the edge stress concentration strength reduction factor, a value of 0.85 is taken according to engineering experience.

$$V_3 = H b_2 f_{ck} \alpha_3 \beta \sin\theta \tag{4}$$

In formula (4), H represents web height. b_2 denotes the width of the inner web of the opening. α_3 is concrete local compressive strength reduction coefficient, according to engineering experience, a value of 0.9 is taken.

$$V_4 = B t_2 f_{ck} \alpha_2 \tag{5}$$

In formula (5), B represents flange width. t_2 is flange thickness. The comparison between the ultimate bearing capacity values calculated by this formula and the experimental values is displayed in Table 6.

Table 6
Comparison of ultimate bearing capacity between calculated and tested values

Specimen	V_1/kN	V_2/kN	V_3/kN	V_4/kN	V_u	V'_u	Aberration
S-1	78.5	12.95	88.1	8.3	375.7	412	9.7%
S-2	78.5	31.3	88.1	8.3	412.4	371	-10.0%

NOTE: Vu is the theoretical value, and $V'u$ is the experimental value.

By comparison, it is found that the discrepancy between the theoretical calculation value and the experimental value of the ultimate bearing capacity of the two new shear keys is within about 10%. On this basis, the design strength of shear keys was analyzed, as follows:

$$V_k = 0.7V_u \tag{6}$$

where f_{ck} is the concrete axial compressive design strength f_c, f_y is the designed value of steel strength f.

According to the results of the push-out test, the slip load of the shear key is taken as the actual strength and compared with the theoretical design value (Table 7). The safety margin of a double-folded plate shear key is about 19%, while that of triple-folded plate shear key is more than 60 %. Considering that (P_{max}/P_y) is more than 1.5, it has a high safety factor. This design method can better meet the engineering safety requirements imposed on the shear key.

Table 7
Comparison of design strength and test values

Specimen	Design strength V_k/kN	Test strength P_y/kN	Safety margin
S-1	179.8	214	19.0%
S-2	156.1	250	60.0%

5.3. Analysis of bond-slip characteristics

Herein, a new type of flange folded web shear key was proposed. Its design purpose is to obtain an effective unity of high bearing capacity and deformation capacity, so that it can reflect the semi-rigid characteristics to the fullest extent. In this study, the commonly used rigid shear-T-shaped shear keys (Fig. 15a) and flexible shear-stud (Fig. 15b) in engineering were selected, and the bond-slip characteristics were analyzed with the shear keys with a double-folded web flange (Fig. 15c). The bearing capacity, deformation capacity, and stiffness were compared.

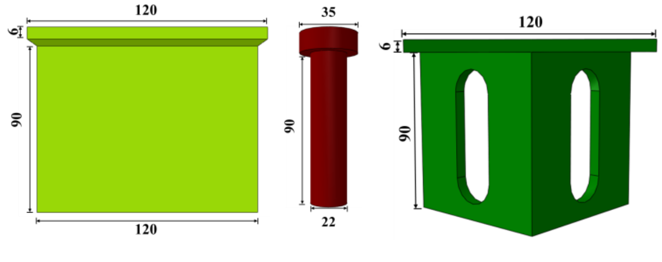

(a) T-shaped shear key (rigidity)　(b) Stud (flexible)　(c) Flange double-folded web shear key (semi-rigid)

Fig. 15 Form of shear connection

The T-shaped shear key was designed according to the principle of equal geometric size. According to the push-out test of the shear key of double-folded web flange, the dimensions of the T-shaped shear key were obtained as follows: the thickness is 6 mm, the length is 120 mm, and the height is 90 mm. The ultimate bearing capacity of the T-shaped shear key is calculated based on the failure of the left and right-hand sides of the concrete block. The bearing capacity [13] is calculated as follows:

$$P_{uT} = n_2 \eta \alpha_b \alpha_h f_t b h \tag{7}$$

where P_{uT} is the bearing capacity of the T-shaped shear key. b is the thickness of the concrete block. h is the height of concrete block. n_2 represents the number of concrete blocks on both sides of the T-shaped plate ($n_2 = 1$). η denotes the uniformity coefficient applicable to the left and right-hand sides of the concrete block in terms of the stress thereon (η=1). α_b is the reduction coefficient related to the thickness of the concrete block ($\alpha_{b=1}$). α_h is the reduction coefficient related to the height of the concrete block (α_h =1). f_t is the designed value of the axial tensile strength of the concrete. The bearing capacity of a T-shaped shear key is given by:

$$P_{uT}=n_2\eta\alpha_b\alpha_h f_t bh=108kN\ .$$

According to the calculation formula of the bearing capacity of the double-folded plate shear key, the shear bearing capacity is written as:

$$.\ P_{uy}=187.85kN$$

The stud was designed according to the principle of equal shear-section area, with a diameter of 22 mm and an overall height of 90 mm. According to the formula for stud bearing capacity proposed in the literature [5]:

$$P_{uS}=0.29\alpha d^2\sqrt{E_{CM}f_{ck}}\,/\,\gamma_v \tag{8}$$

$$P_{uS}=0.8f_u(\pi d^2/4)/\gamma_v \tag{9}$$

where, P_{uS} is the shear bearing capacity of the stud. E_{cm} is the average elastic modulus of the concrete. f_{ck} is the designed value of the compressive strength of the concrete. f_u represents the tensile strength of the stud material. d is the diameter of the stud.γ_v is the partial coefficient of resistance (γ_v= 1.25, and α = 1). Taking formulae (8) and (9) to calculate the smaller value, the shear bearing capacity of the stud is expressed as:

$$P_{uS}=0.29\alpha d^2\sqrt{E_{CM}f_{ck}}\,/\,\gamma_v=73.5kN\ .$$

According to the push-out test on Specimen S-5, the shear bearing capacity of the stud is 70.25 kN, and the error is 4.6%. Formulae (8) and (9) of the stud bearing capacity proposed in the literature [5] are reasonable.

According to *Standard for design of steel structures (GB50017-2017)* [45], shear connector stiffness coefficient is:

$$K=N_v^c(N/mm) \tag{10}$$

where N_v^c is the designed value of the shear connector bearing capacity.

The initial stiffness of the shear connector is the secant stiffness of the straight section of the load-slip curve (Fig. 16), thence the stiffness of the shear connector is deduced:

$$K_1=\frac{P_1}{\Delta_1} \tag{11}$$

$$P_1=\alpha_1 P_u \tag{12}$$

where P_1 and P_u are the slip bearing capacity and ultimate bearing capacity of T-shaped shear keys, studs, and double-folded plate shear keys. α_1 is the reduction coefficient applied to the bearing capacity: for a T-shaped shear key this is 0.7, for a stud it is 0.77, and for a double-folded plate shear key it is 0.56. Δ_1 is the slip corresponding to the slip bearing capacity P_1. Before the analysis of bond-slip characteristics, the following settings are made: the stiffness of T-shaped shear bond is large, and the slip bearing capacity is close to the ultimate bearing capacity. Assuming that it reaches the ultimate bearing capacity P_u, its displacement $\Delta_{uT}=0.1\text{mm}$, and when it reaches the slip bearing capacity P_1, its displacement $\Delta_T=0.07\text{mm}$. The stiffness of the stud is small, and the displacement $\Delta_s=1\text{mm}$ is assumed to reach the sliding bearing capacity P_1. The displacement of the semi-rigid double-folded plate shear key connector is $\Delta_y=0.5\text{mm}$ when the sliding bearing capacity P_1 is reached. After calculation, the stiffness of T-shaped shear key is: $K_{1T}=\frac{P_{1T}}{\Delta_T}=1080\text{kN/mm}$, the stiffness of a stud is: $K_{1s}=\frac{P_{1s}}{\Delta_s}=54\text{kN/mm}$, and the stiffness of a double-baffle shear key is: $K_{1y}=\frac{P_{1y}}{\Delta_y}=232\text{kN/mm}$.

The corresponding displacement P_u when shear connectors reach ultimate bearing capacity Δ_u is:

$$\Delta_u=\Delta_1+\Delta_2 \tag{13}$$

$$\Delta_2=\frac{P_u-P_1}{\alpha_2 K_1} \tag{14}$$

The stiffness reduction coefficient after sliding is given: Δ_2 is the slip occurring from reaching the slip bearing capacity P_1 to the ultimate bearing capacity P_u . α_2 is the stiffness reduction factor, for a T-shaped shear key it is 1, for a double-folded plate shear key it is 0.43, and for a stud it is 0.1. By calculation, the limit displacement of the T-shaped shear key is $\Delta_{uT}=0.1\text{mm}$, the limit displacement of a double-folded plate shear key is $\Delta_{uy}=1.4\text{mm}$, and that of a stud is $\Delta_{us}=4.0\text{mm}$.

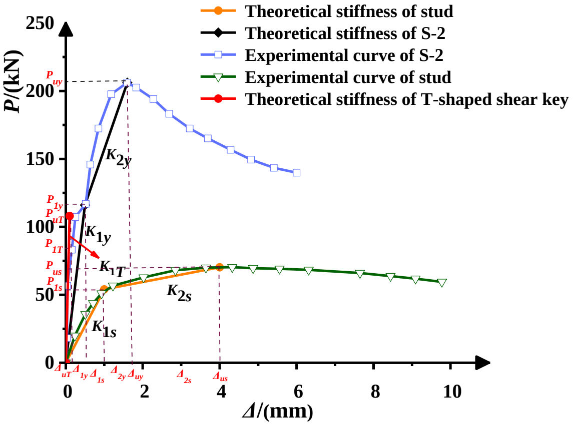

NOTE: P_{1T} , P_{1y} , and P_{1s} denote the sliding bearing capacity of a T-shaped shear key, double-folded plate shear key, and stud;

P_{uT} , P_{uy} , and P_{us} represent the ultimate bearing capacity of a T-shaped shear key, double-folded plate shear key, and stud;

Δ_T , Δ_{1y} , and Δ_s are the displacements corresponding to the sliding bearing capacity P_{1T} of a T-shaped shear key, double-folded plate shear key, and stud;

Δ_{2y} and Δ_{2s} are the displacements generated by the double-folded plate shear key and the stud from the sliding bearing capacity P_1 to the ultimate bearing capacity P_u ;

Δ_{uT} , Δ_{uy} , and Δ_{us} are the displacements corresponding to the ultimate bearing capacity P_u of a T-shaped shear key, double-folded plate shear key, and stud;

K_{1T} and K_{1s} refer to the initial stiffness of a T-shaped shear key, stud and double-folded plate shear key;

K_{s2} and K_{y2} denote the stiffness after sliding of a T-shaped shear key, stud, and double-folded shear key.

Fig. 16 Stiffness, bearing capacity, and displacement of a shear connector

The bond-slip characteristics of double-folded plate shear key, T-shaped shear key, and stud were compared (Table 8). Compared with the T-shaped shear key, the slip load of the double-folded plate shear key is increased by 39%, the ultimate bearing capacity is improved by 74%, and the deformation capacity increases more than 10-fold. The ultimate bearing capacity and deformation capacity of the double-folded plate shear key are better than those of the T-shaped shear key. Compared with the stud, the slip load of the double-folded plate shear key is increased by 86%, the ultimate bearing capacity is increased two-fold, and the stiffness is increased almost five-fold. Compared with studs, the initial stiffness and bearing capacity of double-folded plate shear key are greatly improved, which overcomes the problems of low bearing capacity and low stiffness of studs.

In summary, compared with T-shaped shear keys and studs, the ultimate bearing capacity of the double-folded plate shear key has been significantly improved, which can compensate for the poor deformation ability of the T-shaped shear key and the low bearing capacity of a stud. The stiffness is mobilized between rigid shear connectors and flexible shear connectors, which reflects the obvious semi-rigid characteristics.

Table 8
Comparison of constraint characteristics of a flange double folded web shear key, T-shaped shear key, and stud

Specimen number	Specimen type	Initial stiffness K_1/(kN mm^{-1})	Post-slip stiffness K_2/(kN mm^{-1})	Slip bearing capacity P_1 /(kN)	Ultimate bearing capacity P_u/(kN)	Ultimate displacement Δ_u/(mm)	Initial stiffness ratio	Slip bearing capacity ratio	Ultimate bearing capacity ratio	Limit displacement ratio
1	T-shaped	1080	—	75.6	108	0.1	4.66	0.72	0.57	0.07
2	S-1	232	100	105	187.85	1.4	1	1	1	1
3	Study	54	5.4	56.6	73.5	4.0	0.23	0.54	0.39	2.86

6. Conclusion

In view of the shortcomings of rigid shear keys and flexible shear keys, to obtain the effective unity of high bearing capacity and deformation, the web folding design and hole opening were adopted to improve the bonding effect of the traditional rigid shear bond and concrete, reduce the stiffness, and improve the deformation ability, so as to obtain better performance under load. Through the bond sliding pushing test of the new shear key and the study of force performance analysis and evaluation, the main conclusions are drawn as follows:

(1) Failure mode of a flange folded web shear key: concrete slabs form inclined and vertical trapezoidal main cracking areas, and the range can cover over half of the plate surface. The shear key bends along the push-out direction, and the hole edge undergoes obvious buckling. The new shear key has semi-rigid characteristics. When the concrete is damaged, the shear key also undergoes yield deformation, and the damage to the two materials is quasi-synchronous.

(2) Compared with the stud shear connector, the bearing capacity of flange folded web shear key is increased by more than 40%, and the deformation capacity is increased by more than 60%, showing good bond-slip performance. The effect of inserting steel bars at the opening on the bearing capacity is insignificant.

(3) Strain analysis shows that the strain in the flange folded web shear key is more uniform, the strains are large, and the interaction with the concrete slab is better. The strain in the right-hand folded plate of the shear key (far from the push-out end) is less than 10% of that in the left-hand folded plate, and the reduction is considered in the calculation of the bearing capacity. Based on the shear key stress model, a formula for calculation of the ultimate bearing capacity was proposed, the results from which were in good agreement with the experimental results. The proposed design bearing capacity calculation formula has a high safety margin, which can meet the requirements of engineering application.

(4) The comparison of bond-slip characteristics shows that, compared with the rigid T-shaped shear key, the slip load of the double-folded plate shear key is increased by 39%, the ultimate bearing capacity is increased by 74%, and the deformation capacity increases more 10-fold.

(5) Compared with the flexible stud, the slip bearing capacity of the double-folded plate shear key is increased by 86%, the ultimate bearing capacity is increased nearly two-fold, and the stiffness is increased nearly five-fold, thus fully meeting imposed ductility requirements. The new shear key can overcome the problems of the poor deformation capacity of rigid shear keys and the low bearing capacity of flexible shear keys. It is suggested that the double web form of shear key should be preferred in the future.

References

[1] Ataei A, Zeynalian M."A study on structural performance of deconstructable bolted shear connectors in composite beams", Structures,29 :519-533,2021.DOI: 10.1016/ j.istruc. 2020. 1 1.065.

[2] Zheng S. j, Zhao C, Liu Y.Q, Giovanni Minafò. "Parametric Push-Out Analysis on Perfobond Rib with Headed Stud Mixed Shear Connector", Advances in Civil Engineering, 2019. DOI:10.1155/2019/5952319.

[3] Liu J.P, Zhou B.X , Yu J, Wang Y.H. "Experimental study on the mechanical properties of integral steel-concrete composite beam stud shear connectors", Journal of Building Structures,38 (S1) : 337-341, 2017. DOI:10.14006/j.jzjgxb.2017.S1.047.

[4] Chaves M, Xavier E.M, Sarmanho A, et al. "Study of bolts used as shear connectors in concrete-filled steel tubes", Engineering Structures,231:111697. 2021. DOI: 10.1016 /J. ENGSTRUC T.2020.111697.

[5] D Arévalo, L Hernández, C Gómez, et al. "Structural performance of steel angle shear connectors with different orientation", Case Studies in Construction Materials, 14 (2): e00 523,2021. DOI: 10.1016/J.CSCM.2021.E00523.

[6] Qiu S.Y, Fan J.S, Nie J.G, Tang L, Song S.Y, Xu G.Q. "Shear stiffness test and theoretical study of angle steel connectors", China Journal of Highway and Transport, 34 (03) : 136 – 146, 2021. DOI:10.19721/j.cnki.1001-7372.2021.03.009.

[7] Jiang H.B, Fang H.Z, Liu J, Fang Z.C, Zhang J.F. "Experimental investigation on shear performance of transverse angle shear connectors", Structures,33:2050-2060,2021.DOI: 10.1016/J.ISTRUC.2021.05.071.

[8] Maleki S, Bagheri S. "Behavior of Channel Shear Connectors, Part I:Experimental Study", Steel Construction,64(12):1333-1340,2008. DOI:10.1016/j.jcsr.2008.01.010.

[9] Yan J.B, Hu H.T, Wang T. "Shear behaviour of novel enhanced C-channel connectors in steel-concrete-steel sandwich composite structures", Journal of Constructional Steel Research,166,2020.DOI: 10.1016/j.jcsr.2019.105903.

[10] Vianna J, Costa-Neves L F, Vellasco P, et al. "Structural behaviour of T-Perfobond shear connectors in composite girders: An experimental approach", Engineering Structures,30(9): 2381-2391, 2008. DOI:10.1016/j.engstruct.2008.01.015.

[11] Isabel, Valente, Experimental analysis of Perfobond shear connection between steel and lightweight concrete[J].Journal of Constructional Steel Research,60(3):465-479,2004. DIO:10.1016 /S0143-974X(03)00124-X.

[12] Huang H.L, Bin Z, Zhu M.Q, Zeng C.J, Lv W.R. "Static load push-out test of T-ribbed GFRP shear connectors", Journal of Architecture and Civil Engineering,33 (02) : 77-83, 2016.

[13] Li G.C, Shi X.S, Yang Z.J, Zhang H.E. "Finite element analysis of shear capacity of T-type perforated corrugated plate connectors", Steel Construction,33 (06):6-11, 2018.DOI:1 0.13206/j.gjg201806002.

[14] Yang Y, Chen Y. "Experimental study on shear capacity of PBL shear connectors", Engineering Mechanics,35 (9) : 99-96, 2018.

[15] Mohammed A. Al-shuwaili, Alesssandro Palmeri, Mariateresa Lombardo. "Experimental characterisation of perfobond shear connectors through a new one-sided push-out test", Science Driect Procedia Structural Integrity,13:2024-2029,2018.https://doi.org/10.1016/j. prostr.2018.12.315.

[16] Zhang Y.Z, Li Q, Xia S. "Research on the Influence Factors to the Working Performance of PBL Shear Connectors", Applied Mechanics and Materials,1802,2012.DOI: 10.402 8/ www. scientific.net/AMM.178-181.2192.

[17] João Paulo C. Rodrigues, Luis. Laím. "Experimental investigation on the structural response of T,T-block and T-Perfobond shear connectors at elevated temperatures", Engineering Structures,75(1):299-314,2014.https://doi.org/10.1016/j.engstruct.2014.06.016.

[18] Chen J.B, Wan S, You Y.B. "Experimental study on failure mechanism and bearing capacity of perforated corrugated plate connections", Building Structure, 43 (12) : 74 – 80 + 38, 2013. DOI:10.19701/j.jzjg.2013.12.016.

[19] Yang Y, Yang C. "Experimental Study on Mechanical Behavior of PBL Shear Connectors", Journal of Bridge Engineering,23(9),2018. DOI:10.1061/(ASCE)BE.1943-5592.0001 274.

[20] Yang Y, Yang C, Cai J.W. "Static performance test of perforated steel plate shear connectors", China Journal of Highway and Transport,30 (03) : 255-263, 2017. DOI:10. 197 21/ j.cn ki. 1001-7372.2017.03.028.

[21] Zhu W.Q, Cui Y, Liu Y.J, Heng J.F. "Research on shear capacity of perforated plate connections" Journal of Building Structures,38 (07) : 129-136, 2017. DOI:10.140 06 /j. jzjg xb.2017.07.016.

[22] LF. Costa-Neves, J. P. Figueiredo, P. C. G. da S. Vellasco, et al. "Perforated shear connectors on composite girders under monotonic loading: An experimental approach", Engineering Structures,56(1):721-737,2013. https://doi.org/10.1016/j.engstruct.2013.06.004.

[23] Xue D.Y, Huang Y.C, Wan Q.Y, Zhang Y.D. "Nonlinear analysis of the effect of penetrating steel bars on shear capacity of perforated plate connections", Industrial Construction,50 (11) : 65-70, 2020. DOI:10.13204/j.gyjz201904290005.

[24] Zhang J, Ko L.Y, Hu X.M, Zhang B, Wang C "Experimental study on PBL connectors under long-term load", Industrial Construction,48 (04) :144-152, 2018. DOI:10.1 3204 /j. gyjz20 1804028.

[25] Wang X.W, Zhu B, Cui S.G, Eric M. Lui. "Experimental Research on PBL Connectors Considering the Effects of Concrete Stress State and Other Connection Parameters", Journal of Bridge Engineering,23(1), 2018.DOI: 10.1061/ (ASCE) BE. 1943 – 5592.0001158.

[26] Di J, Zou Y, Qin F.J, Zhou X.H. "Mechanical properties of large-size PBL connectors under strong constraint conditions", China Journal of Highway and Transpor, 31 (03) : 38 – 48 + 58, 2018. DOI:10.19721/j.cnki.1001-7372.2018.03.005.

[27] Zhao C, Liu Y.Q. "Experimental study on shear capacity of perforated plate connectors", Engineering Mechanics,29 (12) : 349-354, 2012.

[28] Shi Q.X, Yang F.Z, Guo J.R. "Study on Bearing Capacity Influence Factors of the PBL Shear Connector", IOP Conference Series: Earth and Environmental Science, 560(1), 2020.DOI: 10.1088/1755-1315/560/1/012038.

[29] Chen H, Guo Z.X, Liu Y, Zheng S.J. "Experimental study on shear performance of PBL shear connector with inclined plate", Journal of Building Structures,43(01):209-218, 2022.DOI:10.14006/j.jzjgxb.2020.0092.

[30] Vetturayasudharsanan Ramasamy,Balaji Govindan. "Feasibility study on triangular perfobond rib shear connectors in composite slab", Materials Today: Proceedings,21 (Pt1): 133-136, 2020.DOI: 10.1016/j.matpr.2019.06.080.

[31] Li Z.X, Wu B, Liao M, Yang X.W, Deng K.L, Zhao C.H. "Experimental investigation on the cyclic performance of perfobond rib shear connectors", Advances in Structural Engineering,23(16):3509-3524, 2020.DOI: 10.1177/1369433220939211.

[32] Suzuki Atsushi, Abe Kanako, Suzuki Kaho, Kimura Yoshihiro. "Cyclic Behavior of Perfobond-Shear Connectors Subjected to Fully Reversed Cyclic Loading", Journal of Structural Engineering,147(3), 2021.DOI:10.1061/(ASCE)ST.1943-541X.0002955.

[33] Zhang Z, Shi J, Li G.Q, Tang Y. "Experimental study on shear capacity of embedded connectors with flanges", Journal of Zhengzhou University (Engineering Science),41 (02) : 86-90, 2020. DOI:10.13705/j.issn.1671-6833.2020.03.008.

[34] Chen J.B, You Y.B, Wan S. "Experimental study on shear behavior of perforated corrugated plate connectors for steel-concrete composite beams", Journal of Building Structures, 34 (04) :

115-123,2013. DOI:10.14006/j.jzjgxb.2013.04.013.

[35] Song R.N, Zhan Y.L, Zhao R.D. "Launch test and numerical analysis of embedded corrugated steel plate shear keys", China Journal of Highway and Transport,32 (05) : 88-99, 2019. DOI:10.19721/j.cnki.1001-7372.2019.05.009.

[36] Su Q.T, Wang R, Wang W. "Basic mechanical properties test of corrugated perforated plate connectors", China Journal of Highway and Transport,25 (02) : 46-52, 2012. DOI: 10. 197 2 1/j.cnki.1001-7372.2012.02.007.

[37] Kim Sang-Hyo, Kim Kun-Soo, Lee Do-Hoon, et al. "Analysis of the Shear Behavior of Stubby Y-Type Perfobond Rib Shear Connectors for a Composite Frame Structure", EngineeringStructures,9(147),114-124,2017.https://doi.org/10.1016/j.engstruct.2017.05.056.

[38] Kun-Soo Kim, Oneil Han, Jonghee Choi, et al. "Hysteretic performance of stubby Y-type perfobond rib shear connectors depending on transverse rebar",Construction and Building Materials,3(200), 64-79, 2019. https://doi.org/10.1016/j.conbuildmat.2018.12.070.

[39] Sang-Hyo Kim, Oneil Han, Kun-Soo Kim, Jun-Seung Park. "Experimental behavior of double-row Y-type perfobond rib shear connectors", Journal of Constructional Steel Research,150: 221-229,2018.DOI: 10.1016/j.jcsr.2018.08.012.

[40] Nie J.G, Li Y.X, Tao M.X. "Slip performance and hysteresis model of new pull-out and non-shear connectors", Engineering Mechanics, 31 (11) : 46 – 52, 2014.

[41] Zhuang D.L, Chen W, Nie X, Duan L.L, Tao M.X, Nie J.G. "Application of non-shear connectors in steel-concrete composite frame structures", Journal of Building Structures,41 (01) : 104-112, 2020. DOI:10.14006/j.jzjgxb.2018.0503.

[42] Li G.C, Wang Z.Y, Yang Z.J, Xu W. "Experimental study on shear performance of π-shaped perforated plate connectors", Journal of Building Structures,42 (02) : 131 – 141, 2021. DOI：10.14006/j.jzjgxb.2021.c176.

[43] Zhao X.B, Zhang J.K, Deng W.Q, Liu D, Zhang J.D. "Mechanical performance analysis of dumbbell stud connectors", World Bridges,48 (06) : 64-69, 2020.

[44] GB/T 10433-2002, "Cheesehead studs for arc stud welding". Beijing: Standards Press of China,2002.

[45] GB50017-2017, "Standard for design of steel structures". Beijing: China Architecture & Building Press, 2017.

Advanced Steel Construction – Vol. 18 No. 4 (2022) 763–772
DOI: 10.18057/IJASC.2022.18.4.4

PERFORMANCE EVALUATION OF INNOVATIVE COCONUT PALM STEM SHAPED STUD SHEAR CONNECTOR FOR COMPOSITE STRUCTURES

Rahul Tarachand Pardeshi [1, *] and Yogesh Deoram Patil [2]

[1] *Research Scholar, Sardar Vallabhbhai National Institute of Technology, Surat, India*
[2] *Associate Professor, Sardar Vallabhbhai National Institute of Technology, Surat, India*
** (Corresponding author: E-mail: rahultpardeshi@gmail.com)*

ABSTRACT

Headed studs are the more frequently employable shear connectors in composite structures. Despite its prevalence, this connector has exhibited remarkable drawbacks, prominently the shear failure at the bottom of the shank. In this research, three novel coconut palm stem (CPS) shaped studs are proposed for composite constructions, aiming to improve the shear capacity and slip performance of the connection. The traditional circular headed stud (CHS) geometry has been restructured to a proposed CPS-shaped stud while maintaining total steel material volume to be the same. Pushout tests were experimentally performed on CHS and CPS-shaped shear connectors to investigate their performance evaluation for ultimate strength, stiffness, ductility, and failure mode. Moreover, the Abaqus/Explicit has been employed to model a pushout specimen. A proposed finite element model was successfully validated with the test results for further parametric analysis. Two distinct grades of concrete and three CPS shapes were considered for the parametric investigation. Finally, three formulas were developed and proposed to predict the shear capacity of the CPS-shaped stud. The performance of the CHS and CPS-shaped stud connections was compared, revealing that the proposed CPS-shaped studs offer 37 to 47% higher shear strength, double stiffness, and slip with better ductility. So, CPS-shaped stud may substitute the traditional headed stud shear connectors in steel-concrete composite structures with added strength, stiffness, and ductility.

ARTICLE HISTORY

Received:	8 March 2022
Revised:	13 May 2022
Accepted:	14 May 2022

KEYWORDS

Composite structures;
Headed stud shear connectors;
Pushout test;
Concrete slab-steel beam;
CPS-shaped stud;
Abaqus

1. Introduction

An assemblies like concrete slab-steel beam composite element are an effective solution for infrastructures like buildings and bridges with substantial structural, economical, and architectural constraints. A concrete slab resists compressive forces, whereas a steel beam transmits tensile loads in composite beams (Ahn et al.[1]). However, the bond between the two components is insufficient to prevent the separation from acting as one unit. Consequently, steel-concrete interface shear connectors were introduced to create structures that unite the benefits of steel beam with reinforced concrete slabs (Viest [2]). Shear connections were shown to improve the bearing capacity of composite beams by more than half in comparison to non-composite beams of the same size (Shariati A et al.[3]). Numerous research has been done to predict their behaviour in composite beams (Mirza and Uy[4], Ding et al. [5], Spremic et al. [6]). Recent development shows the innovativeness in steel connectors like double-tube buckling-restrained braces steel connector (Yin et al.[7]), stiffened angle shear connectors (Nouri et al.[8]), the novel slip-released shear connector (Ding et al.[9]), concave shear connector (Pardeshi et al.[10]) and an innovative perforated steel-engineered cementitious composite connector (Tian et al.[11]) gaining advantages in the utilization of it in composite structures.

However, the most often utilized connecting device in composite constructions is headed stud shear connectors (see Fig. 1). The cylindrical shape of the headed stud offers shear capacity in both directions perpendicular to the shank's axis, but the small bottom circular part provides restricted shear capacity and inertia moment, necessitating the installation of a high number of studs in the composite beam which ultimately leads to uneconomical sections. To that aim, the adoption of alternative efficient connectors that offers high strength may be a viable solution for the assembly of composite connection. In this research, the traditional headed stud shape is restructured aiming to improve the shear capacity and develop the complete composite action of the composite connection by resembling the shanks' circular shape to a proposed coconut palm stem (CPS) shape to the headed stud without changing the total material volume. This connection is designed to be a convenient solution to the issues associated with the usage of the connectors described above, specifically (a) low shear capacity, (b) flexural stiffness, (c) moderate ductility, and (d) sudden failure due to the accumulation of shear stress at the connectors' shank root. In Experimental pushout tests on three types of CPS-shaped stud and two types of conventional headed studs (16 mm and 19 mm CHS) twine specimens were performed to investigate the shear capacity, failure mode, stiffness, and ductility of the composite connection. The performance of both types of connections was then compared. Validated simulations of various push test configurations having Abaqus finite element analysis software were used to appraise the effects of CPS shape and concrete compressive strength on the connection. Finally, three equations for predicting the shear capacity of CPS-shaped connections were established based on codal evaluation.

Fig. 1 Traditional headed stud shear connector

2. CPS-shaped stud shear connector

Shear connections are used in composite beams to withstand shear, bending, and tensile forces. As a result, shape, shearing area, and inertia are the most important factors to consider while ensuring the connection (Tabet-Derraz et al.[12]). Several categories of shear connectors have undergone a great deal of development and study over the last few decades (Pardeshi and Patil [13]). However, in composite construction, the headed stud is the more frequently utilized shear connector. Spite its popularity, this kind of connector has the small round geometric characteristics of the shank providing low inertia to stud bottom, which may ultimately responsible for stud failure (Xu et al.[14]) before reaching the concrete to its maximum limit. As a result, a unique connection in the form of CPS-shaped studs was developed in the current research as a simple solution to the difficulties associated with the failure of headed stud connection and to achieve complete composite action.

Three novel CPS-shaped studs for composite constructions are proposed here, as shown in Fig. 2. These connectors are designed so that the bottom 5 mm height should be used for welding the connector to the flange of the steel beam. These connectors geometry is unique and may suitable for Nelson Stud Welding's gun welding method, easy to install, and takes minimal time. The dimensions of the CPS-shaped studs are specified in Fig. 3. It is assumed that all dimensions can have a variation of ±0.5 mm. The proposed novel CPS-shaped shear connectors are of 3 types with identical heads, 24.6 mm diameter base and varying stem geometry. The head diameter was 32 mm with a depth of 9 mm.

The first type of CPS-shaped connector has a stem divided into two parts having a concave portion with a bottom diameter of 24.6 mm changing to 15 mm within a height of 25 mm, followed by a tapering section having 65 mm of length and a final diameter of 12 mm.

The second CPS-shaped shear connector's stem has three different cross-sectional profiles. A conical profile with a diameter decreasing from 24.6 mm to 14 mm for 20 mm height is followed by two cylindrical profiles with diameters 14 mm and 12 mm, and heights of 50 mm and 20 mm, respectively.

The third CPS-shaped connector was composed of a stem with four different profiles, namely convex, concave, conical, and cylindrical, in order from the base to the top. The diameter of the convex portion varies from 24.6 mm to

21.77 mm between a span of 10.33 mm. The concave portion attains a final diameter of 14mm with a length of 18.85 mm, followed by a conical portion with a final diameter of 12 mm and a height of 15.82 mm. The final cylindrical portion has 12 mm diameter and a length of 45 mm.

(a) CPS-1st (b) CPS-2nd (c) CPS-3rd

Fig. 2 CPS-shaped headed stud shear connectors

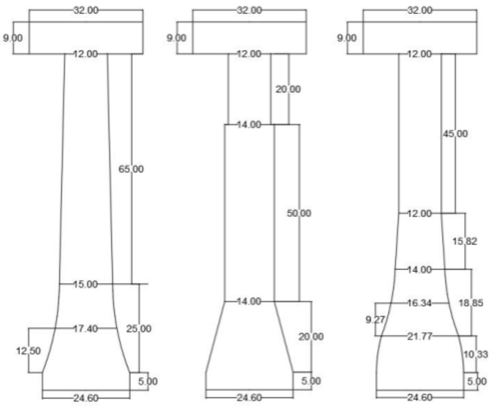

(a) CPS-1st (b) CPS-2nd (c) CPS-3rd

Fig. 3 Detailed dimensions of the CPS-shaped studs (for 16 mm average diameter)

For this research, the proposed geometry of the connection was produced in the central workshop of SVNIT, Surat as it involves cutting and chilling a standard 24.6 mm steel CHS stud into a CPS-shaped stud using lathe machine, see Fig. 4.

Fig. 4 Preparation of CPS-shaped stud using Lathe machine

3. Weld

The enlarged shank bottom area was intended to avoid stud failure at root. The root height was assume enough to guarantee adequate welding. Although the design of CPS-shaped studs allowed for gun welding, owing to its unavailability for limited volumes of research work, the fusion arc welding technique necessitated to weld the connector to the steel beam interface. The fusion arc welding was readily available in the local markets and the moderate skill labours or researchers may be able to use this method for welding.

As previously indicated, electric arc stud welding is used to weld headed studs. For arc fusion welding, E-7018 (10 No.) electrodes were used to weld the headed studs to the steel beam. In theory, the strength of a weld should, in principle, be higher than the strength of the steel plate and headed studs. However, weld quality will be impacted if welding characteristics such as electric current, lift height, and welding time are altered. As a result, weld capacity is not necessarily greater than that of steel plate and headed studs (Cao et al.[15], Cao and Shao [16]). So, the bent tests (Shim et al.[17]) as a basic laboratory test that validates the welding facts of headed studs have been used to test the weld quality (see Fig. 5). The weld was subjected to bending in an unclear way throughout the test. If an arc blow or other apparent flaw is detected, the stud must be bent such that the region to be checked inside the stress zone. Hammer blows were used to accomplish this. The studs using arc fusion welding were bent through 45° or until breakage occurs. There were no visible fractures observed in the weld and stud remain intact with weld, assuring quality of welding for further pushout testing.

(a) Arc welding (b) Hammer blow on stud (c) Initial stud (d) 45° bend stud

Fig. 5 Welding and bend test of shear connector

4. Preparation of test specimens

In the current study, ten specimens were constructed to perform the experimental pushout test. Five groups of twin specimens were considered for the average result. The CHS were used in two sets having 16 mm and 19 mm circular diameter, whereas three sets of CPS-shaped stud specimens were used for experimental testing. Table 1 describes the specimens' identity and quantity of stud material in ratio with 16 mm stud diameter. The volume of material for CPS-shaped studs was kept equal to 16 mm stud and 27% less than 19 mm stud.

Table 1
Identity of specimens with volumetric ratio

Set No.	Specimens No.	Headed Stud	The ratio of materials' volume with	
			16 mm CHS	19 mm CHS
1	1 and 2	16 mm CHS	1	0.73
2	3 and 4	19 mm CHS	1.35	1
3	5 and 6	CPS-1st	1	0.73
4	7 and 8	CPS-2nd	1	0.73
5	9 and 10	CPS-3rd	1	0.73

Moreover, the size of the steel beam does not affect the behavior of the connectors in the pushout tests (Goble and George.[18]), so the specific pushout test was performed in this study as per Eurocode 4[19] guidelines. The 200×20 mm parallel profile was used for the steel beam instead of the HEB260 profile in all specimens. The flange plate thickness of the steel beam was slightly increased to 20 mm to avoid plate buckling and to permit effective fusion arc welding of the connection in the CHS and CPS specimens against a 17.5 mm thick plate of the standard test procedure. For the preparation of parallel profile steel beam, flange plates have been welded to a 10 mm thick web plate using arc welding fusion technique. The connectors were welded to the flanges of the beams and surrounded by the concrete of the slab. It is worth noting that many researchers reduced the size of the concrete slab (Nasrollahi et al.[20], Kumar and Chaudhary[21], Kumar et al.[22]) and employed a single stud on either side of the steel beam (Kumar and Chaudhary.[21], Xue et al.[23]) for specific pushout tests. According to Anderson and Meinheit[24], the thickness of the slab does not affect the behavior and shear capacity of the connections. Therefore, in the CHS and CPS specimens, slab size was selected as 150 mm thick × 300 mm wide × 300 mm deep against the standard test, such that the bearing pressure of single centered stud on concrete during testing will not affect the strength of the connection. To prevent a splitting longitudinal fissure overhead the shear connector, Eurocode 4 [19] stipulates a minimum cover of 20 mm. So, a 25 mm cover to the reinforcement was used. All of the specimens were reinforced with 10 mm diameter rebars. On either side of the steel I-beam, two concrete slabs were placed along flange sides. The surface among the slab and the steel beam flange was lubricated so that the connection's strength will evaluate without considering the effects of surface friction. The formwork as shown in Fig. 6 was used to place the connector welded steel beam along with reinforcement mesh before pouring the concrete. After casting, the ten number of specimens as shown in Fig. 7 were ready for curing. The steel beam-concrete slab pushout specimens were ready for testing after 28 days of water curing (see Fig. 8).

Fig. 6 Progressive preparation of specimen

Fig. 7 Ten number of specimens after concreting

Fig. 8 Ready specimens for testing

4.1. Material testing

To assess the mechanical qualities of concrete, six 150 × 300 mm cylindrical concrete specimens and three 150 × 150 mm cubes were tested under compressive and tensile forces. The average strengths of concrete in compression and tension for the form of a cylindrical specimen were 30.4 MPa and 2.4 MPa, respectively. Young's modulus was 30121.47 MPa. The standard 24.6 mm headed studs were used to fabricate the CPS-shaped connector. Local vendors supplied the standard studs. The yielding and ultimate stress, and modulus of the connector were fy = 450.60 MPa, fu = 515.90 MPa, and Es = 210000 MPa, respectively, and elongation of 20%. For all pushout specimens, the steel beams and reinforcing bars used 450 MPa and Fe 500 grade steel. Fig. 9a and 9b shows the stress-stain behavior of concrete and stud material, respectively.

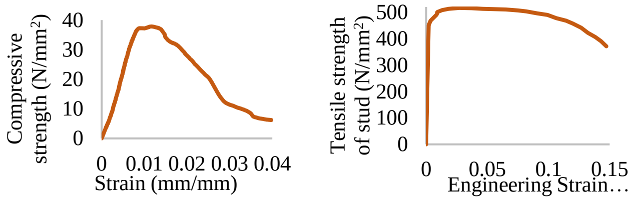

a) cube concrete (b) stud material

Fig. 9 Properties of tested materials

4.2. The portrayal of the pushout test specimens

The behavior, stiffness, and shear strength of steel beam-concrete slabs composite connections are often determined using pushout tests as per Eurocode 4 guidelines. While performing the pushout test, Eurocode 4 [19] guidelines were followed. It is recommended that specimens with CHS studs be built in a standardized design, with the dimensions of the steel beam and slab being specified in this code. On the other hand, another particular pushout test configuration is specified in the same code for specimens with different kinds of connectors. This configuration is provided without any information about the size of the pushout test components used in the setup. In this research, the specific pushout test was used to check the performance of shear connectors.

The continuous slow loading on the upper portion of the beam was applied using hydraulically loaded digital universal testing machines (UTM) (Fig. 10), generating opposite reactions to the bases of the two slabs and shear forces to the connections. UTM with a force capability of 1200 kN was utilized to perform the pushout test. The specimens were positioned beneath the UTM to verify that the weight was distributed evenly over all connectors. According to Eurocode 4 [19], successive loads were introduced slow enough on pushout specimens such that failure did not ensure in less than fifteen minutes. Digital UTM was displayed loading as "slow" on its display panel confirming 15 minutes criteria. 1000 kN capacity Load Cell having 0.04 kN least count was employed above the steel beam between two supporting plates to measure the load. The 16 mm and 19 mm CHS specimen were loaded until the stud failure. The CPS-shaped stud specimens loaded till the 20 mm maximum slip considering the observations of failure pattern/bending of connectors. The value of a slip was decided according to the FE analysis. The validated CHS studs' behavior with experimental results explained in section 8 were used to model the CPS-shaped studs.

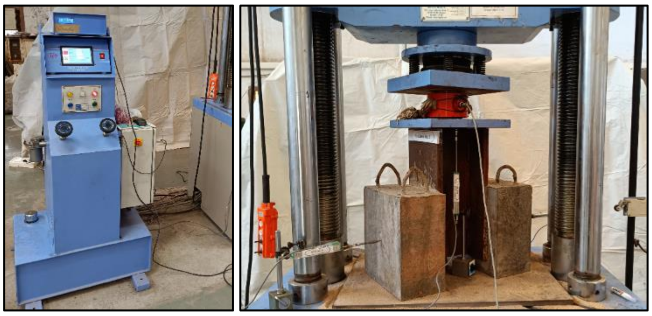

(a) Control system (b) Loading system

Fig. 10 Experimental setup

For measuring the slip among the steel beam and the concrete slab, two linear voltage differential transformers (LVDT) were used. LVDTs having 100 mm displacement capacity and 0.001 mm least count were used. In Fig.10, the various locations of the LVDT sensors on the pushout specimens are shown in more detail. Two vertical LVDTs were installed on either side of the beam web plate to measure the longitudinal slip. The data acquisition system was connected to the load cell and LVDTs for acquiring the load and longitudinal slip. In this research, the average slip was examined, and no individual data was reported.

5. Experimental findings and discussion

5.1. Load-slip performance

For the CPS-shaped connector and headed studs, the load-slip curves obtained from the pushout test are shown in Fig. 11. The average shear capacity of the 1st CPS-shaped connector was observed as 131.39 kN, compared to 95.68 kN for one 16 mm diameter CHS stud. As per Table 2, the capacity ratio of these connectors is around 1.37, indicating a 37% improvement in the CPS-shaped connector's strength over the headed stud. The average shear strength of one CPS-shaped connector for the second and third shapes was 136.92 kN and 140.59 kN. The strength ratio of the two connectors was about 1.43 and 1.47, respectively, indicating a 43% and 47% rise in the CPS-shaped connector's strength over the headed stud due to the change in geometry of the connector. It is worth noting that the shear areas ratio among the CPS-shaped stud and the CHS stud was 2.36, while the total volume was the same. This means that even though the volume of both studs is the same, the CPS-shaped studs have higher inertia at the bottom, leading to 37 to 47% more shear capacity than the CHS studs.

The average shear strength of the 1st CPS-shaped connector was observed as 131.39 kN, compared to 114.23 kN for one 19 mm diameter CHS stud. The capacity ratio of these connectors is around 1.15, indicating a 15% improvement in the CPS-shaped connector's strength over the headed stud. The strength ratio of the second and third shape connectors with 19 mm CHS stud were about 1.20

and 1.23, respectively, indicating a 20% and 23% increase in the CPS-shaped connector's strength. It is worth noting that the shear areas ratio among the CPS-shaped stud and the CHS stud was 1.67, while the total volume of the CPS-shaped stud was 27% less than the 19 mm CHS stud. This means that the CPS-shaped studs have higher inertia at the bottom, leading to 15 to 23% more shear strength than CHS stud and 27% saving in material.

The connectors are classified as ductile according to Eurocode 4 [19] if the maximum slip surpasses 6 mm. The maximum slip should measure at the 10% load fall from the ultimate strength of the connector. Based on the slip measurements, the load-slip curves (Fig. 11) reveal that all connectors showed ductile behavior. It was observed that the stiffnesses of CPS-shaped studs were 2 to 1.5 times the stiffness of 16 mm and 19 mm.

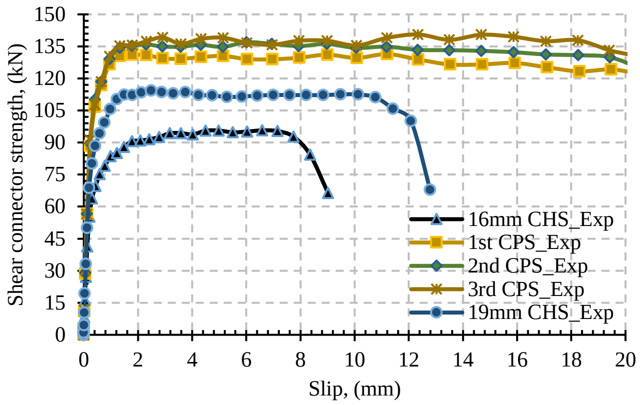

Fig. 11 Test results: Load-slip curve

5.2. Failure mode

The detected failure mechanisms of the two specimens (CHS and CPS) were different after attaining ultimate strength. The 16 mm and 19 mm CHS connectors have been sheared at the base following small deformation (see Fig. 12), whereas all CPS-shaped studs show large deflection without losing strength (See Fig. 11). The CPS-shaped studs deformed by bending away from their bottom stem and never tearing out in any location, as shown in Fig. 13. However, no failure symptoms were observed in the weld surrounding the stud base-beam flange interface. It signifies that conventional arc welding was successful in securing connection installation. The CPS-shaped studs stem bottom section was never sheared off due to a high moment of inertia at the base, whereas the headed studs failed by shear action owing to a smaller area at the base. It is reasonable to conclude that the geometric properties of studs have a great influence on the failure mode of connection.

(a) specimen 1 (16 mm stud)

(b) specimen 3 (19 mm stud)

Fig. 12 Failure of headed stud shear connector

(a) CPS-1st, (b) CPS-2nd, (c) CPS-3rd

Fig. 13 Deflected shape of CPS-shaped stud

The concrete slabs were damaged in proportion to the influence of the connector deflections. In the case of CHS studs, the shearing of the CHS studs produced local concrete crushing near the connection base (see Fig. 12a), but no cracks were seen on the concrete slabs' outside surface highlighting pure stud failure without utilizing complete composite action under given concrete strength. However, in the case of a 19 mm CHS specimen, the central vertical cracks in concrete on inside edge of the slab were observed as shown in Fig. 12b, which was not the case in a 16 mm CHS specimen. For the CPS-shaped studs considering specimen no. 5, due to the multiple stresses imposed, such as the compressive forces surrounding the shank and the tensile forces beneath the stud head, the large deflection in the middle cylindrical portion of the CPS shape caused additional damage to the inside surface of a concrete slab showing composite action (see Fig. 14). External cracking was not found on the concrete slabs' outside surfaces, revealing the scope for a composite action from the concrete. However, the second CPS shape in specimen no. 8 shows small deformation of the shank in the conical portion (see Fig. 15) and more damage to the concrete in the stress zone with open cracks to the exterior surface, exhibiting complete composite action. The third CPS-shaped stud in specimen no. 9 bend in the middle of the shank due to less cross-sectional area (see Fig 16). Furthermore, cracks were discovered on the concrete slabs exterior side surface. Therefore, in conclusion, the moment of inertia and shear area at the different locations of the shank of a stud had a significant effect on connection strength-slip performance and on the failure mode. The third CPS-shaped stud showed better strength and failure performance in achieving complete composite action over the other two CPS-shaped studs.

Fig. 14 Crushing of concrete in specimen 5 (CPS-1st)

Fig. 15 Crushing of concrete in specimen 8 (CPS-2nd)

Fig. 16 Crushing of concrete in specimen 9 (CPS-3rd)

Table 2
Performance of experimentally tested shear connectors

Specimens	Stud diameter	Capacity of shear connection, P_{ult}, (kN)	Stiffness, k, (kN/mm)	(%) Rise in shear strength = $(P_{ult} - P_{16}) \times 100/P_{16}$	Maximum slip at failure, S_{fail}, (mm)	Failure observation
1 and 2	16 mm	P_{16} = 95.68	200.92	-	8.2	Stud fail in shear at the bottom of shank.
3 and 4	19 mm	114.23	299.85	19.38	11.8	
5 and 6	CPS-1st	131.39	394.18	37.32	> 20	Bending added to the middle shank and stud never failed in shear.
7 and 8	CPS-2nd	136.92	373.43	43.10	> 20	
9 and 10	CPS-3rd	140.59	385.1	46.93	> 20	

6. Establishment of finite element models and their verification with testing results

Before parametric analysis, to know the effect of the concrete strength on stud capacity, the experimental outcomes given in this work have been assessed to establish reliability to the finite element model. Abaqus (Dynamic Explicit) tool [25] was utilized to simulate the tests results of the pushout experiment. This section explains the materials model utilized in the simulations, the damage calibration, the assembly of the pushout model, the interaction details, and appropriate meshing.

Stress-strain characteristic of materials derived from testing were used to calibrate material models. Following, the model was built with accurate geometry in the assembly section. The relevant contact definitions to obtain the critical loading transfer mechanism were incorporated in the model. The following steps were performed to reduce the model's analysis run time: (1) proper symmetric boundary conditions on the planes of symmetry were determined for each half of the specimen's geometry, (2) the mesh patterns were biased substantially so that local yielding and failure at the stud base could be captured, and high-curvature surfaces could perform better when they made contact, and (3) the load was slowly applied to reduce inertial noise. The largest swept mesh length was around 25 mm for more significant convergence, while the smallest was 2 mm. In order to determine the validity of model inputs, each simulation's results were checked against the experimental data.

6.1. Material models

It is essential to characterize each component's material behavior precisely to capture the proper failure mechanisms. Material models were calibrated before building the model of the pushout specimen by representing the samples that were utilized for various tests. A similar approach of Nguyen and Kim [26] was used to establish reliable stress-strain correlations of a concrete material model, which were then included in the global model. Moreover, Pavlovic et al. [27] methodology has been adopted to calibrate the steel material properties of a tested stud for FE modeling.

6.2. Steel material models

Structural and reinforcing steel were modeled considering the bi-linear curve shown in Fig. 17. The curve depicts an elastic-plastic model. The material's tension and compression behavior were presumed to be identical. A tri-linear curve was employed to characterize the stress-strain relationship of headed studs in a global model, as represented in Fig. 18.

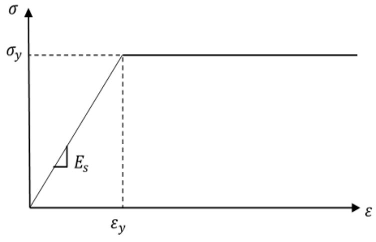

Fig. 17 Stress-strain diagram of structural and reinforcing steel for FE analysis

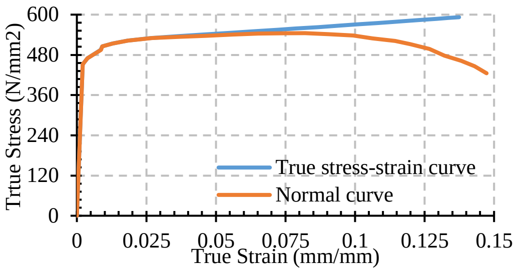

Fig. 18 Stress-strain diagram of stud material for FE analysis

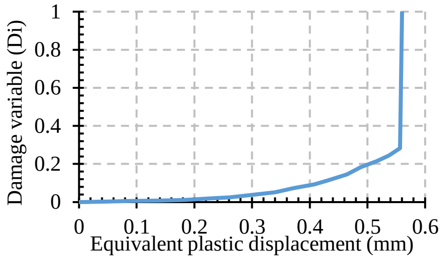

Fig. 19 Damage evolution

It is first necessary to know metal plasticity. Before fracture, the true stress-strain data is crucial for ductile fracture assessment under monotonic loading. The undeformed structure has engineering stress (s) and strain (e), whereas the smaller cross-sectional area has true stress (σ) and true strain (ε). Since the tension state becomes triaxial following necking activation, measuring true stress and strain from uniaxial tensile testing is challenging. However, the metals' real behavior may be computationally simulated for calibration following necking activation. Only stresses and strains in a triaxial stress condition must be associated. The necking activation uses equivalent stress and strain as a function of stress triaxiality (η=1/3 for uniaxial tension). Calibration data set processing of Abaqus [25] may be used to convert engineering stress and strain to true values or can calculate using relations, $\sigma_i = s_i(1+e_i)$ and $\varepsilon_i = ln(1+e_i)$. This study utilized isotropic plasticity, starting modulus of elasticity E = 210 GPa, and Poisson's ratio = 0.3 for the headed stud and steel segments. The tension test's nominal stress and strain curve was calibrated for true stress and strain value for headed stud material in the numerical simulation. The damage variable (*Di*) in consideration with equivalent plastic displacement was utilized in modeling to define the damage of post-necking material behavior as a damage evolution law as shown in Fig. 19. D=0 signifies no damage during necking activation, whereas D=1 represents maximum damage at fracture, according to the software's description [21]. For simulating necking activation, the fracture strain of the material was characterized in the FE model as an equivalent true plastic strain (ε_{up}) at the ultimate true stress state as per Rice and Tracey [28] plastic relationships and fracture law model. Here, $\varepsilon_{up} =$ 0.338 as a function of stress triaxiality (η = -0.33 to 2) (Pavlovic et al. [27]) was calibrated for experimental results using Eq. (1). Here, β is material factor depend on void grow, usually having 1.5 value. $\mathcal{E}_n^{pl}$ stain value at ultimate stress.

$$\varepsilon_{up}(\eta) = \mathcal{E}_n^{pl} \, . exp(-\beta \cdot \eta + \beta . 1/3) \tag{1}$$

It is worth noting that Abaqus [25] has the capability of removing parts that have been severely damaged. *Dmax* = 0.99 is the default threshold value. A damage element is removed from the FE model if its damage index value *D* at each junction of two different point exceeds *Dmax*. The post-necking ductile damage evolution value was extracted using the calibrated simulation, which was then utilized in detailed parametric models for FE analysis. The fracture strain ($\varepsilon_{usp} = 0.645$) as a function of the shear stress ratio, 1.8, are the characteristics that were defined the shear damage. For a failure displacement of 2.67 mm, the evolution response was tuned to linear softening and multiplicative degradation.

6.3. Concrete material models

The Concrete Damage Plasticity (CDP) model simulated the nonlinear concrete behavior, as damage parameters can be calibrated using this model, which allows degradation of stiffness and plastic deformations to be represented [21]. Fig. 20 (a) and (b) illustrate compressive and tensile concrete stress-strain curves. The curve of concrete compression has three parts. The first section is in the elastic range of the relative limit state, $0\ to\ 0.4f_{cm}$. The nonlinear parabolic component of the curve in the second segment starts at the relative limit stress $0.4f_{cm}$ and progresses to the concrete capacity f_{cm} following nonlinear parabolic segment as per Eq. (2) (Eurocode 2[29]). The section of the curve from f_{cm} to a value of αf_{cm} is the third section.

Here, the cylindrical compressive strength of concrete, $f_{cm} = 0.8\, f_{cu}$, and f_{cu} is a cube strength in MPa. The value of strain (‰) corresponding to f_{cm} is $\varepsilon_{c1} = 0.7f_{cm}{}^{0.31}$. The initial young's modulus, E_{cm} was calculated using Eq. (3) [15]. Poisson's ratio was 0.2. Factor α = 1 or less to 0.5 referred to Eurocode 2 [29] and Ellobody et al. [30]. In this study, for a good calibration of FE results, α = 0.85 was referred from the investigation of Nguyen and Kim [26]. The third section ends at $\varepsilon_{cu} = 0.0035$ suggested by Eurocode 2 [29], but for good agreement of experimental results with FE analysis, Nguyen and Kim [26] used $\varepsilon_{cu} = 0.01$, and the same was adopted here in the detailed parametric investigation of this study.

$$f_{ci} = \left(\frac{\kappa\xi - \xi^2}{1+(\kappa-2)\xi}\right) f_{cm}, 0.4\, f_{cm} < f_{ci} < f_{cm} \tag{2}$$

Here,

$$\kappa = 1.1E_{cm} \times (\varepsilon_c \,/\, f_{cm})\ \ and\ \ \xi = \varepsilon_{ci} \,/\, \varepsilon_c, \left(\frac{0.4\, f_{cm}}{E_{cm}}\right) < \varepsilon_{ci} < \varepsilon_c \tag{3}$$

$$E_{cm}\ (Mpa) = 22 \times 10^3 \times (0.1\, f_{cm})^{0.3}$$

Concrete tensile properties refer to Eqs. (4) and (5) for two segments of the tensile curve. The first segment with a linear pattern followed E_{cm} up to the highest tensile strength, f_{ctm} as per Eq. (4) up to the cracking strain, ε_{ctr} specified by Wang and Hsu [31]. The tension stiffening segment as per Eq. (5) defines the weakening function up to the total tensile strain, ε_{ctu} in the second segment. Here, the value of ε_{ctu} was selected as 0.005 for stable post processing of FE analysis and to avoid unnecessary errors.

$$f_{ctm} = 0.3(\,f_{cm} - 8)^{(2/3)} \tag{4}$$

$$f_{ct} = f_{ctm}(\varepsilon_{ctr} \,/\, \varepsilon_{ct})^{0.4}, \varepsilon_{ctr} < \varepsilon_{ct} < \varepsilon_{ctu} \tag{5}$$

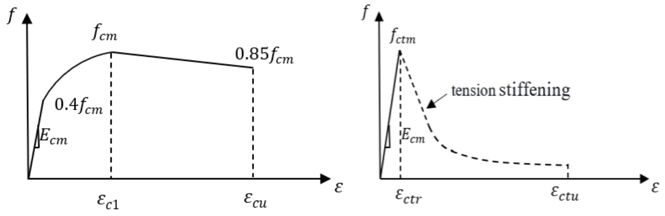

(a) compression (b) tension

Fig. 20 Stress-strain relationship of concrete material

Damaged plastic models with uniaxial material compositions were employed to pretend concrete materials' nonlinearities in compression, D_C and tension, D_t. As part of the modulus deterioration phase, the damage variables $D_C = 1 - (f_{ci}/f_{cm})$ and $D_t = 1 - (f_{ct}/f_{ctm})$ were specified. The CDP was defined by the ratio in biaxial to uniaxial state (1.16), flow potential eccentricity (0.1), deviatoric cross-section parameter (0.667), and material dilation angle (30). For verification and parametric studies, Table 3 lists the concrete properties.

Table 3
Concrete properties

Concrete properties	Grade of concrete		
	Experimental	C30	C40
f_{cm} (MPa)	30.4	38	48
ε_{c1} (‰)	2.01	2.2	2.3
f_{ctm} (MPa)	2.4	2.9	3.5
E_{cm} (GPa)	30.71	33	35

6.4. Finite element model

A pushout test was done on five different models with 16 mm, 19 mm, and three types of CPS-shaped studs. All models represent the half model geometry of test setup considering aspects of the standard pushout test with proper symmetric boundary conditions. The 16 mm and 19 mm detailed half model having CHS stud were used for comparison purposes with three different CPS-shaped studs for performance evaluation under different strength of concrete.

ABAQUS dynamic explicit was used to address the complex geometry and nonlinear FE performance of the CPS-shaped studs' pushout test specimens. Dynamic explicit is capable of dealing with complex nonlinear problems, damage, and failures. The FE analysis included geometry parts and assembly, partitions, meshing and element types, contact-interaction, boundary condition and loading, material constitutive models, damage, and failure. The preceding sections present the detailed FE models and their inclusion. A total of 10 pushout test specimens were evaluated in this investigation. Table 4 reveals the specimen identification used in research study. The CPS-shaped stud specimens have an average 16 mm stud diameter and concrete strength, 30.4MPa, 38Mpa and 48Mpa. The material properties of structural steel beam, headed stud, and reinforcement are considered identical as of testing.

The correctness of the FE analysis relies heavily on the accurate sketching of all connection components in the part module. Steel beam, reinforced concrete slab, and headed stud shear connector are the main components of the connection. Other components include reinforcing rods and a rigid base. The partition of parts has a significant impact on good meshing, so the specimen parts were partitioned to apply the proper meshing technique. The assembly module brought together all of the components that impacted the model's positioning (see Fig. 21).

A successful FE analysis relies heavily on good meshing. There are several factors that mesh components need to consider when determining stress gradients. The coarse mesh was used in the FE model to speed up the study process. Adding a fine mesh to the concrete/stud interface allowed more precise results. Fine mesh size was also employed in the headed stud at the point where the stud will fail under shear stress. The smallest mesh size was chosen to be 2 mm to better convergence, while the maximum mesh length was 25 mm. Generally, there is a specific process that most geometries can be expressed in a structured mesh. To handle complex geometries, swept meshing utilizes an internally generated mesh that is extruded or revolved around an axis of rotation. Due to the complexity of pushout test modeling and the associated difficulties with convergence, swept meshing (shown in Fig. 21) was considered for FE analysis. Along with meshing, one of the most important aspects of FE analysis is the selection of the correct element type. For plasticity, interactions, large deformations, and failure analysis, the 8-node brick (C3D8R) solid elements with reduced integration stiffness were used to mesh with the concrete slab with a geometric hole, steel beam, and the headed stud shear connector in all models. The T3D2 and R3D4 truss elements were applied to model the rigid block and rebars.

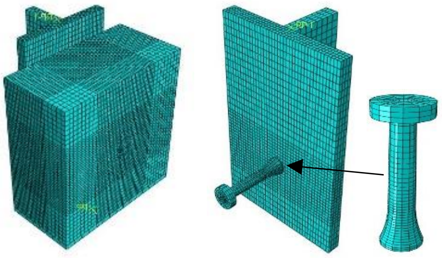

Fig. 21 Assembly and meshing of half-model

General contact and tie constraints have been used to designate the proper interaction between the assembled components. The geometric hole surface and the stud surface were tied together to eliminate relative slip between the two surfaces when using the tie constraint. The steel flange and concrete slab surfaces were typically greased when conducting experimental pushout tests to avoid friction between the two surfaces, so they were subjected to frictionless contact interaction in FE modeling. The interface of the bottom of the stud and beam flange was restrained using a tie constraint. To interpolate the nodes' translational DOF, reinforcement in concrete interacted with an embedded constrain inside the concrete slab. The concrete slab was assumed to rest on a rigid base in detailed FE models, and the surfaces have interacted with each other using contact properties. The "hard contact" and the penalty function with a friction coefficient of 0.2 were used to define the contact interaction between the rigid base and the base of the concrete slab along with normal and tangential directions. With the help of a fixed reference point and rigid body constraint, the rigid base was secured for all DOF boundary conditions. The final detailed FE models applied the z-direction symmetric boundary to the steel web's edge. To avoid a sudden change in inertia forces, the dynamic-explicit analysis generally requires a smooth loading condition. As a result, the displacement-based load was applied to the steel beam's upper area using a smooth load amplitude function of Abaqus [25] in the current analysis.

6.5. Validation

Fig. 22 depicts the theoretical load-slip curves compared with the test results to demonstrate the validity of the FE modeling. Fig. 23 describing the deflected shape of CPS-shaped studs validating the FE analysis and experimental study. No significant discrepancies were found between the experimental test curve and the FE analysis study when verifying the results for elastic and inelastic behavior of the connections. In comparison between the failure mode (fracture) of the studs in the numerical analyses and tests, Fig. 24 highlighting the fracture of stud at the root zone having equal magnitude of slip for test result (see Fig. 22). To validate FE analytical results with the experimental load-slip curve, the values of ductile and shear damage initiation, as well as the damage evolution response of steel material, were calibrated. These calibrated values have been utilized in the modeling of parametric analysis.

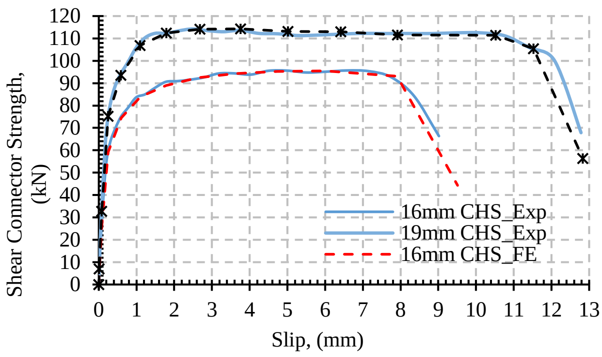

Fig. 22 Verification of FE analysis results with experimental findings

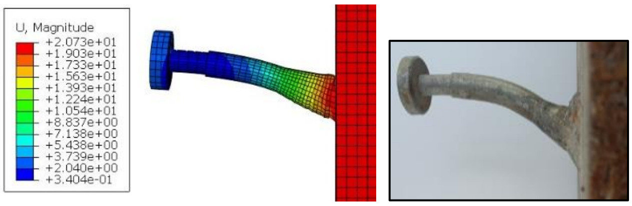

(a) Deflected shape of CPS-2nd

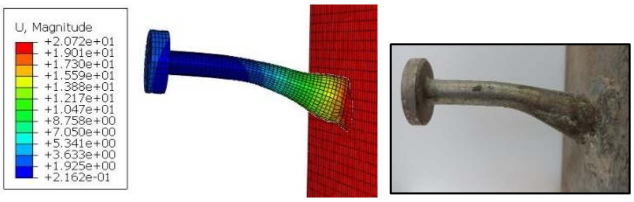

(b) Deflected shape of CPS-3rd

Fig. 23 Deflected shape of CPS-shaped stud for validation of FE analysis and experimental study

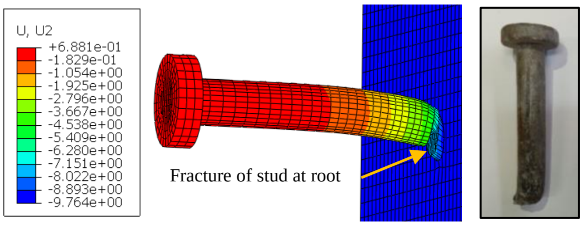

(a) for 16mm headed stud

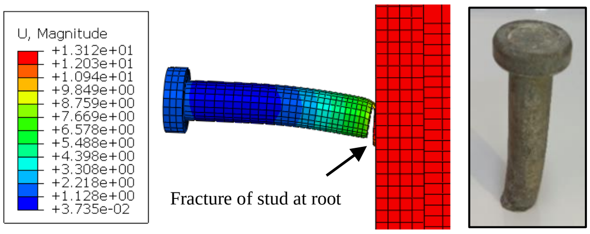

(b) for 19mm headed stud

Fig. 24 Comparison between the failure mode (fracture) of the studs in the numerical analyses and experimental tests

7. Parametric analysis results and discussions

The influence of stud shape and concrete strength on connection performance in terms of capacity, stiffness, and slip performance are discussed here. The CHS is compared to the findings of FE analysis of pushout tests on specimens with three CPS-shaped studs and two varying concrete strengths, f_{cm}, 38 and 48 N/mm^2. FE analysis revealed the ultimate load per stud (*P*), percentage rise in shear strength, stiffness (*k*), and slip at the failure of 10 pushout specimens. The entire response at the reference point acting on the top surface of a steel beam was used to compute the load. The nodes on the flange and slab at the stud center were selected to determine the connection slip. It is necessary to exercise the maximum slip capacity at failure, which is determined as per the characteristic slip given by Eurocode 4 [19]. The maximum slip capacity at failure should be exercised at 10 percent load level descends below the ultimate load as shown in Fig. 25. Following Eurocode 4 [19], the stiffness of the shear connection was estimated according to the formula, $k = 0.7P_{rk}/S_{prk}$, where P_{rk} is the characteristic load, which was taken from the load-slip curve as *0.9P*, and S_{prk} is the slip that corresponded to $0.7P_{rk}$ (see Fig. 25).

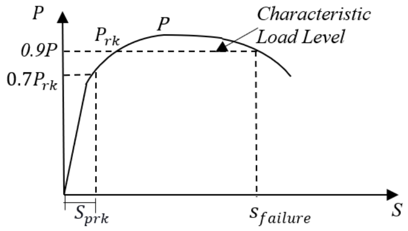

Fig. 25 Determination of stiffness and slip capacity

7.1. Effect of the strength of concrete on ductility and shear capacity of CPS-shaped shear connector

The FE model accurately signified the behavior of the shear connectors in composite beam-slabs specimen. The concrete strength is a well-known factor that influences the behavior of traditional headed studs (Ahn et al.[1], Cao et al.[15], Cao and Shao[16], Anderson and Meinheit [24]). In this parametric study, the effect of varying strength of concrete on CPS-shaped studs performance was analyzed. The FE analysis results show that the CPS-shaped studs under higher strength concrete performed well in strength and ductility than 16 mm and 19 mm CHS. The 16 mm stud was rigid under 38 and 48 N/mm^2 strength concrete (see Fig. 26a), whereas all CPS-shaped studs were ductile in behavior due to improved slip performance. Here, the shear connector is termed ductile if the ultimate slip of the connection is equal to or more than 6 mm, according to Eurocode 4 [19]. Fig. 27 compares the CHS and CPS-shaped studs' performance under C30 and C40 grade concrete. The strength of CPS-shaped studs was approximately improved up to 50 to 65% under higher grade concrete because of unique CPS geometry than 16 mm CHS. Table 4 summarizes the ultimate load per stud (P_{ult}), percentage rise in strength, stiffness (*k*), maximum slip at the failure, and ductility performance of 10 pushout specimens obtained during FE studies. It was observed that the stiffnesses of CPS-shaped studs were 2 to 1.5 times more than the stiffness of 16 mm and 19 mm.

Table 4
Performance evaluation of CPS-shaped studs under varying strength of concrete

Concrete Strength, F_{cm}, (MPa)	Stud type	Capacity of shear connection, P_{ult}, (kN)	Stiffness, k, (kN/mm)	(%) Rise in shear strength = $\frac{(P_{ult}-P_{16})\times100}{P_{16}}$	Maximum slip at failure, S_{fail}, (mm)	Ductility performance
38	16 mm CHS	101.02	212.16	0	5.8	Non-Ductile
	19 mm CHS	130.03	334.36	28.70	9.1	Ductile
	CPS-1st	151.74	413.83	50.19	16.5	Ductile
	CPS-2nd	157.03	426.42	55.43	13.7	Ductile
	CPS-3rd	155.47	416.79	53.89	16	Ductile
48	16 mm CHS	106.81	224.29	-	5	Non-Ductile
	19 mm CHS	143.38	361.32	34.24	7.2	Ductile
	CPS-1st	170.07	459.85	59.23	9.8	Ductile
	CPS-2nd	173.19	474.40	62.16	8.5	Ductile
	CPS-3rd	175.61	472.80	64.41	10.7	Ductile

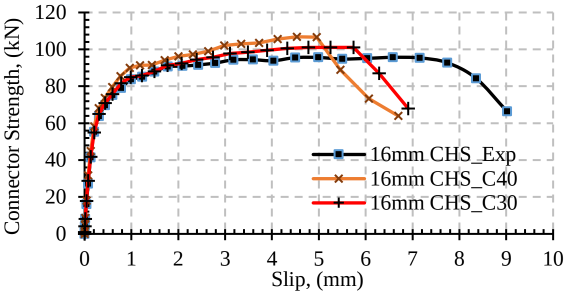

(a) 16 mm CHS load-slip curve

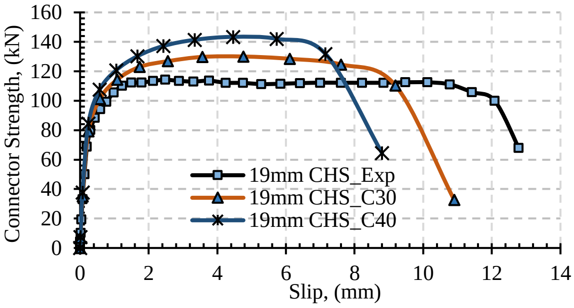

(b) 19 mm CHS load-slip curve

Fig. 26 Ductility (slip) performance of CHS under C30 and C40 grade concrete

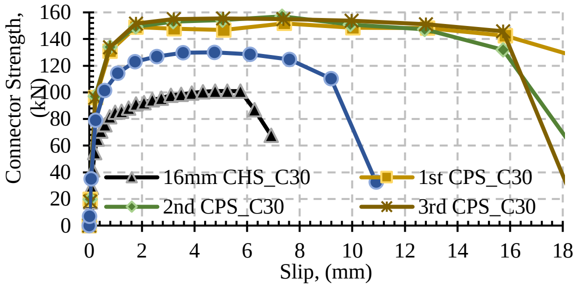

(a) Load-slip curve for C30

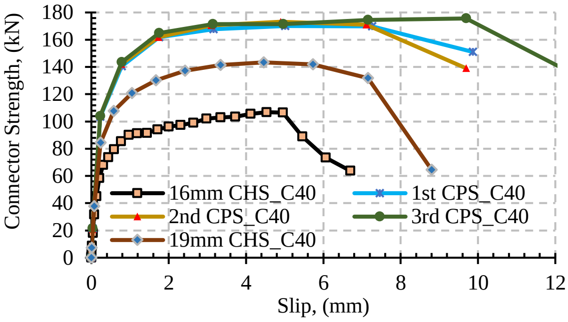

(a) Load-slip curve for C40

Fig. 27 Performance comparison for shear capacity and slip under CHS and CPS-shaped studs

7.2. Evaluation of codes for the strength of CPS-shaped connector

The experimentally evaluated shear capacity of CHS specimens under uniaxial loading is compared with the design codes' assessment findings, particularly for Eurocode4 [14], GB50017-2003 [32], AISC [33], and JSCE [34](Xu et al.[14]). The application of these standards on assessing the shear capacity of CHS studs is addressed here. Table 5 describes the capacity equation as per standard codal provisions. Here, P is the shear strength of a stud in N, h is the connector height in mm, d is the stud shank diameter in mm, and As is the area in mm^2.

Table 5
The code-based equations for calculating the headed stud shear capacity (N).

Sr. No.	Reference	Shear-capacity equations	Equation No
1	Eurocode 4 [19]	$P = 0.29\alpha d^2\sqrt{E_c f_{cm}} \le 0.8A_sF_u$ Here, $\alpha = 0.2\left(\frac{h}{d}+1\right)\ for\ 3 \le h/d \le 4$ $\alpha = 1\ for\ h/d > 4$	(6)
2	GB50017 [32]	$P = 0.43A_s\sqrt{E_c f_{cu}} \le 0.7A_sF_u$	(7)
3	AISC [33],	$P = 0.5A_s\sqrt{E_c f_{cm}} \le A_sF_u$	(8)
4	JSCE [34](Xu et al.14])	$P = 56.4d^2\sqrt{f_{cm}}\quad (h/d \ge 5.5)$ $P = 10.32dh\sqrt{f_{cm}}\quad (h/d < 5.5)$	(9) (10)

Table 6
Evaluation of codes for the strength of shear connection (kN)

Stud Type	P_{EXP}	EC 4	GB50017	AISC	JSCE	P_{EXP}/EC4	P_{EXP}/GB5	P_{EXP}/AISC	P_{EXP}/JSCE
16 mm CHS	95.68	71.73	72.57	97.08	79.60	1.33	1.31	0.98	1.20
19 mm CHS	114.23	101.15	102.33	136.90	112.43	1.12	1.11	0.83	1.01

Table 6 shows the tested stud shear capacity of 16 mm and 19 mm CHS studs and the associated design values based on various design provisions. There have been discrepancies in the specification-based evaluations. In comparison to the test findings, the AISC evaluation results are close to the stud shear capacity for 16 mm CHS; however, the JSCE (Xu et al.[14]) Eq. 10 based evaluation results are closer to the 19 mm CHS tested capacity. The difference in assessment findings of the other two specifications is approximately 11% in variation with experimental test results. AISC underestimated the effects of a larger diameter stud on shear capacity, whereas JSCE forecasted nearly equal value to 19 mm stud capacity. For the estimate of the unfactored shear strength of a connector, Eurocode 4 [19] and GB50017 [32] specifies Eq. (6) and Eq. (7) with a $0.8A_sF_u$ and $0.7A_sF_u$ constraint respectively resulting underestimated shear capacity of connector. Whereas JSCE [34](Xu et al.[14]) Eq. 10 considers the combined effect of varying concrete strength and diameter of stud for forecasting the shear capacity of connector. As a result, Eq. 10 with multiplying modification factor α are considered here, which may to forecast the stud capacity of changed designs geometry in varying concrete grade such as CPS-shaped studs with larger base diameter incorporated in different grade of concrete. The unitless modification factor, α is the ratio of capacities of CPS-shaped stud to the CHS having same larger base diameter (here the diameter of CHS is 24.6 mm), $P_{CPS}/P_{24.6}$, see Table 7. Therefore, the three formulas are proposed to calculate the shear capacity of CPS-shaped studs as follows.

Table 7
Forecasting of the modification factor, α

Code	$P_{24.6}$	α = $P_{CPS}/P_{24.6}$		
		CPS-1st = 131.39 kN	CPS-2nd = 136.92 kN	CPS-3rd = 140.59 kN
Eurocode 4 [19]	169.57	0.77	0.81	0.83
GB50017[32]	171.55	0.76	0.80	0.83
AISC[33]	229.50	0.57	0.59	0.61
JSCE[34][9]	145.57	0.90	0.94	0.96

For CPS-1st, $Q = 9.29 d_b h \sqrt{f_{cm}}$ (11)

For CPS-2nd, $Q = 9.70 d_b h \sqrt{f_{cm}}$ (12)

For CPS-3rd, $Q = 9.91 d_b h \sqrt{f_{cm}}$ (13)

Here, Q is the shear capacity of the connector, d_b is the large bottom diameter of CPS-shaped stud, h is the height of the connector, and f_{cm} be the cylindrical compressive strength of concrete.

Verification of the newly presented equations (Eq. 11 to 13) to calculate the shear capacity of CPS-shaped stud under varying concrete strength is described in Table 8. The strength of CPS-shaped stud by the FE analysis and predicted value by the proposed equations are almost identical. The ratio P_{FE}/Q is in the range of 0.99 to 1.03, verifying that the application of proposed equations to CPS-shaped studs is acceptable.

Table 8
Verification of proposed formulas under varying strength of concrete

Concrete Strength, F_{cm}, (MPa)	Stud type	FE results, P_{FE}, (kN)	Predicted capacity of CPS-shaped stud, Q	P_{FE}/Q
38	CPS-1st	151.74	146.51	1.03
	CPS-2nd	157.03	152.98	1.02
	CPS-3rd	155.47	156.29	0.99
48	CPS-1st	170.07	164.66	1.03
	CPS-2nd	173.19	171.93	1.01
	CPS-3rd	175.61	175.65	1.00

8. Conclusions

New CPS-shaped shear connectors for composite structures are proposed in the present research as an alternative to the traditional headed studs. The CPS-shaped connectors are the restructured geometry of headed studs having a large bottom area and the same overall volume. Three types of CPS-shaped connectors and two traditional-headed studs were experimentally tested under pushout loading to study their shear capacity and slip performance. Whereas the effects of modifying the shape of headed studs as CPS shape and varying concrete strength on shear connections' ultimate capacity and ductility were investigated through FE analysis. From the observations of experimental and FE studies, the following conclusions have been obtained:

- In the case of CPS-shaped studs having the same volume as 16 mm headed stud, the CPS-shaped studs have 37 to 47% higher shear strength and 2 times more stiffness than CHS studs because of the increased inertia at their bottom.
- In the case of CPS-shaped studs having 27% less overall volume than 19 mm headed stud, the CPS-shaped studs offer 15 to 23% more shear strength, 1.5 times more stiffness, and 27% saving in steel material than CHS studs.
- The geometrical design of the CPS-shaped connector conferred ductile behavior to the connection; moreover, it nourished more than twice the ductility to the connection before stud failure compared to the CHS.
- The FE model accurately predicted the behavior of the shear connector and validated the experimental findings of pushout testing.
- The FE analysis results revealed that all CPS-shaped studs exhibited ductile behavior due to enhanced slip performance compared to the rigid behavior of 16 mm CHS studs under C30 to C40 grade concrete. Because of the distinctive CPS shape compared to 16 mm CHS, the strength of CPS-shaped studs was increased by 50 to 65 percent under C30 to C40 grade concrete.
- Finally, based on the FE parametric analysis and codal evaluations, three formulas for predicting the shear strength of the CPS-shaped stud were developed and proposed for composite structures.

Acknowledgement

The authors are grateful to the Ministry of Education (MoE) India, and Sardar Vallabhbhai National Institute of Technology Surat, India, for the support received.

References

[1] Ahn J.H., Kim S.H., and Jeong Y.J., "Shear behaviour of perfobond rib shear connector under static and cyclic loadings," Magazine of Concrete Research, 60(5), 347–357, 2008, doi: 10.1680/macr.2007.00046.

[2]Viest I.M., "Investigation of stud shear connectors for composite concrete and steel T-beams," ACI Journal Proceedings, 52(4), 875–892, 1956, doi: 10.14359/11655.

[3] Shariati A S.M., Sulong NHR, and Suhatril M., "Various types of shear connectors in composite structures: A review," International Journal of the Physical Sciences, 7(22), 2876–2890, 2012, doi: 10.5897/IJPSX11.004.

[4] Mirza O., and Uy B., "Effects of strain regimes on the behaviour of headed stud shear connectors for composite steel-concrete beams," Advanced Steel Construction, 6(1), 635–661, 2010.

[5] Ding Y., Dai X.M., and Yan J.B., "Developments and behaviors of slip-released novel connectors in steel-concrete composite structures," Advanced Steel Construction, 15(1), 30–36, 2019, doi: 10.18057/IJASC.2019.15.1.5.

[6] Spremic M., Markovic Z., Veljkovic M., and Budjevac D., "Push-out experiments of headed shear studs in group arrangements," Advanced Steel Construction, 9(2), 139–160, 2013, doi: 10.18057/IJASC.2013.9.2.4.

[7] Yin Z., Feng D., Yang B., and Pan C., "The seismic performance of double tube buckling restrained brace with cast steel connectors," Advanced Steel Construction, 18(1), 436-445, 2022, doi: 10.18057/IJASC.2022.18.1.2

[8] Nouri K., Sulong N.H.R., Ibrahim Z., and Shariati M., "Behaviour of novel stiffened angle shear connectors at ambient and elevated temperatures," Advanced Steel Construction, 17(1), 28-38, 2021, doi:10.18057/IJASC.2021.17.1.4.

[9] Ding Y., Dai X., and Yan J., "Developments and behaviors of slip-released novel connectors in steel-concrete composite structures," Advanced Steel Construction, 15(1), 30-36, 2019, doi: 10.18057/IJASC.2019.15.1.5 30

[10] Pardeshi R.T., Singh P.A., and Patil Y.D., "Performance assessment of innovative concave type shear connector in a composite structure subjected to push-out loading," Materials Today: Proceedings, 2022, doi:10.1016/j.matpr.2022.03.262

[11] Tian L., Liu T., Li T., and Lin H., "Shear resistance of novel perforated shaped steel-engineered cementitious composite (ECC) connectors," Advanced Steel Construction, 16(1), 30-36, 2020, doi: 10.18057/IJASC.2020.16.1.4 30

[12] Tabet-Derraz M.I., Khelil A., Hamdaoui K., Boumechra N., and Abdallah M., "Experimental and numerical study of an innovative OMEGA-shaped connector for composite beams," Structures, 32(8), 279–297, 2021, doi: 10.1016/J.ISTRUC.2021.02.050.

[13] Pardeshi R.T., and Patil Y.D., "Review of various shear connectors in composite structures," Advanced Steel Construction, 17(4), 394–402, 2021, doi: 10.18057/IJASC.2021.17.4.8.

[14] Xu C., Sugiura K., Wu C., and Su Q., "Parametrical static analysis on group studs with typical push-out tests," Journal of Constructional Steel Research, 72(6), 84–96, 2012, doi: 10.1016/J.JCSR.2011.10.029.

[15] Cao J., Shao X., Deng L., and Gan Y., "Static and fatigue behavior of short-headed studs embedded in a thin ultrahigh-performance concrete layer," Journal of Bridge Engineering, 22(5), p. 04017005, 2017, doi: 10.1061/(asce)be.1943-5592.0001031.

[16] Cao J., and Shao X., "Finite element analysis of headed studs embedded in thin UHPC," Journal of Constructional Steel Research, 161(10), 355–368, 2019, doi: 10.1016/J.JCSR.2019.03.016.

[17] Shim C.S., Lee P.G., and Yoon T.Y., "Static behavior of large stud shear connectors," Engineering Structures, 26(12), 1853–1860, 2004, doi: 10.1016/j.engstruct.2004.07.011.

[18] Goble and George. G., "Shear strength of thin flange composite specimens," Engineering Journal, American Institute of Steel Construction, 5, 62–65, 1968.

[19] Eurocode 4, Design of composite steel and concrete structures - Part 1-1: General rules and rules for buildings. London, 2004.

[20] Nasrollahi S., Maleki S., Shariati M., Marto A., and Khorami M., "Investigation of pipe shear connectors using push out test," Steel and Composite Structures, 27(5), 537–543, 2018, doi: 10.12989/scs.2018.27.5.537.

[21] Kumar P. and Chaudhary S., "Effect of reinforcement detailing on performance of composite connections with headed studs," Engineering Structures, 179(1), 476–492, 2019, doi: 10.1016/J.ENGSTRUCT.2018.05.069.

[22] Kumar P., Patnaik A., and Chaudhary S., "Effect of bond layer thickness on behaviour of steel-concrete composite connections," Engineering Structures, 177(12), 268–282, 2018, doi: 10.1016/J.ENGSTRUCT.2018.07.054.

[23] Xue W., Ding M., Wang H., and Luo Z., "Static behavior and theoretical model of stud shear connectors," Journal of Bridge Engineering, 13(6), 623–634, 2008, doi: 10.1061/(asce)1084-0702(2008)13:6(623).

[24] Anderson N.S., and Meinheit D.F., "Steel capacity of headed studs loaded in shear," RILEM Symposium on Connections Between Steel and Concrete, Illinois, USA, 202–211, 2001.

[25] ABAQUS, "Abaqus user's manual version 2019," Dassault Systèmes Simulia Corp.: Providence, RI, USA. 2019.

[26] Nguyen H.T., and Kim S.E., "Finite element modeling of push-out tests for large stud shear connectors," Journal of Constructional Steel Research, 65(10–11), 1909–1920, 2009, doi: 10.1016/J.JCSR.2009.06.010.

[27] Pavlović M., Marković Z., Veljković M., and Bucrossed D.S.D., "Bolted shear connectors vs. headed studs behaviour in push-out tests," Journal of Constructional Steel Research, 88(9), 134–149, 2013, doi: 10.1016/J.JCSR.2013.05.003.

[28] Rice J.R., and Tracey D.M., "On the ductile enlargement of voids in triaxial stress fields," Journal of the Mechanics and Physics of Solids, 17(3), 201-2017, 1969, doi: 10.1016/0022-5096(69)90033-7

[29] Eurocode 2, Design of concrete structures - Part 1-1: General rules and rules for buildings. London, 2002.

[30] Ellobody E., Young B., and Lam D., "Behaviour of normal and high strength concrete-filled compact steel tube circular stub columns," Journal of Constructional Steel Research, 62(7), 706–715, 2006. doi: 10.1016/J.JCSR.2005.11.002.

[31] Wang T. and Hsu T.T.C., "Nonlinear finite element analysis of concrete structures using new constitutive models," Computers & Structures, 79(32), 2781–2791, 2001. doi: 10.1016/S0045-7949(01)00157-2.

[32] GB50017-2003, Code for design of steel structure. Beijing, 2003.

[33] AISC, ANSI/AISC 360-05 specification for structural steel buildings. Chicago, Illinois, 2005.

[34] JSCE, Committee of steel structure: Standard specifications for steel and composite structures (Design edition). Tokyo, Japan, 2007.

Advanced Steel Construction – Vol. 18 No. 4 (2022) 773–782
DOI:10.18057/IJASC.2022.18.4.5

QUANTITATIVE EVALUATION OF EFFECT OF VARIOUS SPAN-TO-DEPTH RATIOS ON THE COLLAPSE PERFORMANCE OF PLANAR STEEL FRAMES

Zheng Tan [1], Wei-Hui Zhong [1, 2, *], Yu-Hui Zheng [1], Shi-Chao Duan [1], Bao Meng [1] and Cheng Jiang [1]

[1] *School of Civil Engineering, Xi'an University of Architecture and Technology, Xi'an 710055, China*

[2] *Key Laboratory of Structural Engineering and Earthquake Resistance, Ministry of Education, Xi'an University of Architecture and Technology, Xi'an 710055, China*

** (Corresponding author: E-mail: zhongweihui1980@163.com)*

ABSTRACT

After the removal of a column caused by the unexpected extreme loading of the building structure, the remaining structure mainly relies on the double-span beams connected with the failed column to mitigate the progressive collapse, therefore, the span-to-depth ratios of the double-span beams has significant effects on the internal force redistribution among each story and the development of the anti-collapse mechanisms of the multi-story planar frames. To investigate the effect of span-to-depth ratios on the progressive collapse performance of steel frames, the collapse analysis of three-story steel frame models with various beam depths and beam spans was numerically studied. Firstly, the correctness of the numerical modeling method was verified by the collapse test results of a two-story sub-frame. Then, the refined modeling methods were applied to the analysis of progressive collapse performance of steel frames with various span-to-depth ratios. The load response, load distribution, deformation characteristic and load-resisting mechanisms of models are investigated in detail. The results showed that the resistances provided by flexural mechanism and catenary mechanism are mainly determined by span-to depth ratios and beam span, respectively. Through the principle of energy conservation, the different resistant contribution coefficients of each story are quantitatively obtained, and corresponding empirical formulas were proposed, which can be used as a reference for resistance evaluation before the design of structural anti-collapse.

ARTICLE HISTORY

Received: 8 May 2022
Revised: 16 May 2022
Accepted: 17 May 2022

KEYWORDS

Progressive collapse;
Numerical simulation;
Vierendeel action;
Span-to-depth ratio;
Quantitative assessment

1. Introduction

With the rapid tide of development to large-scale and complex nature of modern architectures, especially with the frequent occurrence of natural and man-made disasters, building structures are alarmingly prone to a progressive collapse. Therefore, ensuring the structural overall stability under unexpected extreme loading has become one of the hot research problems in structural engineering [1-2]. The progressive collapse behavior of frame structures has been globally explored by researchers in the past decade. At present, performing a continuous path analysis of the residual load followed by that of the original structure is one of the most commonly applied methods to ensure the structural collapse resistance. Due to the financial and laboratory limitations, the collapse test of frame structures mostly uses a single-story beam-column assembly as the research object, and systematically studies important parameters such as the connection type [3-5], boundary condition [6-7], floor combination action [8], and double-span beams with unequal span [9-11]. These valuable studies preliminarily reveal the development law of the resistance mechanisms of beam members in the process of collapse. However, because the progressive collapse of buildings is a relatively complex mechanical behavior [12-13], it is unreasonable to analyze the structural load-bearing capacity based on the structural scale of a single-story frame [14-15], so as to provide design reference for building structures.

Comparison of the collapse resistance between single-story frames and multi-story frames revealed that the collapse resistance between two different structural scale models is not based on the number of stories because of the existence of Vierendeel action (VA) [16-18]. Qian et al. [19-20], Tsito et al. [21] and Zhong et al. [22] have conducted quasi-static collapse tests, and subsequently, compared and analyzed in detail the influence of connection type, failure column position, and other parameters on the structural performance. Their results show that the connection types and failure column position exhibit a considerable influence on the exertion of catenary action. However, considering the high cost, only the sub-frame in the direct influence area was considered while fabricating the experimental specimens. The extended beams is generally connected to the horizontal restraint device to consider the tie effect resulting from the peripheral frames. However, this simplification of boundary constraint for each story is not consistent with the actual boundary constraint [23-24], which may result in an miscalculation of structural resistant performance. In addition, the above experimental objects were all scaled owing to high cost, however, the scale effect may has an unneglected effect on the structural collapse behavior. Therefore, the collapse research objects should focus on the overall frames with considering the effect of VA, rather than single-story beam-column assemblies.

After a local failure of the structure caused by a sudden load, the vertical load was resisted by redistributing the shear force at beam ends and axial force in the double-span beams [25-26]. Therefore, the span-to-depth ratio of double-span beams affects the development of different resistance mechanisms. At present, research on the anti-collapse behavior of planar frames with various span-to-depth ratios is very limited. The author previously studied the effect of different beam linear stiffness on the collapse behavior of single-story frames [27]. However, there may be a considerable difference between the collapse behavior of components in the overall structure and the structural collapse performance of single-story frame (single component) under column removal scenario.

From the above review, the current researches outcomes mainly focus on the single-story frames under component level, whereas the research on the structural performance of overall planar frames is still scarce. The overall performance analysis of the internal force transfer between beam members and the development law of resistance mechanisms needs to be further studied, especially for the influence of double-span beams with various span-to-depth ratios on the structural performance. In view of the high cost of conducting the collapse tests on overall planar steel frames with various span-to-depth ratios, it is necessary to quantitatively evaluate the effect of the span-to-depth ratios on the collapse behavior of planar frames using the numerical analysis method. Therefore, in this paper, the finite element model (FEM) was first verified by comparing the test results of the two-story sub-frame proposed by Qian et al. [19]. Then, based on the refined model using shell element, a detailed numerical simulation of the resistant collapse performance of three-story planar steel frames with various span-to-depth ratios was investigated in detail, and the different resistant contribution coefficients of different stories of multi-story steel frames were quantitatively separated, which can serve as a reference for collapse resistance evaluation prior to designing the multi-story planar steel frames to mitigate progressive collapse.

2. Numerical verification

2.1. Design of multi-story planar steel frames

Three-story, four-span planar steel frames with various span-to-depth ratios were designed in accordance with the steel structure design standard GB50017-2017 [28]. The dead load (*DL*) used in the design of structures is 5.0 kN/m^2 and the live load (*LL*) is 2.5 kN/m^2. The geometric parameters of the planar frames are as follows: the beam span and story height of the frame structure are 6000 and 3000 mm, respectively. Through structural design and analysis, the column and beam sections with H450 × 300 × 11 × 18 (mm), H400 × 200 × 8 × 13 (mm) were selected, respectively. The reduced beam section (RBS) connection was adopts in the frames, and the dimension of connection is shown in Fig. 1. The RBS connection exhibits good ductility, which was favourable to the development of vertical displacement in the catenary mechanism stage through moving plastic hinge away from the beam ends [29]. The design of the weakening parameters of the beam flange were calculated by the ANSI/AISC 358 standard [30], as sated in Eqs. (1)~(4). The specific dimension of the weakening parameters of RBS cut are shown in Fig. 1, in which *a*, *b* and *c* are 120 mm, 300 mm and 40 mm, respectively.

$$0.5b_{\mathrm{f}} \leq a \leq 0.75b_{\mathrm{f}} \tag{1}$$

$$0.65h \leq b \leq 0.85h \tag{2}$$

$$0.1b_{\mathrm{f}} \leq c \leq 0.25b_{\mathrm{f}} \tag{3}$$

$$R = \frac{4c^2 + b^2}{8c} \tag{4}$$

where b_{f} is flange width of beam; *h* is the beam depth.

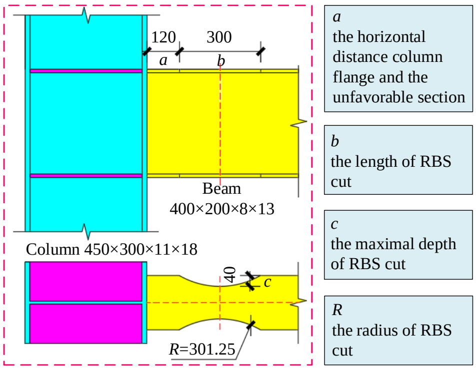

Fig. 1 Dimension of RBS connection (unit: mm)

2.2. Modeling of FEM

2.2.1. Design of structural parameters

Regarding the span-to-depth ratio of the double-span beams connected to the failed column as the research parameter, changing the beam span or beam depth of the double-span beams, corresponding to case (1) and case (2). The multi-story planar frame with beam depth of 400mm and span of 6000mm as the standard model. Models with various span-to-depth ratios in the range of 10~30 were selected. In two different cases, the structural parameters include beam span (*L*), *h*, span-to-depth ratio (*L*/*h*) and beam linear stiffness (*k*), as summarized in Table 1.

Table 1
Design of structural parameters

	Model	*L*/mm	*h*/mm	*L*/*h*	*k*/(kN·m)
Case (1)	RBS-S1	4000	400	10	118270
	RBS-S2	4800		12	98558
	RBS-S3	6000		15	78847
	RBS-S4	8000		20	59135
	RBS-S5	12000		30	39423
Case (2)	RBS-D1	6000	200	30	16839
	RBS-D2		300	20	41498
	RBS-D3		400	15	78847
	RBS-D4		500	12	130257
	RBS-D5		600	10	197105

Note: "S" and "D" presented span and depth of beam; Model RBS-S3 and model RBS-D3 were the same model; *k*=*EI*/*L*, *E* is the elastic modulus of steel, *I* is section moment of inertia of the steel beam.

2.2.2. Material model

In order to make the calculation results meet the requirements of static analysis, the kinetic energy of the model was less than 10% of the total internal energy [31]. Q345 grade steel (yield strength f_{y}=345MPa, tensile strength f_{u}=518MPa) was adopted, respectively. The elastic modulus *E* Poisson's ratio were 2.06×10^{5}MPa and 0.3, respectively. The multilinear constitutive model [11] was used for the stress-strain relationship of steel. The ductile metal failure criterion was employed to reconstruct the fracture process of models under large deformation stage and the equivalent plastic damage strain of steel ($\bar{\varepsilon}_0^{pl}$) [32] can be calculated according to Eqs. (5)~(8) .

$$\bar{\varepsilon}_0^{pl} = \begin{cases} \infty, & \eta \leq -1/3 \\ C_1/(1+3\eta), & -1/3 \leq \eta \leq 0 \\ C_1 + 9(C_2 - C_1)\eta^2, & 0 \leq \eta \leq \eta_0 \\ C_2/3\eta, & \eta_0 \leq \eta \end{cases} \tag{5}$$

Here, η is the triaxial stress; C_1 and C_2 are the $\bar{\varepsilon}_0^{pl}$ of steel under pure shear and uniaxial tension, respectively, and can be determined by Eqs. (6)~(8).

$$C_2 = -\ln(1 - A_{\mathrm{R}}) \tag{6}$$

$$C_1 = C_2(\sqrt{3}/2)^{1/n} \tag{7}$$

$$\sigma = K(\varepsilon)^n \tag{8}$$

where A_{R} is the reduced cross-sectional area; *K* and *n* are the hardening parameters of steel.

2.2.3. Boundary conditions and meshing

All beam and column members adopt S4R shell element. The connection between beam and column adopts the "Tie" command. Because the model size and boundary constraints are completely symmetrical, in order to save the calculation cost, only 1/2 model was established for numerical simulation analysis. The established FEM is illustrated in Fig. 2. For the failed and side columns, it is necessary to limit theirs out-of-plane displacement. The loading process adopts displacement control with a smooth analysis step. The six degrees of freedom of the bottom of the two side columns were constrained. For the stress concentration area of beam-to-column connections, dense grid elements with 10 mm was employed. For other beam and column members, 100mm was selected for other parts considering the calculation efficiency.

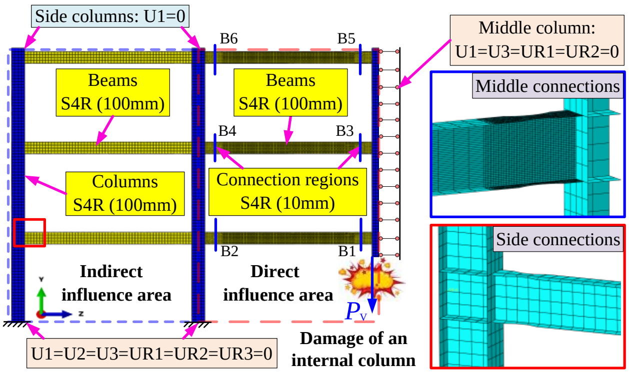

Fig. 2 Numerical modeling information of FEM

2.3. Verification of modeling methods

Before conducting the simulation numerical study, the modeling methods of the FEM was validated by the experimental results by Qian et al. [19]. A 1/2 scaled two-story steel frame with RBS connection was tested subjected to the loss of a middle column. Fig. 3 illustrated the test setup and dimensions of the RBS connections. The beam span and story height of the specimen were 3000 and 1500 mm, the length of the extended beam was 655 mm. H150 × 150 × 7 × 10 (mm) and H200 × 100 × 5.5 × 8 (mm) sections were employed to the beams and columns, respectively. The measured material properties of the frame are summarized in Table 2. The bottom of the side columns are connected with hinged connectors, and the extended beams were connected with the A-frame. At the top of the failed column, the vertical load applied by the jack was applied to simulate the removal process of the internal column until the specimen was completely destroyed. During the loading process, the specimen was restrained by the lateral steel column to prevent lateral instability, and two-point loads were applied to the tops of the side columns. The detail of the experimental test, please refer to Qian et al. [19].

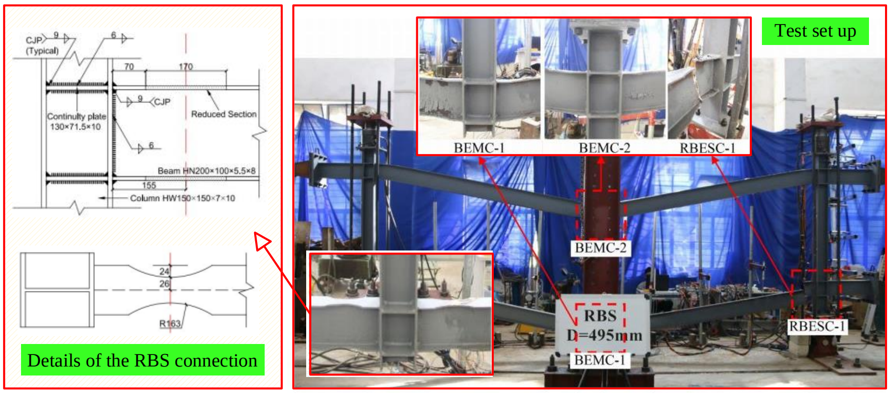

Fig. 3 Collapse test of two-story steel frame with RBS connection [19] (dimension units: mm)

Table 2
Material properties of the steel [19].

Members	Yield strength/ MPa	Ultimate strength/ MPa	Elastic modulus / GPa	Elongation/ %
Beam flange	310	420	315	12.0
Beam web	320	430	340	13.5
Column	300	410	430	14.0
Column web	295	375	265	13.0

The FEM corresponding the two-story sub-frame was established, as shown in Fig. 4. Four axial connectors were employed at the outreached beams to consider the tie effect provided by the A-frame. Axial connectors at the first and second stories with the axial stifnesses of 39.2 and 31.0 kN/mm, while the gaps were 0.7 and 0.9 mm, respectively.

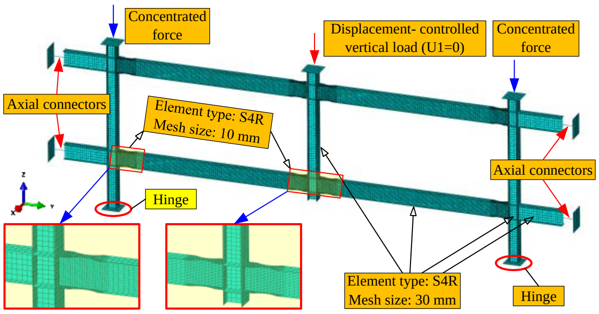

Fig. 4 FEM of the two-story sub-frame

The comparison between the numerical results predicted by FEM and the test results of the two-story sub-frame is presented in Fig. 5. It can be observed that the load–displacement curve from the results of the experimental sub-frame and FEM were in complete agreement, as illustrated in Fig. 5(a). The initial stiffness and plastic load are almost the same, and the error between the ultimate load and corresponding displacement (466 mm, 389 kN) obtained by numerical simulation and the experimental value (468 mm, 407 kN) is less than 5%, which shows that the simulation results have enough accuracy. The comparison of the failure modes predicted by the FEM and test results is shown in Fig. 5(b). It shows that the modeling methods can accurately forecast the fracture location and reproduce post fracture development path of sub-frame. Therefore, the numerical modeling methods can be employed to explore the influence of the span-to-depth ratio on the collapse-resistant performance of planar frames.

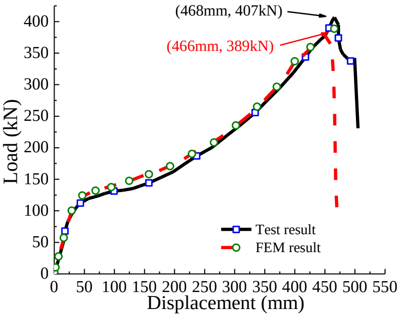

(a) The load-displacement curve

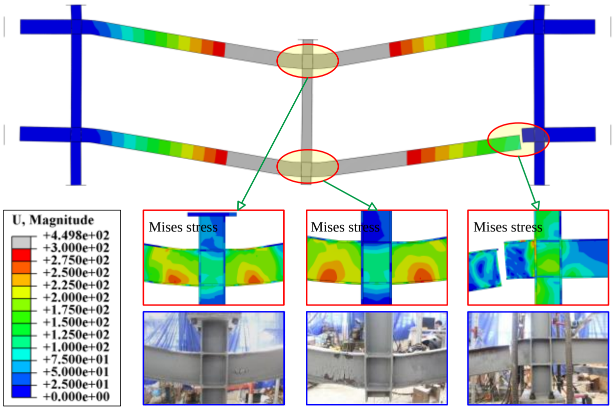

(b) Failure mode

Fig. 5 Comparison of the results of the two-story sub-frame from the test [19] and FEM

3. Analysis of span-to-depth ratio on structural collapse performance

3.1. Parameter normalization

In order to facilitate comparative analysis, the vertical displacement of the failed column, the axial force, the bending moment and the vertical load of the failed column are normalized through appropriate indicators, that is, the resulting parameters are dimensionless. The theoretical values of the corresponding index parameters are illustrated in Table 3. The vertical displacement of the failed column can be normalized by the clear span (l) of the double-span beams to characterize the relative vertical deformation of the double-span beams; The axial force of the midspan section can be normalized by the axial tensile yield force (N_p) of the most unfavorable section, with an aim to characterize the development degree of the axial force; The bending moment of the most unfavorable section can be normalized by the plastic bending capacity (m_{p+} and m_{p-}) of the most unfavorable section to characterize the degree of plastic development of the most unfavorable section, which can be calculated according to Eqs. (9) and (10).

$$N_p = f_y A \tag{9}$$

$$m_p = W_p f_y \tag{10}$$

where A is the cross section area of the most unfavorable section; W_p is the plastic section modulus of the most unfavorable section.

The vertical load was normalized by the theoretical plastic load (P_p) to characterize the structural collapse resistance. The plastic load of three-story steel frame can be calculated by plastic analysis method (see Fig. 6), which was calculated by Eq. (11).

$$P_p v = 2\theta(M_{p+} + M_{p-}), \quad \theta = v/l \tag{11}$$

The bending moments at beam ends (M_p) and most unfavorable section (m_p) can be converted through by Eq. (12).

$$\frac{m_{p-}}{M_{p-}} = \frac{m_{p+}}{M_{p+}} = (l-a-b/2)/l \tag{12}$$

where a and b were defined shown in Fig. 1.

Finally, combining Eqs. (11) and (12), the plastic load of the three-story steel frame can be calculated as follows:

$$P_p = \frac{6(m_{p+} + m_{p-})}{l-a-b/2} \tag{13}$$

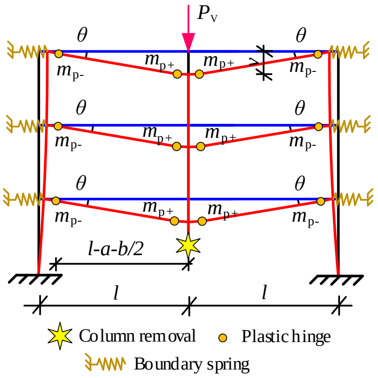

Fig. 6 Plastic analysis method for calculation of the plastic load of multi-story planar frame

Table 3
Theoretical value of structural parameters

	Model	P_p/kN	N_p/kN	m_{p+}/(kN·m)	m_{p-}/(kN·m)
Case (1)	RBS-S1	1116	2109	305	-305
	RBS-S2	897			
	RBS-S3	693			
	RBS-S4	503			
	RBS-S5	324			
Case (2)	RBS-D1	277	1557	122	-122
	RBS-D2	459		206	-206
	RBS-D3	693		305	-305
	RBS-D4	948		417	-417
	RBS-D5	1234		543	-543

3.2. Load response analysis

The load response curves of two models with various span-to-depth ratios are illustrated in Fig. 7, including the static load-displacement, dimensionless load-displacement, and pseudo static load-displacement curves. As shown in Fig. 7(a1) and (b1), the plastic load of each model increases with the increase in the L/h. Except for model rbs-d1, the final failure displacement of other models is approximately 1/5th of the span, which is close to the failure limit of frame structure in the code (1/5th of beam span [2]). Many experimental studies on the collapse of single-story frames [3,5] show that the failure displacement of substructures is far greater than the failure limit specified in the code. The major reasons for the significant difference in the conclusions of structural failure displacement between the two different scale models are the following: (1) the difference of boundary constraints (the main reason) and (2) the scale effect of the substructure (the secondary reason). This further shows that the resistance of single-story frame cannot reflect the mechanical properties of a multi-story frame structure under collapse conditions. In addition, the later bearing capacity of different span models shows a relatively gentle development trend, and its value is equivalent to the plastic bearing capacity. For different beam height models, the later bearing capacity of the model with larger beam depth shows a downward trend, while the later bearing capacity of the model with smaller beam height shows a rising trend.

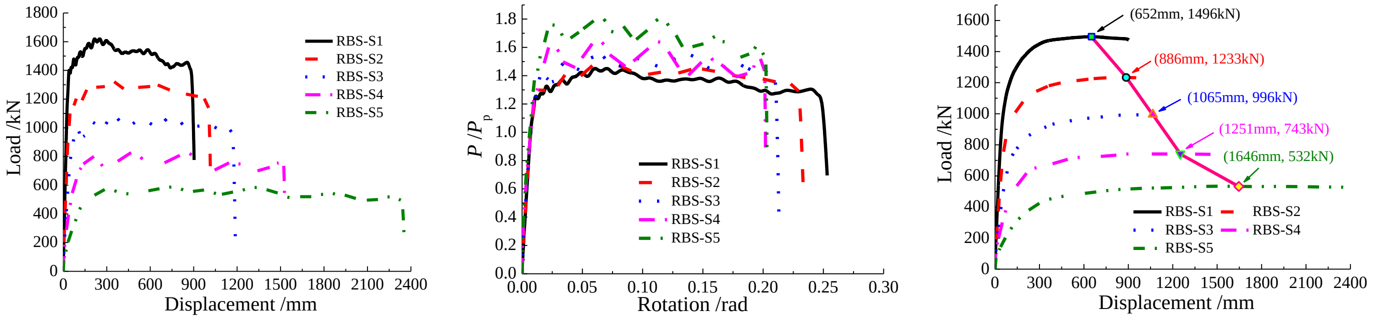

(a1) Load-displacement curve (a2) Load-displacement curve (Dimensionless) (a3) Pseudo static load-displacement curve

(a) Case (1)

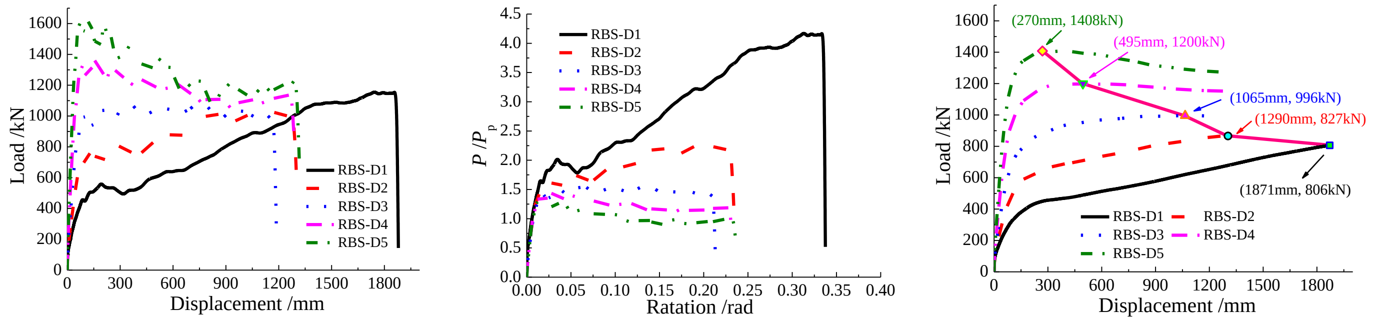

(b1) Load-displacement curve (b2) Load-displacement curve (Dimensionless) (b3) Pseudo static load-displacement curve

(b) Case (2)

Fig. 7 Comparison of load response curves of models under different cases

The dimensionless load displacement curves corresponding to each model are shown in Fig. 7(a2) and (b2). With the increase in the *L*/*h*, the P/P_p value of each model decreases in turn, and the P/P_p value of model RBS-D1 finally reaches 4, indicating that the catenary mechanism of this model has been brought into full play compared with other models. This is because the tie demand of the frame structure in the directly affected area for the surrounding frames is related to the beam-column linear stiffness ratio, so the same peripheral restraint frame exhibits a stronger tie effect for the connections with relatively small beam-column linear stiffness, which was conducive to the effective play of the catenary action in the later stage of the lower beams.

Based on the static load displacement curve, the pseudo static load displacement curve of each model can be obtained through the energy conversion principle [33]. As shown in Fig. 7(a3) and (b3), the pseudo static load of each model increases with the decrease in the *L*/*h*, but the corresponding displacement decreases, indicating that under the action of dynamic load, the model with smaller *L*/*h* of double-span beams has a better bearing capacity, but it was not conducive to the structural vertical displacement in the column removal scenario.

3.3. *Internal force development*

3.3.1. *Axial force development*

The axial force development of models with various span-to-depth ratios is shown in Fig. 8. The axial tension is mainly concentrated in the bottom story ($0.30N_p$~$1.00N_p$), while the double-span beams of the top story is mainly in the compressed state ($-0.15N_p$~0) during the process resisting vertical load, and the middle story exhibits a continuously developing axial tension ($0.10N_p$~$0.25N_p$). All the models exhibit the obvious characteristics of a Vierendeel beam, that is, the bottom story and top story are in a state of tension-bending and compression-bending, respectively. The axial tension force is continuously transmitted upward, and the models with greater the span-to-depth ratio presented more obvious characteristics of the VA, as illustrated in Fig. 8(a3) and (b3). With the increase in the *L*/*h*, the axial force development of all stories at the initial stage of loading is accelerated, while the change of axial force in the second and third stories during the stage of large-scale deformation continues to decrease with the increase in the *L*/*h*. The axial force of the models RBS-S5 and RBS-D1 exert more effectively, and can finally reach $0.80N_p$ and $0.90N_p$, exhibited obvious characteristics of tension-bending, which indicated that the beam with larger *L*/*h* is more conducive to the axial force development.

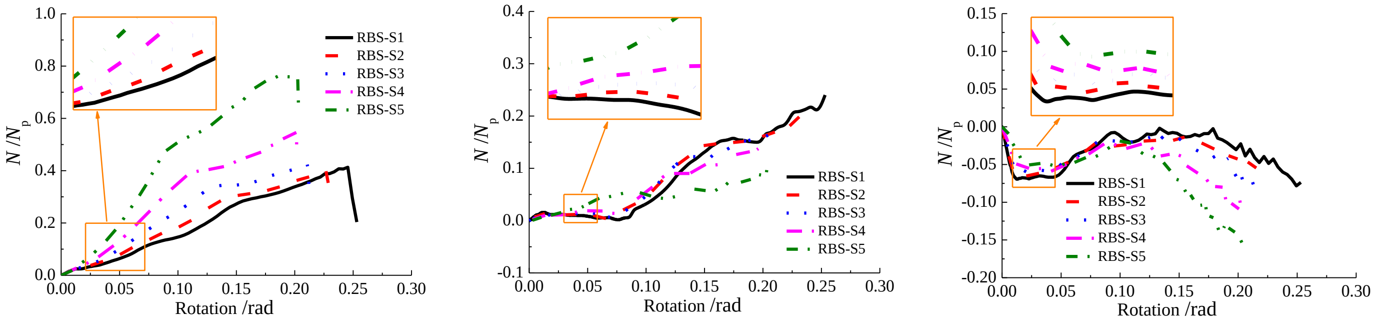

(a1) First story (a2) Second story (a3) Third story

(a) Case (1)

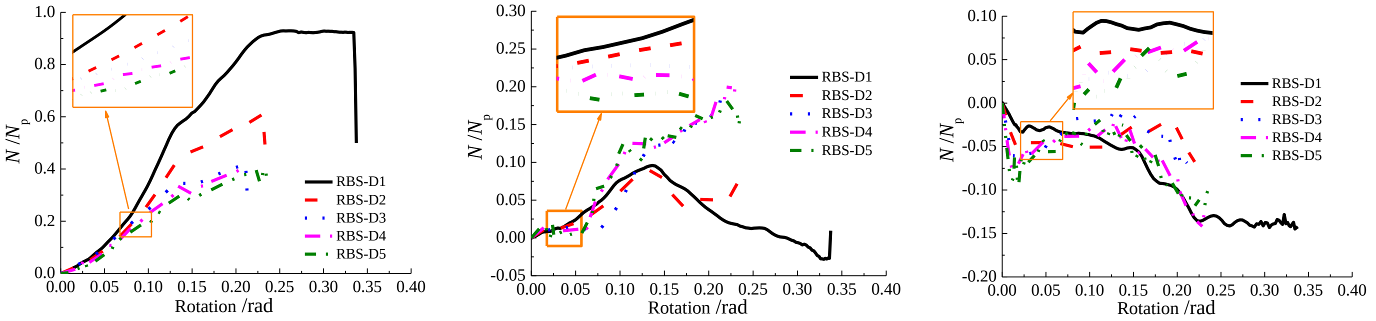

(b1) First story (b2) Second story (b3)Third story

(b) Case (2)

Fig. 8 Comparison of axial force development of models with various span to depth ratios

3.3.2. Bending moment *development*

Fig. 9 compares the normalized bending moment m/m_{pi} at the most unfavorable section of different stories of each model. For the same model, the bending moment of different stories is essentially the same in the initial stage. As the vertical displacement increases, the bending moment of the upper stories decreases continuously, and the higher the number of stories, the greater is the attenuation amplitude. This is mainly because the higher stories in the direct area receive smaller boundary restraint stiffness provided by the peripheral frames. For the different models, the bending moment of models with lager *L*/*h* developed much more quickly. Besides, the development of m_{pi} decreases with the increase of *L*/*h*, and it can be found that the m/m_{pi} of models with a large *L*/*h* does not exceed 1, such as models RBS-S5 and RBS-D1. It shows that the larger *L*/*h* was not conducive to the complete development of the bending capacity of the section and hindered the realization of m_{pi} of the corresponding section.

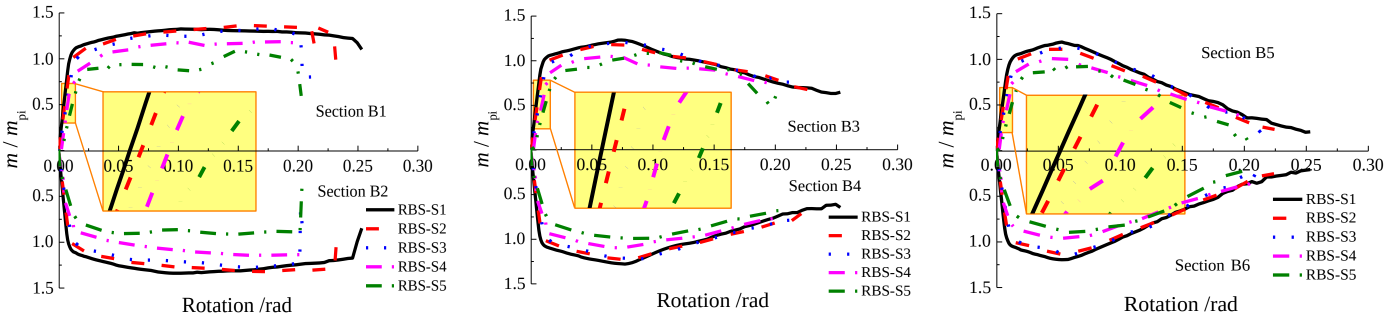

(a1) First story (a2) Second story (a3) Third story

(a) Case (1)

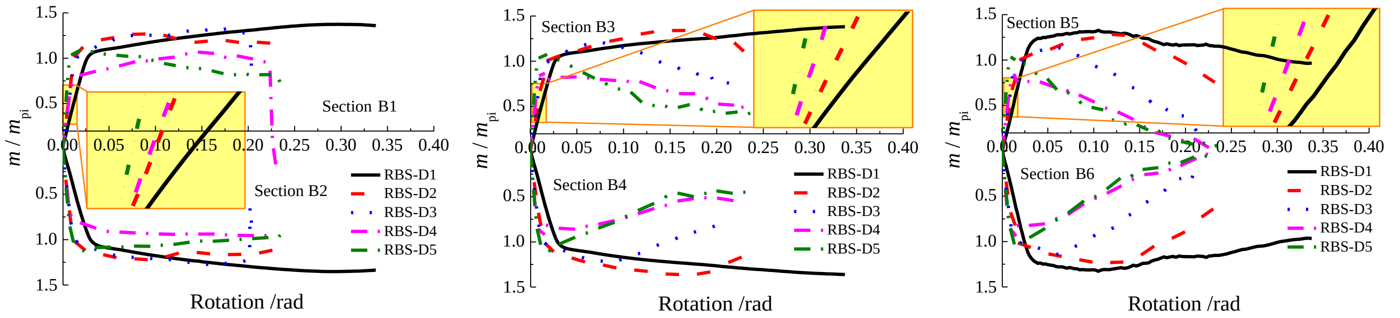

(b1) First story (b2) Second story (b3) Third story

(b) Case (2)

Fig. 9 Comparison of bending moment development of models under different cases

3.4. Overall horizontal deflection

The overall horizontal deflection of models with various span-to-depth ratio is shown in Fig. 10. The horizontal absolute displacement (the horizontal displacement of the side connection of this story relative to the initial position) of side connection at the bottom story of all models is the smallest among each story, while the horizontal relative displacement (the horizontal absolute displacement of the side connection of this story relative to the horizontal absolute displacement of the side connection of the next story) is the largest among each story. On the contrary, the horizontal displacement law of at the top story presented opposite law. Owing to the axial force development of the first story beam has too much demand for peripheral constraints, which leads to the yield of the bottom side column, and causing the peripheral columns of the upper stories can not provide sufficient tie effect for the double-span beams of the corresponding story. On the whole, the horizontal displacement of each story shows the development characteristics of continuous nonlinear decline.

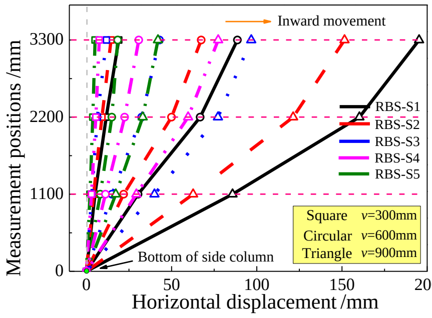

(a) Case (1)

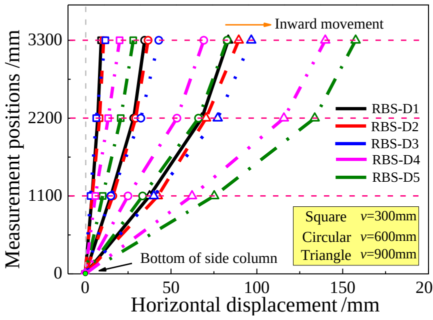

(b) Case (2)

Fig. 10 Comparison of overall horizontal defection of models under different cases

4. Mechanism resistance development and contribution level

The force equilibrium of each story beam of planar steel frame is illustrated in Fig. 11. The catenary mechanism resistance (CMR) and flexural mechanism resistance (FMR) were composed of the axial forces in the beams and shear forces at beam ends, respectively. In general, the resistant contribution of VA to the total resistance was relatively small, which can be classified into FMR [14]. The CMR and FMR can be calculated as stated in Eqs. (14)~(15), and two resistant contribution ratios were introduced to understand the contribution proportion (at one point) of FMR and CMR (μ_F, μ_C) under different vertical loading displacement of failure column. In addition, two resistant contribution coefficients (whole process) of FMR and CMR (α_F, β_C) were proposed based on the energy balance conversion principle [11] to elucidate the contribution proportion of CMR and FMR during entire loading stage, which can be calculated as stated in Eqs. (17)~(18), while α_F is equal to the sum of contribution coefficients of FMR provided by each story (α_{Fi}), and β_C is sum of contribution coefficients of CMR of each story (β_{Ci}). The collapse resistance provided by each story can be calculated according to Eq. (19), and the contribution coefficient of each story (η_i) can be determined in accordance with Eq. (20).

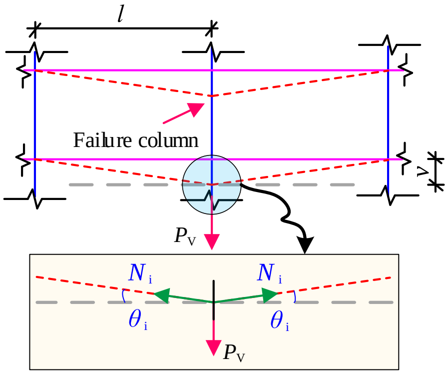

Fig. 11 Force equilibrium of each story beam of planar steel frame

$$P_C = \sum P_{Ci} = \sum (2N_i \sin\theta_i) \tag{14}$$

$$P_F = P_V - P_C \tag{15}$$

$$\mu_F = P_F / P_V,\ \mu_C = P_C / P_V \tag{16}$$

$$\alpha_F = \sum \alpha_{Fi} = \sum (\int_0^v P_{Fdi} dv / \int_0^v P_{di} dv) \tag{17}$$

$$\beta_C = \sum \beta_{Ci} = \sum (\int_0^v P_{Cdi} dv / \int_0^v P_{di} dv) \tag{18}$$

$$P_V = N_{C(max)} = \sum P_i = \sum (N_{C(i+1)} - N_{C(i)}) = \sum (P_{Fi} + P_{Ci}) \tag{19}$$

$$\eta_i = \int_0^v P_{idi} dv / \int_0^v P_{di} dv \tag{20}$$

Here, N_i is the axial force of each story beam; θ_i is the rotation of each story beam end; P_i is the resistance provided by each story; $N_{C(i+1)}$ and $N_{C(i)}$ are the axial forces of the steel columns in the $(i+1)^{th}$ and i^{th} story, respectively; $N_{C(max)}$ is equal to the total resistance; and P_{Fi} and P_{Ci} are the FMR and CMR of each story, respectively.

4.1. Case (1)

The development of the resistance mechanism and related contributions of a multi-story steel frame structure under case (1) are shown in Fig. 12. With the decrease in the *L*/*h*, the resistance introduced by the catenary and flexural mechanisms increases in turn. As shown in Fig. 12(a) and (b), decreasing the beam span is very conducive to the exertion of catenary action, resulting in the rapid transformation from flexural mechanism to catenary mechanism, as illustrated in Fig. 12(c). However, an excessive small beam span is not conducive to the structural vertical displacement under the removal of the middle column. With the increase in the *L*/*h*, P_i decreases continuously, as illustrated in Fig. 12(d) ~ (f). However, the contribution coefficients of each story presents opposite results. The resistance coefficient of the first story increases with the increase in the *L*/*h*, while the resistance coefficient of the second and third stories decreases, as illustrated in Fig. 12(i) and Table 4. The contribution coefficients of CMR and FMR are presented in Fig. 12(g). With the increase in the *L*/*h*, the contribution of the catenary mechanism continues to increase, and that of the flexural mechanism corresponding to each story decreases in turn.

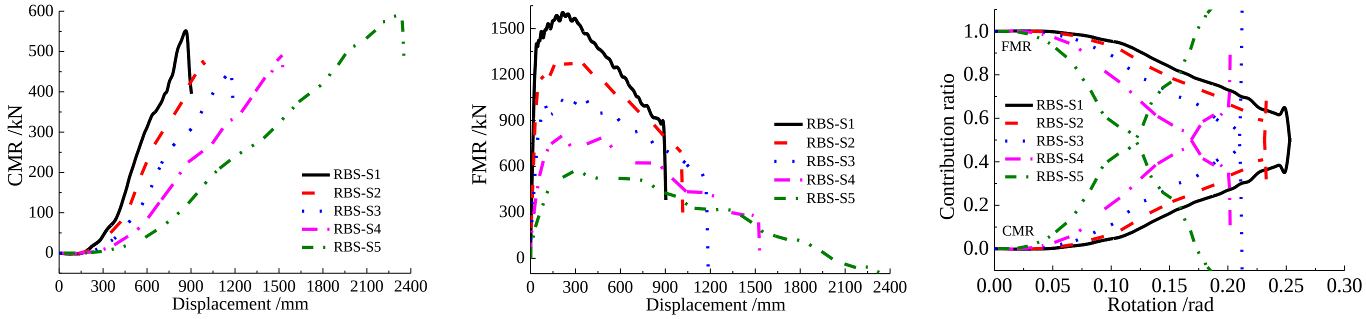

(a) CMR (b) FMR (c) Contribution ratio

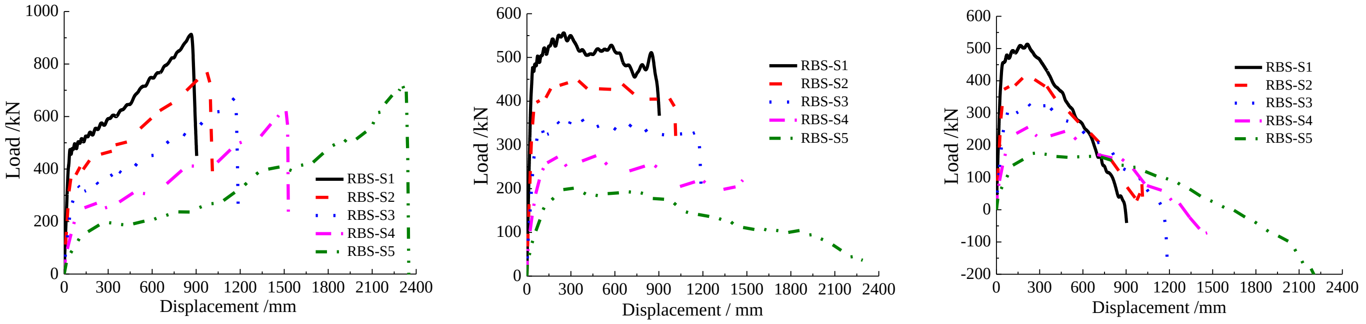

(d) Resistance of first story (e) Resistance of second story (f) Resistance of third story

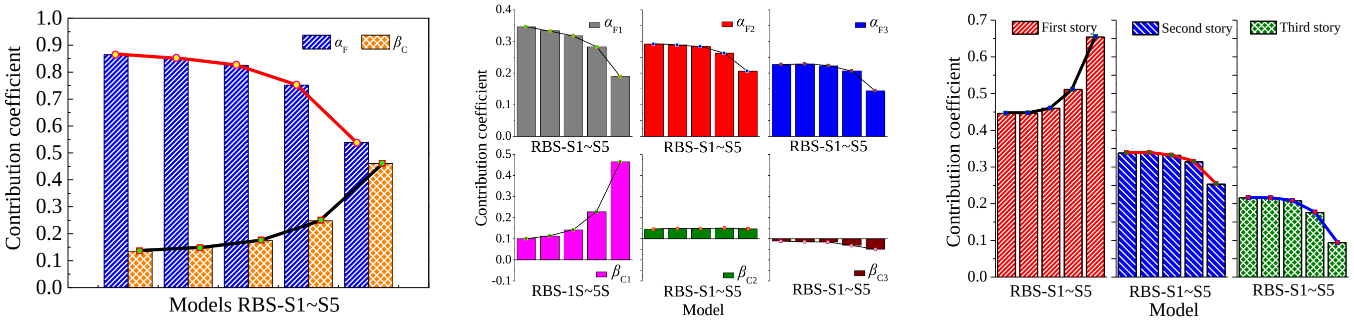

(g) Contribution coefficient of CMR and FMR (h) Contribution coefficient of CMR and FMR of each story (i) Contribution coefficient of each story

Fig. 12 Resistance development and corresponding contribution coefficients of CMR and FMR of models under case (1)

Table 4

Resistant contribution coefficients of each story beam

Models	α_F	β_C	α_{F1}	α_{F2}	α_{F3}	β_{C1}	β_{C2}	β_{C3}	η_1	η_2	η_3
RBS-S1	0.865	0.135	0.346	0.292	0.227	0.100	0.046	-0.011	0.446	0.338	0.216
RBS-S2	0.852	0.148	0.334	0.289	0.229	0.113	0.049	-0.014	0.447	0.338	0.215
RBS-S3	0.825	0.175	0.318	0.284	0.223	0.142	0.048	-0.015	0.460	0.332	0.208
RBS-S4	0.752	0.248	0.283	0.263	0.207	0.228	0.051	-0.031	0.511	0.314	0.176
RBS-S5	0.539	0.461	0.189	0.206	0.144	0.465	0.047	-0.050	0.654	0.253	0.094

4.2. Case (2)

The development of FMR, CMR and corresponding resistant contribution coefficients of three-story planar steel frames under case (2) are shown in Fig. 13. The development of the CMR of each model was very close, thus, the development trend of FMR provided by each model was completely consistent with that of the load-displacement curve, as illustrated in Fig. 13(a) and (b). The contribution ratios of different mechanism resistances during the entire loading stage is shown in Fig. 13(c). The transformation process from the FMR to CMR of models with a smaller beam depth lags behind other models. The resistance provided by each story with different beam depths is shown in Fig. 13(d)~(f). Fig. 13(g) presents the values of α_F and β_C; it can be seen that with an increase in the beam depth, the α_F decreases, whereas the β_C increases continuously. As illustrated in Fig. 13(h), increasing the beam depth can significant improve the

FMR of the first story (α_{F1}), but it is not conducive to (β_{C1}). The contribution coefficients of each story is summarized in Fig. 13(i) and Table 5. The resistance contribution coefficient of the first story decreases at first and then increases with the increasing beam depth, whereas the resistant contribution coefficient of the second and third stoies first increases and then decreases.

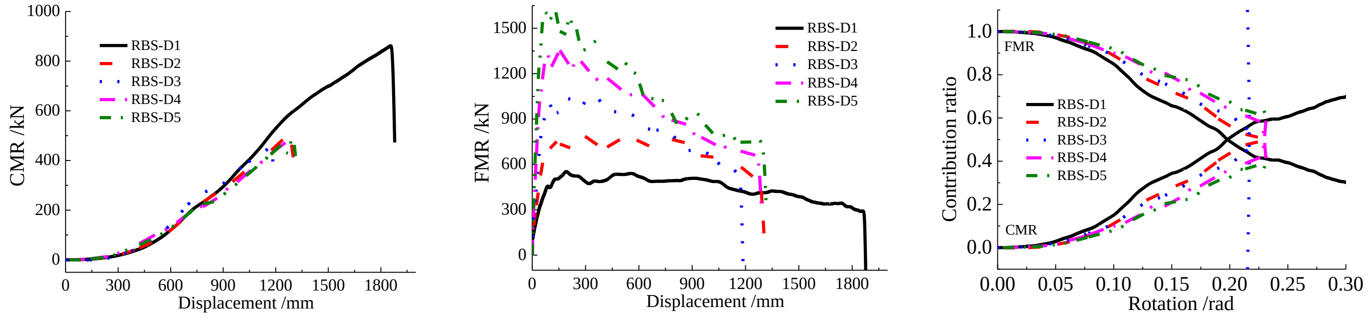

(a) CMR (b) FMR (c) Contribution ratio

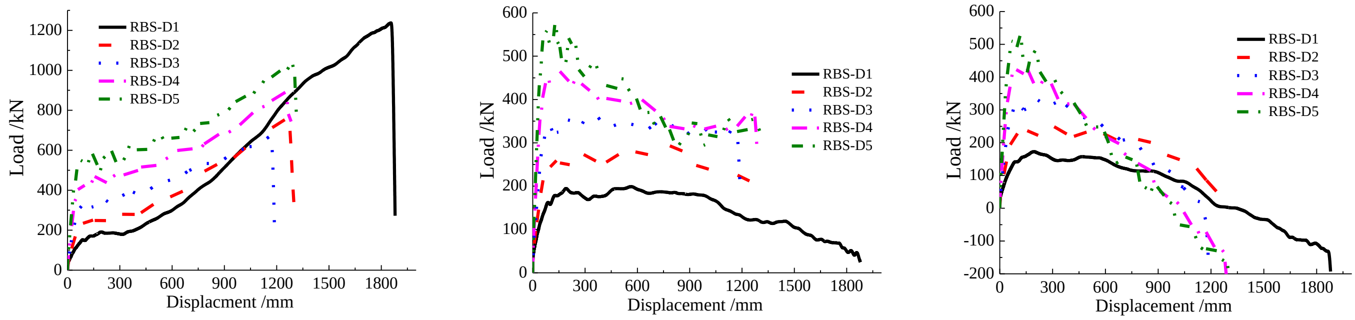

(d) Resistance of first story (e) Resistance of second story (f) Resistance of third story

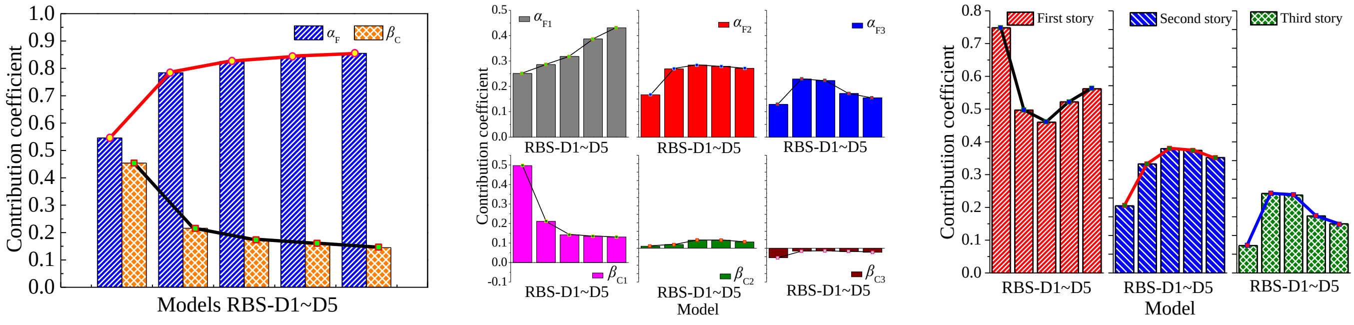

(g) Contribution coefficient of CMR and FMR (h) Contribution coefficient of CMR and FMR of each story (i) Contribution coefficient of each story

Fig. 13 Resistance development and corresponding contribution coefficients of CMR and FMR of models under case (2)

Table 5
Resistant contribution coefficients of each story beam

Models	α_F	β_C	α_{F1}	α_{F2}	α_{F3}	β_{C1}	β_{C2}	β_{C3}	η_1	η_2	η_3
RBS-D1	0.546	0.454	0.251	0.167	0.129	0.497	0.012	-0.056	0.748	0.179	0.073
RBS-D2	0.784	0.216	0.286	0.269	0.229	0.211	0.022	-0.017	0.497	0.291	0.212
RBS-D3	0.825	0.175	0.318	0.284	0.223	0.142	0.048	-0.015	0.460	0.332	0.208
RBS-D4	0.842	0.158	0.387	0.279	0.172	0.135	0.048	-0.020	0.522	0.327	0.152
RBS-D5	0.855	0.145	0.431	0.271	0.155	0.131	0.037	-0.024	0.562	0.308	0.131

5. Development trend analysis of resistant contribution coefficients

5.1. Contribution coefficients of CMR and FMR

According the resistant contribution coefficients of each story beam (Tables 1 and 2), the 3D surface of contribution coefficients of FMR and FMR under cases (1) and (2) can be nonlinear fitted, as presented in Fig. 14. The value of α_F increase with the decrease of L/h. The resistance contribution coefficients of CMR exhibited the opposite law. According to the contribution coefficients of CMR and FMR under cases (1) and (2), the empirical formulas for CMR and FMR of double-span beams under cases (1) and (2) were proposed, as illustrated in Eqs. (21) and (22).

$$\begin{aligned}\beta_C &= 0.958-3.280\times h-2.484\times10^{-2}L+3.123h^2 \\ &\quad +3.672\times10^{-3}L^2-1.838\times10^{-2}hL\end{aligned}\text{，}\quad R^2=0.929 \tag{21}$$

$$\begin{aligned}&\alpha_F = 1-\beta_C \\ &0.043+3.280\times h+2.484\times10^{-2}L-3.123h^2\text{，}\quad R^2=0.929 \\ &+3.672\times10^{-3}L^2-1.838\times10^{-2}hL\end{aligned} \tag{22}$$

R^2 is fitting coefficient, the units of beam span and beam depth were m.

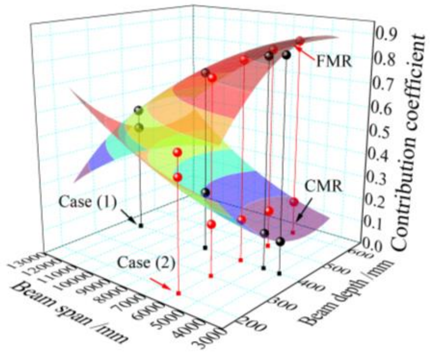

Fig. 14 Contribution coefficient of different mechanism resistances under cases (1)~(2)

5.2. Contribution coefficients of each story

The fitting 3D surface of contribution coefficients of each story under cases (1) and (2) is illustrated in Fig. 15, and the empirical formulas for the contribution coefficients of each story to the total resistance of models with various span-to-depth ratios were proposed, as illustrated in Eqs. (23)~(25), which can be provide a basic and reference for collapse resistance evaluation before the anti-progressive collapse design of multi-story planar steel frames with various span-to-depth ratios.

$$\begin{aligned}\eta_1 &= 1.103 - 0.004\times h - 2.795\times10^{-2}L + 4.797h^2 \\ &\quad + 2.734\times10^{-3}L^2 - 1.128\times10^{-1}hL\end{aligned}, \quad R^2 = 0.937 \tag{23}$$

$$\begin{aligned}\eta_2 &= 0.135 - 0.136\times h - 3.860\times10^{-2}L - 2.202h^2 \\ &\quad - 1.175\times10^{-3}L^2 + 1.166\times10^{-1}hL\end{aligned}, \quad R^2 = 0.986 \tag{24}$$

$$\begin{aligned}\eta_3 &= 1 - \eta_1 - \eta_2 \\ &= -0.236 - 1.031\times10^{-2}h - 2.590\times10^{-3}L \\ &\quad - 1.574\times10^{-3}h^2 - 1.574\times10^{-3}L^2 - 2.003\times10^{-3}hL\end{aligned}, \quad R^2 = 0.876 \tag{25}$$

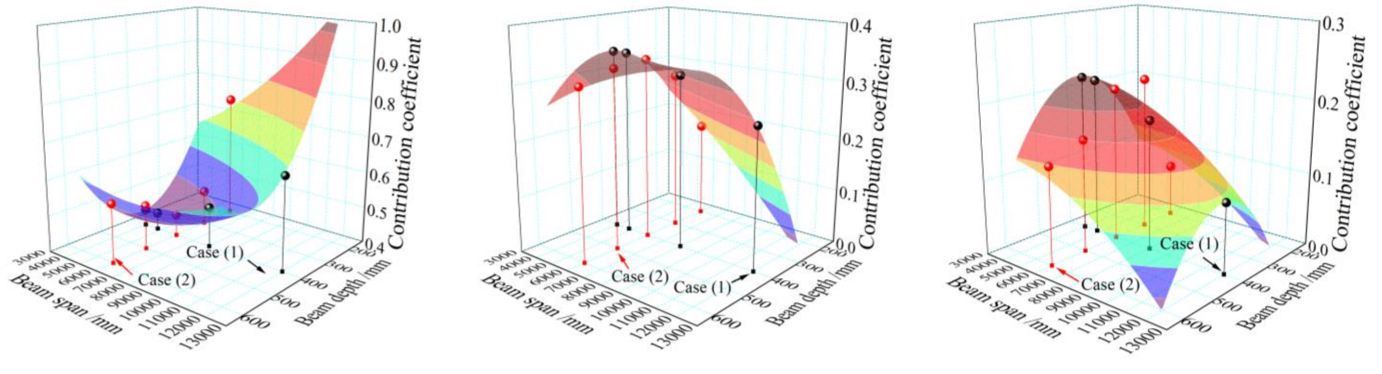

(a) First story (b) Second story (c) Third story

Fig. 15 Resistant contribution coefficient of each story under cases (1)~(2)

6. Conclusion

In this study, the three-story planar steel frames were employed to study the effect of the span-to-depth ratio of double-span beams on the structural collapse performance through the refined numerical modeling method, and makes a more comprehensive analysis on the collapse resistance level, internal force development, deformation characteristics, loading-resisting mechanisms and corresponding resistant contribution coefficients, The following conclusions are obtained:

(1) The effect of VA on the internal force development of each story beam is reflected considering the following two aspects: One hand, VA reflects the lag effect of the axial force transmission across each story, and the axial tension is continuously transmitted upward with as the increasing of structural displacement. On the other hand, VA increases the attenuation degree of bending moment among the stories from bottom to top. A combination of the above two factors leads to the largest contribution of resistance provided by the bottom story, followed by the upper story, and the lowest resistance contributed by the top story. The essence of this phenomenon is that the tie effect of the peripheral frames on the sub-fame decreases from bottom to top.

(2) The FMR and CMR were distributed by the span-to-depth ratio and beam span, respectively. Although decreasing span-to-depth ratio has a beneficial effect on the improvement of structural collapse resistance, but it was also adverse to the vertical displacement development under column removal scenario.

(3) The contribution coefficient of FMR decreases with the increasing span-to-depth ratio, whereas the contribution coefficient of CMR exhibits the opposite development law. Increasing the beam span increases the resistance contribution of the bottom story and decreases the resistance contribution coefficients of the upper stories. With a continuously increasing beam depth, the resistance contribution coefficient of the bottom stories increases at first and then decreases, while the upper stories exhibit an opposite trend.

(4) The theoretical formulas of collapse-resistant capacity were empirical proposed through nonlinear fitting the contribution coefficients of different resistance mechanisms of each story, which can provide a more important reference for collapse resistance evaluation before the design of multi-story steel frames to resist progressive collapse.

Acknowledgments

The works in this paper was sponsored by the National Natural Science Foundation of China [grant numbers 51678476, 51908449], Scientific research plan projects of Shaanxi Education Department [grant number 20JY033, 20JK0713].

References

[1] Meng B., Li L.D., Zhong W.H., et al., "Improving anti-progressive collapse capacity of welded connection based on energy dissipation cover-plates", Journal of Constructional Steel Research, 188:107051, 2022.

[2] DOD. Design of buildings to resist progressive collapse: UFC 4-023-03 [S]. Washington, D. C.: Department of Defense, 2009.

[3] Dinu F., Marginean I., Dubina D., "Experimental testing and numerical modelling of steel moment-frame connections under column loss", Engineering Structures, 151: 861–878, 2017.

[4] Zhong W.H., Tan Z., Meng B., et al. "Comparative evaluation of collapse behavior at different structural levels with different connections", Journal of Constructional Steel Research, 193: 107280, 2022.

[5] Yang B., Tan K.H., "Experimental tests of different types of bolted steel beam-column joints under a central-column-removal scenario", Engineering Structures, 54: 112–130, 2013.

[6] Tan Z., Zhong W.H., Meng B., et al., "Effect of various boundary constraints on the collapse behavior of multi-story composite frames ", Journal of Building Engineering, 52: 104412, 2022.

[7] Weng J., Lee C.K., Tan K.H., et al., "Damage assessment for reinforced concrete frames subject to progressive collapse", Engineering Structures, 149: 147–160, 2017.

[8] Tan Z., Zhong W.H., Tian L.M., et al., "Research on the collapse-resistant performance of composite beam–column substructures using multi-scale models", Structures, 27: 86–101, 2020.

[9] Zhong W.H., Tan Z., Song X.Y., et al., "Anti-collapse analysis of unequal span steel beam-column substructure considering the composite effect of floor slabs", Advance Steel Construction, 15(4): 377–385, 2019.

[10] Zhong W.H., Tan Z., Tian L.M., et al., “Collapse resistance of composite beam-column assemblies with unequal spans under an internal column-removal scenario”, Engineering Structures, 206: 110143, 2020.

[11] Tan Z., Zhong W.H., Tian L.M., et al., “Quantitative assessment of resistant contributions of two-bay beams with unequal spans”, Engineering Structures, 242: 112445, 2021.

[12] Zhang W.J., Li G.Q., Zhang J.Z., “Progressive collapse mechanism of steel frames-structures subjected to a middle-column loss”, Advanced Steel Construction, 17(2):199–209, 2021.

[13] Meng B., Hao J.P., Zhong W.H., “Numerical study on the anti-progressive collapse performance of steel frame-steel plate shear wall structures,” Journal of Building Engineering, 35: 102049, 2021.

[14] Meng B., Li L.D., Zhong W.H., et al., “Enhancing collapse-resistance of steel frame joints based on folded axillary plates”, Advanced Steel Construction, 17(1): 84–94, 2021.

[15] Gao S., Xu M., Guo L.H., et al., “Behavior of CFST-column to steel-beam joints in the scenario of column loss”, Advanced Steel Construction, 15(1): 47–54: 2019.

[16] Li G.Q., Zhang J.Z., Li L.L., et al., “Progressive collapse resistance of steel framed building under extreme events”, Advanced Steel Construction, 17(3): 318–330, 2021.

[17] Sasani M., Bazan M., Sagiroglu S., “Experimental and analytical progressive collapse evaluation of actual reinforced concrete structure”, ACI Structural Journal, 104(6): 731–739, 2007.

[18] Li G.Q., Zhang J.Z., Jiang J., “Multi-story composite framed-structures due to edge-column loss”, Advanced Steel Construction, 16(1): 20–29, 2020.

[19] Qian K., Lan X., Li Z., et al., “Progressive collapse resistance of two-storey seismic configured steel sub-frames using welded connections”, Journal of Constructional Steel Research, 170: 106117, 2020.

[20] Qian K., Lan X., Li Z., et al., “Behavior of steel moment frames using top-and-seat angle connections under various column-removal scenarios”, Journal of Structural Engineering, 147(10): 04021144, 2021.

[21] Tsitos A., Mosqueda G., Filiatrault A., et al., “Experimental investigation of progressive collapse of steel frames under multi-hazard extreme loading”, In The 14th World Conference on Earthquake Engineering, Beijing, China, 2008.

[22] Zhong W.H., Tan Z., Song X.Y., et al., “Collapse-resistant performance of a single-story frame assembly and multi-story sub-frame under an internal column-removal scenario”, Steel and Composite Structures, 41(5): 663-679, 2021.

[23] Tan Z., Zhong W.H., Tian L.M., et al., “Numerical study on collapse-resistant performance of multi-story composite frames under a column removal scenario”, Journal of building Engineering, 44: 102957, 2021.

[24] Yi W.J., He Q.F., Xiao Y., et al., “Experimental study on progressive collapse-resistant behavior of reinforced concrete frame structures”, ACI Structural Journal, 105(4): 433–439, 2008.

[25] Ahmadi E., Hosseini S.A., “Capacity evaluation of eight bolt extended endplate moment connections subjected to column removal scenario”, Advanced Steel Construction, 17(3): 273–282, 2021.

[26] Li H.H., Zhang B.Y. Cai X.H., “Assessment of design requirements against progressive collapse in UFC 4-023-03: numerical simulation”, Advanced Steel Construction, 14(4): 514–538, 2018.

[27] Tan Z., Zhong W.H., Duan S.C., et al., “Research on anti-collapse performance of composite beam-column substructures with different beam line stiffness”, Journal of Vibration and Shock, 40(10): 57–66, 2021.

[28] GB 50017-2017. Standard for design of steel structures, China Architecture & Building Press, Beijing, China, 2017.

[29] Tan Z., Zhong W.H., Meng B., et al., “Numerical evaluation on collapse-resistant performance of steel-braced concentric frames ”, Journal of Constructional Steel Research, 193: 107268, 2022.

[30] ANSI/AISC 358-10. Prequalified Connections for Special and Intermediate Steel Moment Frames for Seismic Applications, AISC; 2014.

[31] ABAQUS. Abaqus Analysis User’s Guide (6.14), ABAQUS Inc.; 2014.

[32] Yu H.L., Jeong D.Y., “Application of a stress triaxiality dependent fracture criterion in the finite element analysis of unnotched Charpy specimens”, Theoretical and Applied Fracture Mechanics, 54(1): 54–62, 2010.

[33] Izzuddin B.A., Vlassis A.G., Elghazouli A.Y., et al., “Progressive collapse of multi-storey buildings due to sudden column loss – Part I: Simplified assessment framework”, Engineering Structures, 30(5): 1308–1318, 2008.

Advanced Steel Construction – Vol. 18 No. 4 (2022) 783–792
DOI:10.18057/IJASC.2022.18.4.6

STUDY ON STATIC AND DYNAMIC EXPERIMENT OF SPATIAL CABLE-TRUSS STRUCTURE WITHOUT INNER RING CABLES BASED ON GRID-JUMPED LAYOUT OF STRUTS

Jian Lu, Su-Duo Xue *, Xiong-Yan Li and Qing Liu

College of Civil and Architecture Engineering, Beijing University of Technology, China
** (Corresponding author: E-mail: sdxue@bjut.edu.cn)*

ABSTRACT

Cable-truss tensile structures are one of the most imperative types of spatial structures, and a spatial cable-truss structure without inner ring cables (SCSWIRC) is a new type of cable-truss tensile structure. Although SCSWIRC has a strong anti-collapse capacity, its construction forming is difficult. Based on the concept of grid-jumped layout for struts, the experimental model with a span of 6 m is designed, and then three grid-jumped layout schemes are proposed to simplify structure system. The static and dynamic properties of experimental and finite element models are systematically studied. The results show that experimental values agree with simulation values. The errors of the static experiment are in the range of 6%~11.53% and the errors of the dynamic experiment are in the range of 5%~8%. The grid-jumped layout has negligible effects on the internal forces of cables. However, it has excellent effects on the internal forces of struts and nodal displacements at the grid-jumped layout, so the mechanical property of struts needs to be rechecked after grid-jumped layout. The mechanical property of the optimal grid-jumped layout scheme does not change compared with original scheme. The optimal grid-jumped layout scheme not only simplifies SCSWIRC, but also reduces the amount of steel. The study can promote the application of SCSWIRC in practical engineering.

ARTICLE HISTORY

Received:	22 February 2022
Revised:	19 May 2022
Accepted:	22 May 2022

KEYWORDS

Spatial cable-truss structure without inner ring cables;
Structural simplification;
Grid-jumped layout;
Static and dynamic property;
A technical paper

1. Introduction

With the development of economy and technology, more and more large-span stadiums are built in the world [1, 2]. Cable-strut tensile structure [3, 4], an essential part of large-span spatial structures, is well known in the construction industry for its light weight, beautiful appearance, fast construction speed, large-spanning ability. Meanwhile, cable-strut tensile structures include many different types of structure, and cable-truss tensile structure is one of the most competitive types in cable-strut tensile structures [5, 6]. Cable-truss tensile structures are generally composed of planar cable-truss frames according to certain layout principles, and one of its common points is that the whole structure can be divided into the same kind of planar cable-truss frames. Meanwhile, planar cable-truss frame shares common characteristics, such as light weight, high stiffness, large-spanning ability and rapid construction speed. At present, cable-truss tensile structures mainly include: spoke cable-truss structure [7, 8], spatial cable-truss structure without inner ring cables (SCSWIRC) [9, 10], and so on.

Spoke cable-truss structures have many advantages of tensile structures, so many practical projects are built in the world, like Foshan Stadium [11], Shenzhen Baoan Stadium [12], Yueqing Stadium [13], Busan Stadium in South Korea [14]. Meanwhile, there are many static and dynamic experimental studies and numerical studies on spoke cable-truss structures [11, 13]. It is found from the existing studies that although the spoke cable-truss structure has many advantages, its progressive collapse ability is weak. The inner ring cable is the crucial component of spoke cable-truss structures, and the rupture of inner ring cables will result in the whole structural failure. SCSWIRC is a new type of cable-truss tensile structure, which is proposed based on the problem of weak progressive collapse ability of spoke cable-truss structures [15, 16]. At present, SCSWIRC is still in the theoretical and experimental research stage, and there are no project cases in the world. Meanwhile, there are still many unfinished studies on SCSWIRC, including how to simplify structure system, how to solve self-stress mode, how to construct forming, and so on. It is found from further studies that although SCSWIRC has a solid progressive collapse capacity, its construction forming is too difficult. With the increase in the span of SCSWIRC, the number and length of struts will be enlarged, and serious collision and winding of struts occur during construction due to SCSWIRC formed by a series of planar cable-truss frames interwoven with each other, which cause many difficulties during construction. If there is a feasible way to reduce the number of struts, it will simplify its construction process, and structural self-weight will be reduced at the same time. Based on the problem of construction forming for SCSWIRC, a grid-jumped layout is proposed to remove the redundant struts, further simplify SCSWIRC and reduce structural self-weight. Grid-jumped layout refers to removing the struts of SCSWIRC but does not destroy the structural integrality. However, the influences of grid-jumped layout on the mechanical property of SCSWIRC are unknown for designers, so it is necessary to study the effects of grid-jumped layout on SCSWIRC through numerical analysis and experimental research.

In the paper, the experimental model with a span of 6 m is firstly built for SCSWIRC. Secondly, three grid-jumped layout schemes are proposed based on experimental model. Thirdly, the static and dynamic properties of three grid-jumped layout schemes and original scheme are compared and studied by theory and experiment. Grid-jumped layout method for large-span SCSWIRC is given. Finally, the main conclusions of the paper are given. Research contents provide a simplified method and promote the application of SCSWIRC in practical engineering.

2. Design and analysis of experimental and FEM model

2.1. Design of experimental and FEM model

In order to study the influence of grid-jumped layout on SCSWIRC, the experimental model with a span of 6 m is designed for SCSWIRC. The experimental model comprises 10 planar cable-truss frames wound and interwoven with each other. Namely, the equivalent ring fractions are 10. The outer shapes of upper and lower chord cables conform to the shape of parabola, and the equations of the parabola are shown in Eq. (1). It can be seen from Ref. [17] that the optimal rise-span ratios of upper and lower chord cables are 1/25~1/20 and 1/20~1/15, respectively. So, the rise-span ratios of upper and lower chord cables for the experimental model are selected as 1/24 and 1/16. Based on structural control parameters including Eq. (1), span, ring equivalent fractions and rise-span ratios, the coefficients of Eq. (1) are obtained, namely A1=-0.091778, B1=0.075665, A2=0.137668, B2=-0.113497. The procedure of solving nodal coordinates is compiled based on structural control parameters and Fortran Language. The finite element model (FEM) is built by the nodal coordinates, and then integral FEM is built considering ring beam and supported column, shown in Fig. 1a. The size and element number of single planar cable-truss frame are shown in Fig. 1b. The feasible pre-stress values are obtained by Ref. [18], which is shown in Table 1.

$$\begin{cases} y_1 = A_1 x_1^2 + B_1 \\ y_2 = A_2 x_2^2 + B_2 \end{cases} \tag{1}$$

Based on FEM, the integral experimental model is designed, including the main cable system structure, cable-strut joint, cable-beam joint, ring beam and supported column, shown in Fig. 2. The material properties of experimental model are obtained by material test, which is shown in Table 2. The natural material properties are used in FEM to make FEM and experimental model the same.

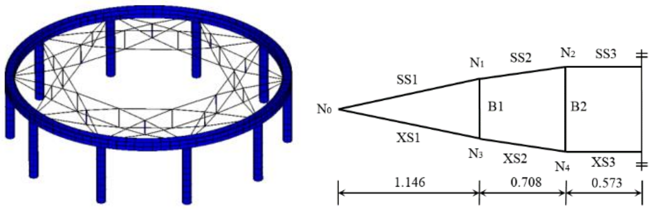

(a) Integral FEM of SCSWIRC (b) Size of planar cable-truss frame

Fig. 1 Integral FEM of SCSWIRC and the size of planar cable-truss frame

Table 1
Feasible pre-stress of FEM

Element number	Cable						Strut	
	SS1	SS2	SS3	XS1	XS2	XS3	B1	B2
Cable length/m	1.157	0.7104	1.146	1.163	0.7106	1.146	0.354	0.463
Non-stress cable length/m	1.153	0.7090	1.142	1.161	0.7094	1.144	-	-
Internal force/kN	3.618	3.573	3.558	2.730	2.712	2.704	-0.349	-0.352

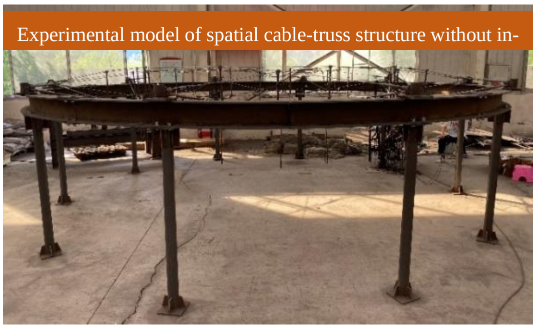

Fig. 2 Integral experimental model of spatial cable-truss structure without inner ring cables

Table 2
Material properties of cable and strut

Element Type	Size	Area/mm^2	Elastic modulus/MPa	Broken force/kN
Cable	Φ6	21.487	$1.21*10^5$	36.00
Strut	P20*3	141.300	$2.05*10^5$	52.02

2.2. Design of Grid-jumped layout schemes

The B1~B10 refers to the number of struts located at the outer ring of experimental model, which is shown in Fig. 3. As the struts located at the inner ring decides the structural outer shape, the rise-span ratio of upper and lower chord cables and drainage slope, the vector height of SCSWIRC is not changed. Namely, the struts located at the inner ring are not removed, so the planar layout diagram of SCSWIRC shown in Fig. 3. Meanwhile, as the span of experimental model is small, three grid-jumped layout schemes are proposed according to the different layout types of struts located at the outer ring. Namely, grid-jumped layout scheme 1 (or Scheme 1) refers to only removing a strut; grid-jumped layout scheme 2 (or Scheme 2) refers to removing struts after every other strut; grid-jumped layout scheme 3 (or Scheme 3) refers to remove all outer ring struts.
Scheme 1: remove B1
Scheme 2: remove B1, B3, B5, B7, B9
Scheme 3: remove B1~B10

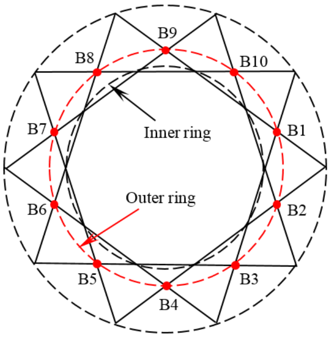

Fig. 3 Planar arrangement diagram of SCSWIRC

In order to easily remove struts located at the outer ring, the particular cable-strut joint is designed and it is shown in Fig. 4a, which is connected by bolts between cables and struts. The cable-strut joints of struts located at the inner ring are shown in Fig. 4b, which is connected by welding between cables and struts.

(a) Joint located at outer ring

(b) Joint located at inner ring

Fig. 4 Cable-strut joint

2.3. Comparative analysis of three grid-jumped layout schemes and original scheme

After construction forming, the feasible pre-stress is near the design pre-stress by repeatedly adjusting the threaded sleeves in two terminals of cables. Meanwhile, when the struts are removed for grid-jumped layout schemes, the lost cable forces are compensated by repeatedly adjusting the threaded sleeves in two terminals of cables.

The feasible pre-stresses of four schemes (original scheme and three grid-jumping layout schemes) in initial states are shown in Table 3 when structural self-weight is considered. The theory values of feasible pre-stresses of four schemes are solved by Ref. [18]. The internal force cloud diagrams of four schemes are shown in Fig. 5.

Table 3
Feasible pre-stresses of four schemes in initial states Unit: kN

Element number	Original scheme			Scheme 1			Scheme 2			Scheme 3		
	E-value	S-value	Error /%	E-value	S-value	Error /%	E-value	S-value	Error /%	E-value	S-value	Error /%
SS1	3.49	3.62	3.56	3.46	3.63	4.89	3.48	3.63	4.31	3.54	3.60	1.77
SS2	3.45	3.57	3.50	3.43	3.62	6.35	3.45	3.62	4.93	3.48	3.59	3.20
SS3	3.41	3.56	4.51	3.43	3.61	5.28	3.50	3.61	2.92	3.45	3.57	3.61
XS1	2.62	2.73	4.02	2.68	2.81	4.70	2.85	2.89	1.18	2.88	2.99	3.70
XS2	2.57	2.71	5.55	2.69	2.81	4.28	2.79	2.81	0.74	2.90	2.99	3.03
XS3	2.68	2.70	0.72	2.66	2.76	4.04	2.72	2.77	2.00	2.88	2.96	2.83
B1	-0.34	-0.35	2.94	-0.44	-0.46	4.50	-0.64	-0.67	4.70	—	—	—
B2	-0.34	-0.35	3.71	-0.46	-0.48	4.37	-0.62	-0.64	3.24	-0.80	-0.81	1.25

Note: E-value stands for experimental value; S-value stands for simulation value.

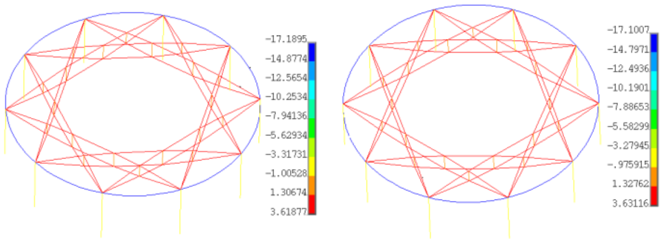

(a) Original scheme (b) Grid-jumped layout scheme 1

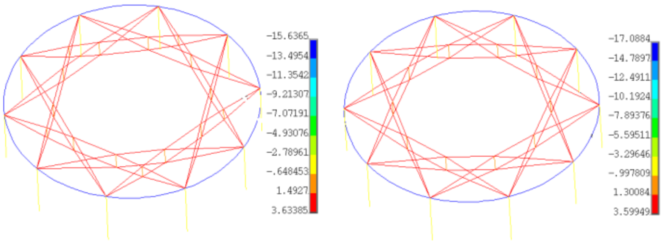

(c) Grid-jumped layout scheme 2 (d) Grid-jumped layout Scheme 3

Fig. 5 Internal force cloud diagram of four schemes

It can be seen from Table 3 that the errors between experimental values and theory values are within 6%, which is acceptable. It can be further concluded that the grid-jumped layout has a tremendous influence on the nodal displacement and the internal forces of struts, and the grid-jumped layout has negligible influence on the internal forces of cables. Meanwhile, the mechanical property of three grid-jumped layout schemes has not changed compared with original scheme.

The total weight and the number of struts of four schemes are statistically analyzed, and the results are shown in Table 4.

Table 4
Comparison results of the total weight and the number of struts of four schemes

Type	Original scheme	Scheme 1	Scheme 2	Scheme 3
Total weight/kg	25.55	25.15	23.58	21.62
The number of removing struts	0	1	5	10
The amount of saving steel/kg	—	0.39	1.57	1.96
Percent/%	—	1.54	6.24	8.33

It can be seen from Table 4 that the total weight of scheme 3 is the smallest among four schemes. Namely, scheme 3 most saves steel consumption. Meanwhile, scheme 3 has removed 10 struts, so it is the most concise structural type. Scheme 3 is the simplest structural model and it most save structural self-weight.

3. The experimental study of static property

3.1. Static experimental scheme

Based on the experimental model and SHELL154 element, the virtual membrane is built on the grids formed by the upper chord cables of cable-truss frames. The virtual membrane transfers the loads and does not participate in the calculation. Then the membrane loads are chosen as 0.6 kN/m2 according to Ref. [3]. The z-direction constraints are applied to all lower nodes of SCSWIRC, and the constraint reaction forces obtained by finite element analysis are the vertical equivalent nodal loads. The different types of equivalent nodal loads are obtained when the structural self-weight is considered. The equivalent nodal loads are F_{N_1}=-0.429 kN and F_{N_2}=-0.361 kN (the minus sign stands for the vertical direction). The total load is F=10*[F_{N_1}, F_{N_2}]. The N_1 and N_2 are shown in Fig. 1b.

Iron blocks are used to replace the equivalent loads to complete the hierarchical loads in static experiment. The loading process are divided into five steps, including 0.8F, 0.9F, 1.0F, 1.1F, 1.2F. The loading devices are made of PVC membrane, so the self-weight of loading devices is not considered because PVC is very light. The full-span loading and half-span loading experimental models are shown in Fig. 6.

(a) Full-span loading experimental model

(b) Half-span loading experimental model

Fig. 6 Full-span and half-span loading experimental model

As the experimental model comprises 10 planar cable-truss frames, two of 10 planar cable-truss frames are chosen as the monitored objective. The chosen planar cable-truss frames are symmetrically distributed. The monitoring points of internal forces and nodal displacements are shown in Fig. 7a. The strain gauges monitor the change of the internal forces of cables and struts attached to the pre-designed threaded sleeves shown in Fig. 7a. The strain gauges are connected to the static collection instrument JM3813 through collection lines, as shown in Fig. 7b. Static collection instrument JM3813 collects the signals and transmits signals to a computer. Then the signals are converted into strain by computer, and the internal forces of cables and struts can be obtained by further calculations. Level gauge and steel ruler are used to monitor nodal displacements of cable-truss frame at critical positions, shown in Fig. 7c.

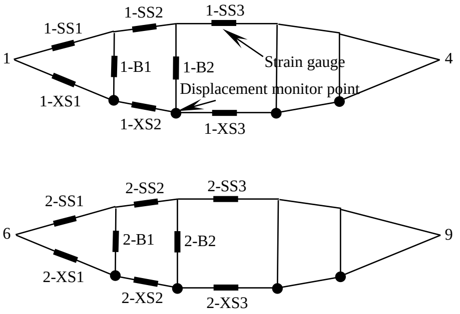

(a) The monitoring points of internal forces and displacements

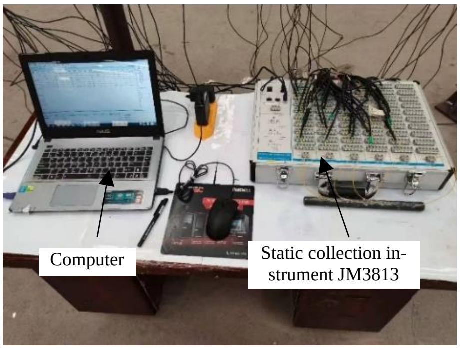

(b) Static collection instrument

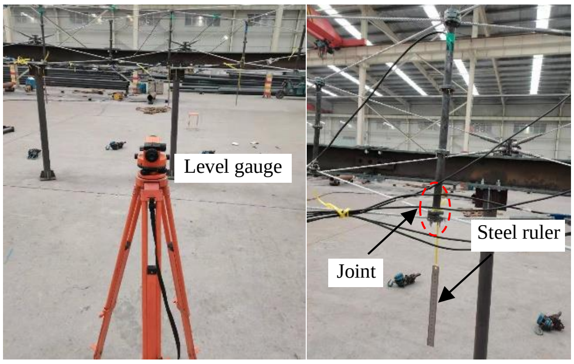

(c) Level gauge and steel ruler

Fig. 7 Static collection instrument JM3813, level gauge and steel ruler

3.2. The static property under the actions of full-span loads

The experimental model is loaded with full-span loads shown in Fig. 6a, and the internal forces and nodal displacements are monitored according to the measuring points in Fig. 7a. The half planar cable-truss frame is taken as a research objective due to the symmetry of structure and loads. The change laws of internal forces and nodal displacements of experimental model and FEM are shown in Fig. 8~Fig. 9 under the actions of full-span loads. The internal forces and nodal displacements of experimental model and FEM are shown in Fig. 10~ Fig. 11 under the actions of full-span load 1.0F.

It can be seen from Fig. 8~ Fig. 11 that experimental values agree with simulation values, and the errors are within 10%. Meanwhile, the change laws of experimental values and simulation values are similar. Namely, under full-span loads, the internal forces of upper chord cables and struts gradually decrease with external loads. The internal forces of lower chord cables gradually increase with external loads. So, upper chord cables can loosen when external loads are enormous. It can be known from the comparison results of four schemes that the order of internal forces of all components is scheme 3＞scheme 2＞scheme 1＞original scheme. Under the action of full-span load 1.0F, the internal forces of upper chord cables have been increased from 2.49 kN in

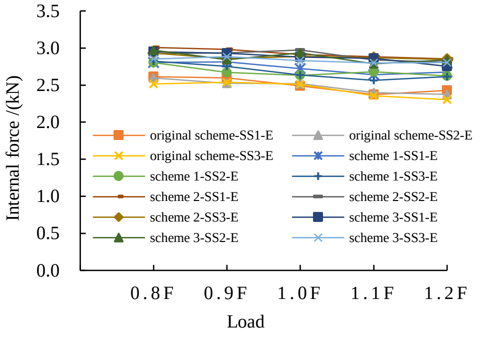

(a) Upper chord cables

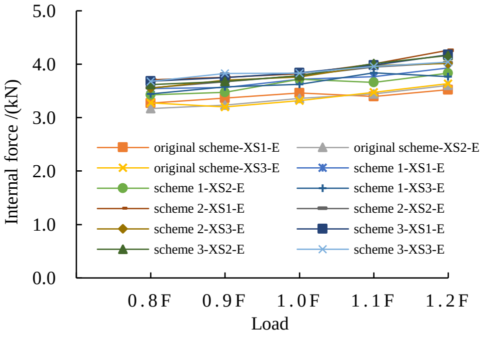

(b) Lower chord cables

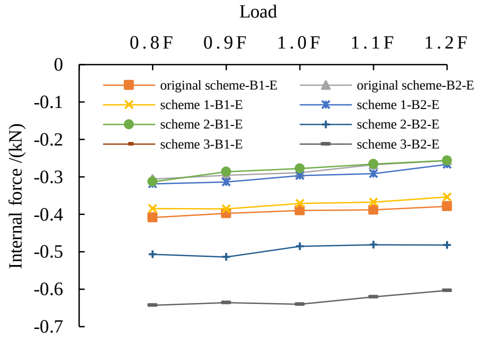

(c) Struts

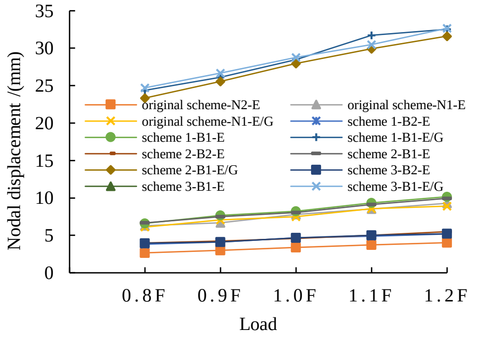

(d) Nodal displacements

Fig. 8 Internal forces and nodal displacements under the actions of full-span loads for experimental model

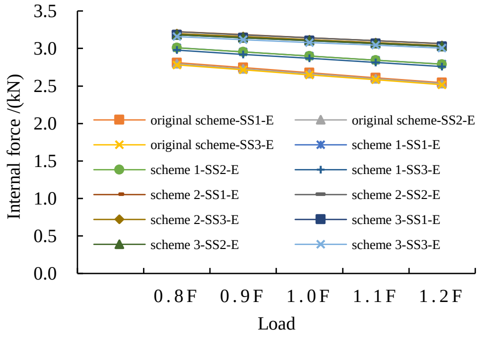

(a) Upper chord cables

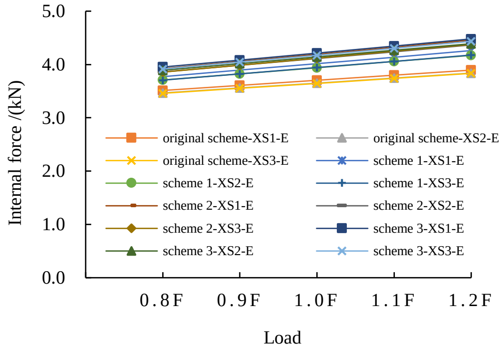

(b) Lower chord cables

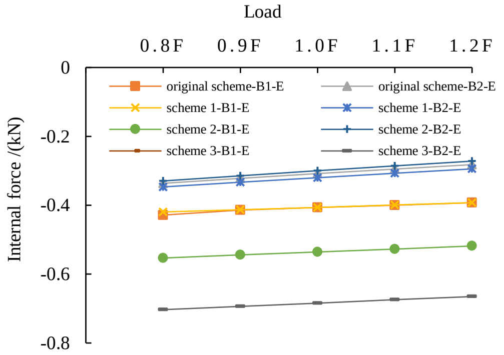

(c) Struts

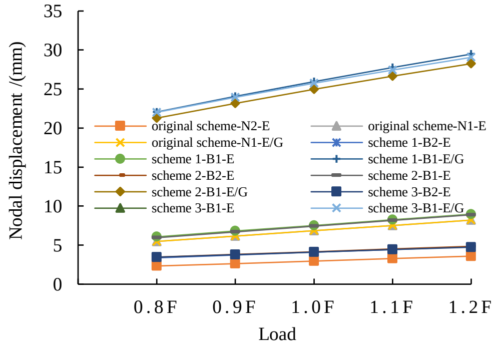

(d) Nodal displacements

Fig. 9 Internal forces and nodal displacements under the actions of full-span loads for FEM

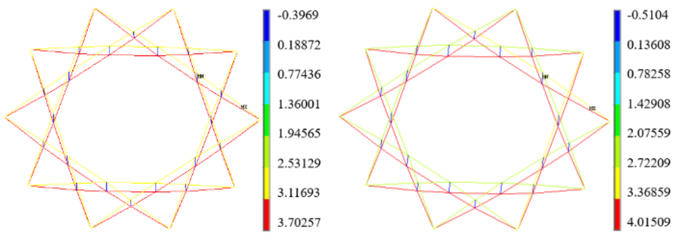

(a) Original scheme (b) Scheme 1

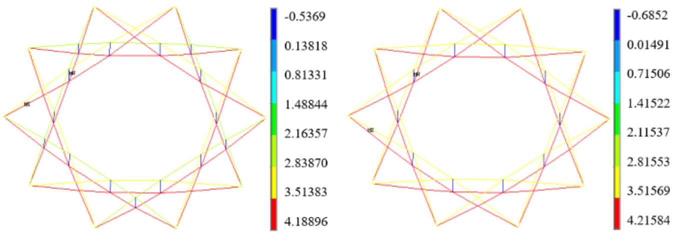

(c) Scheme 2 (d) Scheme 3

Fig. 10 Internal forces of four schemes under the actions of full-span load 1.0F Unit: kN

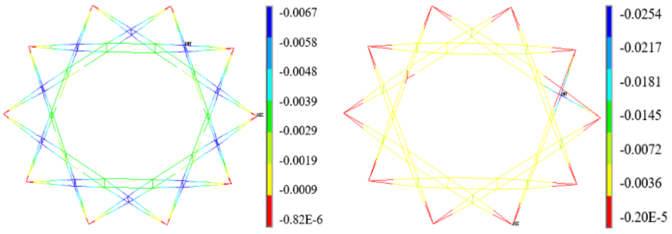

(a) Original scheme (b) Scheme 1

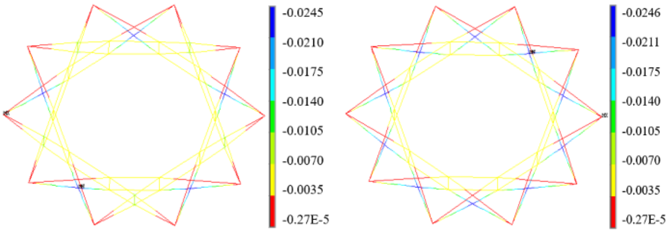

(c) Scheme 2 (d) Scheme 3

Fig. 11 Nodal displacements of four schemes under the actions of full-span load 1.0F
Unit: m

original scheme to 3.11 kN in scheme 3, and it increases by 24.91%; The internal forces of lower chord cables have been increased from 3.46 kN in original scheme to 3.84 kN in scheme 3, and it increases of 10.98%; The internal forces of struts have been increased from -0.39 kN in original scheme to -0.65 kN in scheme 3, and it increases of 66.67%. It can be known that the changes of internal forces of cables are relatively small, and the changes of internal forces of struts are significant after grid-jumped layout.

The order of all nodal displacements is similar to that of internal forces of all components. The maximum nodal displacement of four schemes meets tolerable displacement [δ]=30 mm in Technical Specification of Cable Structures [19], and the nodal displacements of schemes 1~3 are the same. It can be seen from Fig. 8d and Fig. 9d that the nodal displacements at inner ring are smaller than those of the nodal displacements at the outer ring. Meanwhile, the nodal displacements at grid-jumped layout are significantly larger than the nodal displacements at non-grid-jumped layout, which shows grid-jumped layout weakens the local stiffness of SCSWIRC. So, the nodes at grid-jumped layout are more sensitive to external loads, and the designer should pay more attention to internal forces and nodal displacements at grid-jumped layout not to excess the requirements of Code.

3.3. The static property under the actions of half-span loads

The change laws of internal forces and nodal displacements for experimental model and FEM are shown in Fig. 12~Fig. 13 under the actions of half-span loads. The internal forces and nodal displacements of four schemes are shown in Fig. 14~ Fig. 15 under the actions of half-span load 1.0F.

It can be known from Fig. 12~Fig. 15 that experimental values agree with simulation values and experimental values are slightly larger than simulation values. With the increase of the half-span loads, the internal forces of upper chord cables and struts gradually decrease, and the internal forces of lower chord cables gradually increase in the loading part. However, the internal forces of components have no noticeable change in the non-loading part. The change laws of nodal displacements agree with those of internal forces. The maximum internal forces and nodal displacements are scheme 3＞scheme 2＞scheme 1＞original scheme. For the loading part, the internal forces of upper chord cables have been increased from 2.38 kN in original scheme to 3.02 kN in scheme 3, and it increases by 26.89%; The internal forces of lower chord cables have been increased from 3.58 kN in original scheme to 3.92 kN in scheme 3, and it increases of 9.5%; The pressure forces of struts have been increased from 0.35 kN in original scheme to 0.46 kN in scheme 3, and it increases of 82.86%. For the non-loading part, the internal forces of upper chord cables have been increased from 3.23 kN in original scheme to 3.3 kN in scheme 3, and it increases by 1.54%; The internal forces of lower chord cables have been increased from 2.52 kN in original scheme to 2.94 kN in scheme 3 it increases of 16.67%; The pressure forces of struts have been increased from 0.42 kN in original scheme to 0.76 kN in scheme 3. From the comparison results of mechanical property in the non-loading and loading parts, it can be concluded that with the increase of the number of removed struts, the internal forces of struts significantly change and the internal forces of cables change slightly. So, the bearing capacity and stability of struts should be rechecked after grid-jumped layout.

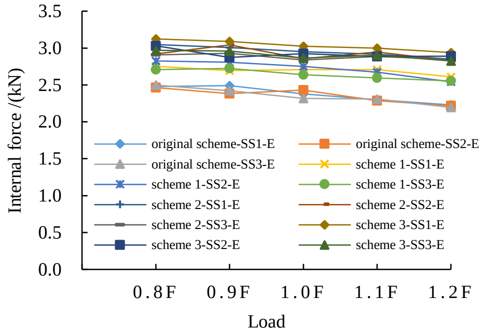

(a) Upper chord cables

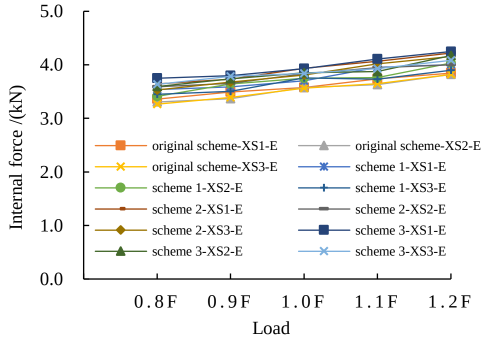

(b) Lower chord cables

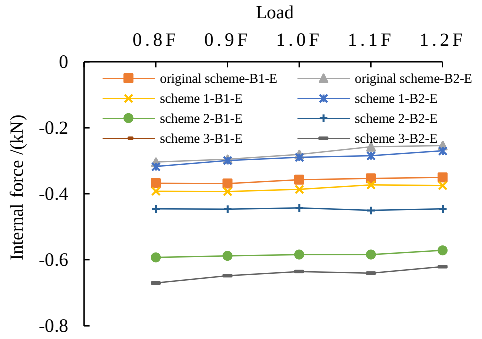

(c) Struts

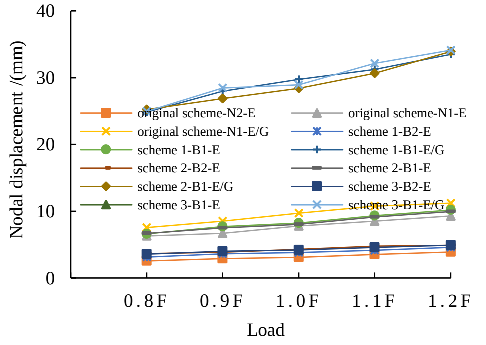

(d) Nodal displacements with half-span load

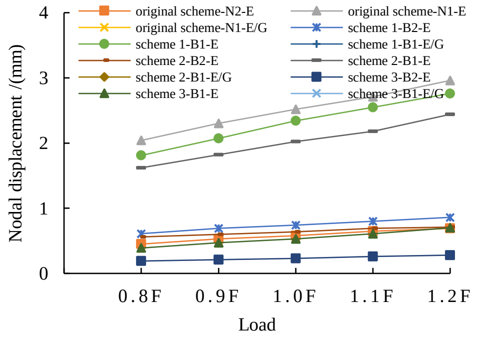

(e) Nodal displacements without half-span load

Fig. 12 Internal forces and nodal displacements under the actions of half-span loads for experimental model

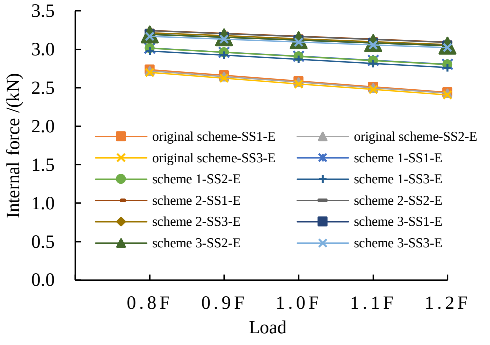

(a) Upper chord cables

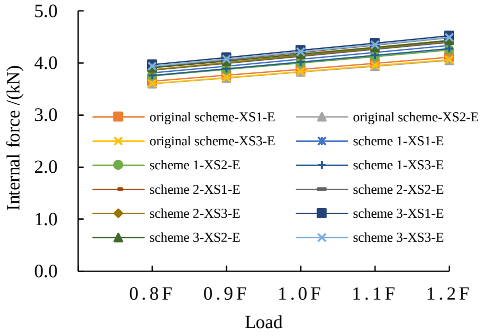

(b) Lower chord cables

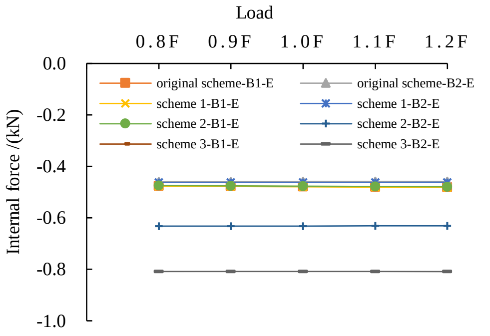

(c) Struts

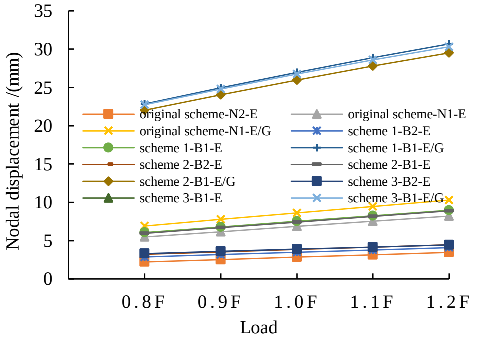

(d) Nodal displacements with half-span load

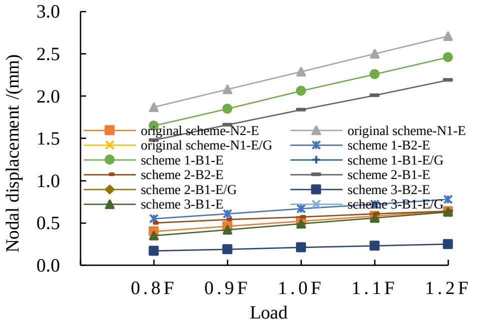

(e) Nodal displacements without half-span load

Fig. 13 Internal forces and nodal displacements under the actions of half-span loads for FEM

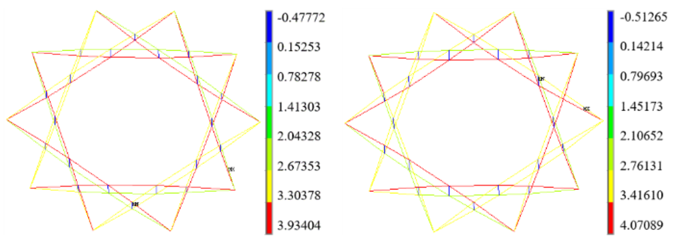

(a) Original scheme (b) Scheme 1

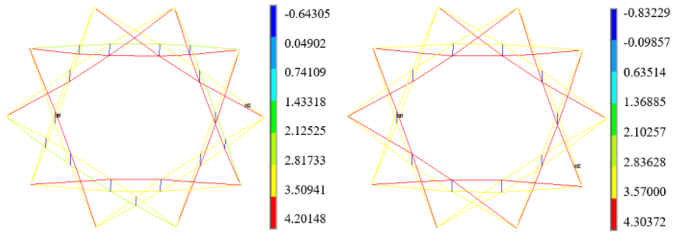

(c) Scheme 2 (d) Scheme 3

Fig. 14 Internal forces of four schemes under the actions of half-span load 1.0F Unit: kN

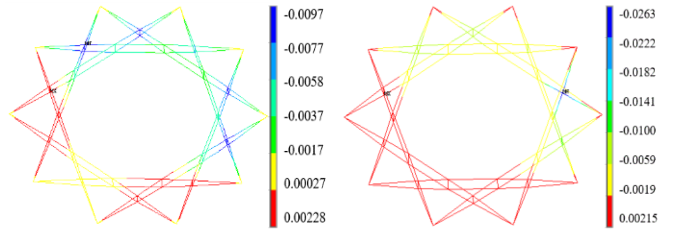

(a) Original scheme (b) Scheme 1

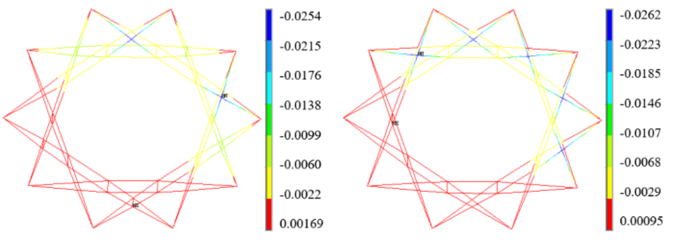

(c) Scheme 2 (d) Scheme 3

Fig. 15 Nodal displacements of four schemes under the actions of half-span load 1.0F Unit: m

3.4. discussions

From the analysis results under the actions of full-span loads and half-span loads, it can be concluded that the optimal grid-jumped layout scheme is scheme 3. Scheme 3 reduces structural self-weight and simplifies structural system. Namely, scheme 3 saves project costs and decreases the difficulty of construction forming.

Form Fig. 8 ~Fig. 9, the errors of internal forces are in the range of 6%~8.91% and the errors of nodal displacements are in the range of 8%~10.27% under the actions of full-span loads. Form Fig. 12 ~Fig. 13, the errors of internal forces are in the range of 8%~10.13% and the errors of nodal displacements are in the range of 9%~11.53% under the actions of half-span loads. From the errors between experimental values and simulation values, the reasons of producing errors mainly include that (1) Measuring devices make errors; (2) Strain gauges make errors; (3) The stiffness of two ends of cables make errors; (4) The manufacturing accuracy of lengths of cables and struts makes errors.

4. The experimental study of dynamic property

4.1. The purpose, theory and scheme of dynamic experiment

4.1.1. The purpose of dynamic experiment

Dynamic experiments can further know the effects of grid-jumped layout on the dynamic property of SCSWIRC. At the same time, the natural frequency, damping ratio and vibration mode of SCSWIRC can be obtained by dynamic experiments. Natural frequency, damping ratio and vibration mode are the most critical three parameters that reflect the capacity of bearing dynamic loads and evaluate the structural dynamic property. The three parameters are also the basis of wind spectrum analysis and seismic response spectrum analysis. So, it is necessary to further study the effects of grid-jumped layout on the dynamic property of SCSWIRC.

4.1.2. The theory of dynamic experiment

SCSWIRC is a kind of tensile structure, which is a very flexible structure, so the grid-jumped layout of struts will reduce structural stiffness in the experiment. As the structural self-weight is light, the hammer is used to apply inspiration to acceleration sensors in experimental model. The dynamic collection instrument JM3841 is sued to collect the signals of acceleration sensor arranged at some nodes. Then put the obtained signals into the dynamic collection instrument JM3841, and the corresponding acceleration time history curves can be obtained by JM3841 Software. The corresponding frequency spectrum curves can be obtained based on the obtained signals through frequency spectrum analysis. The maximum values of frequency spectrum curves are the natural frequencies of structures. The structural damping ratio can be calculated according to the vibration attenuation curve of measuring points based on the viscous damping theory.

The calculation equation of damping ratio is as follows:

$$\ln\frac{y_n}{y_{n+1}} = \xi\omega\frac{2\pi}{\omega'} \tag{2}$$

In Eq. (2), y_n and y_{n+1} illustrate the amplitude significance of one week apart; ξ is the damping ratio; ω and ω' stand for the undamped and damped vibration frequency, respectively.

It is assumed that δ is the logarithmic attenuation rate of vibration amplitude, and δ is as follows:

$$\delta = \ln\frac{y_n}{y_{n+1}} \tag{3}$$

So, Eq. (2) can be written as Eq. (4):

$$\zeta = \frac{\delta}{2\pi}\frac{1}{\sqrt{1+(\delta/2\pi)^2}} \tag{4}$$

When $\xi < 0.2$, the Eq. (4) can be written as Eq. (5):

$$\zeta = \frac{\delta}{2\pi} \tag{5}$$

In order to reduce the effects of external excitation on the dynamic experiment, each excitation point is subjected to 10 times excitation, and the average values of 3 times experimental results are used as the final experimental values.

4.1.3. Experimental scheme

The dynamic collection instrument JM3841 is used in the experiment, shown in Fig. 16a. The IEPE acceleration sensors are used in the dynamic experiment, shown in Fig. 16b. The acceleration sensor has the advantages of lightness, little volume, a wide frequency response range and high stability, which is suitable for the dynamic experiment. The layout diagram of acceleration sensors is shown in Fig. 16c. The acceleration time-history curve of measuring point A-2 is shown in Fig. 16d. In the experiment, the external excitation is produced by hammering and hammering the excitation points every 30 s for 5 min at the same time, and then two sets of data are collected.

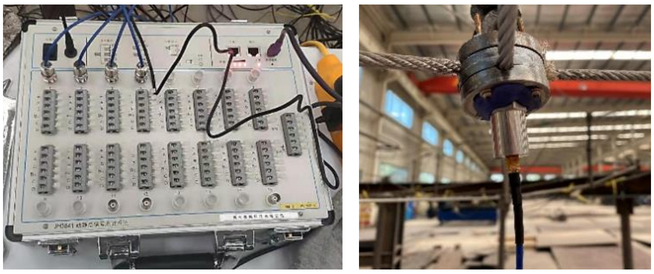

(a) Dynamic collection instrument JM3841 (b) Acceleration sensor

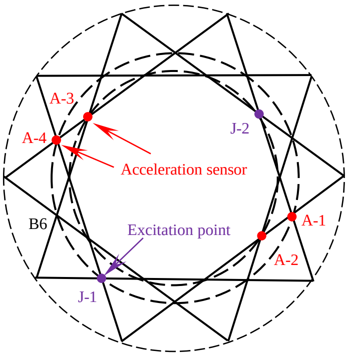

(c) Layout diagram of acceleration sensors

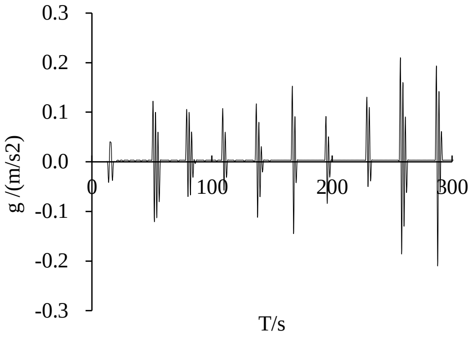

(d) Time-history curve of acceleration sensor

Fig. 16 Correlation diagrams of experimental model

As the torsional rigidity of experimental model is relatively large, the first few modes are all vertical. Meanwhile, there is the deformation coupling phenomenon in each mode of experimental model. Regarding structural symmetry, adjacent frequencies may have slight differences and it is difficult to identify all frequencies. Meanwhile, there are some errors between the site environment and dynamic collection instrument in the process of collecting signals, so the partial frequencies are obtained in the dynamic experiment.

4.2. The dynamic property under the actions of non-loads

The natural frequencies and damping ratio of four schemes under the actions of no external loads are shown in Table 5 and Table 6.

Table 5
Natural frequencies of four schemes in initial state

Order of frequency	Original scheme /HZ		Scheme 1 /HZ		Scheme 2 /HZ		Scheme 3 /HZ	
	Trial Value	Theory Value	Trial Value	Theory Value	Trial Value	Theory Value	Trial Value	Theory Value
1	6.409	6.742	4.571	5.065	6.531	6.768	4.700	5.053
3	6.922	7.296	—	6.945	—	7.023	—	5.064
5	—	8.573	7.089	7.790	7.584	7.214	—	5.097
7	8.734	9.087	—	8.806	8.553	8.703	—	5.159

Table 6
Damping ratio of experimental model in initial state

Order of frequency	Original scheme	Scheme 1	Scheme 2	Scheme 3
1	0.0099	0.0090	0.0153	0.0198
3	0.0174	—	—	—
5	—	0.0159	0.0065	—
7	0.0190	—	0.0075	—

From Table 5, the experimental values of natural frequency agree with the simulation values. The maximum error is 7.6%, and most errors are within 6%~7%, which shows that simulation values agree with experimental values. As the experimental model is symmetric, there are many similar frequencies, so the partial frequencies are identified in the experimental model. It can be seen from Table 6 that the damping ratios of structure are little in initial state, which is within 0.02.

4.3. The dynamic property under the actions of full-span loads

Generally speaking, the structural natural frequency is an inherent feature not correlated with external loads. However, external loads can be equivalent to extra mass in dynamic analysis so that external loads will affect the natural feature of structure.

In order to study the natural vibration of different grid-jumped layout schemes with the change of extra mass (or external loads), the natural frequency and damping ratio of experimental model are studied under the actions of full-span loads and half-span loads. The external loads are replaced with iron blocks shown in Fig. 6, which is applied on the lower nodes of experimental model. The extra mass is divided into five steps, similar to Section 3. The experimental and simulation values of natural frequency for four schemes are shown in Fig. 17 under the actions of full-span loads. As the 1st, 3rd, 5th, 7th order frequencies are equal to the 2nd, 4th, 6th, 8th order frequencies, the 1st, 3rd, 5th, 7th order frequencies are given in Fig. 17. The vibration modes of four schemes under the actions of full-span load 1.0F are shown in Fig. 18.

It can be seen from Fig. 17 and Fig. 18 that the experimental values and simulation values of natural frequencies are similar under the actions of full-span loads. The errors between experimental values and simulation values of natural frequencies are within 11.75%, and the errors mainly focus on the range of 6%~8%. The order of natural frequencies of four schemes is original scheme ＞scheme 1＞scheme 2＞scheme 3, and the natural frequencies of four schemes are near at the same time. The natural frequencies of four schemes gradually increase with the increase of external loads. The main reason is that the structural mass becomes more extensive, and the natural frequencies of four schemes become small when the external loads are converted into structural mass. The grid-jumped layout has changed structural high order frequencies.

Meanwhile, grid-jumped layout has changed the local stiffness of structure and further changed its vibration modes. However, the first vibration mode of four schemes is the upper and lower vibration accompanied by the local torsion of planar cable-truss frames. It can be known from Ref. [13] that there is no harm to the structure when the first vibration mode is the local torsion of planar cable-truss frames. So, the dynamic property of the four schemes is rather good.

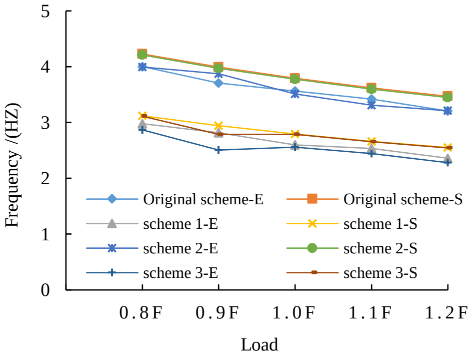

(a) First order frequency

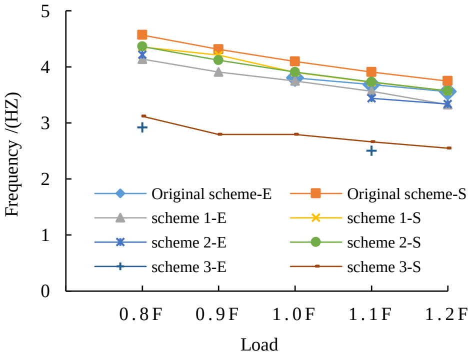

(b) Third order frequency

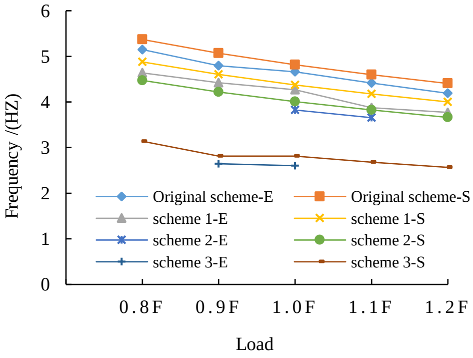

(c) Fifth order frequency

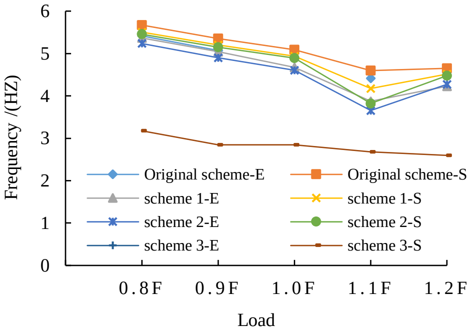

(d) Seventh order frequency

Fig. 17 The comparison results of natural frequencies of four schemes under the actions of full-span loads

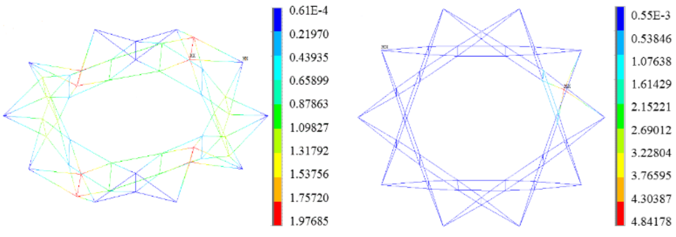

(a) Original scheme (b) Scheme 1

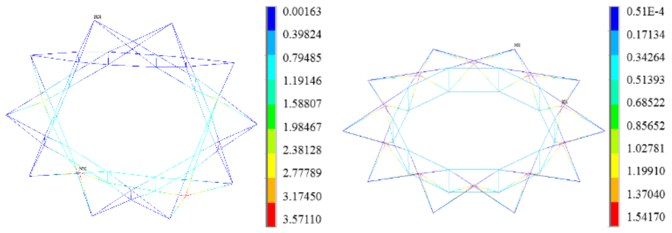

(c) Scheme 2 (d) Scheme 3

Fig. 18 First vibration modes of four schemes under the actions of full-span load 1.0F

4.4. The dynamic property under the actions of half-span loads

The experimental and simulation values of natural frequency for four schemes under the actions of half-span loads are shown in Fig. 19. The first vibration modes of four schemes under the actions of half-span load 1.0F are shown in Fig. 20. The experimental values of damping ratios of four schemes under the actions of full-span and half-span loads are shown in Table 7.

It can be seen from Fig. 19 and Fig. 20 that the most error between experimental values and simulation values of natural frequencies is 10.06% for four schemes, and the errors mainly focus on the range of 5%~7%. Experimental values agree with simulation values, which verify the experiment is correct, and experimental results can reflect on the fundamental property of structure. The grid-jumped layout changes the structural high order frequency.

Meanwhile, grid-jumped layout also changes the local stiffness of structure and further changes the structural vibration modes. However, the first vibration

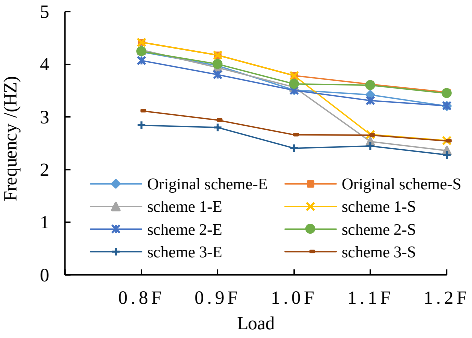

(a) First order frequency

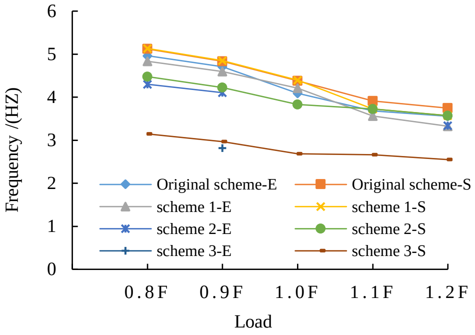

(b) Third order frequency

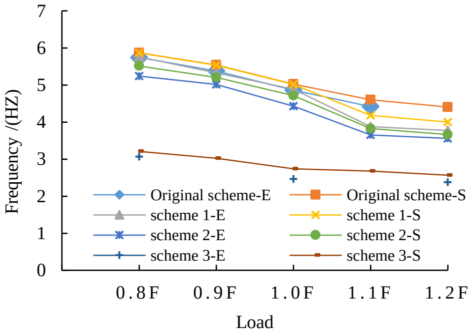

(c) Fifth order frequency

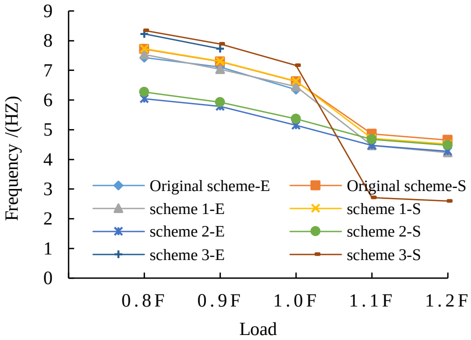

(d) Seventh order frequency

Fig. 19 The comparison results of natural frequencies of four schemes under the actions of half-span loads

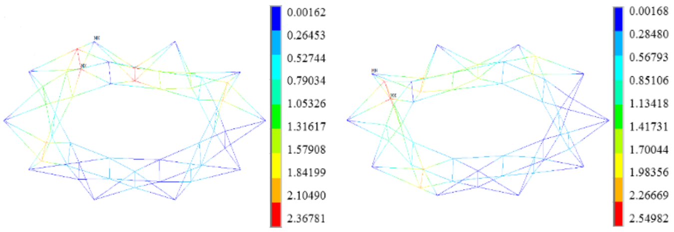

(a) Original scheme (b) Scheme 1

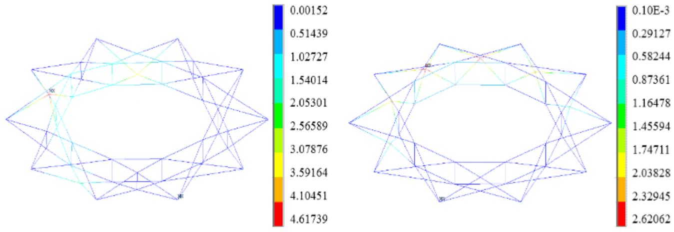

(c) Scheme 2 (d) Scheme 3

Fig. 20 First vibration modes of four schemes under the actions of half-span load 1.0F

mode of four schemes is upper and lower vibration accompanied by the local torsion of planar cable-truss frames. It can be known from Ref. [13] that there is no harm to structure when the first vibration mode is the local torsion of planar cable-truss frames. So, the dynamic property of the four schemes is rather good.

4.5. Damping ratio of experimental model

From the measured data of damping ratio, the damping ratios corresponding to all different natural frequencies are in the range of 0.005~0.02. The damping ratios of four schemes do not change with the order of frequency. Generally speaking, the external loads affect structural damping ratios. However, it is not found that the damping ratios of four schemes changes with the change of external loads during the experiment. The experimental values of damping ratios of four schemes are shown in Table 7 under the actions of full-span loads and half-span loads.

5. Further discussions

Although the span of experimental model is 6 m, the relative conclusions can explain the actions and effects of grid-jumped layout on SCSWIRC. In order to further explain the actions and meanings of grid-jumped layout, the SCSWIRC with the span of 100 m is given, shown in Fig. 21a.

The struts at virtual inner ring are not removed because the struts at virtual inner ring decide drainage slope, outer shape and the rise-span ratio of upper and lower chord cables. According to the SCSWIRC in Fig. 21a and the positions of grid-jumped layout, the three grid-jumped layout schemes can be proposed. The three grid-jumped layout schemes include grid-jumped layout scheme 1 (scheme 1), grid-jumped layout scheme 2 (scheme 2), and grid-jumped layout 3 (scheme 3). In Fig. 21b, scheme 1 refers to removing the struts at inner ring 1; scheme 2 refers to removing the struts at inner ring 2; scheme 3 refers to removing the struts at inner ring 3.

The optimal grid-jumped layout schemes can be obtained by using the same analysis method as experimental model in Section 2. The optimal grid-jumped layout scheme is scheme 1. The optimal scheme 1 simplifies structural system and reduces forming construction difficulty and structural self-weight, and saves costs.

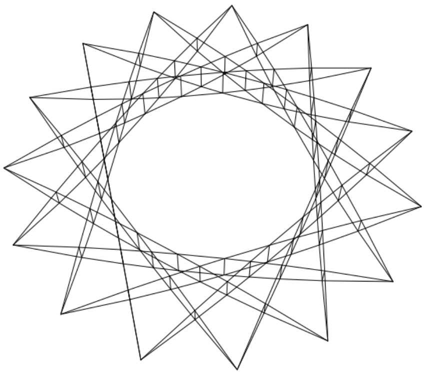

(a) SCSWIRC with a span of 100 m

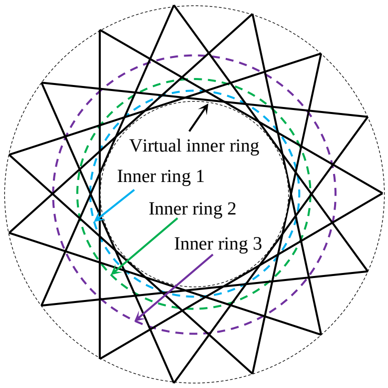

(b) Planar diagram of grid-jumped layout

Fig. 21 Perspective diagram and planar diagram of grid-jumped layout of SCSWIRC

When the span of SCSWIRC does not exceed 400 m, the strut can be the form of a circular steel pipe. When the span of SCSWIRC is larger than 400 m, the length of struts will be too long. In order to reduce the crossed-sectional areas of struts and enhance the stiffness and stability of struts, the form of struts can be the form of an open-web fusiform truss shown in Fig. 22a. The open-web fusiform truss can be divided into different lattice column forms, shown in Fig. 22b. The different lattice columns can be connected by bolt and weld.

Table 7
Experimental values of damping ratios of four schemes under the actions of full-span and half-span loads

Order of frequency	Damping ratios under the actions of full-span loads				Damping ratios under the actions of half-span loads			
	Original scheme	Scheme 1	Scheme 2	Scheme 3	Original scheme	Scheme 1	Scheme 2	Scheme 3
1st	0.01917	0.01646	0.0134	0.00621	0.01831	0.01789	0.00797	0.01843
3rd	0.01764	0.01256	—	—	0.01261	0.00512	—	—
5th	0.01404	0.01355	0.00982	0.0087	0.01303	0.01846	0.01935	0.01278
7th	—	0.01732	0.01732	—	0.01109	0.00953	0.01653	—

The design recommendations for SCSWIRC based on the above discussions include: (1) Cable-strut joints are essential for the mechanical property of structure, so cable-strut joints can make the cable forces of all kinds of cables pass smoothly. (2) The grid-jumped layout can simplify structure when original scheme is already decided, which can reduce self-weight and save project costs. (3) The structural rise should meet drainage slope and optimal rise, which is beneficial for the structural mechanical property. (4) The suitable construction method and construction steps should be considered in the design. (5) The influences of wind load on SCSWIRC should be further considered because it belongs to flexible tensile structures.

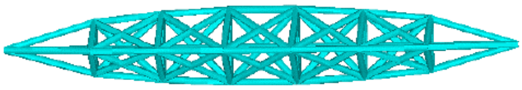

(a) Open-web fusiform truss

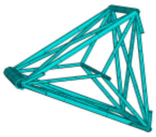

(b) Lattice column

Fig. 22 Relative diagram of open-web fusiform truss

6. Conclusions

Based on the above studies and discussions, some conclusions can be given as follows:

(1) The three grid-jumped layout schemes are proposed according to the experimental model. The results of static experiment show that the change laws of mechanical property for SCSWIRC are similar. The experimental values are agree with simulation values. The errors mainly focus on the range of 6%~10.27% under the actions of full-span loads, and the errors mainly focus on the range of 8%~11.53% under the actions of half-span loads.

(2) The grid-jumped layout has minor effects on the internal forces of cables. It dramatically affects the nodal displacements and the internal forces of struts at the grid-jumped layout, so the strength and stability of struts should be rechecked after grid-jumped layout.

(3) The results of dynamic experiment show that the errors of natural frequencies primarily focus on the range of 6%~8% and 5%~7% under the actions of full-span and half-span loads, respectively. The grid-jumped layout has changed structural local stiffness and vibration modes, but the first vibration mode of four schemes is upper and lower vibration accompanied by the local torsion of planar cable-truss frames, which is not harmful to SCSWIRC.

(4) The results of static and dynamic experiments show that the grid-jumped layout has not changed the basic mechanical property of SCSWIRC and the optimal grid-jumped layout scheme is scheme 3. The optimal scheme 3 removes the redundant struts, simplifies structural system, reduces structural self-weight, and saves project costs.

Acknowledgements

The authors would like to acknowledge the financial support of the National Natural Science Foundation of China (51778017). Acknowledge graduated students Renqi Ji and Runsheng Zhao for their efforts in experiment. Thank Majid Dezhkam for helping me revising grammar errors in language.

References

[1] Guo Y L. Tian G Y. Cable structure system, design theory and construction control. Beijing: Science Press, 2014.

[2] Guo Y L, Zhang X Q. Influence of temperature changes and cable length errors on tension structures using un-adjustable cable length design. China Civil Engineering Journal, 2017, 50(6): 11-22.

[3] Guo J M, Jiang J Q. An algorithm for calculating the feasible pre-stress of cable-struts structure. Engineering Structure, 2016, 118(1), 228-39.

[4] Chen L M, Hu D, Gao W F, Dong S L, Zhou Y Y, Zhang F B. (2018). Support node construction error analysis of a cable-strut tensile structure based on the reliability. Advances in Structural Engineering, 2008, 21(10), 1553-1516.

[5] Zhang A L, Sun C, Jiang Z Q. Experimental study on the construction shape-forming process and static behavior of a double strut cable dome. Journal of Zhejiang University-Science (Applied Physics and Engineering), 2018, 19(03), 225-239

[6] Ge J Q, Zhang A L, Liu X G, Zhang G J, Ye X B, Wang S, Liu X C. Analysis of tension form-finding and whole loading process simulation of cable dome structure. Journal of building structures, 2012, 33(04):1-11.

[7] Deng H, Zhang M R, Liu H C, Dong S L, Zhang Z H, Chen L Q. Numerical analysis of the pretension deviations of novel Crescent-shaped tensile canopy structural system, Engineering Structures, 2016, 119, 24-33.

[8] Zhang W J, Hu S L, Zhang Y G. A review on progressive collapse of large-span space structure. The 9th National Modern Structure Engineering, Jinan, 2009: 334-338.

[9] Lu J, Li X Y, Xue S D, Liu R J, Majid D. Study on force Mechanism of Cable-truss Frame and jumped layout of Annular Crossed Cable-truss Structure, Advanced Steel Construction, 2021, 17(03), 243~252.

[10] Lu J, Xue S D, Li X Y, Liu R J. Study on membrane roof schemes of annular crossed cable-truss structure. International Journal of Space Structures, 2019, 34(3-4):85-96.

[11] Huang H, Xian Y Q, Xi K L, Liu B Q. Experimental study and numerical analysis on the progressive collapse resistance of SCMS. International Journal of Steel Structures, 2019, 19(01): 301-318.

[12] Zhao R, Wei D M, Sun W B, Xu M. Form-finding method of cable-membrane structures considering cable force-finding form appropriate moment. International Symposium on Innovation and Sustainability of Structures in Civil Engineering, Guangzhou, PEOPLES R CHINA, 2009: 814-818.

[13] Guo Y L, Wang K, Tian G Y, Zhang B H. Research and design of structural form of spoke structure. Journal of Building Structures, 2013, 34(5): 11−19.

[14] Jeon B, Lee J. Cable membrane roof structure with oval opening of stadium for 2002 FIFA world Cup in Busan. In: Proceedings of sixth Asian-Pacific conference on shell and spatial structures, 2000, 2, 1037-42.

[15] Liu R J, Xue S D, Li X Y. Preventing disproportionate displacements in an annular crossed cable-truss structure, International Journal of Space Structures, 2017, 32(1), 3-10.

[16] Liu R J, Li X Y, Xue S D. Experimental and numerical research on Annular Crossed Cable Truss Structure under cable rupture, Earthquake Engineering and Engineering Vibration, 2017, 16(3), 557-569.

[17] Shen S D, Xu C B, Zhao C, W Y. Suspension structure design. Beijing: China Architecture & Building Press, 2006.

[18] Xue S D, Lu Jian, Li X Y, Liu R J. Improved force iteration method based on rational shape design solving self-stress modes of cable-truss tensile structure, Advanced Steel Construction. 2020, 16(2), 170-180.

[19] Technical Specification for Cable Structure, JGJ257-2012. Beijing: China Architecture & Building Press, 2008.

Advanced Steel Construction – Vol. 18 No. 4 (2022) 793–803
DOI:10.18057/IJASC.2022.18.4.7

FATIGUE TESTS OF COMPOSITE DECKS WITH MCL CONNECTORS

Ping-Ming Huang, Xiao-Long Li *, Kui-Hua Mei and Yue Zhao

School of Highway, Chang'an University, Xi'an, China
** (Corresponding author: E-mail: 1047829409@qq.com)*

ABSTRACT

Full-scale fatigue tests were performed on three composite decks with the MCL (modified clothoid) connectors to investigate their fatigue performance. Fatigue life and failure mode of the composite bridge decks were explored by measuring the specimens with three different stress amplitudes. The deflection, strain, carrying capacity, and stiffness degradation of the composite decks were measured and analyzed in the test. In addition, parameter analysis was performed using finite-element method in this study. Results showed that the mechanical performance of the composite decks accorded with the plane-section assumption under constant amplitude load, and the fatigue failure mode of the composite decks was the local fracture of the bottom steel plate. The stiffness degradation law and S-N curve were obtained in this study. Moreover, the concrete slab depth had a remarkable effect on the fatigue performance of the composite decks.

ARTICLE HISTORY

Received:	22 February 2022
Revised:	6 June 2022
Accepted:	8 June 2022

KEYWORDS

Corrugated steel-concrete composite decks;
MCL connectors;
Fatigue test;
Constant amplitude load;
Cracks

1. Introduction

Steel-concrete composite structures are generally used in buildings, bridges, underground structures, and other construction fields due to their excellent bearing capacity, high stiffness, convenient construction, and short construction period [1-3].

Bridge decks often suffer from severe damage under the long-term action because of directly bearing vehicular loads. In this situation, the composite structures composed of corrugated steel, reinforced concrete slab, and steel connectors have been proposed to overcome the limitation of the shear performance of the bridge decks under the heavy vehicular loads. Corrugated steel-concrete composite decks have the advantage of small weight and large bearing capacity over reinforced concrete beams. Compared with orthotropic steel decks, the corrugated steel-concrete composite slab structures can eliminate vulnerable details at the welded junctions of the orthotropic steel bridge decks and reduce the impact of stress concentration and problems caused by the fatigue load [4,5].

Nowadays the static behavior of the composite deck has been extensively investigated by scholars [6-10]. To study the static properties of the composite decks with bolted connectors, Patel analyzed the shear behavior of the connectors with ABAQUS [11]. Mirza performed the numerical simulation and experimental test to investigate the strength of headed studs in the composite decks [12]. Bahaz investigated the influence of the effective width on the composite beams through parameter analysis and proposed design formulas for the composite beams [13]. Wang analyzed the stress at the weld joints of the steel bridge according to the LEFM theory [14]. Chen developed a vehicle model to simulate the bridges in service [15].

Due to their aesthetics and practicability [16], the profiled steel plates are primarily used in the composite deck systems [17]. With the rapid development of the transportation, vehicular loads may cause fatigue damage in the composite beams [18]. Hence, it is necessary to study the fatigue performance of the corrugated steel-concrete composite decks. However, the study on the dynamic behavior of the composite decks is limited [19-22]. The bearing capacity and stiffness of the composite decks will degrade to a certain extent due to the effect of fatigue loads [23]. Fatigue damage causes failures of the composite decks. Therefore, studying the fatigue behavior of the composite decks is essential.

This study investigated a novel type of composite structure [24]. It consisted of concrete deck, corrugated steel plate, MCL (modified clothoid) connectors, and reinforcements, as shown in Fig. 1. Compared with the headed studs, the MCL connectors exhibit the advantage of higher load-bearing capacity [25]. In this study, three specimens were performed under the fatigue load to explore the fatigue characteristics. The fatigue life and failure mode of the composite bridge decks were evaluated under different stress amplitudes. Factors influencing the fatigue behavior of the composite decks were analyzed by the finite-element method (FEM). The significance of this research is helpful for the anti-fatigue design of the composite decks.

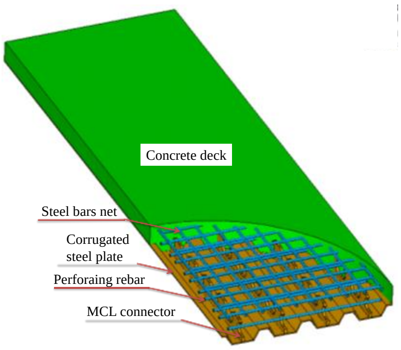

Fig. 1 Corrugated steel-concrete composite decks

2. Testing program

2.1. Dimensions of the composite deck

Three 1:1 full-scale corrugated steel-concrete composite bridge decks (1000 mm × 180 mm × 3100 mm) with MCL connectors were fabricated and tested to examine their fatigue performance. Table 1 presents the dimensions of the composite decks and Fig. 2 shows the shape of the cross-section. The details of the cross-section are listed in Table 2. The MCL connectors (3000 mm × 14 mm × 110 mm) are illustrated in Fig. 3. Steel components made of Q345 were fabricated in the factory. The MCL connectors were welded to the steel plate and the concrete deck made of C50 was cast in place after erection of the formwork. Fig. 4 shows the fabrication of the composite decks.

2.2. Material properties

Standard cube blocks were prepared for each composite deck specimen. They were cured under the same circumstance as the specimens for 28 days. The cubes were tested to obtain the average compressive strength before the fatigue test was performed. The yield and ultimate strength of the steel structures were evaluated in the tensile test. Table 3 presents the details of the material properties.

Table 1
Parameters of the composite bridge decks (unit: mm)

No.	*L*	*W*	*H*	*T*	MCL connector spacing		Longitudinal Bars	Transverse Bars
					Longitudinal spacing	Transverse spacing		
FT-1	3100	1000	180	6	200	250	A16 × 10@10	A16×64@10
FT-2	3100	1000	180	6	200	250	A16 × 10@10	A16×64@10
FT-3	3100	1000	180	6	200	250	A16 × 10@10	A16×64@10

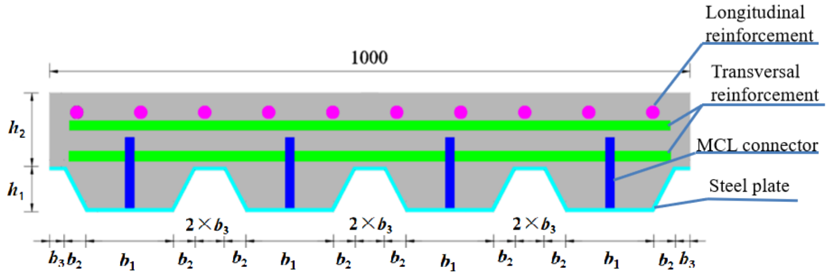

Fig. 2 Cross section (unit: mm)

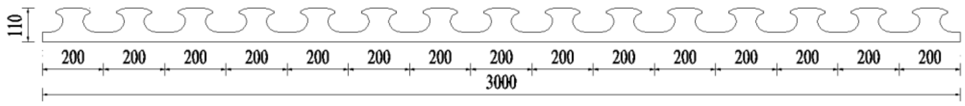

Fig. 3 MCL Connectors (unit: mm)

Table 2
Cross section size of the decks (unit: mm)

Specimen No.	b_1	b_2	b_3	h_1	h_2
FT-1	130	30	30	65	115
FT-2	130	30	30	65	115
FT-3	130	30	30	65	115

(a) Fabrication of the steel structure (b) Erection of the formwork

Fig. 4 Fabrication of the composite deck

Table 3
Material properties of the composite deck specimens (unit: MPa).

Specimen No.	Corrugated steel plate		MCL connectors		f_{cu} (MPa)
	f_y (MPa)	f_u (MPa)	f_y (MPa)	f_u (MPa)	
FT-1	415.6	568.8	438.6	584.3	62.8
FT-2	416.5	569.2	438.6	584.3	61.5
FT-3	414.9	569.5	438.6	584.3	59.4

Note: f_{cu} = average compressive strength of cubic concrete.

Table 4
Fatigue test variables for composite decks.

Specimen No.	Ultimate bearing capacity P_u (kN)	Fatigue Load (kN)		Fatigue load range (kN)	Cycle times ($\times10^4$)	Failure mode
		Upper Limit	Lower Limit			
FT-1	750	450	90	360	25.7	Fracture of steel plate
FT-2	750	360	90	270	83.1	Fracture of steel plate
FT-3	750	260	90	170	242.0	Fracture of steel plate

2.3. Fatigue test program

2.3.1. Loading scheme

Three specimens were tested under the constant amplitude load, and the 500 kN MTS was used in the fatigue test. Fig. 5 depicts the set-up of the tests. The corrugated steel-concrete composite deck was simply supported, with one end hinged and the other end rolling supported. The fatigue loading frequency was 3 Hz. Details of the fatigue loading scheme are displayed in Table 4.

Firstly, the pre-static test was carried out to determine whether the instruments could work. The pre-static load was 10% to 15% of the maximum fatigue load [26]. The MTS system was halted during the fatigue test, and the static loading would be performed to analyze the residual deflection and stiffness degradation when the number of load cycles approached 1×10^4, 3×10^4, 5×10^4, 10×10^4, 20×10^4, 50×10^4, 150×10^4, and 200×10^4, respectively.

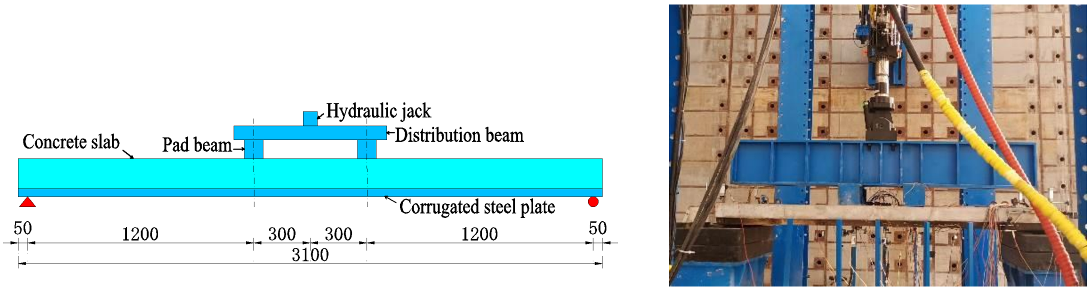

(a) Fatigue loading diagram (unit: mm)

(b) Fatigue loading arrangement

Fig. 5 Fatigue test set-up

2.3.2. Measurement scheme

Ten displacement transducers labeled D1 to D12 were set up to measure the deflection and displacement of the corrugated steel-concrete composite deck. D3 and D8 were used to measure the displacement at the mid-span of the composite deck. D11 and D12 were arranged at the ends of the composite deck to obtain the relative slippage at the interface between the steel plate and the concrete deck.

Fig. 6(a) shows the layout of the displacement transducers. Strain gauges labeled C1 to C4 were used to investigate the concrete strain, and C5 to C15 were used to get the strain of the steel component, as shown in Fig. 6(b).

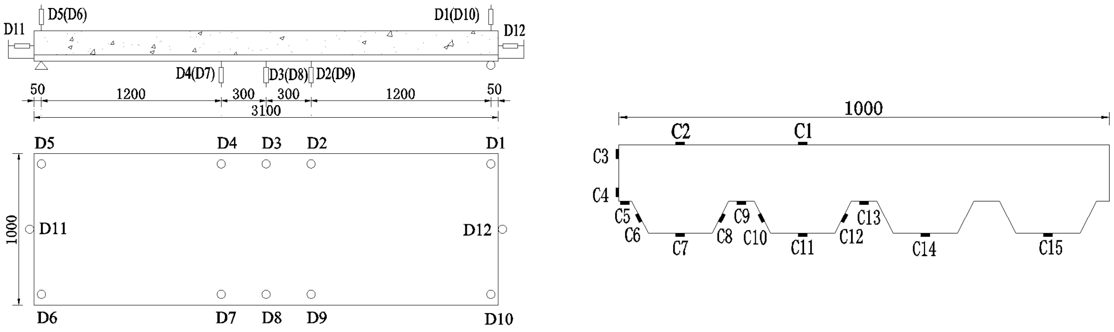

(a) Placement of displacement transducers

(b) Arrangement of strain gauges

Fig. 6 Layout of the instruments (unit: mm)

3. Results and discussion

3.1. Fatigue failure mode

The fatigue life of specimen FT-1 was 25.7×10^4. For specimen FT-2, it was 83.1×10^4, and 242×10^4 for specimen FT-3. Moreover, their failure mode was the fracture of the steel plate. No cracks were observed at the bottom of the steel plate. One fine crack was discovered at the pure bending section of the composite decks when the cycle number reached a specific value. Fig. 7(a) shows the crack found at the steel plate of specimen FT-3 when the cycle number reached 2.04 million. The fatigue crack extended horizontally to both sides of the steel plate with the increase of the cycle number till the corrugated steel plate failed. Fig. 7(b) shows the crack when the cycle number approached 2.4 million.

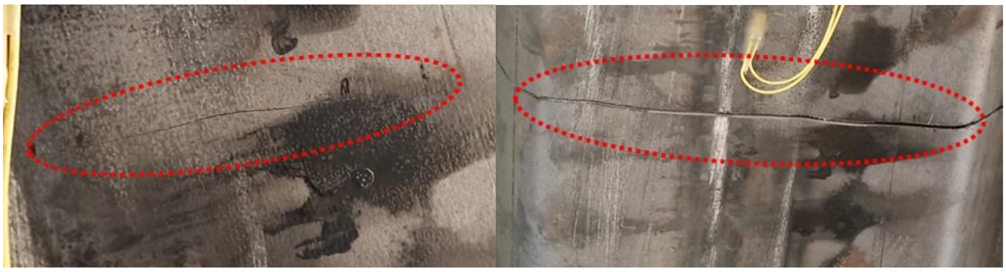

(a) Crack initiation

(b) Development of the fatigue crack

Fig. 7 Fatigue crack

(a) Fatigue failure of FT-1 (b) Cracks at the bottom of FT-1

(c) Fatigue failure of FT-2 (d) Cracks at the bottom of FT-2

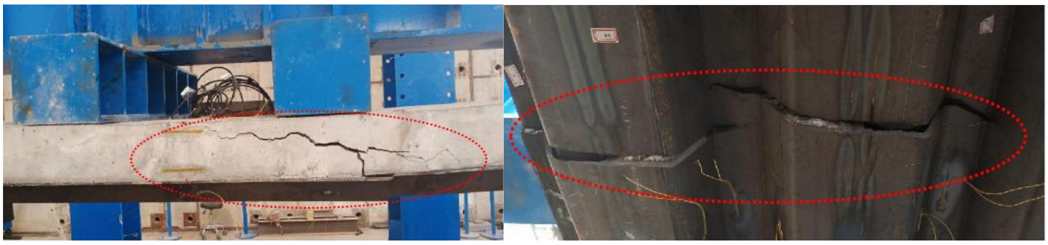

(e) Fatigue failure of FT-3 (f) Cracks at the bottom of FT-3

Fig. 8 Fatigue failure

Fig. 8 illustrates the fatigue failure of the composite decks. The fatigue cracks commonly occurred at the pure bending section of the composite decks, as shown in Fig. 9, which could be attributed to the maximum tensile stress generated there. One Y-shaped crack was observed in the concrete slab. Notably, the cracks were mainly found at the pure bending section of the steel plate. None of them penetrated through the whole steel plate. It could be inferred that the composite deck still had some bearing capacity after fatigue failure. Furthermore, the MCL connectors welded to the steel plate were also broken after the fracture of the steel plate. For specimen FT-3, the failure mode of the concrete deck was different from that of the other two specimens, which could be ascribed to the crack locations. When the cracks did not occur at the pure bending section of the composite decks, the fracture of specimen FT-3 seemed to be diagonal-tension failure, as shown in Figs. 8(e) and (f).

For specimen FT-1, only two cracks penetrated through the lower flange of the steel plate, while for specimen FT-2 and specimen FT-3, three cracks did, as shown in Fig. 9. The reason was that the load amplitude was relatively higher so that specimen FT-1 failed to bear the fatigue load before the crack continued to propagate.

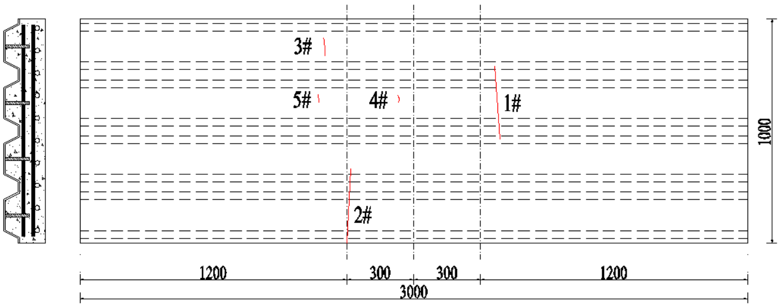

(a) FT-1

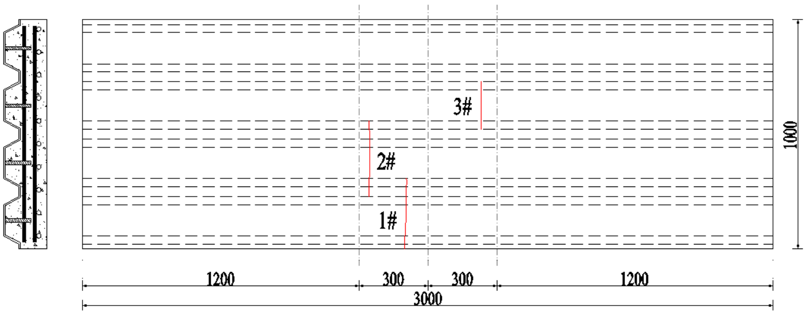

(b) FT-2

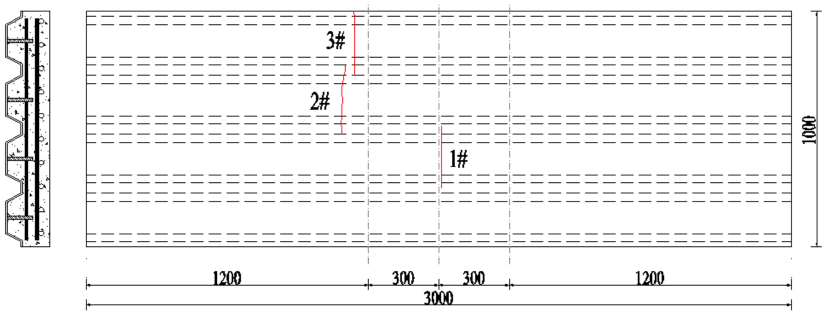

(c) FT-3

Fig. 9 Fatigue cracks of the corrugated steel-concrete composite decks

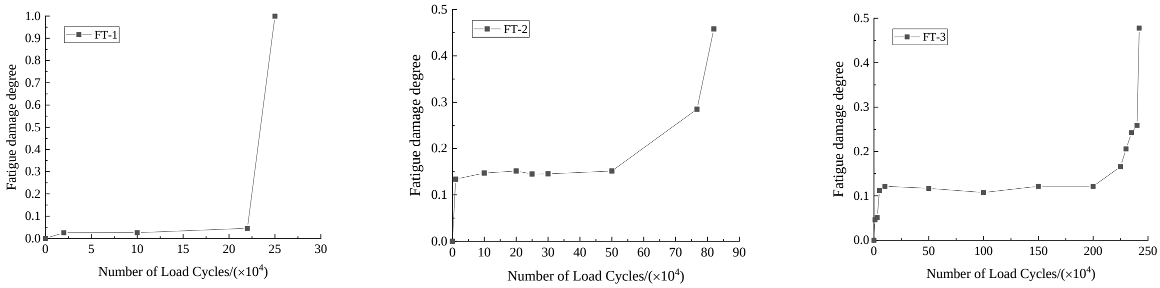

(a) FT-1 (b) FT-2 (c) FT-3

Fig. 10 Fatigue damage degree

3.2. Fatigue damage analysis

To investigate the development of fatigue damage of the composite decks, the fatigue damage degree D_n is adopted in the following equation [27]:

$$D_n=1-B_n/B_0 \tag{1}$$

where B_n is the stiffness of the composite decks at the *n*th fatigue loading cycle, B_0 is the initial stiffness of the composite decks.

Fig. 10 depicts the relationship of D_n versus n. The development of the fatigue damage could be divided into three stages. The fatigue damage increased sharply in the first stage, and some cracks initiated in the concrete deck. In the second stage, the fatigue damage tended to be stable. In the third stage, cracks initiated in the steel plate and propagated, and finally the composite deck failed to bear the fatigue load due to the crack propagation. During this stage, the fatigue damage increased rapidly.

By comparing the fatigue damage degree of the three composite decks, it could be found that the D_n of specimen FT-1 was lower than that of specimens FT-2 and FT-3 in the first two stages. However, in the third stage, the D_n of specimen FT-1 was twice as large as that of specimens FT-2 and FT-3. This might be that the fatigue load amplitude of specimen FT-1 was larger than that of specimens FT-2 and FT-3, which meant that once specimen FT-1 had fatigue damage, it would be destroyed in a short time under the fatigue load.

Fig. 11 shows the stiffness degradation and the curve fitting of FT-2 and FT-3. The relationship of stiffness degradation and the cycle number of FT-2 and FT-3 can be expressed by Equations (2) and (3), respectively. The fitting precision of Equations (2) and (3) are 0.9979 and 0.9737, respectively.

$$\frac{B_n}{B_0}=1-0.55107\times\left\{0.24282\times\left(\frac{n}{N}\right)^{2.93956E-10}+0.58875\times\left[1-\left(1-\frac{n}{N}\right)^{0.21683}\right]\right\} \tag{2}$$

$$\frac{B_n}{B_0}=1-0.47898\times\left\{0.15554\times\left(\frac{n}{N}\right)^{0.02458}+0.84446\times\left[1-\left(1-\frac{n}{N}\right)^{0.12344}\right]\right\} \tag{3}$$

where and N is the fatigue life.

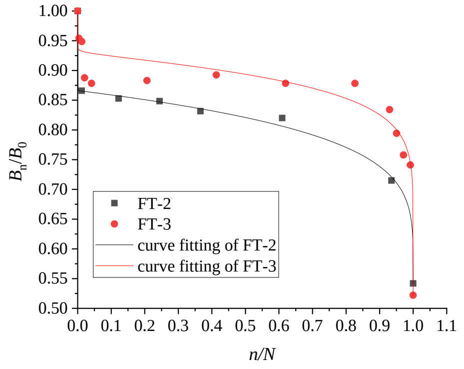

Fig. 11 Stiffness degradation

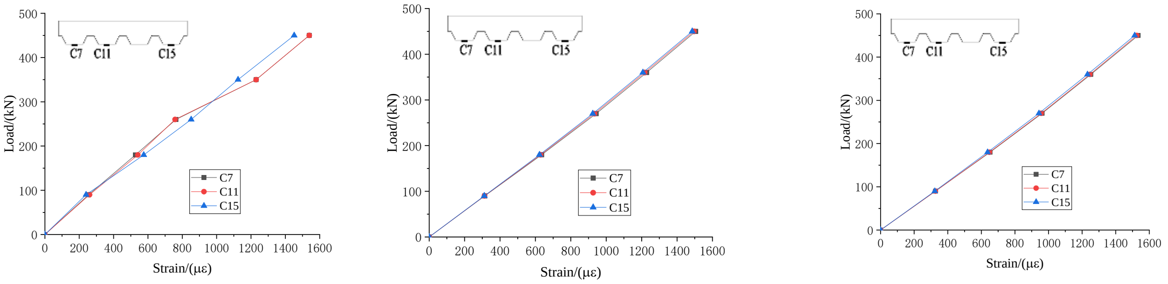

(a) 0 (b) 10000 (c) 220000

Fig. 12 Strain variations of FT-1 specimen under different loading cycles

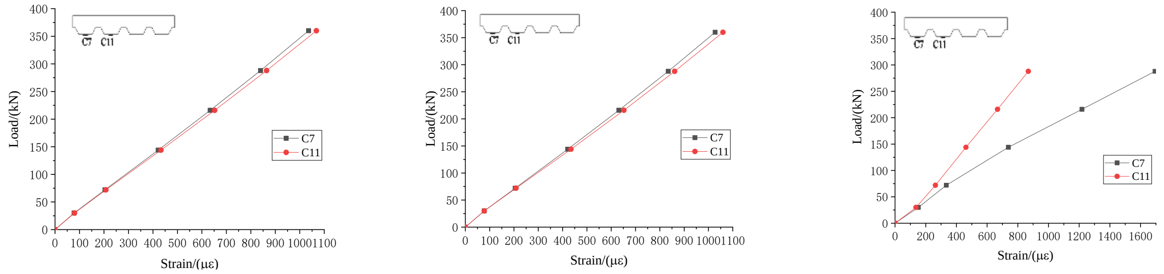

(a) 0 (b) 500,000 (c) 831,000

Fig. 13 Strain variations of FT-2 specimen under different loading cycles

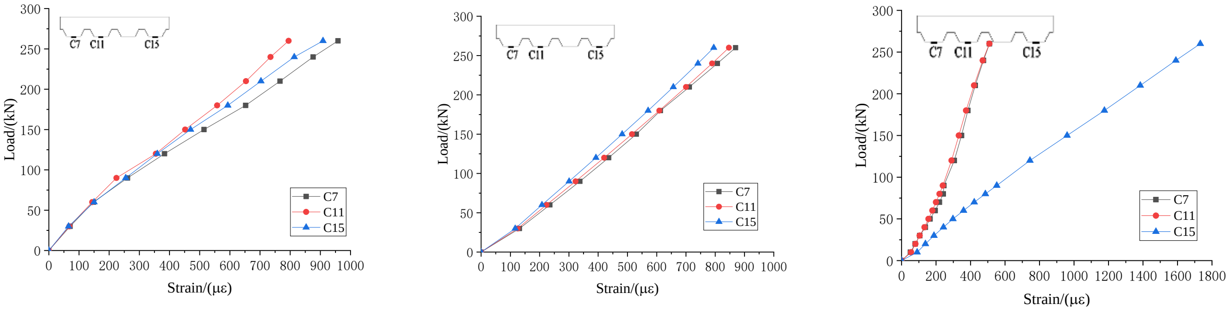

(a) 0 (b) 2 million (c) 2.42 million

Fig. 14 Strain variations of FT-3 specimen under different loading cycles

3.3. Strain analysis

Figs. 12, 13, and 14 show the strain variations of the steel plate under different load cycles, respectively. The strain variations of the steel plate were identical and linear under lower fatigue load, as shown in Figs. 12(a), 13(a), and 14(a). However, for FT-2, strains at C3 were lower than strains at C11 under identical load. This might be the reason that the bottom flanges to which the strain gauges with lower strains were attached fractured under fatigue load, while the undamaged bottom flanges at other parts of the composite deck continued to bear the fatigue load, as shown in Figs. 13(c) and 14(c).

Figs. 15, 16, and 17 present the strain variations at the mid-span of the specimens under different number of load cycles, respectively. The strain variations along the height direction of the composite deck were basically linear during the fatigue test. It was indicated that the composite bridge decks satisfied the plane-section hypothesis when the static load value was relatively lower.

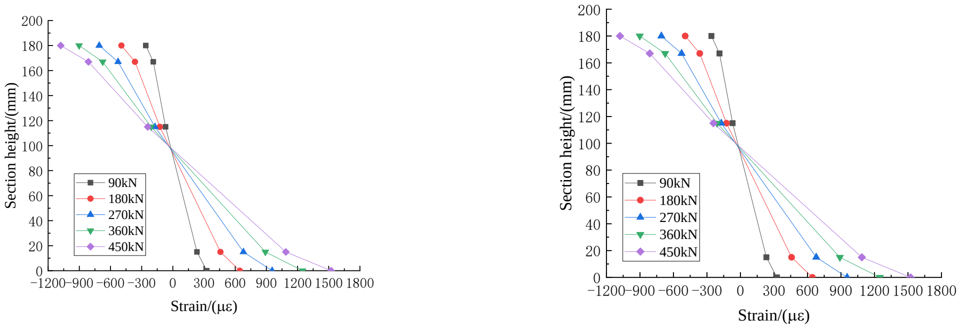

(a) 20000 (b) 100000

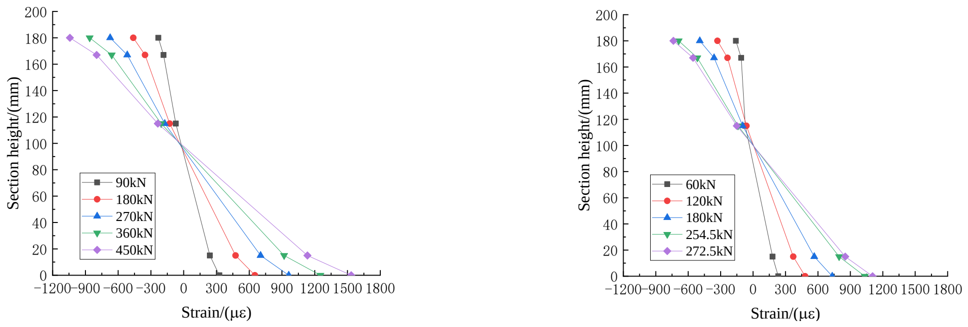

(c) 220000 (d) 257000

Fig. 15 Strain variations of specimen FT-1

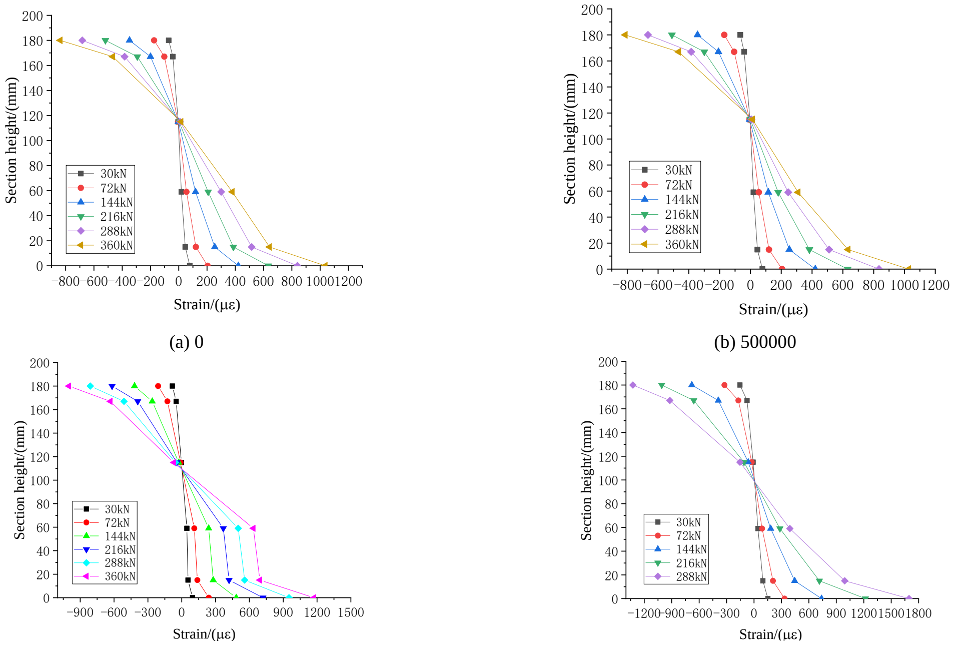

(a) 0 (b) 500000

(c) 767000 (d) 831000

Fig. 16 Strain variations of specimen FT-2

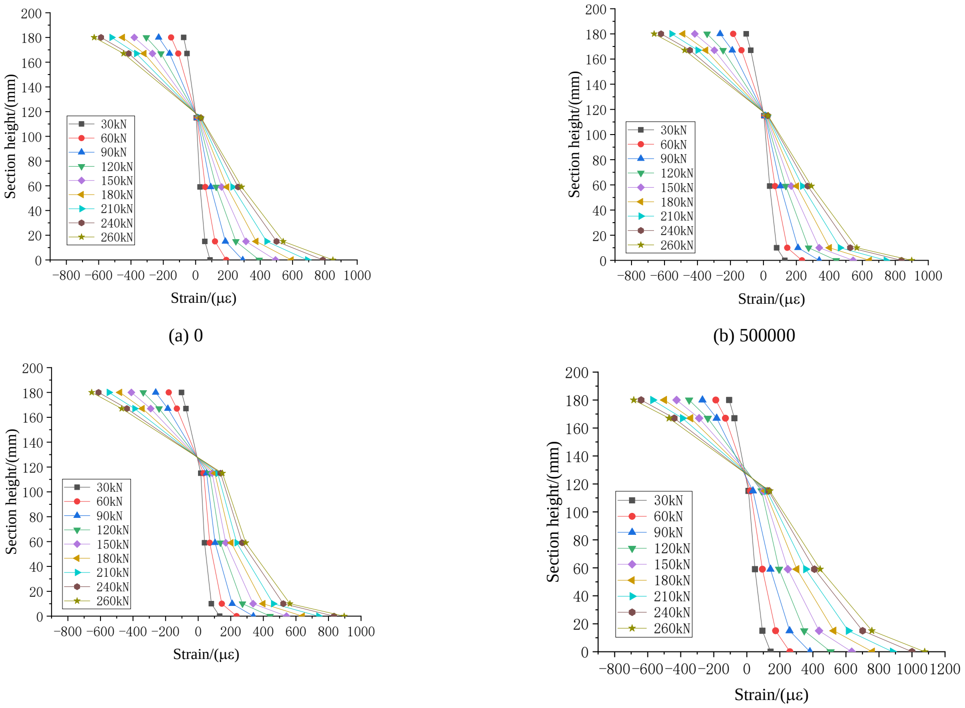

(a) 0 (b) 500000

(c) 1500000 (d) 2400000

Fig. 17 Strain variations of specimen FT-3

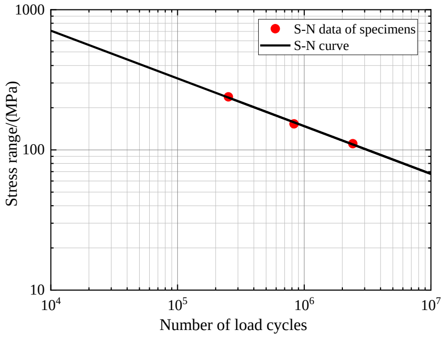

Fig. 18 S-N curve fitting of specimens

3.4. Statistical evaluation of stress category

The S-N curve of the specimens was obtained by fitting the results of the fatigue test, as shown in Fig. 18. The fatigue life of specimens can be expressed as follows:

$$\mathit{Log}_{10}\Delta\sigma + 0.3405\mathit{Log}_{10}N = 4.21237 \tag{4}$$

where $\Delta\sigma$ represents the tensile stress amplitude; N represents the fatigue life.

3.5. Residual bearing capacity

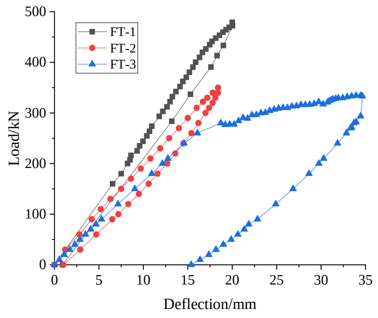

Fig. 19 Residual bearing capacity of the composite decks

The static test was performed to obtain the residual bearing capacity of the specimens when they failed to bear the fatigue load. Fig. 19 depicts the displacement of the composite decks under the static load. The residual carrying capacity of specimen FT-1 was 479.2 kN (0.639 P_u). For FT-2, the residual carrying capacity was 330 kN (0.440 P_u). For FT-3, the residual carrying capacity was 334.5 kN (0.446 P_u). The investigation on the residual bearing capacity of the composite decks would be helpful for the reinforcement and maintenance.

4. Parameter analysis

4.1. Fatigue load model

The fatigue vehicle model should be adopted to get the stress history of the fatigue concern points. There are three types of anti-fatigue design in JTG D64 [28]. The first type adopts equivalent lane load, called the fatigue load calculation model I. The second type adopts the double-vehicle model, called the fatigue load calculation model II. The model details are shown in Fig. 20. The third type adopts a singular-vehicle model, called the fatigue load calculation model III, Fig. 21 shows the details of the fatigue vehicle model. The model III can be used to calculate the bridge deck components. Two loading schemes, the central loading and the eccentric loading, were implemented to obtain the stress at different fatigue concern points. Fig. 22 shows the schematic diagram of the fatigue load layout.

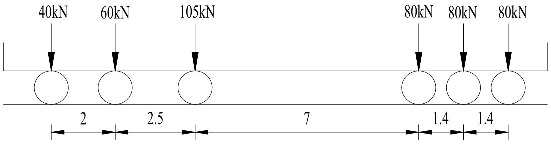

Fig. 20 Model Ⅱ (unit: m)

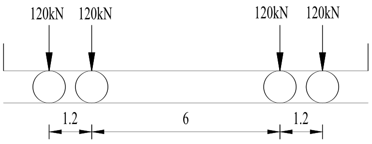

(a) Elevation

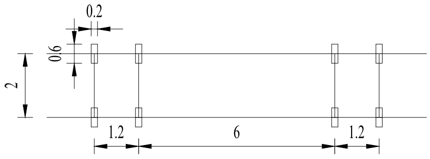

(b) Loading cases

Fig. 21 Model Ⅲ (unit: m)

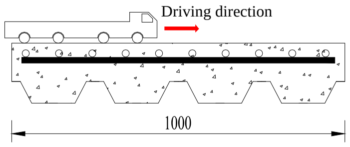

(a) Driving direction

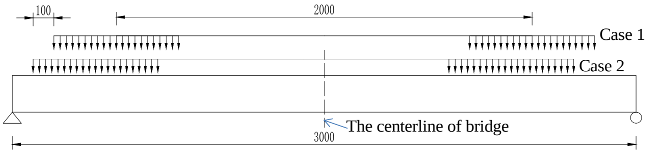

(b) Loading cases

Fig. 22 Schematic diagram of fatigue load layout (unit: mm)

4.2. Numerical analysis model

The numerical analysis model was established using the finite-element method to investigate the influence of the concrete slab depth, the steel plate thickness, and the concrete strength on the fatigue performance of the composite decks. The solid element was applied to the simulation of the composite decks, as depicted in Fig. 23. The relative slippage between the concrete deck and steel plate was ignored. The elastic modulus and Poisson ratio of steel are 2.06×10^5 MPa and 0.3, respectively. For the concrete deck, they are 3.45×10^4 MPa and 0.2, respectively.

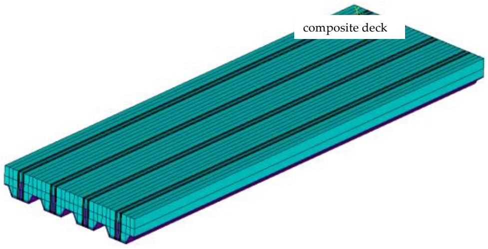

(a) Geometric model

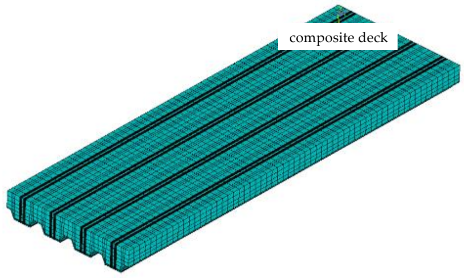

(b) Mesh model

Fig. 23 FEM model

Due to the fact that the steel plate fracture occurred near the mid-span of the composite decks during the test. Two points numbered 1 and 2 were selected to investigate the stress history, and their locations were at the mid-span of the steel plate. Fig. 24 shows the details of the points' locations.

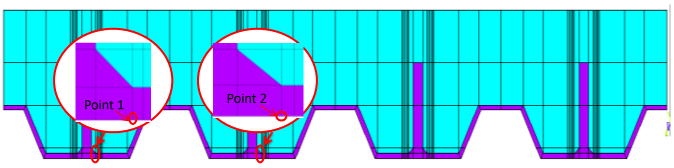

Fig. 24 Fatigue points

The analysis of stress history was beneficial for understanding the fatigue behavior of the composite decks. The model III was employed to investigate the stress variation of the fatigue concern points under different conditions, Table 5 lists the tensile stress at different points.

Table 5
Fatigue test variables for composite decks (unit: MPa)

No.	JTG D64	
	Case 1	Case 2
1	23.62	23.42
2	23.40	23.42

By comparing the stress variations at the two fatigue concern points with each other, the maximum tensile stresses at Points 1 and 2 were approximately similar, as shown in Fig. 25. Vehicles passing through the composite decks would cause the different load amplitudes. Different load amplitudes can be represented by the equivalent stress amplitude [29] based on the Miner standard to estimate the fatigue characteristics of the composite decks in a simple way [30]. The equivalent stress amplitude can be calculated by Eq. (5).

$$\Delta\sigma_0 = \left[\frac{\sum n_i\left(\Delta\sigma_i\right)^m}{N_0}\right]^{\frac{1}{m}} \tag{5}$$

where n_i is the cycle number of stress range $\Delta\sigma_i$; $\Delta\sigma_i$ is the stress amplitude corresponding to the *i*th cycle loading; $\Delta\sigma_0$ is the equivalent stress range; N_0 is the cyclic number concerning $\Delta\sigma_0$; *m* is a constant.

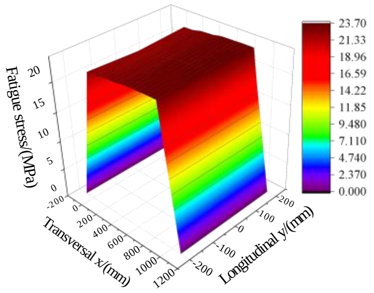

(a) Point 1

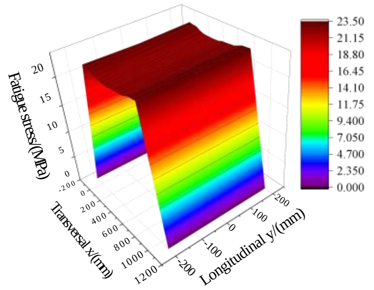

(b) Point 2

Fig. 25 Tensile stress at different positions

The loading method Case 1 was adopted to explore the $\Delta\sigma_0$ of the concern points. The stresses at each point under different load cases were similar, as shown in Fig. 26. Table 6 presents the tensile stress amplitude and the corresponding equivalent stress amplitude. Calculated by Eq. (4), the fatigue life of the composite deck at Point 1 under Case 1 was 119 million. The results showed that the specimens' fatigue resistance was excellent.

To analyze the factors affecting the fatigue performance of the composite decks, three parameters, including the concrete strength, the concrete slab depth and the steel plate thickness, were selected in this study. Fatigue concern Point 1 was selected as an example for the parameter analysis, and Case 1 was selected as the normative fatigue vehicle loading layout.

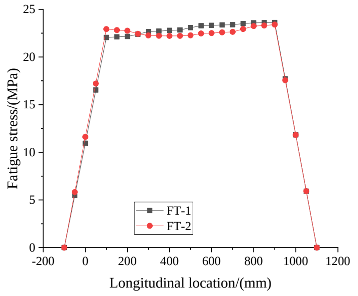

(a) Case 1

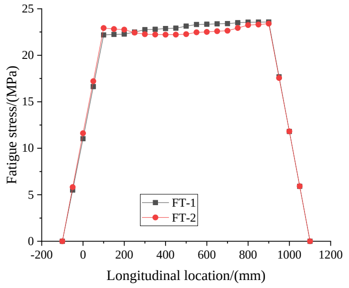

(b) Case 2

Fig. 26 Tensile stress at different positions

Table 6

Tensile stress amplitude at different fatigue concern points

Concern points	Tensile stress amplitude (MPa)	Number of cycles	Equivalent stress amplitude (MPa)
1	23.62	1	23.62
2	23.40	1	18.57
	1.19	1	

4.3. Strength variation of concrete slab

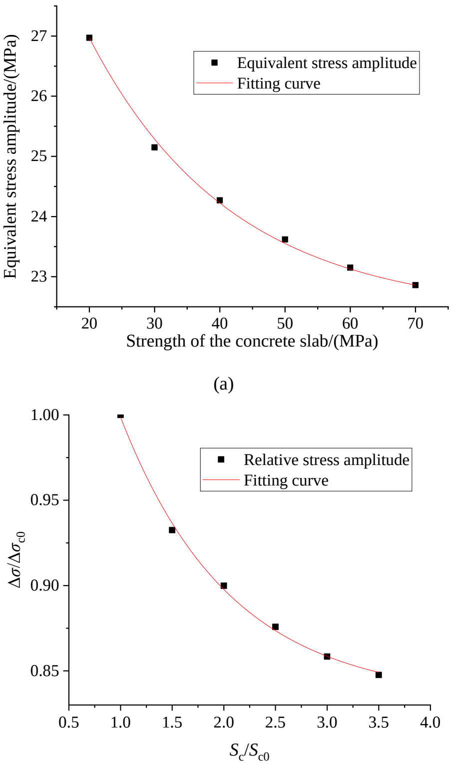

(a)

(b)

Fig. 27 Relation of the concrete strength vs. the equivalent stress amplitude

Six concrete strength grades were adopted in the FEM analysis to study the relation of the concrete strength versus the equivalent stress amplitude. The equivalent stress amplitude $\Delta\sigma$ decreased with the increase of the concrete strength S_c. When $\Delta\sigma/\Delta\sigma_{c0}$ increased from 1 to 3.5 (by 250%), S_c/S_{c0} decreased from 1 to 0.85 (by 15%), as shown in Fig. 27. It could be concluded that the influence of the concrete strength above 50 MPa was relatively lower on the fatigue characteristics of the composite decks. The formulas of S_c versus $\Delta\sigma$ at Point 1 can be described as follows:

$$\frac{\Delta\sigma}{\Delta\sigma_{c0}} = 0.4252e^{\left(-\frac{S_c}{S_{c0}}\right)} \tag{6}$$

where S_c is the concrete strength; $\Delta\sigma_{c0}$ is the equivalent stress amplitude corresponding to S_{c0}; S_{c0} = 20 MPa.

4.4. Depth of concrete slab

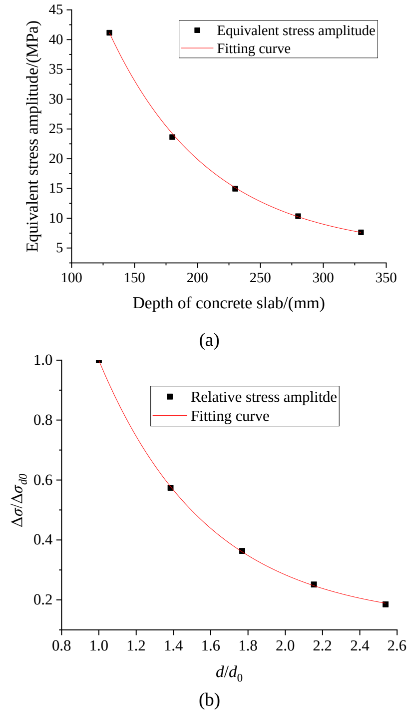

(a)

(b)

Fig. 28 Relation of the concrete deck depth vs. the equivalent stress amplitude

The concrete slab depth (abbreviated as *d*) was adopted as 130 mm, 180 mm, 230 mm, 280 mm, and 330 mm in the FEM analysis. The equivalent stress amplitude decreased significantly with the increase of *d*, as shown in Fig. 28(a). When d/d_0 increased from 1.0 to 2.5 (by 150%), the $\Delta\sigma/\Delta\sigma_{d0}$ decreased from 1 to 0.2 (by 80%). The relationship between $\Delta\sigma$ and *d* obtained from Fig. 28(b) can be expressed as follows:

$$\frac{\Delta\sigma}{\Delta\sigma_{d0}} = 4.83e^{\left(-\frac{d}{0.58d_0}\right)} \tag{7}$$

where *d* is the concrete deck depth and the value of d_0 is 130 mm $\Delta\sigma_{d0}$ is the equivalent stress amplitude corresponding to d_0.

4.5. Thickness of steel plate

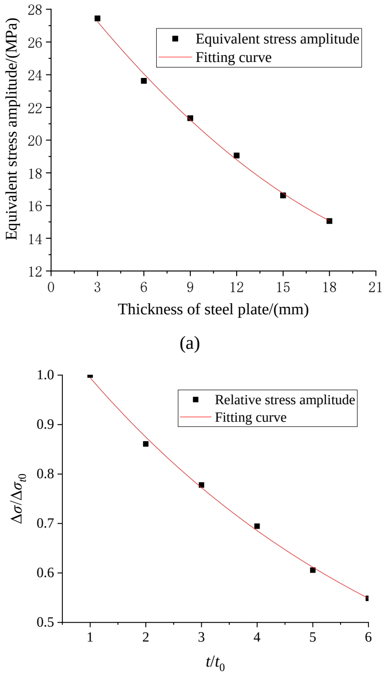

(a)

(b)

Fig. 29 Relation of steel plate thickness vs. the equivalent stress amplitude

The thickness of the steel plate (abbreviated as *t*) was set at 3 mm, 6 mm, 9 mm, and 12 mm. Fig. 29(a) depicts the variation of $\Delta\sigma_0$. When t/t_0 increased from 1 to 6 (by 500%), $\Delta\sigma/\Delta\sigma_{t0}$ decreased from 1 to 0.54 (by 46%). For the composite decks, the influence of steel plate thickness was evident. According to Fig. 29(b), the relationship between *t* and $\Delta\sigma_0$ can be obtained by the following:

$$\frac{\Delta\sigma}{\Delta\sigma_{t0}} = 29.04 - \frac{0.81t}{t_0} \tag{8}$$

where *t* is the thickness of steel plate and t_0 is 3 mm; $\Delta\sigma_{t0}$ is the equivalent stress amplitude corresponding to t_0.

The concrete slab depth had a remarkable influence on the fatigue performance of the composite decks. And the influence of the concrete slab strength on the fatigue performance of the composite decks was little.

5. Conclusions

Three full-scale specimens were examined via fatigue tests and the fatigue performance of the composite bridge decks was analyzed using FEM.

The fatigue failure of the composite decks typically occurred near the mid-span of the composite decks. Cracks initiated in the pure bending section of the composite decks and propagated transversely with the increase of cycle number, and finally led to the failure of the composite decks.

The stiffness degradation law and the S-N curve of the composite decks had been obtained in this paper. It was found that the influence of the concrete slab depth on the fatigue performance of the composite decks was remarkable.

References

[1] Nie J., Wang Y., "Research status on fatigue behavior of steel-concrete composite beams", Eng. Mech., 29(6), 1-11, 2012.

[2] Zhang Q., Yuan D., Wang B., et al, "Fatigue performance of innovative both-side welded rib-to-deck joints", China J Highs Transp, 33(5), 79-91, 2020.

[3] Pardeshi R. T., Patil Y. D., "Review of various shear connectors composite structures", Adv. Steel Constr., 17(4), 394-402, 2021.

[4] Zhang Q., Bu Y., Li Q., "Review on fatigue problems of orthotropic steel bridge deck", China J Highw Transp, 2017; 30(3): 14-30.

[5] Kim H. Y., Jeong Y. J., "Experimental investigation on behavior of steel–concrete composite bridge decks with perfobond ribs", J Constr Steel Res, 2006 ,62(5): 463-471.

[6] Kim H. Y., Jeong Y. J., "Experimental investigation on behavior of steel-concrete composite bridge decks with perfobond ribs", J Constr Steel Res, 2006, 62(5): 463-471.

[7] Kim H. Y., Jeong Y. J., "Ultimate strength of a steel-concrete composite bridge deck slab with profiled sheeting", Eng Struct, 2010, 32(2): 534-546.

[8] Kim H. Y., Jeong Y. J., "Steel-concrete composite bridge deck slab with profiled sheeting", J Constr Steel Res, 2009, 65(8-9): 1751-1762.

[9] Jeong Y. J., Kim H. Y., Koo H. B., "Longitudinal shear resistance of steel-concrete composite slabs with perfobond shear connectors", J Constr Steel Res, 2009, 65(1), 81-88.

[10] Jeong Y. J., "Simplified model to predict partial-interactive structural performance of steel-concrete composite slabs", Journal of Constructional Steel Research, 2008, 64(2), 238-246.

[11] Patel V. I., Uy B., Pathirana S. W., et al., "Finite element analysis of demountable steel-concrete composite beams under static loading", Adv. Steel Constr., 14(3), 392-411, 2018.

[12] Mirza O., Uy B., "Effects of strain regimes on the behaviour of headed stud shear connectors for composite steel-concrete beams", Adv. Steel Constr., 6(1), 635-661, 2010.

[13] Bahaz A., Amara S., Jaspart J. P., et al., "Numerical analysis and evaluation of effective slab width of composite continuous beams with semi-rigid joint", Adv. Steel Constr., 17(4), 331-339, 2021.

[14] Wang C. S., Zhai M. S., Duan L., et al., "Fatigue service life evaluation of existing steel and concrete bridges", Adv. Steel Constr., 11(3), 305-321, 2015.

[15] Chen W. Z., Xu J., Yan B. C., et al. "Fatigue load model for highway bridges in heavily loaded areas of China", Adv. Steel Constr., 11(3), 322-333, 2015.

[16] Islam S., Abang-Abdullah A. A., Jafar M. S., "An investigation on structural performance of profiled steel to develop self-supporting roofing system", Adv. Steel Constr., 2(1), 87-108, 2006.

[17] Ayman E., Hani S., Aaron S., "Fatigue tests on steel-concrete composite beams subjected to sagging moments", J Struct Eng, 2019, 145(5): 04019029.

[18] Liu R., Yang Y., Zhou X., "Experimental study on fatigue performance of composite beam with steel-plate-concrete composite decks", Constr Build Mater, 2018, 188: 833-849.

[19] Ahn J. H., Sim C., Jeong Y. J., et al., "Fatigue behavior and evaluation of the stress category for a steel-concrete composite bridge deck", J Constr Steel Res 2009, 65(2), 373-385.

[20] Gao Q., Dong Z., Cui K., et al., "Fatigue performance of profiled steel sheeting-concrete bridge decks subjected to vehicular loads", Eng Struct 2020, 213: 110558.

[21] Schuster R. M., Suleiman R. E., "Composite slabs subjected to repeated point loading", Eighth International Specialty Conference on Cold-Formed Steel Structures ST. Louis, Missouri, U.S.A., 1986, November, 453-485.

[22] Mouw K. W., "Fatigue testing of light gage metal forms", Center for Cold-Formed Steel Structures Library, 1969, January, 1-35.

[23] Yang Y., Nie J., Du M., et al., "Study on fatigue performance of closed profiled steel sheeting-concrete composite slabs", Civil Eng J, 2008, 41(12), 35-41.

[24] Kong F., Huang P., Han B., Wang X., Liu C., "Experimental study on behavior of corrugated steel-concrete composite bridge decks with MCL shape composite dowels", Eng Struct,

2021, 227, 111399.
[25] Kopp M., Wolters K., Classen M., et al., “Composite dowels as shear connectors for composite beams-Background to the design concept for static loading”, J Constr Steel Res, 2018, 147, 488-503.
[26] Nie J., “Steel-concrete Composite Beams: Experiment, Theory and Application”, Beijing: Science Press; 2005.
[27] Hu R., Fang Z., Jiang R., Xiang Y., Liu C., “Fatigue prediction model of ultra-high-performance concrete beams prestressed with CFRP tendons”, Adv Struct Eng, 2021, 25, 3, 611-624.
[28] JTG D64-2015. Specification for Design of Highway Steel Bridge. Chinese specification, 2015.
[29] Miner M. A., “Cumulative damage in fatigue”, J. Appl. Mech. 1945, 12, 159-164.
[30] Huang Y., Zhang Q. H., Bao Y., Bu Y., “Fatigue assessment of longitudinal rib-to-crossbeam welded joints in orthotropic steel bridge decks”, J. Constr. Steel Res. 2019, 159, 53-66.

Advanced Steel Construction – Vol. 18 No. 4 (2022) 804–817
DOI:10.18057/IJASC.2022.18.4.8

RETROFITTING COLLAPSE BEHAVIOR OF DOUBLE LAYER SPACE TRUSSES AGAINST PROGRESSIVE COLLAPSE BY FORCE LIMITING DEVICES

Saman Rashidyan [1, *] and Mohammad Reza Sheidaii [2]

[1] *Clinical Assistant Professor, Department of Mechanical Engineering, University of North Texas, 1155 Union Circle #305027, Denton, Texas 76203-5017*
[2] *Professor, Urmia University, Civil Engineering Department, Urmia University, West Azerbaijan Province, 24, Urmia Lake Bridge*
** (Corresponding author: E-mail: srashidyan@yahoo.com)*

ABSTRACT

Previous collapses of Double Layer Space Trusses (DLSTs) show that they are vulnerable to progressive collapse phenomenon. Under certain circumstances, a local failure can propagate throughout the structure and lead to occurring a brittle failure in the structure. Therefore, it is crucial to identify and exploit proper retrofitting methods against progressive collapse in DLSTs. In the current study, the method of utilizing Force Limiting Devices (FLDs) to improve the collapse behavior against progressive collapse have been investigated for flat DLSTs with overall collapse and dynamic snap-through. The results show that introducing FLDs to the critical members of the top layer of a flat DLST with dynamic snap-through failure mode and a member imperfection of 0.005L provides 18.2 to 23.86% load bearing increase and ductility between 1.55 to 1.67. The results also show that when the DLSTs is made of members with geometric imperfections between 0.001 L and 0.004 L, the FLDs can convert the overall collapse of the DLSTs to a ductile collapse. For this member imperfection range, the obtained data show that the method can increase the load bearing capacity of the models from 18.35to 26.8% and provide ductility between 1.56 to 1.76. The provided ductility in models with smaller member imperfection is slightly greater than those provided in models with larger member imperfection. In the current study the activation level of FLDs are selected between 85 to 95 percent and the effect of FLD activation level is also investigated. In addition, the results showed that placing FLDs on critical members could provide a ductility significantly greater than the ductility provided by another method of retrofitting DLSTs called the method of over designing the members of compression layer and under designing the members of tension layer.

ARTICLEHISTORY

Received:	13 September 2020
Revised:	20 July 2021
Accepted:	22 July 2021

KEYWORDS

Force limiting device;
Double layer space truss;
Progressive collapse;
Snap-through;
Buckling

1. Introduction

Double Layer Space Trusses (DLSTs) are among proper structures to cover large areas since their stiffness and load bearing capacity are high due to their efficient geometry. In general, these structures collapse in one of the modes shown in Fig. 1. In the ‘overall collapse’ mode, when a member buckles the distribution of the load happens quickly; therefore, the rest of the structure is not able to hold the distributed load and the structure will collapse after the first set of members fail. In the ‘local collapse along with dynamic snap-through’ the load shedding by the failure of compression member occurs abruptly, however, the rest of the structure can hold the load which is distributed. In this case, the buckling of this first of members will result in a large change in displacement. For cases in which the released energy is enormous, other members may not be able to absorb the excessive released energy and consequently the structure collapses due to the large released energy. The chain of the failures occurring in such cases is called a progressive collapse phenomenon. In contrast, in ‘local collapse without dynamic snap-through’, the load distribution occurs gradually; therefore, no additional dynamic load distribution is generated in such collapse modes.

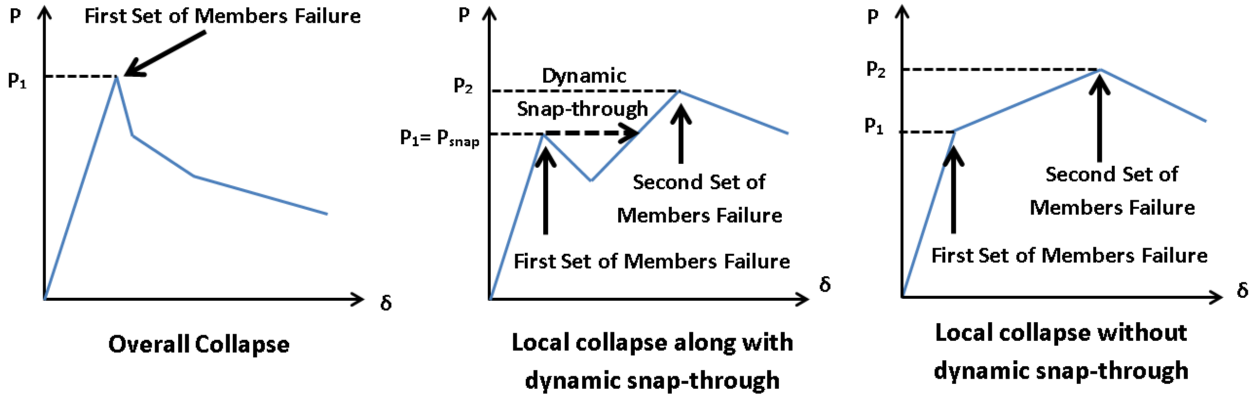

Fig. 1 Collapse modes in DLSTs

The collapse form of the DLSTs can be identified using a static collapse analysis. Since the failure behavior of the DLSTs is highly dependent on the behavior of the constituting members, the behavior of the tensile and compression members should be determined in the first step. In tensile members, when load increases, the stress reaches to the yielding stress. At this time, the member does not collapse, and it still can carry loads due to its strain hardening behavior. This behavior continues with large strains until the member ruptures. In contrast, the load bearing capacity reduction usually occurs in a brittle manner in members under compression forces. Even in trusses where yielding occurs in tension members, the failure is finally dictated by the buckling of the compression members [1–3]. Under common slenderness ratios, the buckling of a compression members is brittle in most of the cases [4].

After completing the static analysis if the obtained graphs show the occurrence of snap-through in the DLST, a dynamic snap-through analysis is done to determine the real strength of the structure during the occurrence of progressive collapse [5]. Many references show the necessity of considering the dynamic effects of progressive collapse in trusses [6] and frame structures [7–9]. It should be noted that when dynamic snap-through happens in the structure, conducting a dynamic analysis is necessary in such cases to obtain a realistic behavior of the structure.

After completing the failure analysis of the DLST, if the results show the occurrence of ‘overall collapse’ or ‘local collapse along with dynamic snap-through’, appropriate methods should be used to improve the behavior of the DLST against the brittle failure in such structures.

One proper method is over designing the members of the top layer along with under designing the members of bottom layer. In this method the tension members yield before the compression members buckle. This delays the failure of the compression members and consequently a good level of ductility will be provided [4]. A comprehensive study regarding this method is conducted by Rashidyan and Sheidaii [10].They used this method on five DLST models with various conditions. They showed that 30%-40% overdesign of all top and under design of bottom members results in satisfactory ductility level and load bearing capacity in their investigated models.

The method of using Force Limiting Devices (FLD) to change the brittle behavior of members under compression to a ductile behavior is another proper method to enhance the collapse behavior of DLSTs. These devices have a rigid-plastic behavior and are installed on selected critical compression members of the DLST. The load under which the devises start working is slightly less than the load under which the member buckles. This load level will be kept constant even when the load on structure increases. Therefore, a compression member protected by an FLD would have an elastic-plastic behavior rather than a brittle behavior.

The theoretical benefits of FLDs were first shown by Schmidt and Hanaor [11] and results of some prototype devices were demonstrated by Hanaor and Schmidt [12]. To investigate the ability of the FLDs in enhancing the collapse behavior of the DLSTs, Hanaor et al. [4] tested Bamford and Mero shaped DLSTs with FLDs and the results were compared to trusses with no devices. The DLSTs equipped with FLDs withstood up to 23% higher than the control truss, with considerably enhanced ductility. Parke [13] showed the effectiveness of a devised FLD system indicated in Fig. 2 on the collapse behavior of space trusses. His devised FLD system consists of tubes and strips as indicated in Fig. 2. When a compressive load is applied on the member, both tubes subject to compression whereas the strips are under tension forces. If the system is designed such that the strips yield prior to the failure of the tubes, the overall behavior of the member would be ductile as can be seen in Fig.2b.

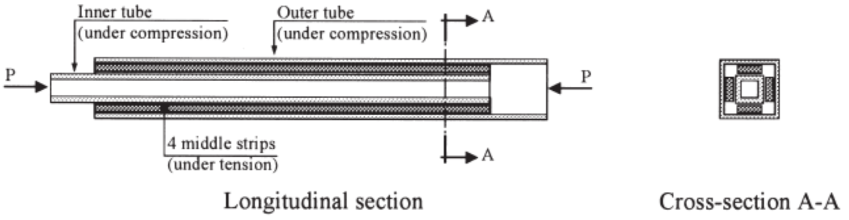

(a) Detail of a member with an FLD

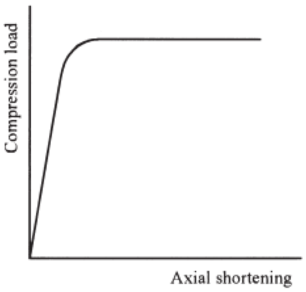

(b) Typical behaviour pattern of a member with an FLD

Fig. 2 (a) Detail of a member with an FLD and (b) typical modified behavior pattern [13]

El-Sheikh [14] showed the influence of FLDs on the behavior of 3-D trusses through a parametric study on trusses with overall and local collapse without dynamic snap-through. He investigated the effect of both the location and number of the compression members with FLDs on the ductility level and strength of the space trusses. His studies revealed that, using FLDs on top chord members that are under largest stresses can improve the overall behavior and strength of the DLSTs with overall and local collapse without dynamic snap-through. The method could also improve the ductility of his investigated space trusses. Bai and Zhang [15] presented the performance of FLDs on roof trusses under combined static and transient wind loading. Kim and Chae [16] studied ‘out of plane’ type, ‘slit’ type and ‘folded plate’ type FLDs and showed the effectiveness of such devices using experimental and numerical methods. Poursharifi et al. [17] introduced an Accordion Force Limiting Device (AFLD). They studied their proposed AFLD under compressive forces and showed that the AFLD could modify the brittle behavior of the members. Abedi and Kolachahi [18] applied FLDs on double-layer barrel vault space structures. Their results demonstrated the efficiency of the FLDs in preventing progressive collapse. The influence of FLDs on tensegrity structures has also been investigated by Shekastehband [19]. He showed that using FLDs in critical members can lead to a ductile behavior and increases the strength of the investigated tensegrity structures up to 52%.

In the above-mentioned investigations, the applicability of the method in improving the collapse behavior of various DLSTs, double-layer barrel vaults and tensegrity structures has been demonstrated. However, the performance of FLDs on flat DLSTs with dynamic snap-through collapse has not been discussed in the literature. Since the large released snap-through energy can have an important adverse impact on the collapse behavior of the DLSTs it was decided to see how the FLDs affect the collapse behavior of such structures. In addition, there is still a need to reveal more aspects of the performance of FLDs on flat DLSTs with overall collapse and the effect of important factors such as member imperfection and FLDs activation level should be scrutinized. Thus, this study first tries to investigate how FLDs can enhance the collapse behavior of flat DLSTs where dynamic snap-through occurs. Second, DLSTs with overall collapse behavior having different member imperfection and FLD activation level are analyzed to examine the effect of such factors on the effectiveness of using FLDs. In the end, the results of this study were also compared to another retrofitting method called the method of over designing the members of compression layer and under designing the members of tension layer to improve the collapse behavior of flat DLSTs suggested by Rashidyan and Sheidaii [10]. Since the DLST models used in both studies are the same, the comparison of the results can help obtaining more insight regarding the effectiveness of installing FLDs on DLSTs. Also, we would like to acknowledge that the analysis method that we have utilized in this paper has previously been used and verified in several studies [5,10,20,21].

2. Parametric study

2.1. Investigated models

Five flat square on square offset DLST [22] models are initially investigated in this research. The initial models were selected with various support conditions, member imperfection, structure height and plan shapes in order to investigate the impact of such leading factors on the failure behavior of DLSTs. The investigated models are also the same as the ones used by Rashidyan and Sheidaii [10]. This let the research team compare some results from applying the FLDs on the DLST models with the results obtained from the method of over designing the members of compression layer and under designing the members of tension layer. The characteristics of the DLST models are shown in Table 1. The geometry of Models G1 to G5 is shown in Fig. 3. Pin supports were used in all the models. The pin supports were located only at the four corners of the bottom layer for models G1 to G4. However, Model G5 has pin supports at all the 32 bottom joints located on the external perimeter.

Table 1
Characteristics of investigated models [10]

Model	Length (m)	Width (m)	h(m)	Geometrical imperfection of members	Supports location
G1	9.6	9.6	0.75	0.001 L[a]	Corner nodes of bottom layer
G2	9.6	9.6	0.75	0.005 L	Corner nodes of bottom layer
G3	9.6	9.6	0.5	0.001 L	Corner nodes of bottom layer
G4	9.6	7.2	0.75	0.001 L	Corner nodes of bottom layer
G5	9.6	9.6	0.75	0.001 L	All bottom layer external nodes

[a] Length of member

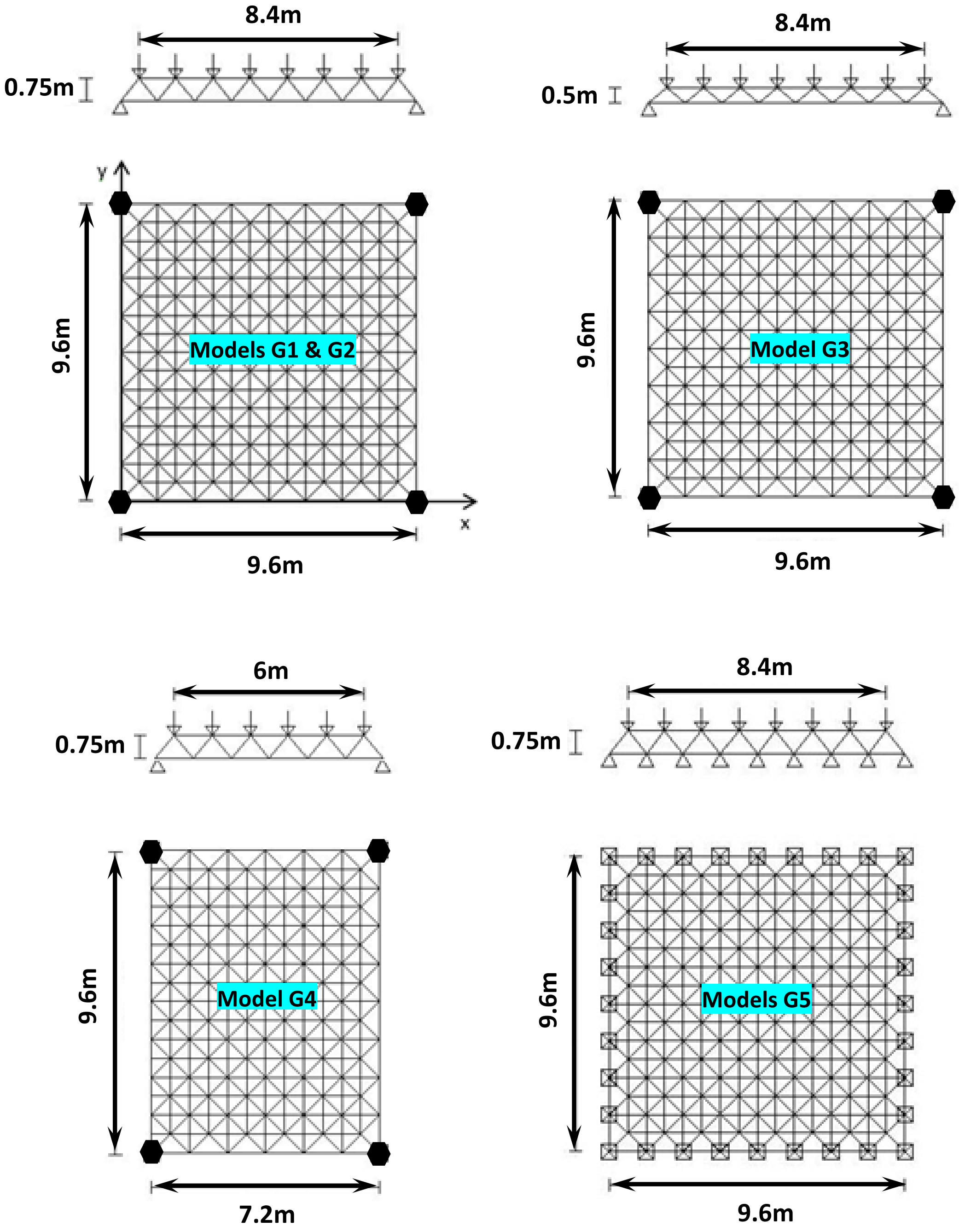

Fig. 3 Geometry of Models G1 to G5

2.2. Design of the investigated models

The steel DLSTs were analyzed and designed using SAP 2000 software [23]. To do so the dead and snow loads indicated in Table 2 were applied on the DLSTs according to ASCE/SEI 7-1[24]. In order to transfer the snow loads to the structure, a flat sandwich panel cover was considered at the top of the DLST. The dead loads from the weight of the roof cover and from the weight of the DLST members have been distinguished in Table 2. The yielding stress and the modulus of elasticity were assumed 240 and 210000 MPa respectively.

Table 2
Assumed dead and snow loads in models G1 to G5

Model	Dead load due to the weight of roof cover (Kgf/m^2)	Dead load from the weight of members of the DLST (Kgf/m^2)	Snow Load (Kgf/m^2)
G1	70	38	100
G2	70	38	100
G3	70	46	100
G4	70	25	100
G5	70	15	100

In the next step the uniform dead and snow loads were multiplied by the tributary area of the top joints of the DLST and the product was applied at the top joints as concentrated loads and the DLSTs were analyzed. After analyzing the structures, the DLST members were designed in accordance to AISC 360-16 [25]. Identical steel hollow-circular cross sections were utilized for all the members. Solid members were used at the corners in Models G1 to G4 though. The characteristics of the chords used in each model are shown in Table 3.

Table 3
Characteristics of chords in G1 to G5 [10]

Model	Member	External diameter (mm)	Thickness (mm)	Slenderness ratio	Geometrical imperfection
G1	P1	48	5.6	79	0.001 L*
G2	P2	48	5.6	79	0.005 L
G3	P3	89	3.6	40	0.001 L
G4	P4	57	2.9	63	0.001 L
G5	P5	38	2.6	96	0.001 L

*Member's length

2.3. Collapse behavior of the investigated models

As stated earlier, a static analysis needs to be done to determine the failure mode of the DLST models. The behavior of the tensile and compression members was determined using finite element method. In this research LUSAS software [26] was used to determine the behavior of the members and collapse behavior of the DLSTs.

Following assumptions [5] were assumed for the finite element analysis:

- The material has an Elasto-plastic behavior.
- The members are pined at the two ends.
- Kirchhoff thin beam elements are used.
- 10 finite elements were considered for each member.
- Nonlinear behavior pertaining to materials and geometry are considered.
- Intrinsic geometrical imperfections are considered by assuming a pre-made curvature as indicated in Fig. 4. Maximum geometrical imperfection (Δ) exists at the middle of the member.

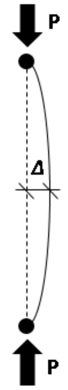

Fig. 4 Hinge-end compression member with initial curvature (geometrical imperfection)

Considering the abovementioned assumptions, the curves indicated in Fig. 5 were obtained for members P1 to P5.

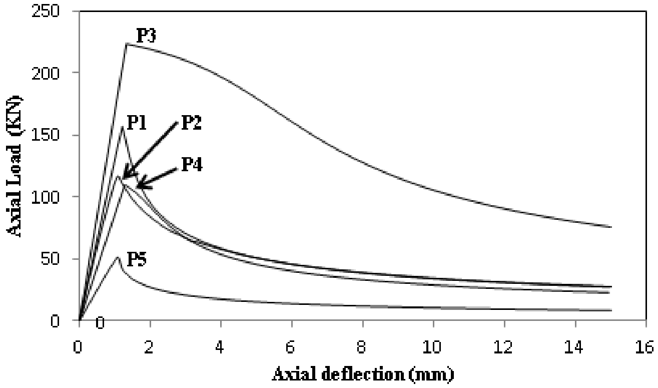

Fig. 5 Axial force-deformation curves for P1 to P5 [10]

After determining the load deformation of the members, their stress-strain behavior graphs were obtained using piece-wise linearization method [27]. The stress-strain curves for P1 to P5 are shown in Fig. 6. Theses graphs in addition to 2-node truss elements were used to perform the failure analysis of the DLST models. This strategy can remarkedly reduces time especially in large DLSTs.

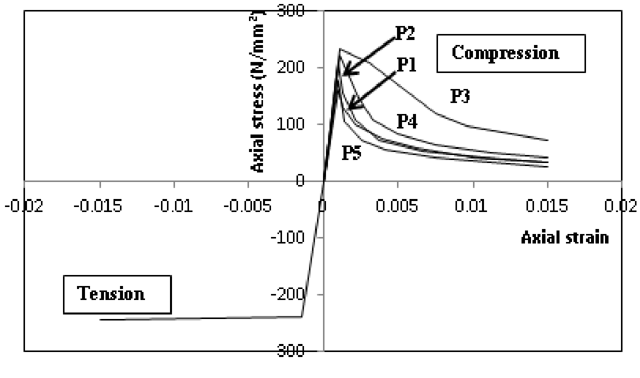

Fig. 6 Stress-strain curves for members P1 to P5 [10]

After determining the behavior of the members, nonlinear static collapse analysis was performed on the DLST models G1 to G5. In the nonlinear static analysis, the matrix form of the equilibrium of the structure is as follows:

$$KD = P \tag{1}$$

where K, D, and P are the stiffness matrix, displacement vector and load vector respectively. After conducting the nonlinear static analysis on Models G1 to G5, the load deflection curves of the node located at the center of the top layer of each model are obtained and shown in Fig. 7.

The graphs shown in Fig. 7 indicate that the failure mode in models G1, G3, G4 and G5 is an overall collapse. However, a local failure accompanied with dynamic snap-through takes place in Model G2. The first set of failure in model G2 happens at 4782 N (which is P_{snap}) and the maximum load bearing capacity is achieved at 5232 N. The P_{snap} (Point 1) and maximum load bearing capacity of Model G2 are shown on the load deflection diagram of the node located at the center of the top layer in Fig. 8. The state of the structure at Point 2 is also called a 'configuration strain' state.

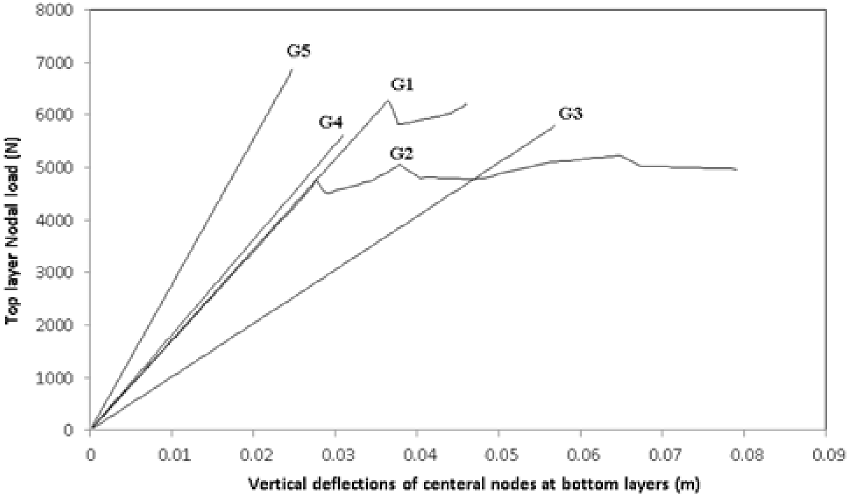

Fig. 7 Load deflection curves of nodes located at the center of top layer of models G1 to G5 [10]

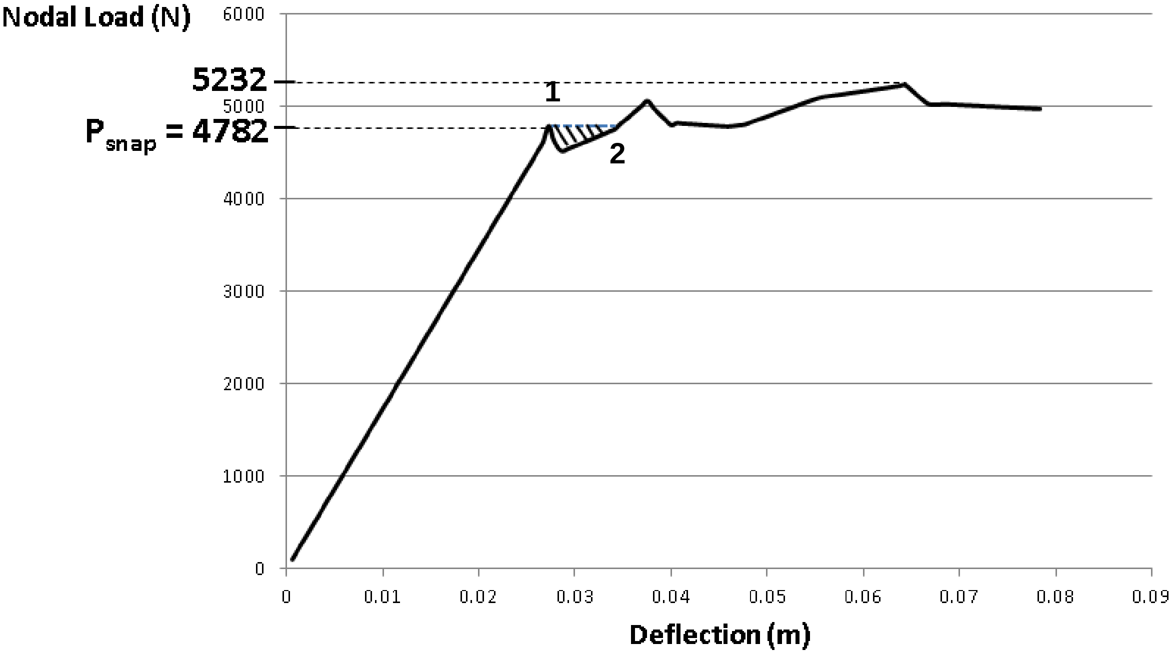

Fig. 8 Load deflection curve of the node located at the center of the top layer in model G2 [10]

Although the maximum load bearing capacity of Model G2 is obtained as 5232 N, the actual value may be smaller due to the released energy during the dynamic snap-through phenomenon. Thus, a dynamic snap-through analysis should be done at this time.

Among various dynamic methods, the energy method was selected and utilized in this study since it is a proper method to evaluate the dynamic behavior of DLSTs [20]. The energy method was performed according to the following procedure.

The matrix form of the static equilibrium of the structure was indicated in Equation 1. By gradually increasing the applied load in the static analysis, the structure will approach a state point where snap-through occurs. Assuming that the snap through happens at a load level of P_{snap}, the equilibrium equations at the time of snap-through will be:

$$K_{snap} D_{snap} = P_{snap} \tag{2}$$

where D_{snap} is the static displacement at the time of snap-through and K_{snap} is its corresponding stiffness matrix. When structure reaches to this point, snap-through takes place and accordingly a huge energy is released since some compression members buckle. The released energy can now be expressed as the sum of kinetic energies corresponding to nodal snap-through of all loaded nodes. The kinetic energy corresponding to the nodal snap-through of a loaded node can be obtained by measuring the area bounded between the load deflection curve and a horizontal line drawn from P_{snap}. The shaded area corresponding to the released energy at the node located at the center of the top layer of Model G2 is indicated in Fig. 8.

Based on the abovementioned discussion, the kinetic energy was determined for all top loaded nodes of Model G2 using the load deflection diagrams of the top nodes. Due to symmetry, only the diagrams of ten top layer loaded nodes of Model G2 are shown in Fig. 9. The locations of the nodes are also indicated on Fig. 10.

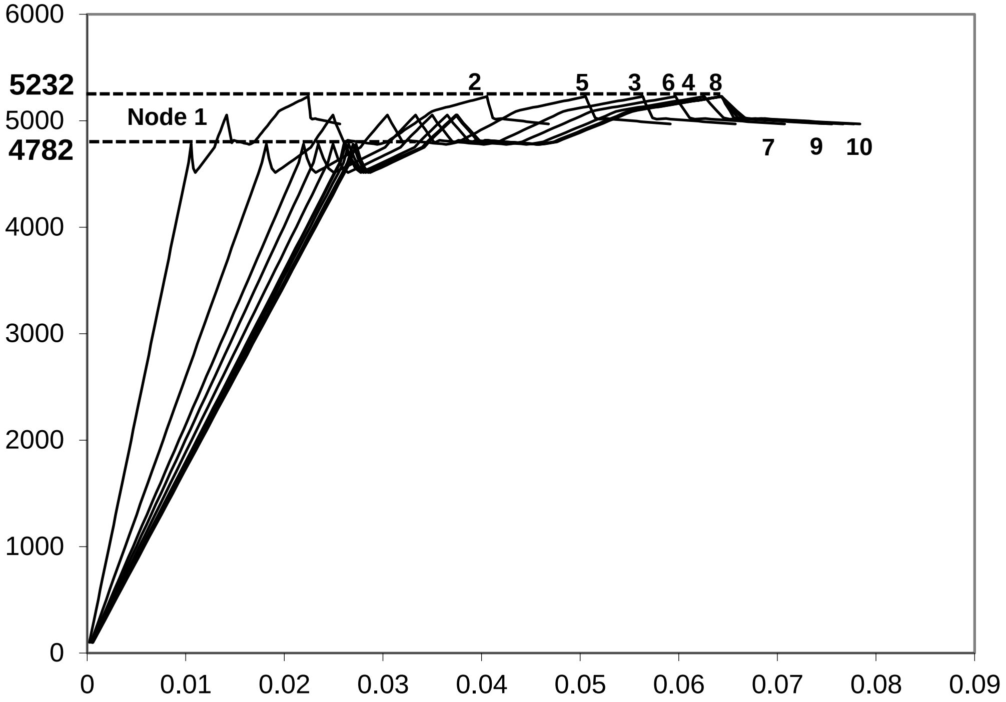

Fig. 9 The load deflection graphs of ten top layer loaded nodes of Model G2

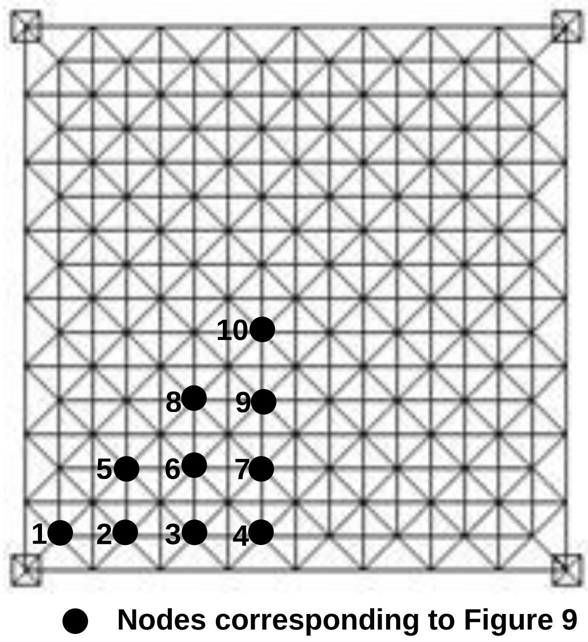

Fig. 10 Ten loaded nodes of the top layer of Model G2

Table 4
calculated kinetic energies and their corresponding velocities for ten nodes of Model G2 indicated in Fig. 10

Node	U (N.m)	*v* (m/s)
1	12.30	0.225
2	23.45	0.310
3	34.90	0.378
4	40.70	0.409
5	29.85	0.350
6	35.40	0.381
7	38.35	0.400
8	36.05	0.385
9	36.55	0.387
10	35.70	0.383

After computing the kinetic energies, the associated velocities at the abovementioned nodes are determined with the help of Equation 3. The calculated energies and their associated velocities for the ten nodes of Model G2 shown in Fig. 10 are summarized in Table 4.

$$v = \sqrt{\frac{2Ug}{P_{snap}}} \tag{3}$$

U: Shaded area
g: acceleration of gravity (m/s^2)

In the next step a nonlinear eigen value analysis is performed and the natural frequencies of the models were calculated. The Rayleigh coefficients can then be calculated and used to obtain the damping matrix using mass matrix M and stiffness matrix K as follows:

$$C = \alpha_m M + \beta_s K \tag{4}$$

α_m and β_s are the mass and stiffness proportional damping coefficients. In order to determine Rayleigh coefficients, the natural frequencies of the first five modes of the vibration of the structures should be obtained from the eigen value analysis. In DLSTs, the damping ratios of the first and fifth modes (ζ_1 and ζ_5) can be assumed 1.5 % and 2.5% respectively[28]. Thus, the Rayleigh coefficients can be calculated as:

$$\alpha_m = 2\omega_1\omega_5(\xi_1\omega_5 - \xi_5\omega_1)/(\omega_5^2 - \omega_1^2) \tag{5}$$
$$\beta_s = 2(\xi_5\omega_5 - \xi_1\omega_1)/(\omega_5^2 - \omega_1^2)$$

where w_1 and w_5 are the natural frequencies of the first and fifth modes respectively.

Considering the above-mentioned procedure, the natural frequencies and Rayleigh coefficients of Model G2 are calculated and shown in Table 5.

Table 5
Natural frequencies and Rayleigh coefficients of Model G2

Model	w_1 (hz)	w_5 (hz)	α_m	β_s
G2	58.12	171.53	0.8575	0.0001623

In the final step, a dynamic nonlinear analysis is conducted to determine the dynamic response to snap-through. This analysis is performed on the strain configuration of the structure (Point 2 in Fig. 8) considering both geometric and material nonlinearities. In order to do this dynamic analysis, the strain configuration becomes subjected to the load P_{snap} and nodal velocities calculated previously. In this case, considering the initial conditions:

$$M\,\ddot{D}_d + C\,\dot{D}_d + K(D_d + D_{snap}) = P_{snap} \tag{6}$$

where M, C and K are dependent on static deflection D_{snap} and dynamic deflection D_d. By solving this equation of motion, the time-history graphs for each node can be obtained.

The time-history graph of the deflection of the node located at the middle of the top layer of Model G2, is shown in Fig. 11. This graph shows that progressive collapse occurs in Model G2 since the deformation is getting larger significantly. Thus, the actual maximum load is 4782 N which is 9.4 percent smaller than the one determined from the static failure analysis (5232N).

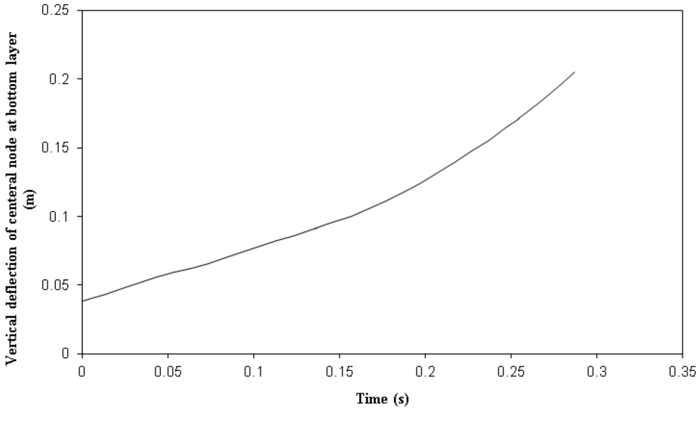

Fig. 11 Deflection curve obtained at the node located at the center of the bottom layer of Model G2 [10]

Since the results of the collapse analysis show that Model G2 has a brittle behavior due the occurrence of to snap-through, suitable methods should be utilized to convert its brittle collapse to a ductile collapse. The method of utilizing FLDs to achieve this goal is considered and explained in the next section.

2.4. Discussion of Utilizing Force Limiting Devices (FLDs) Method on Models

2.4.1. Results of applying FLDs on the top layer members of Models G1 to G5

In this section, first the effect of FLDs on the ductility and strength of Model G2 with dynamic snap-through collapse is investigated. All the members of Model G2 are P2 rods (see Table 2). The FLDs that are introduced to the members are activated when the axial load of the member P2 reaches to 85 percent of its failure load. The data of Fig. 5 shows that the failure load of member P2 is 117 kN. Therefore, the activation level of its introduced FLD is set on 99.5 kN which is 85 percent of 117kN. The axial load-deflection graphs of the member P2 and its introduced FLD are shown in Fig. 12.

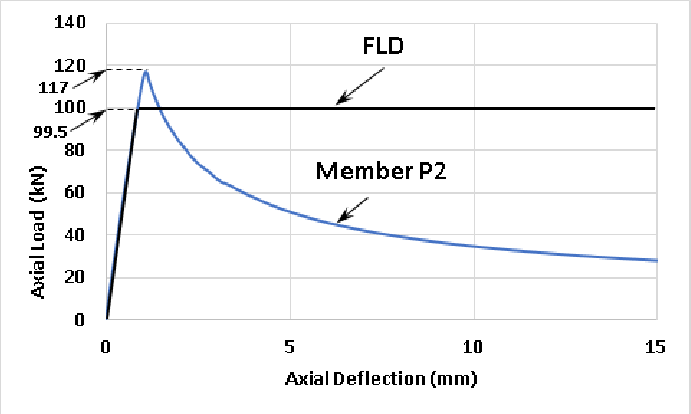

Fig. 12 Axial load-deflection of member P2 and its introduced FLD

It should be noted that FLDs are expensive devices. Therefore, they should only be installed on selected critical members. In order to identify the most critical members of the structure, the FLDs were first installed on all the members of the top layer to see which members have already been activated at the time of the collapse of Model G2. Those members then would be considered critical compression members. Placing the FLDs on all the top members not only helps identifying the critical members but also disclose the maximum ideally achievable load bearing capacity and ductility, without limiting the number of the FLDs to only critical members of the top layer.

The vertical load-displacement graphs of the original (without FLD) and modified Model G2 (with FLD on all top members) is depicted in Fig. 13. The location of the critical members in which the FLDs have been activated are shown in Fig. 14. The results of collapse analysis of modified and initial Model G2 are summarized in Table 6. In this table the ductility (μ) is computed using Equation 2.

$$\mu = \frac{\delta_u}{\delta_1} \tag{2}$$

δ_u: Ultimate deflection
δ_1: Deflection corresponding to first failure

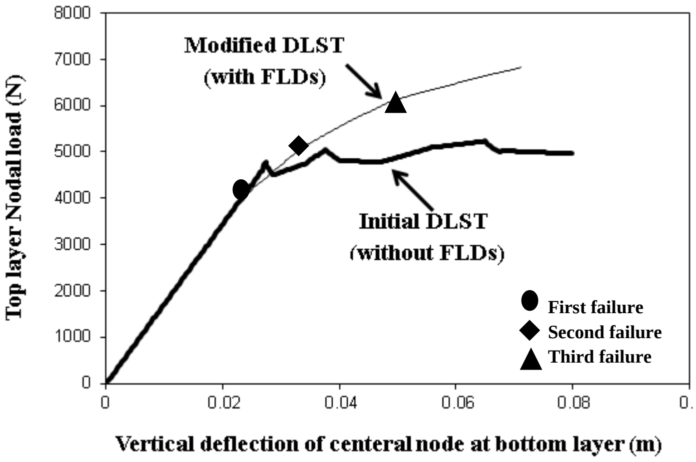

Fig. 13 Vertical load-displacement graphs of initial and modified Model G2

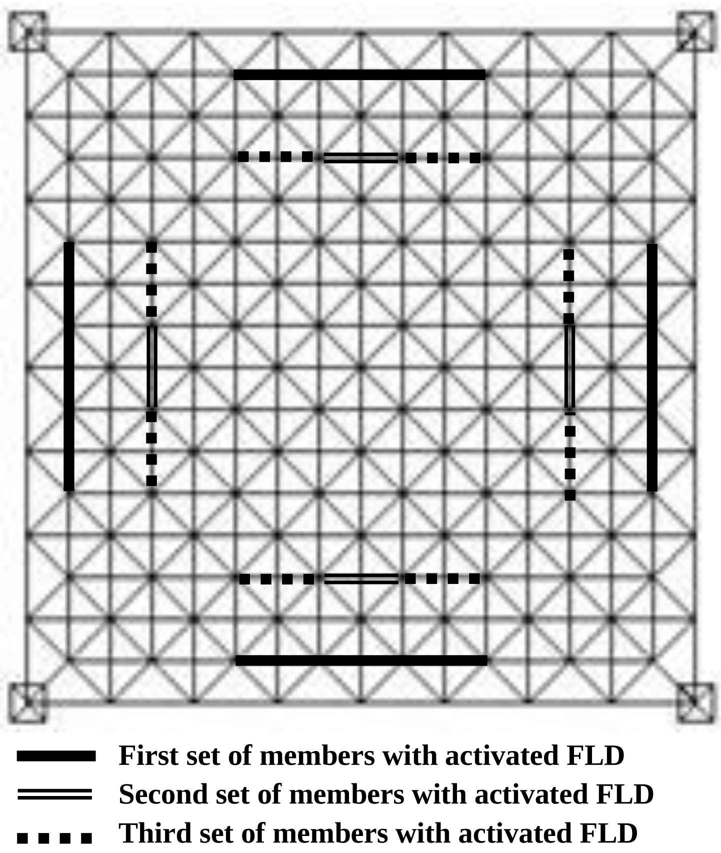

Fig. 14 Location of the critical members in which the FLDs have been activated

Table 6

Results of collapse analysis of modified DLST model G2

Maximum Load Bearing Capacity of Original DLST (N)	Maximum Load Bearing Capacity of Modified DLST (N)	Load Bearing Capacity Increase (%)	Ultimate Deflection in Central Node of Modified DLST (cm)	Central Node Deflection Corresponding to First Failure in Modified DLST (cm)	Ductility
4782	6824	42.7	7.10	2.41	2.95

The curves shown in Fig. 13 demonstrate that a significant ductility can be achieved by using FLDs on top layer members of the Model G2. While the FLDs are activated at %85 of the load bearing capacities of the members, Model G2 does not fail and it can withstand excessive plastic deformations without being collapsed. Model G2 collapses when the central node deflections reached 2.95 times of the deflection corresponding to the first failure occurred in the structures. The results of Table 6 also show that using FLDs on top layer members can increase the load bearing capacity of Model G2 by 42.7 percent. Thus, the method not only alters the collapse behavior from brittle local collapse with dynamic snap-through to a ductile type, but also significantly increases the strength of the structure.

Before discussing the effect of placing FLDs on the critical members of Model G2 it was decided to see if similar observations can be made from models with different conditions and collapse behavior. Therefore, the FLDs were introduced to all top members of Models G1, G3, G4 and G5 with overall collapse and different imperfection, support condition, and shape. The vertical load-displacement graphs of the initial and modified Models G1, G3, G4 and G5 are shown in Fig. 15. The results of the analysis are also summarized in Table 7.

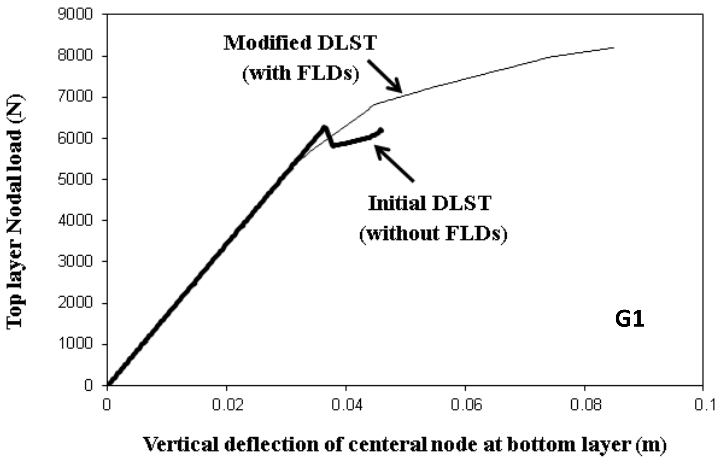

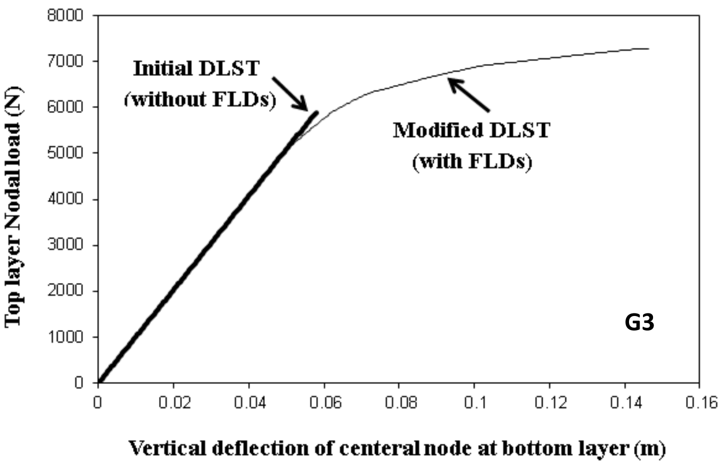

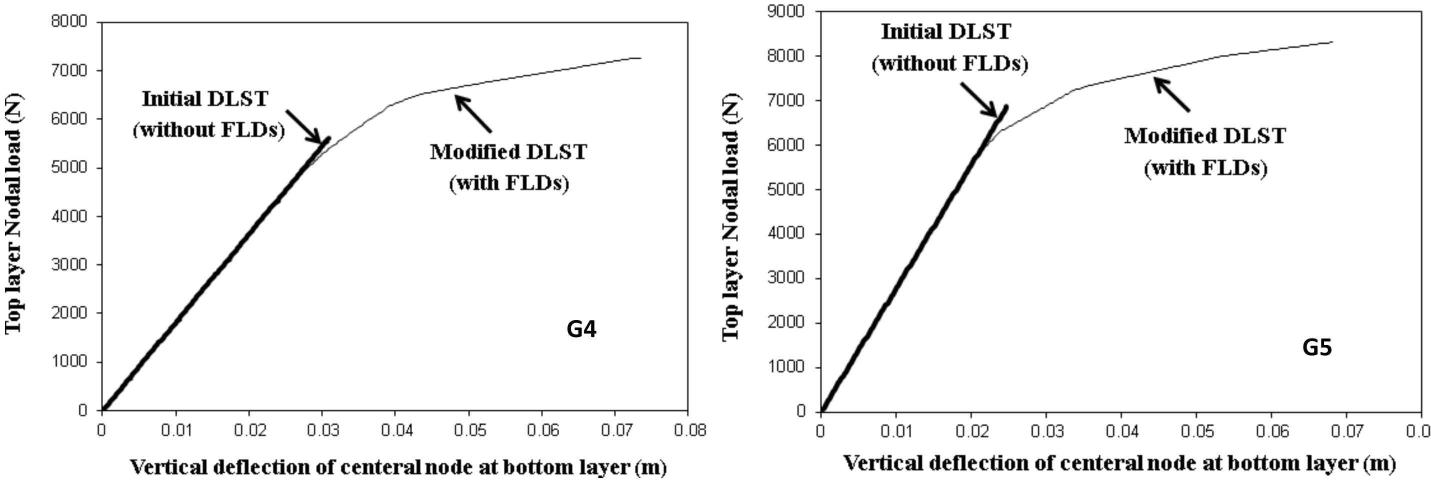

Fig. 15 Vertical load-displacement graphs of initial and modified Models G1, G3, G4 and G5

Table 7
Summary of the collapse analysis of modified DLST models G1, G3, G4 and G5

Model	Maximum Load Bearing Capacity of Original DLST (N)	Maximum Load Bearing Capacity of Modified DLST (N)	Load Bearing Capacity Increase (%)	Ultimate Deflection in Central Node of Modified DLST (cm)	Central Node Deflection Corresponding to First Failure in Modified DLST (cm)	Ductility
G1	6279	8200	30.6	8.49	3.02	2.81
G3	5794	7284	25.7	14.61	4.94	2.98
G4	5613	7266	29.4	7.35	2.63	2.80
G5	6875	8304	20.8	6.80	2.05	3.32

The graphs indicated in Fig. 15 show that a considerable ductility can be achieved by using FLDs on top layer members of the DLST models. The model with supports located at the corners shows the best results with maximum ductility of 3.317. Similar to Model G2, utilizing FLDs converts a brittle collapse into a ductile failure in the investigated models with overall collapse. The results of Table 7 show that using FLDs on the top members can increase the load bearing capacity of the models from 20.8 to 30.6 percent which are less than the capacity increase values in the Model G2 with dynamic snap through. In summary, the method can convert the collapse behavior from brittle overall collapse and snap through to a ductile failure as well as increase the strength of the structures.

2.4.2. Comparing the Results of applying FLDs on the top layer members of Models G1 to G5 with the method of overdesigning top members with undersigning bottom layer members

Here the abovementioned conclusions are compared to the results obtained from the study conducted by Rashidyan and Sheidaii [10]. As indicated previously, Rashidyan and Sheidaii [10] used the method of overdesigning the compression members with undersigning the bottom layer members of flat DLSTs to improve the collapse behavior of such structures. They showed that 30%-40% overdesign of all top and under design of bottom members would result in satisfactory ductility and load bearing capacity in models G1 to G5. The results of their study and the current study are compared in Table 8.

Table 8
The results of study performed by Rashidyan and Sheidaii (2017) and Tables 6 and 7

Model	Load Bearing Capacity Increase (%)			Produced Ductility		
	Using FLD	30% Over and under design	40% Over and under design	Using FLD	30% Over and under design	40% Over and under design
G1	30.6	10.9	7.7	2.8	1.4	1.7
G2	42.7	17.5	18.5	2.95	1.0	1.2
G3	25.7	5.3	3.2	2.98	1.38	1.81
G4	29.4	14.02	11.33	2.80	1.48	1.92
G5	20.8	11.81	5.63	3.32	1.37	1.84

The results indicated in Table 8 show that the method of using FLD on all top members can provide more load bearing capacity increase and ductility compared to the method studied by Rashidyan and Sheidaii [10] in all the investigated models.

2.4.3. Results of applying FLDs on critical top layer members of Model G2 with various member imperfection and FLD activation level

In this section, Model G2 is focused again to investigate the effect of introducing FLDs on critical members of the top layer. The analysis was performed with three various activating levels of 85, 90 and 95 percent of the load bearing capacity of the members. The critical members of Model G2 are indicated in Fig. 14. As stated previously, the critical members have been obtained from the results of collapse analysis when all the top members are equipped with FLDs. At the time of failure of Model G2, the FLDs had been activated in the critical members shown in Fig. 14 which were the most highly stressed members of the top layer. The number of the critical members in Model G2 is approximately 5 percent of all the top layer members.

The vertical load-displacement graphs of the original (without FLD) and modified models equipped with FLD are depicted in Fig. 16a. The results reported by Rashidyan and Sheidaii [10] are also indicated in Fig. 16b for comparison. The results of the comparison of the two methods are summarized in Table 9.

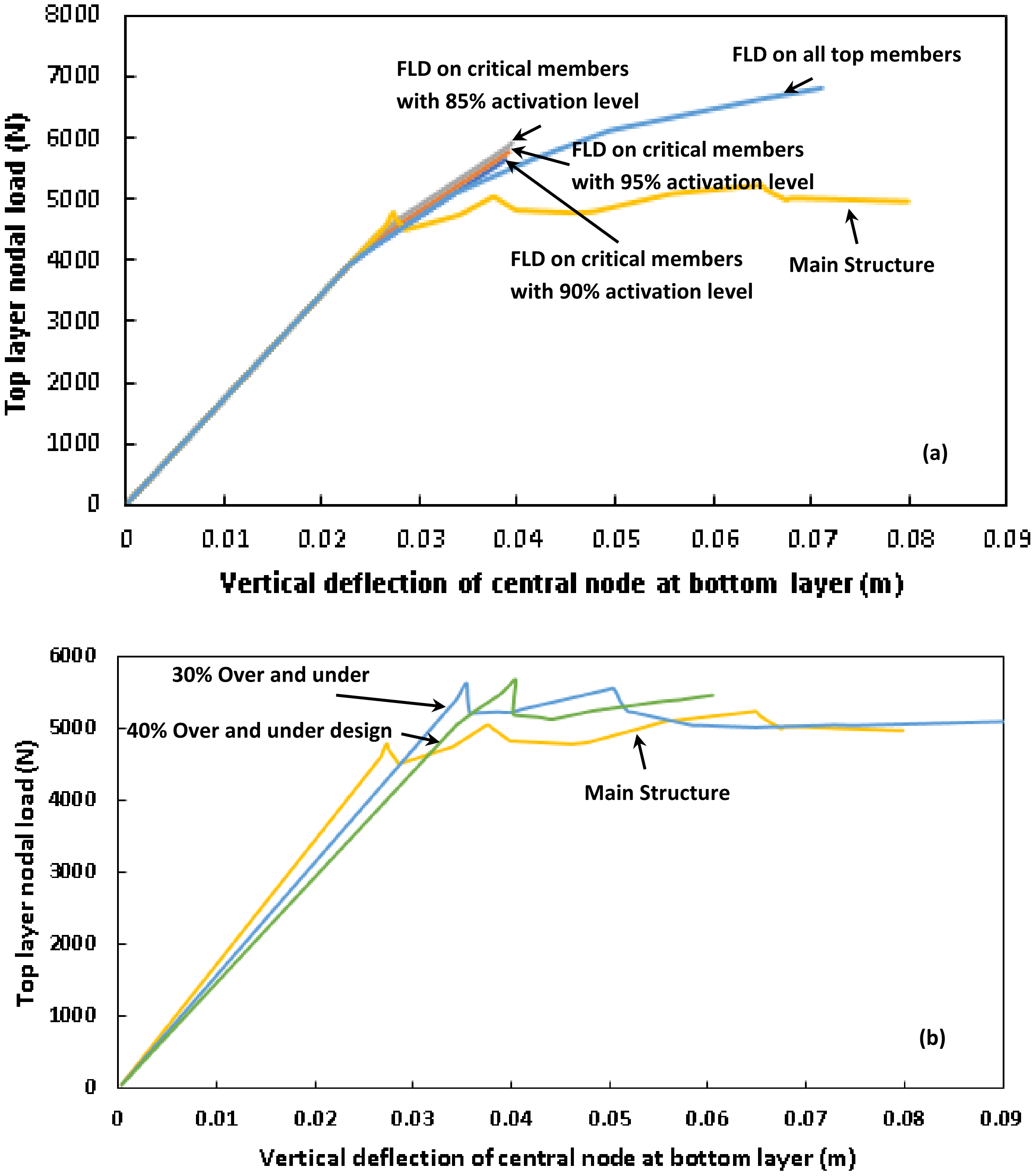

Fig. 16 (a) Vertical load-displacement graphs of the original (without FLD) and modified models with FLD activation levels pertaining to 85%, 90% and 95% of the bucking load of compression members (b) vertical deflection of central node vs. top layer nodal load for model G2 when top members are overdesigned and under designed by 30% and 40%.

Table 9
Collapse analysis summary for modified DLST model G2

Improving Method	Maximum Load Bearing Capacity of Original DLST (N)	Maximum Load Bearing Capacity of Modified DLST (N)	Load Bearing Capacity Increase (%)	Ultimate Deflection in Central Node of Modified DLST (cm)	Central Node Deflection Corresponding to First Failure in Modified DLST (cm)	Ductility
FLDs on all top members	4782	6824	42.7	7.10	2.41	2.95
FLDs on critical members with 85% activation limit		5651	18.20	3.88	2.27	1.67
FLDs on critical members with 90% activation limit		5776	20.79	3.91	2.41	1.62
FLDs on critical members with 95% activation limit		5923	23.86	3.94	2.53	1.55
30% Under and over design		5619	17.50	3.55	3.55	1
40% Under and over design		5669	18.55	4.04	3.41	1.18

The results indicated in Table 9 shows that applying FLDs on critical members provides 18.2 to 23.86% load bearing increase values which are close to those provided by the method presented by Rashidyan and Sheidaii (2017). The load bearing capacity of the model increases when the activation level become greater. The data indicated in Table 9 also shows that the ductility provided by placing the FLDs on critical members is between 1.55 to 1.67 which is significantly greater than 1 and 1.18 that are obtained from Rashidyan and Sheidaii [10]. Although all three levels of 85, 90 and 95 percent result in a considerable ductility, the achievable ductility become greater when the activation level of the FLDs is lower. The data of Table 9 shows that the ductility obtained from 85 percent activation level is 3.1 and 7.7 percent greater than those obtained from 90 and 96 percent respectively.

In addition to the effect of activating levels of the FLDs, it was decided to examine the effect of various member imperfections in Model G2. The member imperfections 0.001 to 0.004L and FLD activation levels of 85, 90 and 95% were considered. Models G2-1, G2-2, G2-3, and G2-4 have the same geometry as Model G2 but member imperfections equal to 0.001L, 0.002 L, 0.003L, and 0.004 L respectively. After assigning the FLDs to the critical top members of Models G2-1, G2-2, G2-3, and G2-4, the collapse analyses were carried out. It should be noted that the critical members have been identified using the same procedure which was mentioned previously for Model G2. The vertical load-displacement graphs of the original (without FLD) and modified models (with FLD) are shown in Fig. 17. The conclusions are indicated in Table 10.

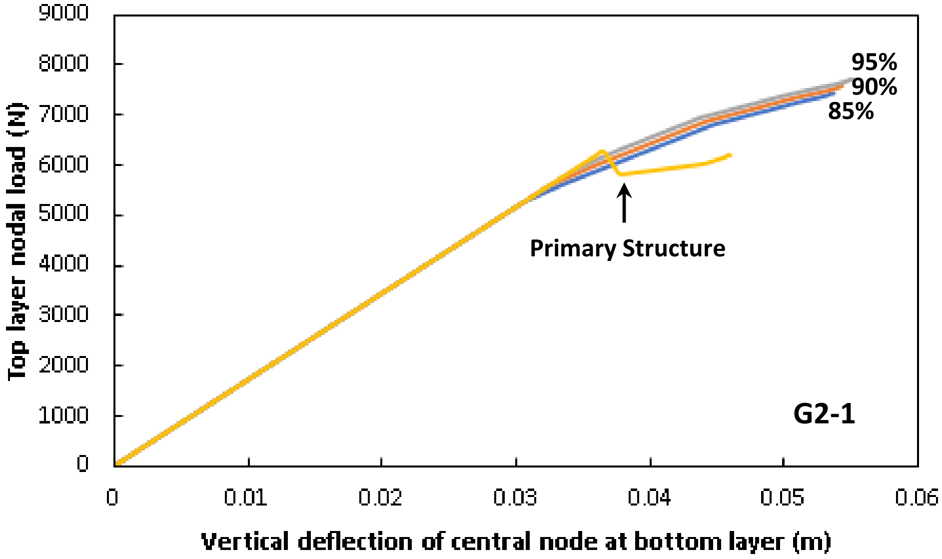

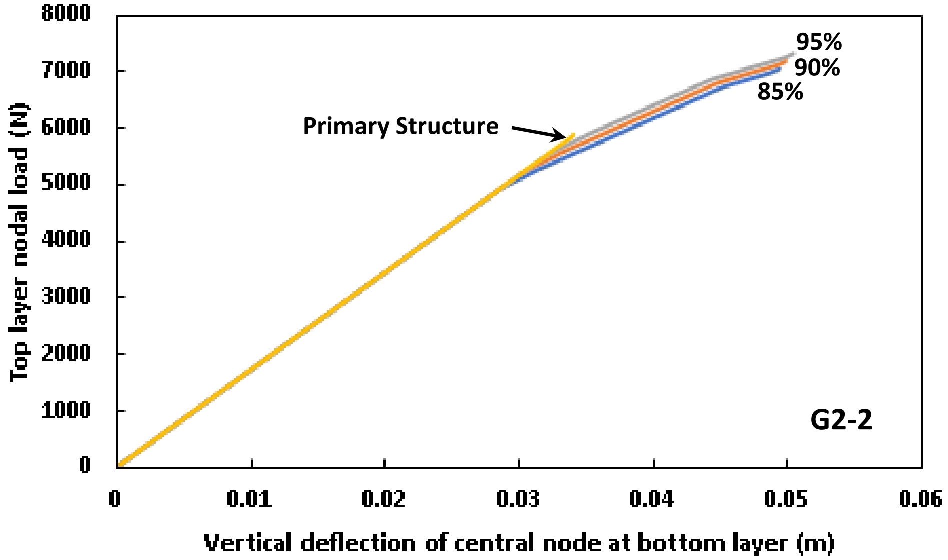

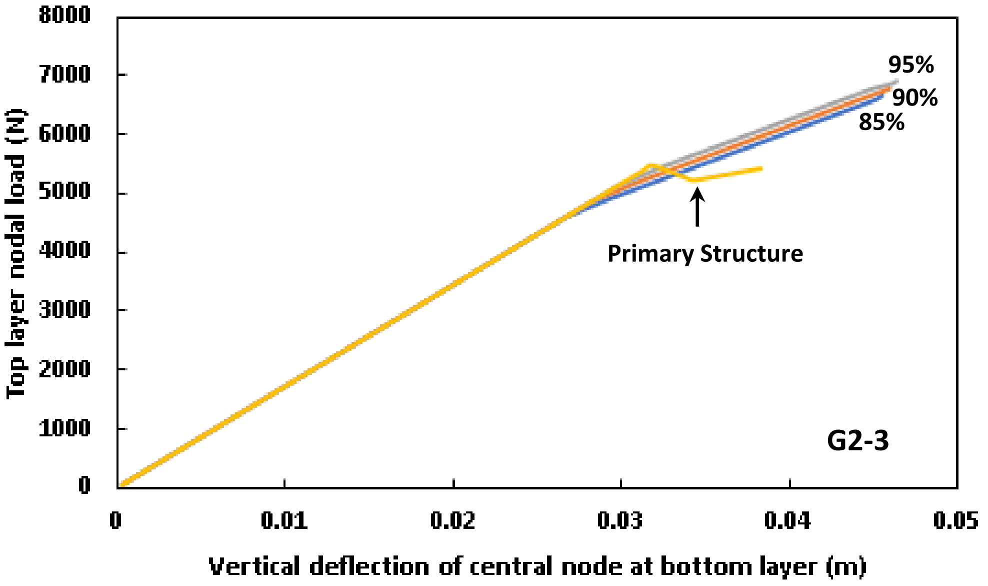

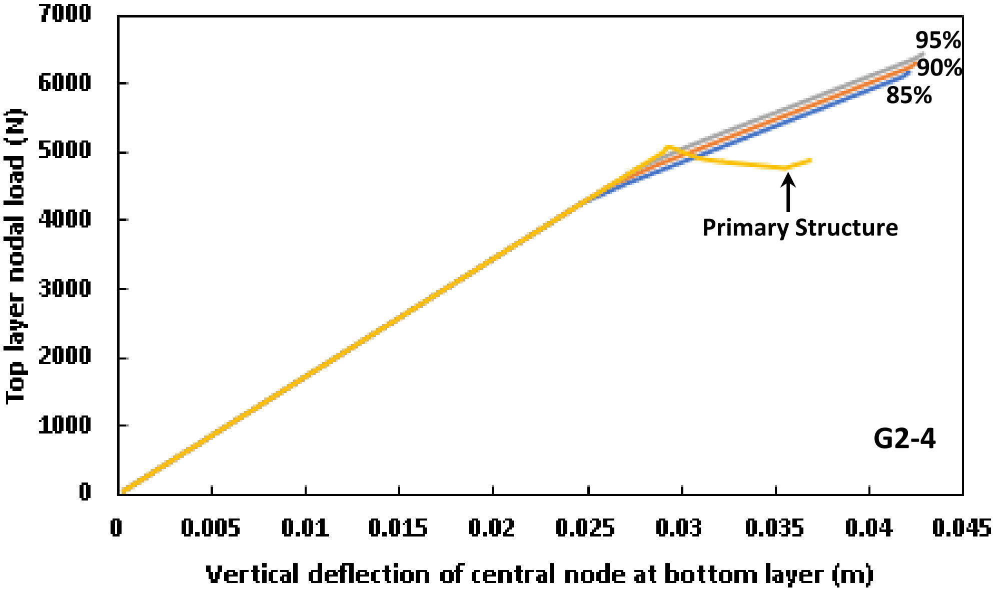

Fig. 17 Vertical load-displacement graphs of the primary (without FLD) and modified Models G2-1, G2-2, G2-3, and G2-4 with various activation levels

Table 10
Collapse analysis summary of modified DLST models G2-1, G2-2, G2-3 and G2-4

Model	Member Imperfection	FLD Activation Limit Percent	Maximum Load Bearing Capacity of Original DLST (N)	Maximum Load Bearing Capacity of Modified DLST (N)	Load Bearing Capacity Increase (%)	Ultimate Deflection in Central Node of Modified DLST (cm)	Central Node Deflection Corresponding to First Failure in Modified DLST (cm)	Ductility
G2-1	0.001 L	85	6279	7431	18.35	5.37	3.05	1.76
		90		7571	20.58	5.43	3.25	1.67
		95		7708	22.76	5.51	3.43	1.61
G2-2	0.002 L	85	5879	7050	19.92	4.93	2.82	1.75
		90		7188	22.27	4.98	3.02	1.65
		95		7306	24.27	5.03	3.17	1.59
G2-3	0.003 L	85	5478	6670	21.76	4.55	2.67	1.71
		90		6782	23.80	4.60	2.84	1.62
		95		6910	26.14	4.64	2.96	1.58
G2-4	0.004 L	85	5079	6169	21.46	4.21	2.47	1.70
		90		6285	23.74	4.24	2.61	1.62
		95		6440	26.80	4.29	2.76	1.56

First the curves shown in Fig. 17 show that when the imperfections of the members are changed from 0.005 L in Model G2 to imperfections between 0.001 L and 0.004 L in Models G2-1 to G2-4, the collapse modes are not dynamic snap-through anymore. They are overall collapse, instead. Second, the curves shown in Fig. 17 show that the method of applying FLD on critical members can convert the brittle collapse to a ductile collapse for all models with imperfections between 0.001 L and 0.004 L. The results indicated in Table 10 shows that the method can increase the load bearing capacity of the models between 18.35 to 26.8%. The provided ductility of the modified models is between 1.54 to 1.74 which shows a significant ductility. These ranges of increase in load bearing capacity and ductility are very close to those obtained from model G2 with dynamic snap through. The data of Table 10 also shows that the provided ductility in models with smaller member imperfection is slightly greater than those provided in models with larger member imperfection. In addition, the ductility provided by FLDs with various levels of activation looks different based on data indicated in Table 10. A comparison of the ductility obtained from activation levels of 85, 90 and 95 is demonstrated in Table 11. The data of Table 11 shows that the achievable ductility from FLDs with activation level of 85 percent is 4.9 to 6.1 and 8.2 to 10.1 greater than those obtained from 90 and 95 percent respectively. Therefore, an activation level of 85 percent has superiority over 90 and 95 percent. The activation level of 85 percent has two more advantages. First, it has a reasonable clearance with respect to the failure load of the member which leads to more safety. This clearance assures that the FLD is activated before the member reaches to its failure load. Second his level is far enough from the level of service loads and it won't be activated on slight variations of the service loads.

Table 11
Comparison of ductility obtained from activation levels of 85, 90 and 95percent

(1) Model	(3) Ductility (%85 activation level)	(4) Ductility (90% activation level)	(5) Ductility (95% activation level)	(6) $\frac{(3)-(4)}{(4)} \times 100$	(7) $\frac{(3)-(5)}{(5)} \times 100$
G2-1	1.76	1.67	1.61	5.4	9.3
G2-2	1.75	1.65	1.59	6.1	10.1
G2-3	1.71	1.62	1.58	5.6	8.2
G2-4	1.70	1.62	1.56	4.9	9.0

In summary, the presented results show that the method of applying FLDs on the critical members of the DLSTs not only can provide ductility to the structures with dynamic snap-through but also can increase the ductility and load bearing capacity when the imperfection of the members are between 0.001 L and 0.005 L and the activation level of the FLDs is between 85 and 95 percent.

3. Conclusion

The method of using FLDs on critical members of the DLSTs is a proper method to improve the collapse behavior of these structures against progressive collapse. In the current study, first the critical members of a DLST were identified and the FLDs were installed on them. Then the collapse analysis was performed with three different FLD activation levels. The results showed that applying FLDs on critical members provided 18.2 to 23.86% load bearing increases and ductility values between 1.55 to 1.67. The results were compared with the method of overdesigning the top compression members with undersigning the bottom layer tension members of flat DLSTs. The FLD method was then applied on four DLSTs with the same geometry but made of members with different geometrical imperfections. The results showed that when the imperfections of the members in the unequipped models were changed from 0.005 L to values between 0.001 L and 0.004 L the collapse modes were converted to overall collapse from a risky dynamic snap-through mode. The results also showed that the method of applying FLD on critical members could convert a brittle overall collapse to a ductile collapse for all models with imperfections between 0.001 L and 0.004 L. The obtained data showed that the method could increase the load bearing capacity of the models between 18.35 and 26.80%. The ductility of the models was also obtained withing the range of 1.56 and 1.7. The data also confirmed that the provided ductility in models with smaller member imperfection was slightly greater than those provided in models with larger member imperfection. In addition, the comparison of the ductility obtained from FLD activation levels of 85, 90 and 95 showed that the achievable ductility from FLDs with activation level of 85 percent is 4.9 to 6.1 and 8.2 to 10.1 greater than those obtained from 90 and 95 percent respectively. Therefore, an activation level of 85 percent showed superiority over 90 and 95 percent in providing ductility for the structure. The activation level of 85 percent, however, has two more advantages. First, it has a reasonable clearance with respect to the failure load of the member which result in more safety for the entire structure. This clearance assures that the FLD is activated before the member reaches to its failure load. Second his level is far enough from the level of service loads and it won't be activated on slight variations of the service loads. In summary, the presented results show that the method of applying FLDs on the critical members of the DLSTs not only can provide significant ductility to the structures with dynamic snap-through and overall collapse but also can increase the load bearing capacity when the imperfection of the members are between 0.001 L and 0.005 L and the FLDs activation level is set between 85 to 95 percent.

References

[1] L. Schmidt, K. Cogan, P. Morgan, A. Omeagher, Ultimate load behaviour of a full scale space truss., Proceedings of the Institution of Civil Engineers. 69 (1980) 97–109.

[2] L.C. Schmidt, P. Morgan, A. Hanaor, Ultimate load testing of space trusses, Journal of the Structural Division. 108 (1982).

[3] C. Vatansever, Investigation of buckled truss bars of a space truss roof system, Engineering Failure Analysis. 106 (2019).

[4] A. Hanaor, C. Marsh, G.A.R. Parke, Modification of Behavior of Double-Layer Grids: Overview, Journal of Structural Engineering. 115 (1989) 1021–1037.

[5] M.R. Sheydaii, A. K, B. A.a.d, P. G.a.r, An investigation into the collapse behaviour of double-layer space trusses, 27 (2003) 0–0.

[6] R.B. Malla, P. Agarwal, R. Ahmad, Dynamic analysis methodology for progressive failure of truss structures considering inelastic postbuckling cyclic member behavior, Engineering Structures. 33 (2011) 1503–1513.

[7] M. Ferraioli, Dynamic increase factor for pushdown analysis of seismically designed steel moment-resisting frames, Int J Steel Struct. 16 (2016) 857–875.

[8] Y. Li, X. Lu, H. Guan, P. Ren, Numerical investigation of progressive collapse resistance of reinforced concrete frames subject to column removals from different stories, Advances in Structural Engineering. 19 (2016) 314–326.

[9] A.Ch. Salmasi, M.R. Sheidaii, Assessment of eccentrically braced frames strength against progressive collapse, Int J Steel Struct. 17 (2017) 543–551.

[10] S. Rashidyan, M.-R. Sheidaii, Improving double-layer space trusses collapse behavior by strengthening compression layer and weakening tension layer members, Advances in Structural Engineering. 20 (2017) 1757–1767.

[11] L.C. Schmidt, A. Hanaor, Force Limiting Devices in Space Trusses, Journal of the Structural Division. 105 (1979) 939–951.

[12] A. Hanaor, L.C. Schmidt, Space Truss Studies with Force Limiting Devices, Journal of the Structural Division. 106 (1980) 2313–2329.

[13] G.A.R. Parke, A novel soft member for space-trusses, in: SPACE STRUCTURES 4, VOL 1, UNIV SURREY, GUILDFORD, ENGLAND, 1993: pp. 116–126.

[14] A. El-Sheikh, Effect of force limiting devices on behaviour of space trusses, Engineering Structures. 21 (1999) 34–44.

[15] L. Bai, Y. Zhang, Nonlinear dynamic behavior of steel framed roof structure with self-centering members under extreme transient wind load, Engineering Structures. 49 (2013) 819–830.

[16] C.H. Kim, W.T. Chae, A Study on the Development of Force Limiting Devices of Cross-Section Cutting Types, Journal of Korean Society of Steel Construction. 27 (2015) 77–85.

[17] M. Poursharifi, K. Abedi, M. Chenaghloua, 05.32: Experimental and numerical study on the collapse behavior of an all-steel accordion force limiting device, Ce/Papers. 1 (2017) 1315–1324.

[18] K. Abedi, S.R. Kolachahi, Investigation into the double-layer barrel vault space structure resistance to progressive collapse, Proceedings IRF2018: 6th International Conference Integrity-Reliability-Failure, Lisbon, Portugal. (2018).

[19] B. Shekastehband, The influences of force-limiting devices and high-stiffness cables on behavior of tensegrity structures, Arch Appl Mech. 88 (2018) 2293–2316.

[20] K. Abedi, M.R. Sheidaii, Investigation of Double-layer Grid Space Structurer Resistance to Progressive Collapse, Computational Methods in Engineering. 26 (2007) 149–164.

[21] M.R. Sheidaii, G.A.R. Parke, K. Abedi, A. Behravesh, Dynamic snap-through buckling of truss-type structures, International Journal of Space Structures. 16 (2001) 85–93.

[22] G.S. Ramaswamy, M. Eekhout, Analysis, Design and Construction of Steel Space Frames, Thomas Telford, 2002.

[23] SAP 2000, Computers and Structures Inc., Berkeley, CA.

[24] Minimum Design Loads and Associated Criteria for Buildings and Other Structures (ASCE/SEI 7-16), American Society of Civil Engineers, Reston, Virginia, USA.

[25] Specification for Structural Steel Buildings (ANSI/AISC 360-16) | American Institute of Steel Construction,

[26] LUSAS, Surrey, UK.

[27] M.R. Sheidaii, S. Gholizadeh, An investigation into the collapse behavior of double-layer space truss using neural networks, in: 7th International Congress on Civil Engineering, 2006.

[28] K. Abedi, G.A.R. Parke, Progressive Collapse of Single-Layer Braced Domes, International Journal of Space Structures. 11 (1996) 291–306.

Advanced Steel Construction – Vol. 18 No. 4 (2022) 818–825
DOI:10.18057/IJASC.2022.18.4.9

EXPERIMENTAL STUDIES OF THE SORBITE STAINLESS STEEL PLUG-PIN SCAFFOLD JOINT

Nan Xie [1], Tao Du [1, *], Fei-Fei Qin [2] and Peng-Sheng Geng [3]

[1] *School of Civil Engineering, Beijing Jiaotong University, Beijing 100044, China*
[2] *Cost Management Department, Zhongliang Holdings Group Shandong Regional, Jinan 250000, China*
[3] *Engineering Department, China LVFA Investment Group Shandong Regional, Qingdao 266000, China*
** (Corresponding author: E-mail: dutao347@sina.com)*

ABSTRACT

Systematic experimental studies were performed for the purpose of obtaining the material properties of cold-formed sorbite stainless steel and the mechanical parameters of plug-pin joint. As a new type of material, the scaffold made of sorbite stainless steel has the advantages of convenient construction, high strength and stainless steel. The static tensile tests for S500 sorbite stainless steel investigating the material characteristics of plug-pin joint were carried out. The bending moment, the compressive force, the tensile force and the shear force were applied to the joint respectively. To get the failure modes and moment-rotation (or load-displacement) curves, the joint behavior, including the semi-rigidity between the ledger and the standard, compression and shear of the standard, and the tension of the ledger joint were studied. The result can determine the load-bearing capacity and the performance of the joint. The joint stiffness was determined according to different methods and four models were proposed to describe the bending behavior. By analyzing the different modes of joint failure, the weak part can be determined to provide basis for actual joint design.

ARTICLE HISTORY

Received:	13 April 2022
Revised:	20 May 2022
Accepted:	22 May 2022

KEYWORDS

Sorbite stainless steel;
Plug-pin joint;
Bending model;
Stiffness;
Strength

1. Introduction

Scaffold system is a temporary structure commonly used to support workers, materials and buildings during construction. Recently, many scaffold collapse accidents have occurred all over the world, which may not only cause project delay but also lead to a large number of casualties [1, 2]. The scaffold collapse occurred at a construction site in China as shown in Fig. 1. Therefore, the safety of scaffold system is more and more widely concerned.

Fig. 1 Scaffold collapse at a construction site in China

The behavior of joint has significant effects on the overall properties of scaffold system. It is necessary to deeply study the mechanical behavior of scaffold joint. The behavior of joint is complex, mainly due to the rapid assembly of scaffold system in construction and the connection of components at different angles. The joints are the weakest components in the scaffold system, and structural components are less likely to be damaged than the connections between joints [3, 4]. In the scaffold system, since the joint plays the role of connecting the standard, ledger and brace and the mechanical behavior of the joint is not rigid or hinge but semi-rigid, the stiffness of the joint has a significant impact on the bearing capacity of the scaffold system [5-8]. Therefore, in order to avoid the collapse of scaffold system, it is necessary to analyze the connection characteristics of joints in detail. Laboratory tests and numerical simulations are the important ways to obtain the mechanical properties of the joints.

It is the most important problem to determine performance of the joints for studying the bearing capacity of scaffold system. There are many types of scaffold joints, including coupler joints, cuplock joints, mortise-tenon joints and wedge joints, etc. Many researchers have done a lot of research on them and achieved significant results. Jia et al. [9] conducted experimental research on the slip stiffness and rotational stiffness of right-angle coupler joints, and obtained the failure modes. Several tests have been conducted on the performance of couplers under cyclical loads, and obtained the influence of looseness on the bearing capacity through tests and calculations [10-12]. Chandrangsu and Rasmussen [13] performed experiments on the behavior of coplock joints and proposed to use the trilinear moment-rotation curve to describe the stiffness of the joints. For a mortise-tenon joint, a series of frame experiments were carried out. The results showed that compared with the fastener scaffold, the mortise-tenon scaffold had significant advantages in the mechanical properties of the joints and the bearing capacity of the frame [14]. Peng et al. [15] investigated the effects of different parameters such as number of stories, ground heights and joint positions on the behavior of spigot joints, and determined the corresponding joint stiffness. Bong et al. [16] conducted tests on the repeatedly used wedge joints, and obtained initial stiffness by probability analysis. The experiments were carried out on the ringlock joints under different forms of forces, and the behavior and the load-bearing capacity were obtained [17]. Zhao et al. [18] and Dong et al. [19] studied the mechanical properties of socket joints and the overall performance for the scaffold by tests and finite element numerical analysis. Chen and Zhao [20] proposed a new numerical method that can be used in analysis of joint stiffness, and discussed the influence of splice joint stiffness on the ultimate bearing capacity of modular scaffold. Liu et al. [21] investigated the mechanical performance of the plug-pin joints based on the visual system, and obtained the joint stiffness corresponding to different forms of loads by fitting method. As a new type of material, the scaffold made of sorbite stainless steel has the advantages of convenient construction, high strength and stainless steel. At present, there is little research on the behavior of plug-pin joints made of sorbite stainless steel, which are widely used to build temporary stands and stages.

In this paper, the mechanical behavior of sorbite stainless steel plug-pin joints (Fig. 2) was comprehensively studied with experiments. The S500 sorbite stainless steel material used in this study was 12Cr14Ni2 [22]. The properties of the new material used to make joint components were obtained by the static tensile tests. Tests were performed on the joints under different forms of loads, including bending moment, tension, compression and shear force, to determine the connection performance and load-bearing capacity. Moreover, the weak part in the plug-pin joint was determined.

2. Material test of sorbite stainless steel

For the plug-pin joints, except that the wedge is made of cast iron, and the rest are made of sorbite stainless steel. In order to obtain the material properties of sorbite stainless steel made into the main joint components, static tensile tests were carried out on 8 groups of specimens. A 25cm long pipe section was cut from a batch of the joint element. Two arc specimens were cut longitudinally at 90° positions on both sides of the weld. Schematic diagram of the specimen is shown in Fig. 3. Vernier caliper was used to measure the dimensions of each test specimen. The statistical results are shown in Table 1. After the specimens were measured, a strain gauge was pasted at the center point of concave and convex of each longitudinal arc specimen (Fig. 4).

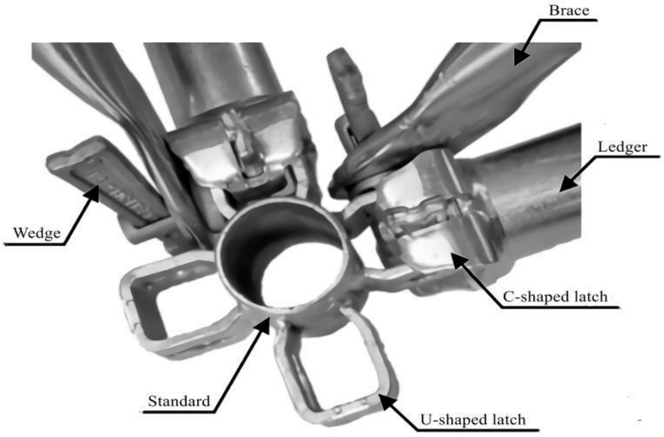

Fig. 2 Components of a plug-pin joint

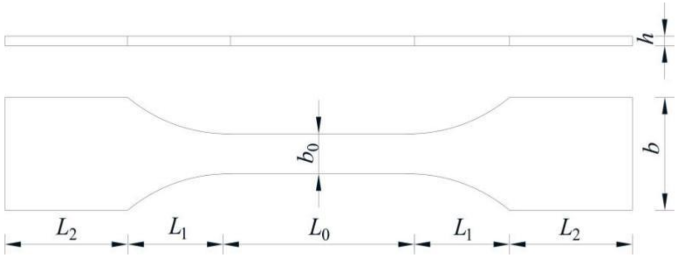

Fig. 3 The schematic diagram of specimen

Table 1
Measured dimensions of specimens

Specimen NO.	Dimensions (mm)					
	b_0	L_0	L_1	L_2	L	h
T48-1	10.1	50.1	25.6	40.9	157.4	2.4
T48-2	10.3	50.4	25.6	40.6	157.1	2.2
T48-3	10.0	50.0	25.4	40.9	157.1	2.3
T48-4	10.1	50.4	25.5	40.7	157.3	2.3
T48-5	10.1	50.5	25.5	40.7	157.3	2.4
T48-6	10.2	50.1	25.6	40.8	157.3	2.5
T48-7	10.1	50.5	25.5	40.6	157.1	2.4
T48-8	9.9	50.3	25.4	40.8	157.3	2.4

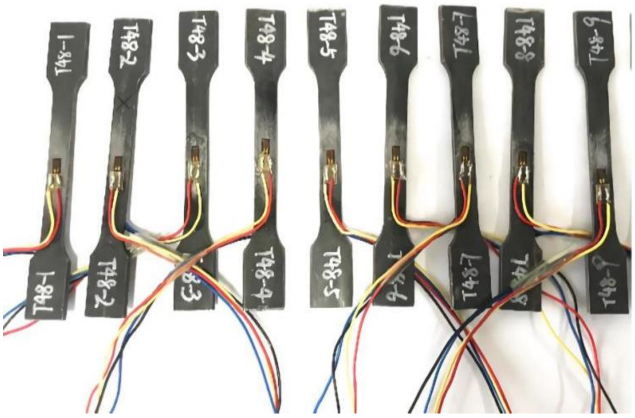

Fig. 4 Specimens with strain gauges

The equipment used for loading was WAW200 microcomputer controlled electro-hydraulic servo universal testing machine. Before the strain reached 2%, the loading rate was 0.2mm/min. When the strain reached 2%, the deformation rate accelerated with the increase of tensile force. The loading rate was changed to 0.5mm/min until the specimen was failure. Fig. 5 presents the tensile test setup before loading.

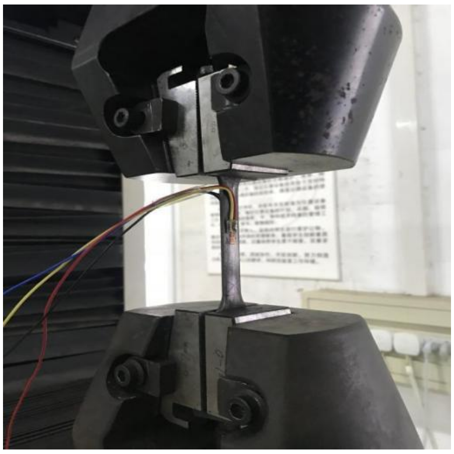

Fig. 5 Tensile test setup

Eight stress-strain curves and corresponding average curve were obtained through the tests (Fig. 6). As seen, a nonlinear stress-strain relationship was observed. As the strain increased, the slope of the curve decreased gradually. After the strain gauge fell off, the stress still continued to increase, indicating that the material has obvious strain hardening. The test results of material properties for specimens are presented in Table 2. Where, E is the elastic modulus, f_y is the yield strength, f_u is the ultimate strength.

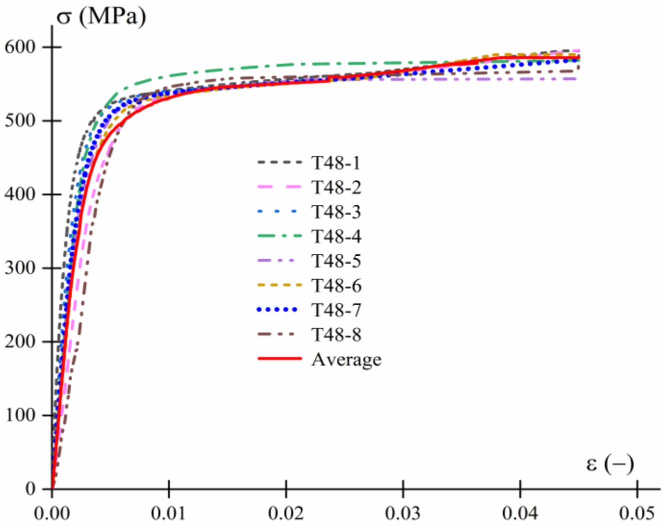

Fig. 6 Stress-strain characteristics of the material

Table 2
Material characteristics of sorbite stainless steel

Specimen NO.	E (GPa)	f_y (MPa)	f_u (MPa)
T48-1	194	509	594
T48-2	197	491	596
T48-3	181	510	585
T48-4	189	530	582
T48-5	178	499	552
T48-6	207	495	589
T48-7	206	509	583
T48-8	197	518	600
Average	194	508	585

3. Test of joint

The plug-pin joint is mainly composed of C-shaped latch, U-shaped latch and wedge. A C-shaped latch is welded to the ledger end, which has upper and lower sockets. The U-shaped latch is welded on the surface of the standard. And the wedge is a steel plate part used to connect the C-shaped latch to the U-shaped latch. The detailed dimensions of these main elements are shown in Fig. 7.

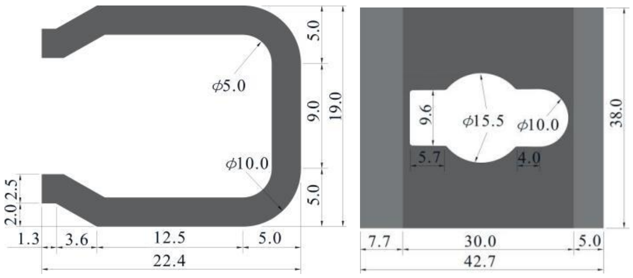

(a) U-shaped latch

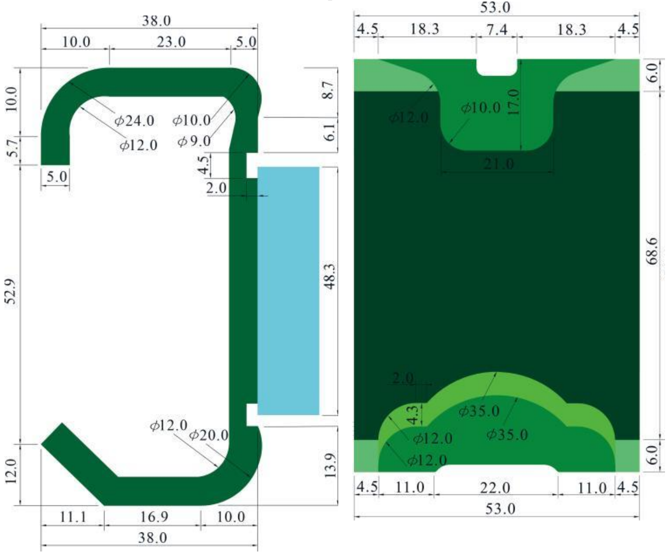

(b) C-shaped latch

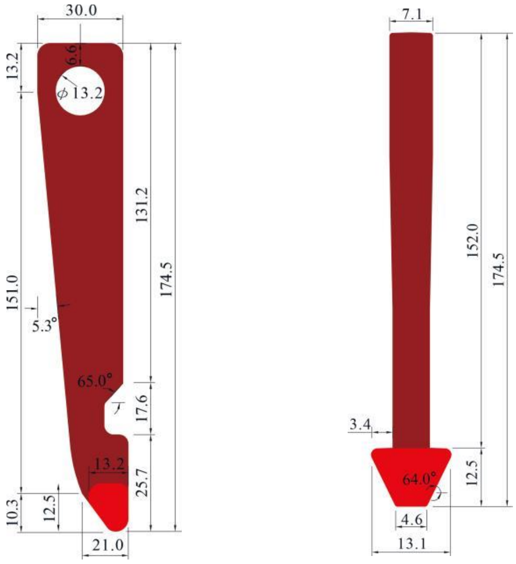

(c) Wedge

Fig. 7 The detailed dimensions of the main elements (mm)

The plug-pin joint was tested under different forms of loads including bending moment, tension, compression and shear force. The circular section size of the standard and the ledger pipe is Φ48.3 mm×2.2 mm. The samples adopted in each test were the same material that have not been used. Tests were carried out under displacement control until the specimen was failure or the force increased no more.

3.1. Joint bending test

Positive and negative bending tests were conducted on plug-pin joints to obtain the rotational performance. Firstly, the lower end of the standard was fixed with the support. Secondly, fixing the support with the testing machine by M12 high-strength bolts. Finally, the pressure head of the testing machine was pressed on the ledger. The rotational stiffness between standard and ledger varies with the rotational direction. For positive bending test (Fig. 8(a)), the bending moment M_P was generated by applying force F_P on the ledger. For negative bending test (Fig. 8(b)), the bending moment M_N was generated by applying force F_N on the ledger.

In order to measure the rotation angle, four Linear Variable Differential Transformers (LVDTs) were adopted to measure the displacement of standard and ledger in the test. The schematics of the load and LVDTs arrangement for the positive and negative bending tests are given in Figs. 8(c) and 8(d). Displacement controlled loading was adopted in the tests, and the loading rate was 0.5 mm/min. Preloading was carried out before the test began.

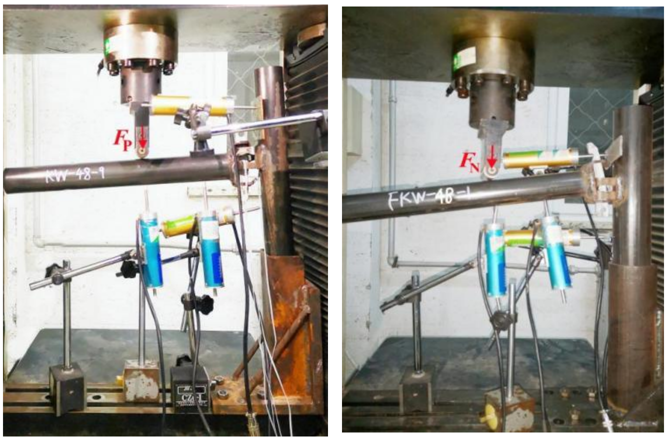

(a) Test setup of positive bending (b) Test setup of negative bending

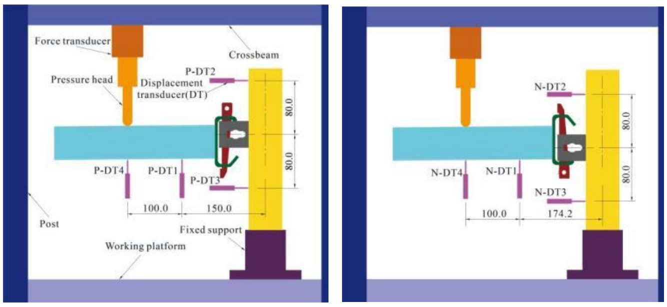

(c) Layout of LVDTs for positive bending (d) Layout of LVDTs for negative bending

Fig. 8 Bending test configuration and LVDTs locations (mm)

The calculation formula for the positive bending moment M_P is given by

$$M_P = F_P L_P \tag{1}$$

Where F_P is the vertical concentrated load at the loading point of the ledger, and L_P =250.0 mm is the distance from the loading point to the standard pipe center.

The calculation formula for the negative bending moment M_N is given by

$$M_N = F_N L_N \tag{2}$$

Where F_N is the vertical concentrated load at the loading point of the ledger, and L_N =374.2 mm is the distance from the loading point to the standard pipe center.

The formula for calculating the rotation angle θ can be determined as follows

$$\theta = \arctan\left(\frac{\Delta_4 - \Delta_1}{d_{14}}\right) - \arctan\left(\frac{\Delta_2 - \Delta_3}{d_{23}}\right) \tag{3}$$

Where for positive bending test, Δ_1, Δ_2, Δ_3, Δ_4 are the displacements of transducers P-DT1 to P-DT4, d_{14} is the distance between transducers P-DT1 and P-DT4, and d_{23} is the distance between transducers P-DT2 and P-DT3; for negative bending test, Δ_1, Δ_2, Δ_3, Δ_4 are the displacements of transducers N-DT1 to N-DT4, d_{14} is the distance between transducers N-DT1 and N-DT4, and d_{23} is the distance between transducers N-DT2 and N-DT3.

According to Equation (1), Equation (2) and Equation (3), the bending moment M of each test and its corresponding rotation angle θ were obtained, from which the M-θ curve can be drawn.

Two failure modes occurred in the positive bending test (Fig. 9) and one failure mode occurred in the negative bending test (Fig. 10). As shown in Fig. 9(a), the joint failure mode I in the positive bending test was that the C-shaped latch at the contact position with the wedge. The fracture occurred in the C-shaped latch and the wedge presented obvious plastic deformation at the contact areas. The fracture of C-shaped latch is mainly because the C-shaped latch is formed by cold bending of sorbite stainless steel plate, and it is relatively weak in the cold bending position. As shown in Fig 9(b), the joint failure mode II in the positive bending test was that the surface of the standard at the lower edge of the U-shaped latch was squeezed and concave by the C-shaped latch and the lower edge of the U-shaped latch presented obvious plastic deformation at the contact position. The concave surface occurred is mainly because the stress point changes after the C-shaped latch contacts standard pipe surface, and the contact position of the standard becomes the main stress point. Among the nine groups of specimens, KW48-2 belonged to failure mode II, and the rest belonged to failure mode I. The failure mode was the wedge buckling, which was obvious for the negative bending test (Fig. 10). No significant change was observed in the weld area connecting the U-shaped latch and the standard in both the positive bending test and the negative bending test.

(a) Failure mode I

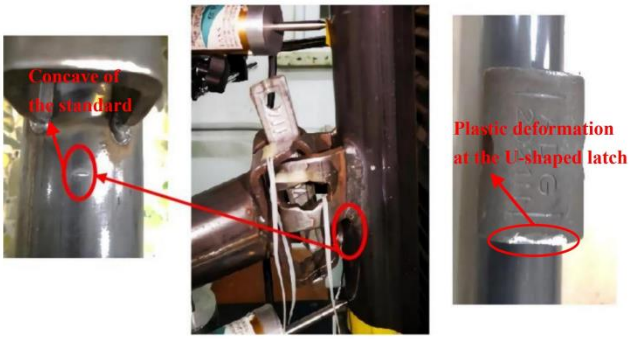

(b) Failure mode II

Fig. 9 Failure behavior after positive bending test

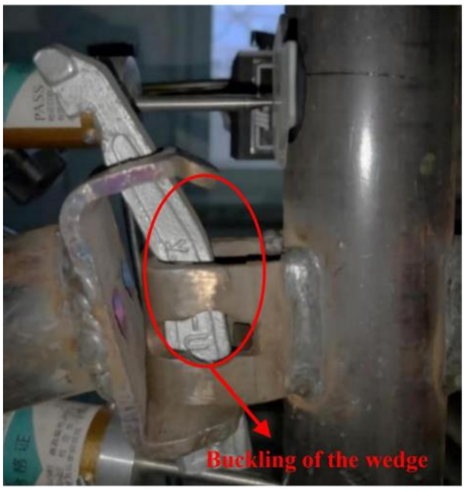

Fig. 10 Failure behavior after negative bending test

According to nine groups of bending test results, the bending moment-rotation curves and the average curve of the joint were obtained (Fig. 11). As can be seen from Fig. 11, the plug-pin joint has non-linear moment- rotation curves. Because of the asymmetrical nature, the plug-pin joint presents different behaviour under positive and negative rotations. The ultimate bearing capacity and rotational stiffness of the positive bending are greater than those of the negative bending.

3.2. Joint tensile test

The tensile test was performed to obtain the tensile performance and failure mode. In order to smoothly conduct the test, two steel bars with a diameter of 16 mm instead of the ledgers were welded on the C-shaped latches (Fig. 12). The constant displacement of each test was increased by 0.5 mm/min until the specimen was completely damaged. Preloading was carried out before the test began.

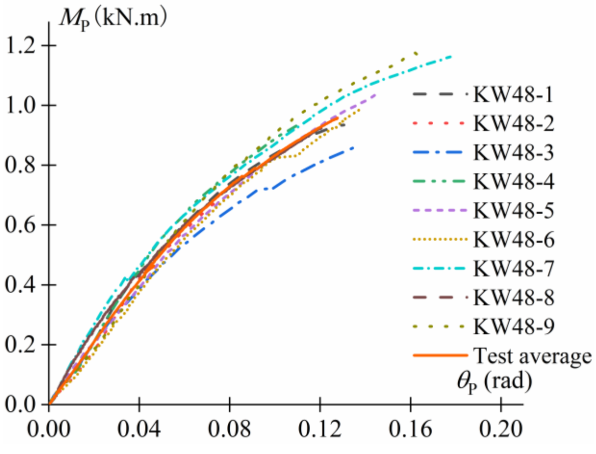

(a) Moment-rotation curves for positive bending test

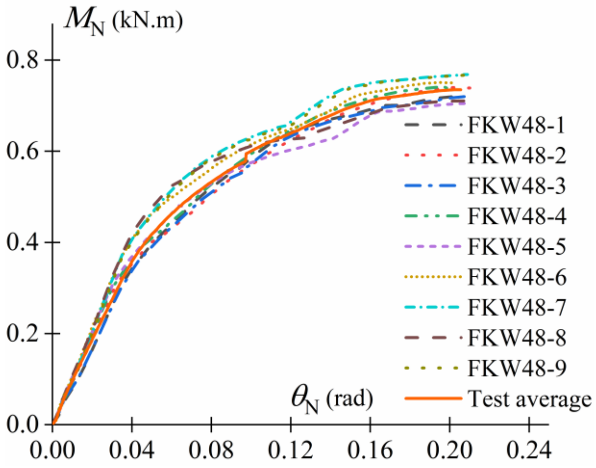

(b) Moment-rotation curves for negative bending test

Fig. 11 Moment-rotation curves for bending test

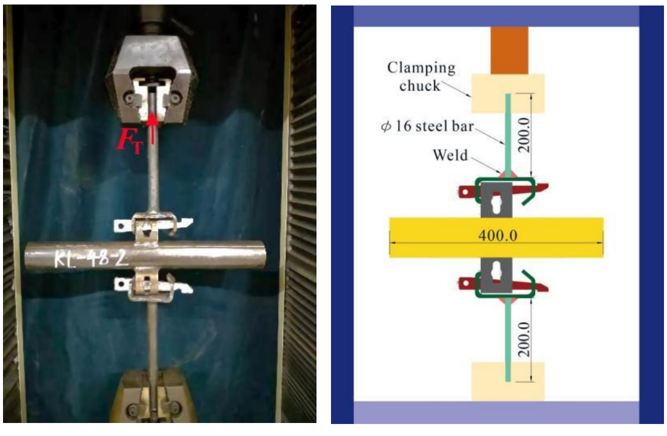

(a) Tensile test setup (b) Tensile test scheme

Fig. 12 Tensile test configuration (mm)

Six groups of tensile tests were carried out. The failure mode of the plug-pin joint was at the contact position between the C-shaped latch and the wedge (Fig. 13). The fracture occurred in the upper bending part of the C-shaped latch (Fig. 13(a)). There were two failure modes of the wedge. The wedge for KL48-2, KL48-3 and KL48-5 was bending and torsional failure (Fig. 13(b)), while for other specimens were pure bending failure (Fig. 13(c)). The installation without centered and defects of the wedge lead to bending and torsional failure. The specimen of each tensile test was observed to be brittle failure. Therefore, the upper bending part of the C-shaped latch needs to be improved in the design.

(a) Fracture at the C-shaped latch

(b) Bending and torsional failure of the wedge

(c) Pure bending failure of the wedge

Fig. 13 Failure behavior after tensile test

Based on the tensile test results, the load-displacement F_T-d_T curves and the average curve of the joint can be obtained (Fig. 14). As can be seen from Fig. 14, the maximum load of the specimens including KL48-2, KL48-3, KL48-5 is obviously less than that of other specimens. In order to avoid the bending and torsional failure of the wedge, the wedge should be installed correctly and checked whether the material is qualified in practical applications.

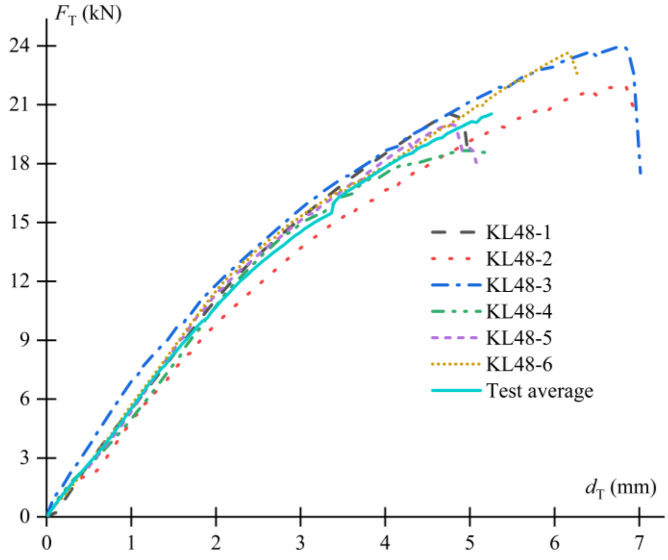

Fig. 14 Load-displacement curve for tensile test

3.3. Joint compressive test

The compressive test was performed to obtain the compressive performance and failure mode of the joint. Each end of the standard was respectively covered with a support, and the wedge was inserted tightly (Fig. 15). The constant displacement of each test was increased by 0.5 mm/min, until the force increased no more. Preloading was carried out before the test began.

Three groups of compressive tests were carried out. The failure mode of the plug-pin joint was that the standard was observed to have obvious depression. The standard showed buckling and there was no obvious deformation in other positions of the joint (Fig. 16).

According to test results, the load-displacement F_C-d_C curves and the average curve of the joint are plotted (Fig. 17). As shown in Fig. 17, the experimental results are discrete. After measurement, the main reason is that the U-shaped latches on both sides are not welded in a straight line with the standard.

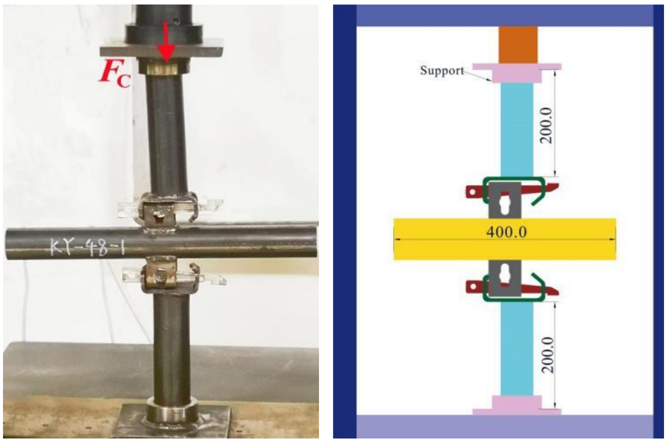

(a) Compressive test setup

(b) Compressive test scheme

Fig. 15 Compressive test configuration (mm)

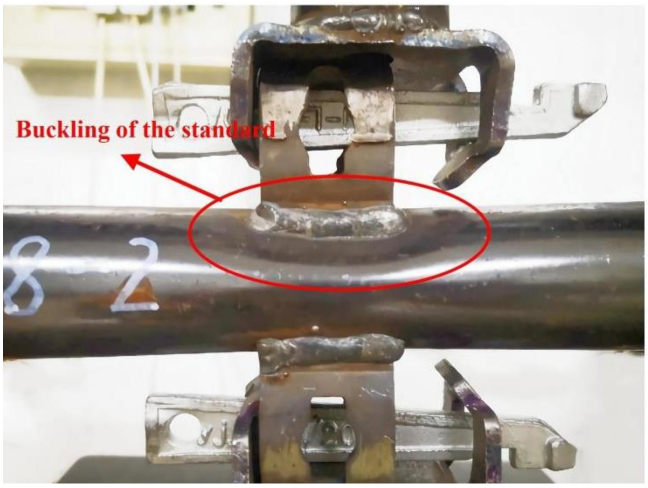

Fig. 16 Failure behavior after compressive test

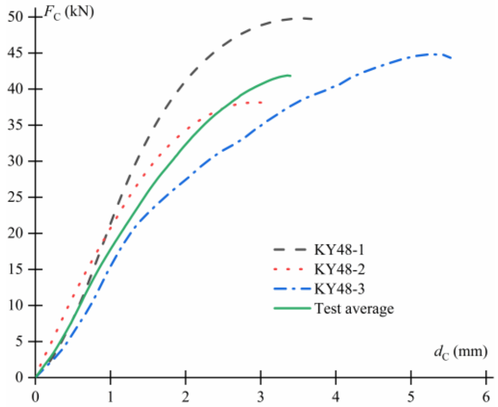

Fig. 17 Load-displacement curve for compressive test

3.4. Joint shear test

The shear test was conducted to obtain the shear performance and failure mode of the joint. Two cylindrical iron blocks were placed on both sides of the specimen. A steel base plate is placed on the upper part of the iron block, and a support was placed on the top of the standard (Fig. 18). According to different shear methods, the shear test included the internal and external shear test. The internal shear test refers to placing the iron blocks and steel base plates on both sides close to the surface of the standard. The schematics of setup and loading scheme for the internal shear test are given in Figs. 18(a) and 18(b). The external shear test refers to placing both sides of the iron blocks and steel base plates at 7 mm away from the lower edge of the U-shaped latches. The schematics of setup and loading scheme for the external shear test are presented in Figs. 18(c) and 18(d). The constant displacement of each test was increased by 1 mm/min until the force increased no more. Preloading was carried out before the test began.

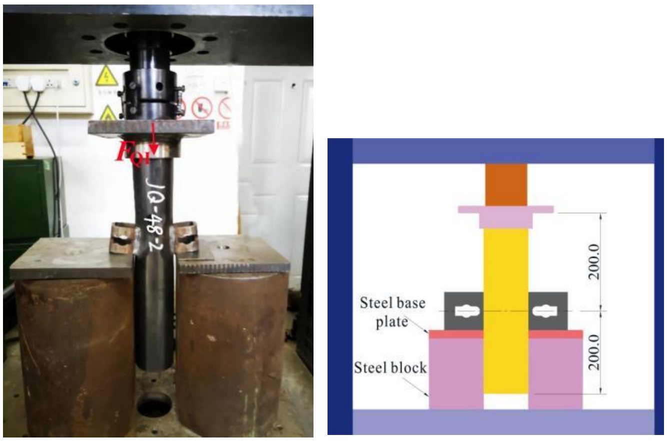

(a) Internal shear test setup (b) Internal shear test scheme

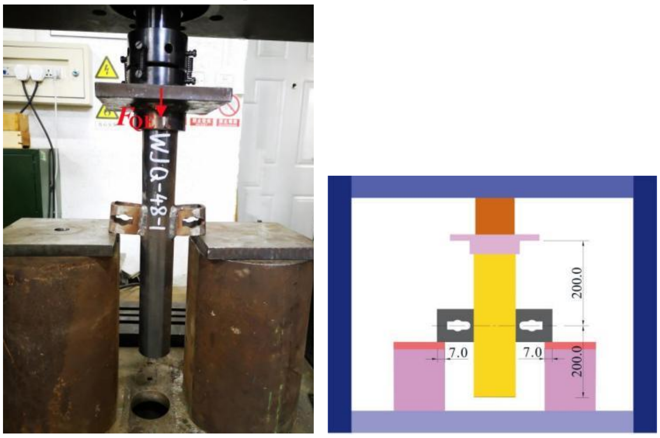

(c) External shear test setup (d) External shear test scheme

Fig. 18 Shear test configuration (mm)

The failure modes are presented in Fig. 19. For the internal shear test, the failure modes were the extrusion deformation of the standard and the obvious deformation of the U-shaped latches (Fig. 19(a)). For the external shear test, the failure modes were weld cracking at the connection and the extrusion deformation of the standard (Fig. 19(b)).

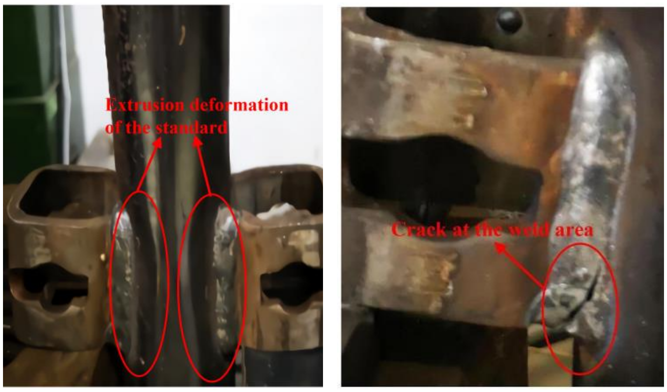

(a) Failure mode of internal shear test (b) Failure mode of external shear test

Fig. 19 Failure behavior after shear test

According to test results, the load-displacement curves and the average curve are plotted (Fig. 20).

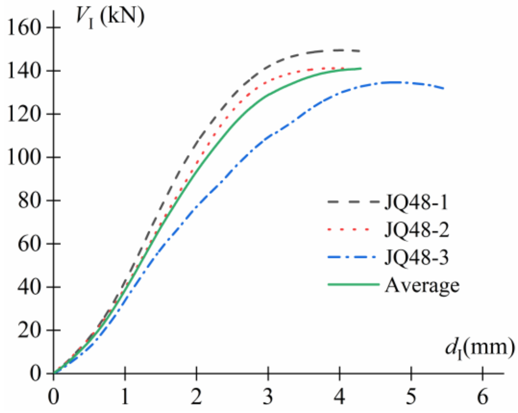

(a) Load-displacement curve for internal shear test

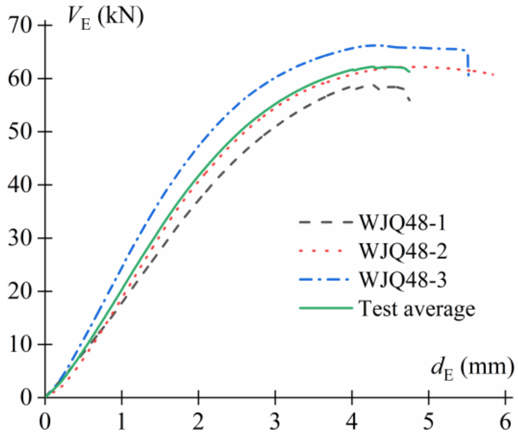

(b) Load-displacement curve for external shear test

Fig. 20 Load-displacement curve for shear test

4. Load bearing capacity and bending models

After determining the moment-rotation curves and load-displacement curves from the test results, Eurocode EN 12811-3:2002 [23] can be adopted to predict the load bearing capacity of plug-pin joint. Eurocode EN 12811-3:2002 [23] specifies the rules for the evaluation of test results in the field of temporary works. For the scaffold joint, due to the repeated use of the components, it is unacceptable if irreparable damage occurs. The bearing capacity of the joint is determined from the limit imposed by Eurocode EN 12811-3[23] on the ultimate load value. Under this restriction, it is ensured that the joint mainly works within the linear-elastic range. Therefore, the possibility of plasticity can be limited by reducing the ultimate load value measured in the test. According to the nominal characteristic value $R_{k,norm}$ predicted in EN12811-3:2002 [23], this value is the maximum allowable strength value namely the load bearing capacity [12]. The nominal characteri- stic value $R_{k,norm}$ is determined as follows:

$$R_{k,norm} = \frac{R_{k,b}}{\gamma_{R,2}} \tag{4}$$

Where $R_{k,b}$ is the basic characteristic value of resistance, γ_{R2} is the partial safety factor depending on the ductility. The value of γ_{R2} is determined as follows:

$$1.25 \ge \gamma_{R2} = -0.025\overline{q}_e + 1.275 \ge 1.0 \tag{5}$$

Where is $\overline{q}_e$ the mean value of plastic and elastic energy quotient [23].

Based on the experimental results and Eurocode, the load bearing capacity of the plug-pin joint under corresponding loads can be obtained by combining Equation (4) with Equation (5), as indicated in Table 3.

The rotational behavior of the joint has significant effects on overall performance of the scaffold structure. The structure tends to bend and damage in the direction parallel or perpendicular to the elevation of the joint [8]. The rotational behavior is expressed via the instantaneous rotational stiffness. It is necessary to develop the bending model of the joint for the establishment of the numerical model. Due to the asymmetry, in the case of positive rotation and negative rotation, the behavior of joint is usually different. Therefore, based on the bending test results, this paper developed the bending model of the joint in the vertical plane for the positive and negative rotation.

Table 3

Load bearing capacity of the plug-pin joint

Load forms	Basic characteristic value	Load bearing capac-
Positive bending moment	0.85 kN.m	0.82 kN.m
Negative bending moment	0.68 kN.m	0.64 kN.m
Tensile force F_T	20.53 kN	17.70 kN
Compression force F_C	38.16 kN	35.98 kN
Internal shear force V_I	128.97 kN	121.63 kN
External shear force V_E	56.13 kN	52.88 kN

Four methods were used to obtain nonlinear bending models within the load range related to the characteristic value $R_{k,norm}$. The first method was a bilinear curve obtained according to SEMA code [24]. The initial stiffness value was the slope determined by the line between the original point and the point from the test curve at maximum bending moment. When the rotation was greater than that determined by the maximum bending moment point at the initial line, the moment remained unchanged. The second method was a bilinear curve obtained according to the initial stiffness value and maximum bending moment, assuming that the initial stiffness value resulting from the tangent slope of the test curve. The initial line was defined by approximate the tangent of the test curve at original point. The linear function was used to simulate the tangent passing through the zero load point. The bilinear curve was called the initial stiffness curve. The third method was the equal area approach proposed in Eurocode EN 1551- 2:2009 [25]. This method was originally developed based on the Federation Europeenne de la Manutention (FEM) to model the behavior of pallet racks. Because the mechanical proper- ties of scaffold and pallet structure are similar, this method is considered to be a suitable method to simulate the bending model of joint. The initial stiffness value was the slope of the line passing through the origin point, which divided the test curve below the maximum bending moment into two parts. Finally, the area of the two parts was kept equal. The last method was to obtain trilinear curves by fitting the test data in the range of maximum bending moment. The simple polynomial function was used to simulate the experim- ental curve in order to provide the best fitting for the test data. The polynomial function was derived by approximating the test result.

The model was developed by using simple expressions. Fig. 21 shows the test curve for the positive and negative rotation and the approximate bending model obtained by four methods. The mathematical expressions corresponding to the four bending models are given in Table 4.

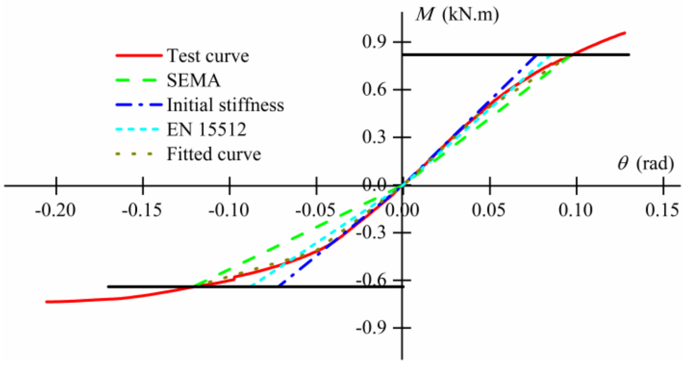

Fig. 21 Joint bending models

5. Conclusions

In this paper, the material properties of cold formed sorbite stainless steel and the mechanical behavior of the plug-pin joint made of cold formed sorbite stainless steel were studied. The results can provide material properties and mechanical parameters for developing numerical models of the joint, which can determine the load bearing capacity and weak parts under different forms of loads. The following conclusions can be obtained:

The material properties of sorbite stainless steel has nonlinear stress- strain relationship and obvious strain hardening phenomenon.

The failure modes of the joint under tensile force was brittle failure. The upper bending part of the C-shaped latch needs to be improved in the design. The plug-pin joint had different failure modes under various forms of loads, which can provide reference for practical design and analysis. The ultimate bearing capacity and rotational stiffness of the positive bending are greater than those of the negative bending. Four methods were adopted to build the bending model within the range of load bearing capacity. It can provide enough mechanical parameters for the refined numerical model established by the three-dimensional nonlinear analysis of the structure, which can also provide a reference for the stability calculation of the overall structure.

Based on the test results, the weak part is the upper bending position of the C-shaped latch, which can greatly affect the bearing capacity of the joint under different forms of load. Therefore, the the upper bending position of the C-shaped latch should be optimized in the design of the plug-pin joint. However, the influence of the reuse and welding residual stress on the mechanical behavior for joint were not considered in this work. In the future research, the two aspects will be further studied and the conclusion will be improved.

Table 4

Four bending models for the plug-pin joint

Model	Positive bending		Negative bending	
	Rotation (rad)	Expressions	Rotation (rad)	Expressions
SEMA	$0 \le \theta_P < 0.097$	$M_P = 8.45\theta_P$	$-0.121 \le \theta_N < 0$	$M_N = 5.33\theta_N$
	$\theta_P \ge 0.097$	$M_P = 0.82$	$\theta_N < -0.121$	$M_N = -0.64$
Initial stiffness	$0 \le \theta_P < 0.077$	$M_P = 10.61\theta_P$	$-0.072 \le \theta_N < 0$	$M_N = 8.92\theta_N$
	$\theta_P \ge 0.077$	$M_P = 0.82$	$\theta_N < -0.072$	$M_N = -0.64$
EN 15512	$0 \le \theta_P < 0.085$	$M_P = 9.65\theta_P$	$-0.088 \le \theta_N < 0$	$M_N = 7.27\theta_N$
	$\theta_P \ge 0.085$	$M_P = 0.82$	$\theta_N < -0.088$	$M_N = -0.64$
Fitted curve (Trilinear curve)	$0 \le \theta_P < 0.045$	$M_P = 10.14\theta_P$	$-0.051 \le \theta_N < 0$	$M_N = 8.35\theta_N$
	$0.045 \le \theta_P < 0.097$	$M_P = 6.92\theta_P + 0.15$	$-0.121 \le \theta_N < -0.051$	$M_N = 3.01\theta_N - 0.28$
	$\theta_P \ge 0.097$	$M_P = 0.82$	$\theta_N < -0.121$	$M_N = -0.64$

References

[1] Buitrago M., Moragues J.J., Calderón P.A. and Adam J.M., "Structural failures in cast-in-place reinforced concrete building structures under construction", Handbook of Materials Failure Analysis, 6, 153–170, 2018.

[2] Beale R.G., "Scaffold research — a review", Journal of Constructional Steel Research, 98, 188–200, 2014.

[3] Pieńko M. and Błazik-Borowa E., "Numerical analysis of load-bearing capacity of modular scaffolding nodes", Engineering Structures, 48,1-9, 2013.

[4] Abdel-Jaber M., Beale R.G., Shatarat N.K. and Shehadeh M. A., "Experimental and theoretical investigations of spigot connections under cyclic loading", Advanced Steel Construction, 15(1), 37-46, 2019.

[5] Cimellaro G.P. and Domaneschi M., "Stability analysis of different types of steel scaffolds", Engineering structures, 152, 535-548, 2017.

[6] Chandrangsu T. and Rasmussen K.J.R., "Structural modelling of support scaffold systems", Journal of Constructional Steel Research, 67(5), 866-875, 2011.

[7] Jia L., Liu H.B., Chen Z.H., Liu Y. and Wu Y.P., "Experimental study on bearing capacity

of reinforced steel tubular scaffold under uniform loads", Advances in Civil Engineering, 14, 1-20, 2019.

[8] Peng J.L., Wang S.H., Wang C.S. and Yang J.P., "Stability study on scaffolds with inclined surfaces and extended jack bases in construction", Advanced Steel Construction, 17(1), 73-83, 2021.

[9] Jia L., Liu H.B., Chen Z.H., Liu Q. and Wen S.L., "Mechanical properties of right-angle couplers in steel tube-coupler scaffolds", Journal of Constructional Steel Research, 125, 43-60, 2016.

[10] Abdel-Jaber M.S., Beale R.G., Godley M.H.R. and Abdel-Jaber M., "Rotational strength and stiffness of tubular scaffold connectors", Proceedings of the Institution of Civil Engineers Structures and Buildings, 162(6), 391-403, 2009.

[11] Abdel-Jaber M., Abdel-Jaber M.S., Beale R.G., Allouzi R. and Shatarat N.K., "Properties of tube and fitting scaffold connections under cyclical loads", Journal of Constructional Steel Research, 168, 106008, 2020.

[12] Prabhakaran U., Beale R.G. and Godley, M.H.R., "Analysis of scaffolds with connections containing looseness", Computers & Structures, 89, 1944-1955, 2011.

[13] Chandrangsu T. and Rasmussen K.J.R., "Investigation of geometric imperfections and joint stiffness of support scaffold systems", Journal of Constructional Steel Research, 67 (4), 576-584, 2011.

[14] Liu H.B., Zhou Y., Chen Z.H. and Liu, Q., "Structural performance and design method of new mortise-tenon full steel-tube scaffold", Advanced Steel Construction, 14(2), 291-307, 2018.

[15] Peng J.L., Wu C.W., Chan S.L. and Huang, C.H., "Experimental and numerical studies of practical system scaffolds", Journal of Constructional Steel Research, 91, 64-75, 2013.

[16] Bong J.K., Lee H.D., Kim S., Mha H.S., Yim D.K. and Won J.H., "Probabilistic characteristics of moment capacity and rotational stiffness of wedge joints used in support systems reflecting reused members", Applied Sciences, 9(19), 4056, 2019.

[17] Pieńko M. and Błazik-Borowa E., "Experimental studies of ringlock scaffolding joint", Journal of Constructional Steel Research, 173, 106265, 2020.

[18] Zhao Z.W., Liu H.Q., Dong J.F. and Bian Y.X., "Buckling Capacity of Socket-Template Scaffold System without X-Bracing", Journal of Performance of Constructed Facilities, 34(1), 04019089, 2020.

[19] Dong J. F., Liu H. Q., and Zhao Z. W., "Buckling behavior of a wheel coupler high-formwork support system based on semi-rigid connection joints", Advanced Steel Construction, 18(1), 425–435, 2022.

[20] Chen Z.H. and Zhao Z.W., "Analysis of door-type modular steel scaffolds based on a novel numerical method", Advanced Steel Construction, 12(3), 316-327, 2016.

[21] Liu C., He L., Wu Z.Y. and Yuan J., "Experimental study on joint stiffness with vision-based system and geometric imperfections of temporary member structure", Journal of Civil Engineering and Management, 24(1), 43-52, 2018.

[22] High strength sorbite stainless structural steel welded steel pipe: T/SSEA 0007-2017. Beijing: China special steel enterprises association, 2017.

[23] Temporary works equipment, Part 3: Load testing: EN 12811-3. London: British Standards Institute, 2002.

[24] The storage equipment manufacturers association: SEMA. London: UK Trade Association, 1985.

[25] Steel Static Storage Systems-Adjustable Pallet Racking Systems-Principles for Structural Design: EN 15512:2009. London: British Standards Institute, 2009.

Advanced Steel Construction – Vol. 18 No. 4 (2022) 826–835
DOI:10.18057/IJASC.2022.18.4.10

MECHANICAL PROPERTIES OF HGMFSST COLUMNS UNDER AXIAL COMPRESSION-EXPERIMENT AND ANALYSIS

Yan Zhou, Yu-Tong Duan, Hong-Gang Lei *, Fu-Yu Lu, Xin-Yu Chang and Tie-Ying Li

College of Civil Engineering, Taiyuan University of Technology, Shanxi 030024, China
** (Corresponding author: E-mail: lhgang168@126.com)*

ABSTRACT

High-strength grouting material (HGM) has the characteristics of early strength, high strength, high self-flow, and micro-expansion, but research on composite columns formed by steel tube and HGM is relatively scarce. Therefore, in this paper, the mechanical properties of HGM-filled square steel-tube columns (HGMFSST columns) under axial compression were experimentally studied. The main parameters included tube thickness (t) and HGM strength (fck). The test results showed that members with t = 4 mm failed due to local buckling, and members with thicker steel tube thickness failed mainly due to overall buckling. The measured and predicted ultimate bearing capacity values of the HGMFSST columns based on the existing standards of GB 50936-2014, CECS 159: 2004, AISC/ANSI 360-16, EC4, and AS/NZS 2327: 2017 were compared. The ultimate bearing capacity derived with CECS 159: 2004 was the closest to the measured values and had minimum discreteness.

ARTICLE HISTORY

Received: 14 July 2022
Revised: 14 October 2022
Accepted: 19 October 2022

KEYWORDS

Square steel tube;
High-strength grouting material;
Ultimate capacity;
Strength factor;
Ductility

1. Introduction

High-strength grouting material (HGM) contains well-graded aggregates, cement, and special chemical additives, which enable HGM to achieve high early and final strengths and free-flowing property, and prevent shrinkage upon setting. Currently, a lot of experimental and theoretical studies on the flow performance[1-4] and expansibility[5] of HGM have been carried out. These studies show that the use of HGM can help prevent plastic settlement at the initial stage owing to their free-flowing property and special plastic expansibility. This leads to a high level of compactness and avoids hollowing of infilled material during the pouring process.

As for concrete-filled steel tube (CFST) members, hollowing and voids are generated naturally during the pouring of core concrete due to poor vibration, stiffeners, and reinforcement framework inside the steel tube[6-8]. They affect the bonding ability between the inner concrete and steel tube and reduce the bearing capacity of CFST members[9]. Some studies have shown that increasing the bond performance[10], density[11, 12] and expansibility[13, 14] of core concrete can improve the bonding strength and consequently elevate the bearing capacity of CFST members.

Considering the advantages of HGM, its use as a filling material in square steel tube columns is regarded as a practical structural application. However, current research on HGM-filled square steel-tube (SST) columns (HGMFSST columns) is limited, and the application of HGM mainly focuses on two fields. On the one hand, HGM has been used as a primary medium for load transfer in reinforcement sleeve grouting connection joints, and relevant research mainly focuses on bonding strength and interaction between grout and reinforcement through monotonic tensile[15-17] and cyclic load tests[18, 19]. On the other hand, HGM has been used as a reinforcement material for structures or components. It enables pouring of foundations and supports with large volumes, dense reinforcement, and small spacing with high fluidity[20]. In addition, the use of HGM instead of ordinary concrete in some special projects overcomes the problems of poor compactness and self-shrinking[21, 22]. These two applications indicate that HGM has high fluidity, better bond behavior, and micro-expansion.

Therefore, it is meaningful to study the mechanical properties of composite columns formed by HGM and steel tubes. In this paper, the failure patterns and ultimate bearing capacity of HGMFSST members were studied by axial compression test, and the effect of the tube thickness and HGM strength on the mechanical properties of the members was investigated. The ultimate bearing capacity of the HGMFSST members was predicted and analyzed based on existing standards including GB 50936-2014[23], CECS 159: 2004[24], AISC/ANSI 360-16[25], EC4[26] and AS/NZS 2327: 2017[27].

2. Experimental study

2.1. Specimen preparation

A total of eight members were tested, including six HGMFSST columns and two hollow steel tube (HST) columns as a comparison. Fig. 1 shows schematic views of the HST and HGMFSST columns. The main parameters of the components included tube thickness and HGM strength. The steel tubes selected were Q355-grade high-frequency welded square steel tubes with cross-sectional dimensions of 100 mm × 4 mm and 100 mm × 6 mm. The HGMs used in this test were commercially available finished grouting materials. The strengths of the HGM were determined through material property tests. End plates were welded on both upper and lower ends of the columns. To facilitate the pouring of HGMs, a circular hole with a diameter of 50mm was drilled in the middle of the upper end plate of every column.

The basic parameters of the columns are shown in Table 1. The HGMs used with different strengths were denoted as HGM1, HGM2, and HGM3 respectively. The test members were labelled based on the sectional form of the steel tubes, HGM type, and tube thickness. For example, S-HGM1-4 corresponded to a square steel tube with a thickness of 4 mm, and the in-filled grouting material was HGM1. The members were classified into two groups, namely group I and group II. The length of the members was 1500 mm, approximately half the height of an ordinary residential floor. Table 1 shows the width (*B*) of the cross-section, the steel tube wall thickness (*t*), the length (*L*) and the slenderness ratio (λ) of the members.

Table 1
The basic parameters of the members

No.	Group	Member label	*L* (mm)	*B* (mm)	*t* (mm)	λ	HGM type
1	I	S-4	1500	100	4	26.8	—
2		S-HGM1-4	1500	100	4	23.7	HGM1
3		S-HGM2-4	1500	100	4	24.0	HGM2
4		S-HGM3-4	1500	100	4	24.7	HGM3
5	II	S-6	1500	100	6	27.3	—
6		S-HGM1-6	1500	100	6	25.0	HGM1
7		S-HGM2-6	1500	100	6	25.2	HGM2
8		S-HGM3-6	1500	100	6	26.0	HGM3

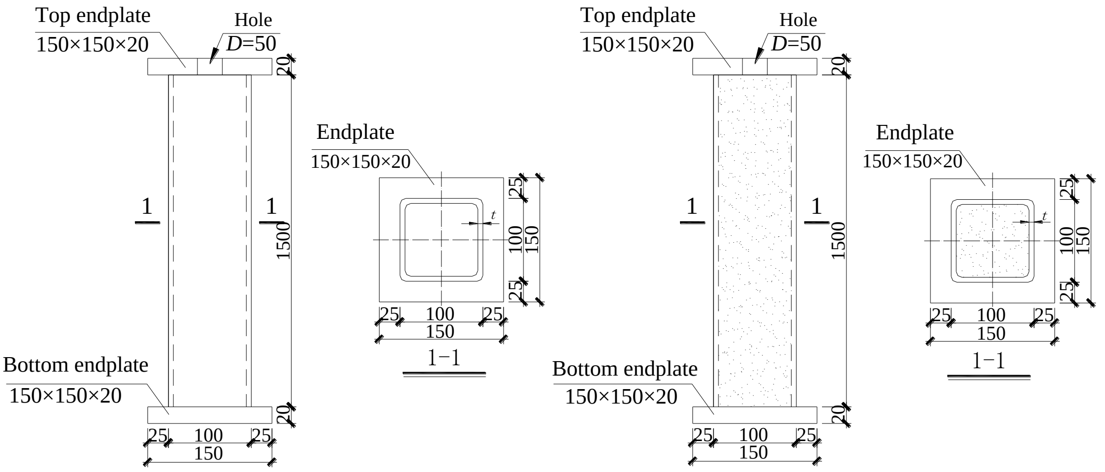

(a) HST (b) HGMFSST

Fig. 1 Schematic views of the HST and HGMFSST members

2.2. Material properties

2.2.1. Steel

The mean values of the mechanical properties of Q355-grade steel are listed in Table 2, including steel plate thickness (t), yield strength (f_y), ultimate strength (f_u), elastic Young's modulus (E_s), percentage elongation ($\mathit{\Delta}$%), and yield strain (f_y/E_s).

Table 2
Material properties of Q355-grade steel

Size	t (mm)	f_y (MPa)	f_u (MPa)	f_y/f_u	E_s (MPa)	$\mathit{\Delta}$ (%)	Yield strain ($\mu\varepsilon$)
□100×4	3.72	405.0	621.50	0.652	197991	29.38	2045
□100×6	5.74	467.9	659.70	0.709	195352	24.96	2405

2.2.2. HGM

Based on GB/T 50448-2015[28] and GB/T 50081-2019[29], nine 100 mm × 100 mm × 100 mm cubic blocks were made for each type of HGM to test the cube compression strength (f_{cu}) at Day 3, Day 7, and Day 28. Six 100 mm × 100 mm × 300 mm prismatic blocks were made for each type of HGM to determine the axial compressive strength (f_c) and elastic modulus at Day 28.

Each type of grouting material was prepared by adding a correct amount of water, pouring the mixture into a mixer, and mixing it for 300 s. The mixture was then poured into moulds and released after 24 h. After removal from the moulds, the grouting material members were wrapped with plastic and kept in a maintenance room for 3, 7, and 28 d respectively for the compressive strength experiments. Each specimen was labelled. The members were maintained as shown in Fig. 2.

(1) Cube compressive strength (f_{cu})

Cube compressive strength f_{cu} is not only an essential index for evaluating concrete strength grades, but also a basic index for calculating other mechanical properties. The compressive strengths of the grouting blocks at Day 3, Day 7, and Day 28 were measured using a STYE-2000 pressure testing machine.

The failure modes of HGM1exhibited pyramidal failure forms, which were similar to those of ordinary concrete at Day 3, Day 7, and Day 28. The main phenomenon was the bond failure between aggregate and mortar. No aggregate cracking was found. Unlike HGM1, the failure modes of grouting materials HGM2 and HGM3 originated from vertical cracks, and finally developed into multiple small cylinders. Weak sounds were heard during the loading process. After the strength reached its peak value, loud sounds were produced, which was caused by fracturing of blocks and falling of debris. The typical failure modes of the cube members at Day 3, Day 7, and Day 28 are shown in Fig. 3.

Fig. 2 Maintenance of test blocks

	HGM1	HGM2	HGM3
3-day			

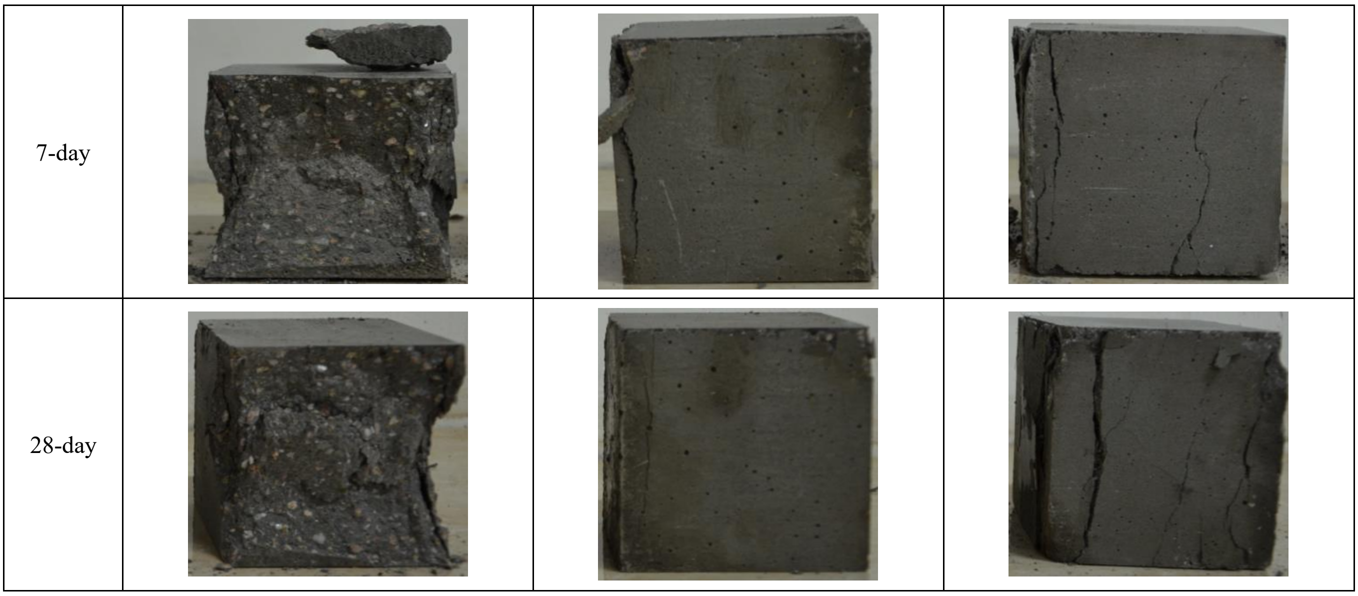

Fig. 3 Failure modes of cube blocks

The mean values of the cube compression strength of the three grouting materials are shown in Table 3. All the blocks had high early strengths, and the strengths increased slowly in later stages.

Table 3
Mechanical properties test results of HGM

HGM type	Cube compression strength f_{cu} (MPa)			Axial compressive strength f_c (MPa)	Elastic moduli E_c (MPa)
	day 3	day 7	day 28		
HGM1	47.6	60.5	74.8	62.3	3.38×10^4
HGM2	51.2	60.2	79.1	67.5	3.47×10^4
HGM3	95.3	107.3	125.6	100.5	4.27×10^4

(2) Axial compressive strength

The friction force between the testing machine and the contact surface of members had a confinement effect on the members in the cube compressive strength test, which affected the actual compression of the materials. Therefore, the axial compressive strength of the prismatic blocks was considered to be a true reflection of the concrete strength, which weakened the confinement effect[30]. The axial compressive strength of the grout prismatic blocks at Day 28 was measured according to the requirements of the standards [28] and [29].

As shown in Fig. 4, the failure states of the prismatic members occurred with the cracks penetrating through the upper and lower bearing surfaces along the diagonal of the blocks. The members in the middle part were dominated by some vertical cracks, because this part of the specimen did not experience the confinement effect of the testing machine and was therefore in a state of uniform compression. The HGM3 test blocks were kept intact with no falling debris, which was due to the presence of steel fibers in this type of grouting material. As can be seen from the crack surface of the HGM3 blocks after test, the steel fibers were pulled out without breaking. HGM1 and HGM2 blocks largely broke into two pieces along the cracks that penetrated the diagonal of the blocks. All the members cracked with loud sounds when the maximum strength was reached. The mean values of the axial compressive strengths of the prismatic members are shown in Table 3.

(3) Elastic modulus

The elastic modulus of a material is the main index of its deformation performance in elastic stage. The elastic moduli of the HGMs were measured according to standard [29], and the mean values are listed in Table 3.

(a) HGM1 (b) HGM2 (c) HGM3

Fig. 4 Failure states of the prismatic members

2.3. Loading device and scheme

The loading device presented in Fig. 5 was operated with a spherical hinge bearing on the top endplate, and the bottom endplate was directly connected to the test bed, where the desired loading conditions were achieved by using a hinged joint on one endplate and a fixed one on the other. Two displacement transducers (D1 and D2) were placed between the two endplates to measure longitudinal displacement, and lateral deformation was measured in the middle section of the members using two displacement transducers (D3 and D4), which were placed perpendicular to each other. Longitudinal and transverse strain gauges were arranged around the columns on the outer surface of a mid-height tube (Section A-A) to measure strain of the members, and four more strain gauges were arranged to measure longitudinal strains at Section B-B.

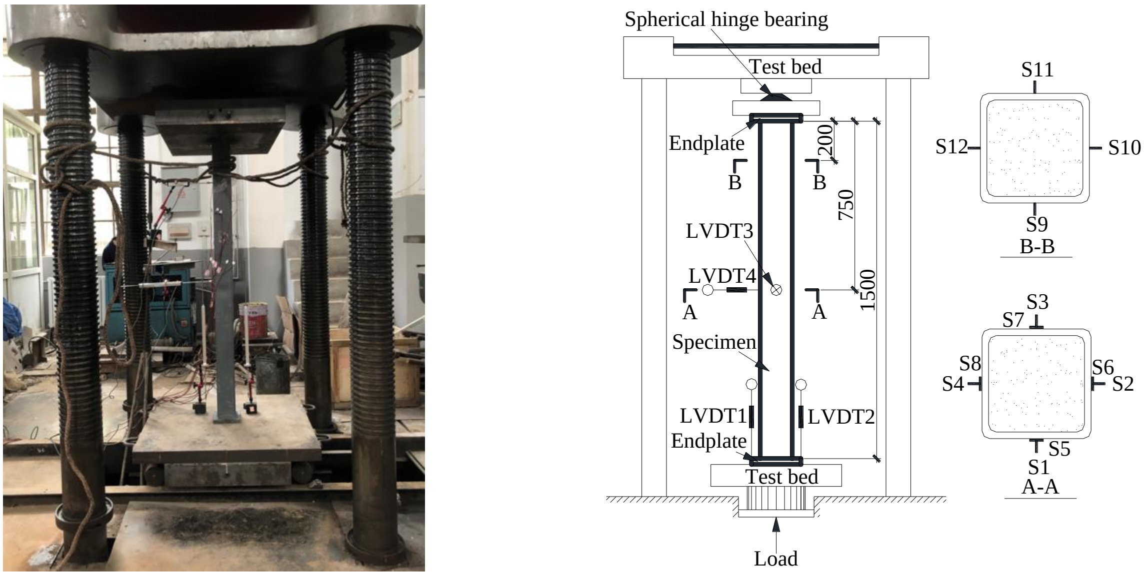

(a) Specimen (b) Instrumentation

Fig. 5 Test setup and instrumentation layout

A multistage loading approach was adopted in the test process. The load control mode was applied until the members reached 75% of the estimated ultimate load. After 75% of the estimated ultimate load was achieved, the displacement was adjusted at a rate of 0.005 mm/s. The tests were stopped when the deformation of the members was too large or the bearing capacity of the members dropped to 80% of the ultimate bearing capacity.

3. Experimental results and discussion

3.1. Failure pattern

Based on the test results, the failure patterns could be classified into two groups: (a) failure with both local buckling and overall buckling (Group I) and (b) failure with only overall buckling (Group II). The observed failure patterns of the tested members are shown in Fig. 6.

During the initial stage of loading, all the members were in an elastic stage. When the load reached approximately 85% of the ultimate bearing capacity, local buckling occurred in the middle of member S-4, upper point of trisection of member S-HGM1-4 relative to the top endplate, and the middle of member S-HGM2-4. As the load was increased, slight bending occurred at the points of local buckling. After reaching the ultimate value, the bearing capacity decreased rapidly with significant bending, and the bulge developed to the adjacent surface. The failure pattern of member S-HGM3-4 was similar to that of the first three members before reaching the ultimate bearing capacity. In the decline stage of the bearing capacity, the bearing capacity underwent a fluctuating decline owing to the presence of steel fibers, which enhanced the ductility of grouting HGM3.

During the whole loading process, due to the thicker steel tube wall, the members of Group II did not have the same local buckling phenomenon as the members of Group I, but the bending phenomenon occurred in the middle of all members. For member S-HGM3-6, when the load decreased to approximately 0.815N_{ue}, an inflection point occurred in the load-deflection curve owing to the presence of steel fibers, as in the case of member S-HGM3-4. After the load was increased to approximately 0.853N_{ue}, the bearing capacity gradually decreased, and bending of the member became increasingly obvious.

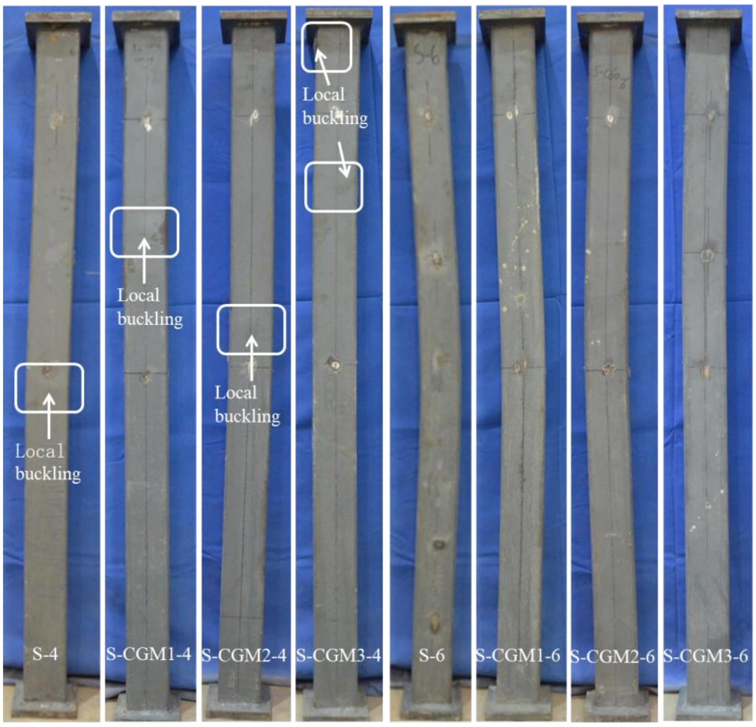

Fig. 6 Failure pattern of tested members

3.2. Load-displacement relationship

3.2.1. Effect of HGM strength

The measured ultimate bearing capacity (N_{ue}) and axial load (N) versus displacement ($\mathit{\Delta}$) relationship are presented in Table 4 and Fig. 7, respectively. The nominal member capacity N_{es} was calculated using the equation $N_{es}=f_yA_s+f_cA_c$, where f_y is the yield strength of steel, f_c is the axial compressive strength of the inner HGM (Table 4), and A_s and A_c are the cross-sectional areas of the tube and the inner HGM, respectively. ξ is the confinement factor ($\xi = A_sf/A_cf_c$), and f is the compressive strength design values of steel. $\mathit{\Delta}_{e85\%}$ is the vertical deformation when the bearing capacity is reduced to 85% of the ultimate bearing capacity, and $\mathit{\Delta}_{ue}$ is the vertical deformation corresponding to N_{ue} of a tested member. ω_e is the increase in the ultimate bearing capacity compared with the HST. ω_{es} is the increase in the nominal member capacity compared with the HST. *SI* is the strength index of the member. *DI* is the ductility index of the member.

Table 4
Summary of test results

Group	Specimen label	Ultimate point		$\mathit{\Delta}_{e85\%}$/mm	ω_e (%)	N_{es}/kN	ω_{es}(%)	ω_e/ω_{es}	ξ	*SI*	*DI*
		N_{ue}/kN	$\mathit{\Delta}_{ue}$/mm								
I	S-4	630	6.30	8.18	—	622	—	—	—	1.013	1.334
	S-HGM1-4	1295	5.88	6.33	105.5	1149	84.8	1.245	1.180	1.127	1.076
	S-HGM2-4	1294	5.85	6.30	105.4	1226	97.1	1.085	1.089	1.055	1.077
	S-HGM3-4	1554	5.97	6.40	146.6	1473	136.7	1.072	0.731	1.055	1.072
II	S-6	1013	8.40	26.06	—	1056	—	—	—	0.960	3.102
	S-HGM1-6	1516	7.08	13.76	49.6	1538	45.7	1.085	2.188	0.985	1.943
	S-HGM2-6	1587	6.57	10.13	56.7	1609	52.4	1.082	2.019	0.987	1.542
	S-HGM3-6	1778	6.93	8.61	75.5	1834	73.7	1.023	1.356	0.969	1.241

Table 4 and Fig. 7 show that the ultimate capacity of the members significantly improved after HGM pouring, and the ultimate values improved with an increase in the strength of the HGMs. The ultimate capacities of members S-HGM1-4, S-HGM2-4, and S-HGM3-4 increased by 105.5%, 104.4%, and 146.6%, respectively, compared with the hollow tube specimen S-4. Though the ultimate capacities of members in Group II didn't increase as significantly as those in Group I, they were 49.6%–75.5% higher than that of the hollow tube specimen S-6. This is because the local buckling of the steel tube was effectively suppressed by the inner HGM that had a larger restraint effect on members of Group I. Table 4 shows that ω_e was larger than ω_{es} for HGMFSST members compared with the HST under compression. This illustrates the advantages of combining steel and HGM in HGMFSST composite members: The performance of such combination is greater than the simple sum of HGM and steel tube.

The effect of HGM strength on the load-displacement curves is shown in Fig. 7. As shown in the figure, the whole loading process of the test members could be divided into three stages: elastic stage, elastic-plastic stage, and decline stage. In the initial stage of loading (the elastic stage), the curve slope of the HGMFSST members was significantly larger than that of the steel tube without HGM inside, indicating that the overall initial stiffness of the steel tube members was significantly improved after HGM pouring and increased slowly with the increase of HMG strength. As the applied load was further increased, the growth rate of the vertical displacement gradually accelerated before the ultimate value was reached, and the growth rate of the bearing capacity of the members gradually decreased, which is the elastic-plastic stage.

After the bearing capacity of the members reached the peak load, it began to decrease, but the vertical displacement continued to increase. Consequently, the load-displacement curves of the members entered the decline stage. At the beginning of the decline stage, the descent speed of the bearing capacity of the HGMFSST members was faster than that of the hollow members owing to the abrupt cracking of the HGMs when the bearing capacity reached the ultimate value. When the load dropped to a certain level, the descent speed gradually decreased because the infilled HGMs became more compact after cracking under the loaded state and a confinement effect was provided by the steel tube.

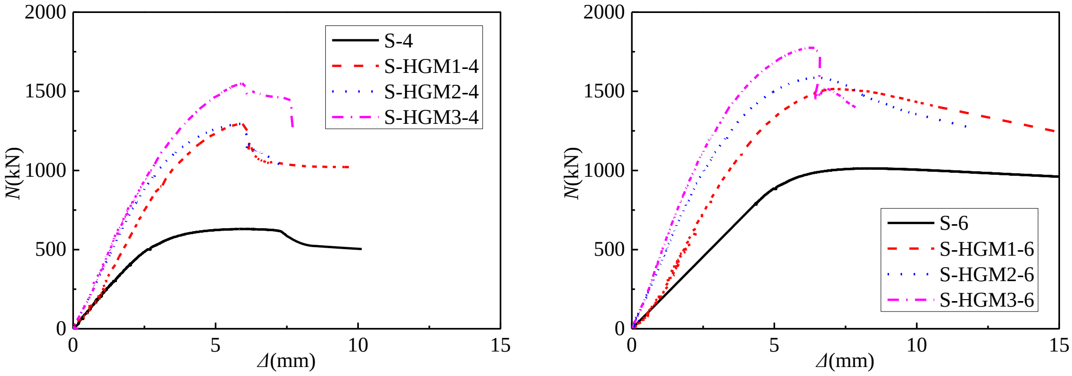

(a) Members of Group I

(b) Members of Group II

Fig. 7 Effect of HGM strength on load-displacement curves

3.2.2. Effect of tube thickness

The load-displacement curves with different tube thicknesses are listed in Fig. 8. As shown in the figure, the curve slopes of the members with different tube thicknesses roughly coincided at the initial loading stage, indicating that the tube thickness had little effect on the overall initial stiffness of the members. Meanwhile, the ultimate bearing capacity of the members increased with the increase of the tube thickness. After the bearing capacity reached the ultimate level, the decrease in the bearing capacity of members of Group II was lower than that of members of Group I. This was because the increase in the tube thickness effectively delayed the local buckling of the steel tube and improved the ductility of the members.

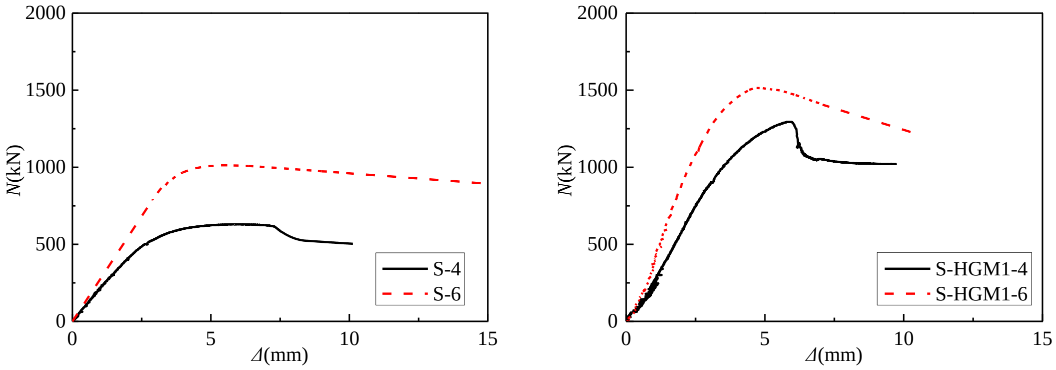

(a) Hollow tube (b) HGM1 members

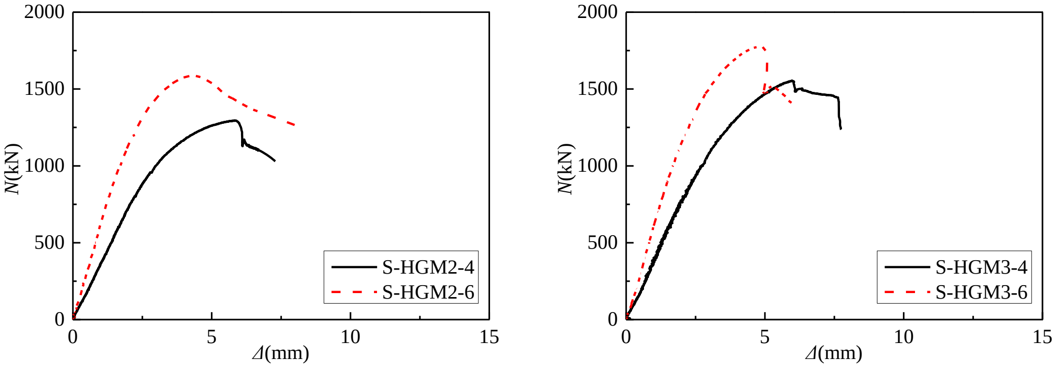

(c) HGM2 members (d) HGM3 members

Fig. 8 Effect of steel tube thickness on load-displacement curves

3.3. Strength index

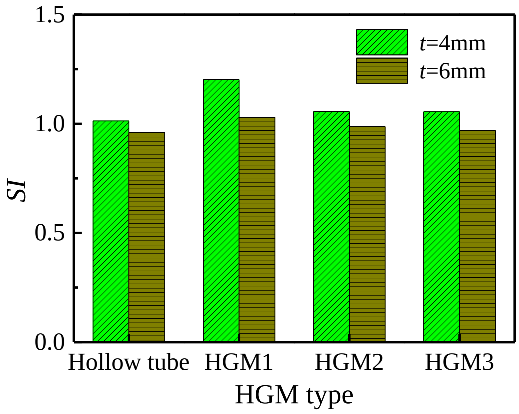

Fig. 9 *SI* of the members

The strength index (*SI*) can be calculated in this study with the following formula defined by Yang[31] and Han[32].

$$SI=\frac{N_{\text{uc}}}{N_{\text{es}}} \tag{1}$$

Table 4 and Fig. 9 show the strength indices of the members. It can be seen that the *SI* of HST improved after HGM pouring. This was because the inner HGM delayed the local buckling of the steel tube, and the influence was more significant for the thinner steel tube members. In addition, the *SI* of the HGMFSST members slightly decreased with the increase in the HGM strength, which was mainly because the increase in the HGM strength reduced the constraint effect (Table 4) of the steel tube on the inner HGM[32].

3.4. Ductility index

The ductility index (*DI*) can be calculated using the following formula defined by Ge [33] and Zhao[34]:

$$DI=\frac{\Delta_{\text{c85\%}}}{\Delta_{\text{ue}}} \tag{2}$$

Table 4 and Fig. 10 show the ductility indices of the members. The *DI* of the HGMFSST members decreased with an increase in the HGM strength. This can be explained with the confinement factor ξ, because the constraint effect of the steel tube on the inner HGM decreased with an increase in the HGM strength. Compared with the HGMFSST members of Group II, the effect of the HGM strength on the *DI* was minimal for the HGMFSST members of Group I. This was due to the local buckling that occurred easily in members with thinner plates and limited the development of the plastic section. Table 4 shows that the *DI* increased by 80.58%, 43.18%, and 15.76% as the tube thickness was increased for the HGM1, HGM2, and HGM3 members, respectively. In addition, the increase ranges became narrower, indicating that the *DI* gradually became dominated by the infilled HGM with an increase in the HGM strength for the HGMFSST members.

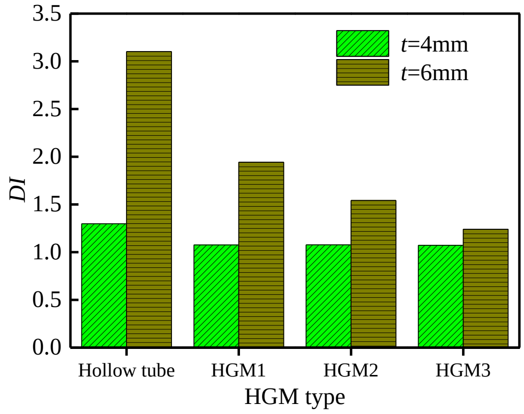

Fig. 10 *DI* of the members

3.5. Load-strain relationships

In order to study the cross-sectional stress distribution of the compressed members, strain gauges were set around the members, and the specific layout is shown in Fig. 5. The strain gauges S1~S4 were used to measure the longitudinal strain of the members and analyze the yielding condition of the steel tube under axial load. The strain gauges S5~S8 were used to measure the transverse strain of the members and analyze the restraint of the steel tube on the inner HGM.

The load-strain relationships are shown in Fig. 11, where ε_y ($\varepsilon_y = f_y/E_s$) is the yield strain of the steel tube, and the positive and negative values represent tensile and compressive strains, respectively. As shown in the figure, prior to reaching the yield strain of the steel, the longitudinal and transverse strains of the members showed a linear upward trend with the increase in the load, and the strains of the four surfaces of the steel tube were almost coincident, indicating that the members were well centered and generally in the state of axial compression. The strain information collected by the strain gauges at the locations of local buckling or bulge can directly reflect the deformation of the members. When the axial load decreased, the longitudinal strain of the tensile surface of the bending part of the steel tube gradually decreased with an increase in the bending deformation, and even lead to tensile strain. Meanwhile, the longitudinal strain of the compressive surface continued to increase. In steel tube parts other than the bending or bulging part, the strain increased gradually with a decrease in the axial compressive load. Taking specimen S-HGM2-6 as an example, strain gauge S2 was on the tension surface at the buckling position, where the measured strain initially increased and then decreased in the loading process. Strain gauge S4 was on the compressive surface of at the buckling position, where the measured strain increased or remained unchanged during the loading.

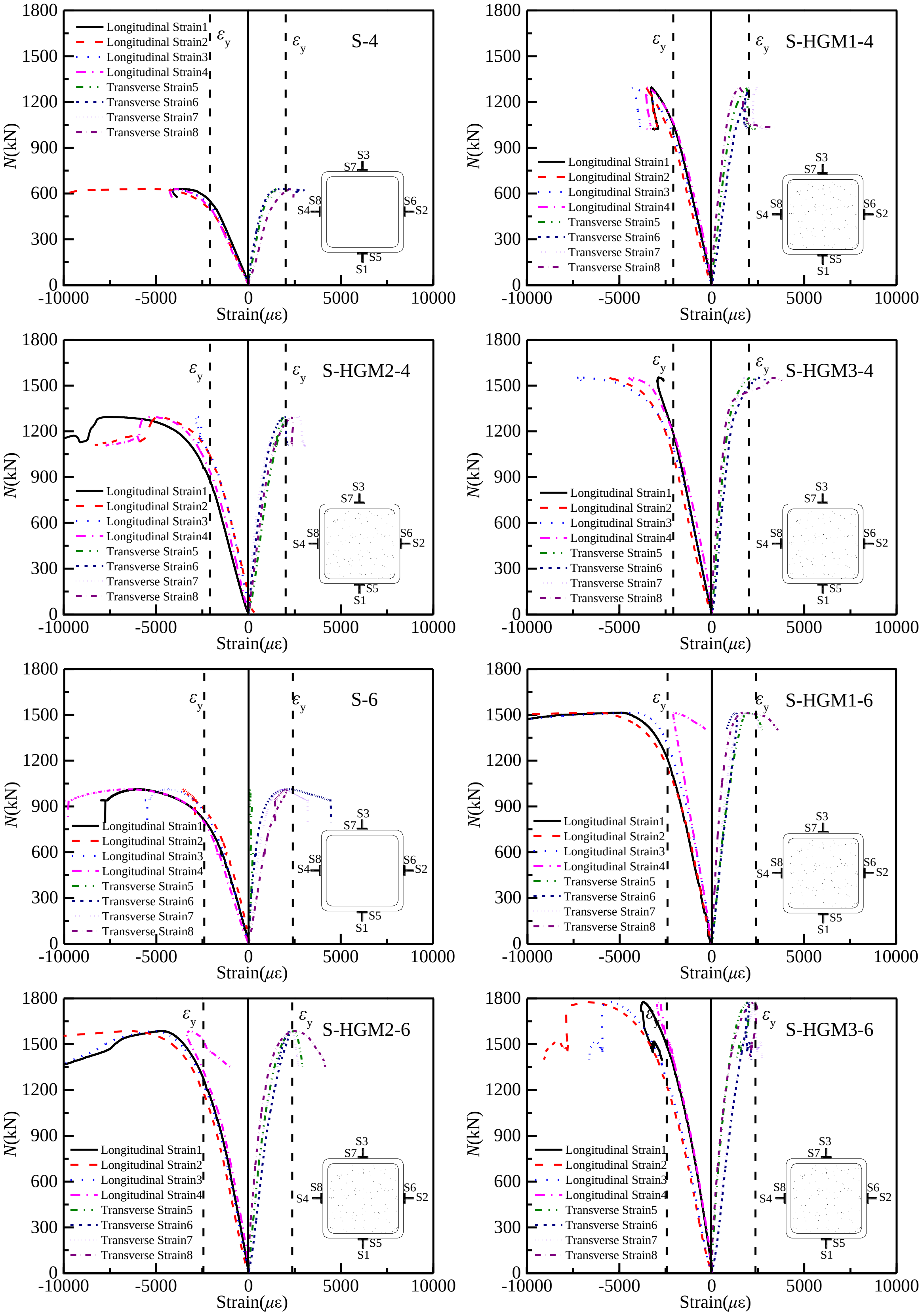

Fig. 11 Load-tube strain responses

The average cross-sectional longitudinal strains in the middle of the members are shown in Fig. 12, where ε_u ($\varepsilon_u = f_u/E_s$) is the ultimate strain of the steel tube.

Fig. 12 shows that the strains of the HGMFSST columns were larger than those of the HSTs at the ultimate load, which is consistent with the experimental finding of Han[35]. In addition, the loading-stain curve slopes of the HGMFSST columns were significantly larger than those of the HST, indicating that the steel tube and inner HGM worked well in conjunction under axial compression. Besides, the increase in the HGM strength had little effect on the longitudinal strains of the HGMFSST members with similar tube thicknesses.

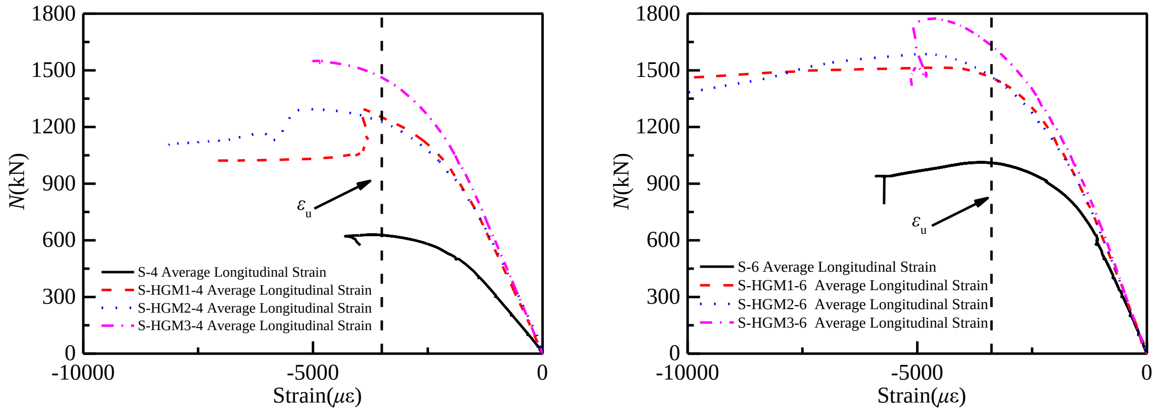

(a) Members with $t = 4$ mm (b) Members with $t = 6$ mm

Fig. 12 Average load-tube cross-sectional strain responses in the middle part

4. Prediction of ultimate bearing capacity

The ultimate bearing capacity of structural members is an important indicator of their static performance. Hence, a reliable method for calculating their ultimate strength is essential for practical application of these structural members in engineering design. At present, there is still no common standard for ultimate bearing capacity of HGMFSST members, but Wu[36] pointed out that the constitutive relation of ordinary concrete can be used for HGM after experimental investigation. Therefore, some calculation formulas of ultimate bearing capacity of CFST members were selected in this study to calculate the bearing capacity of the tested HGMFSST members under axial compression. The applicability of these formulas was verified by comparison with the experimental results. The calculation formulas used were derived based on the following standards: GB 50936-2014, CECS 159: 2004, AISC/ANSI 360-16, EC4 and AS/NZS 2327: 2007.

4.1. Calculation formulae

Table 5 lists the calculation formulas for the bearing capacity of CFST members under axial compression based on five standards.

Table 5
Calculation formulae for bearing capacity of CFST members

Standard	Calculation formulae	Formula description
GB 50936-2014	$N = \varphi N_0$; $N_0 = A_{sc} f_{sc}$; $f_{sc} = (1.212 + B\xi + C\xi^2) f_c$; $\xi = A_s f / A_c f_c$	N denotes the design value of stable bearing capacity. N_0 denotes the design value of axial compression strength of a short column. φ denotes the stability factor. A_{sc} denotes the cross-sectional area of a CFST member, $A_{sc} = A_s + A_c$. A_s, and A_c denote the cross-sectional areas of steel tube and inner concrete, respectively. f_{sc} denotes the compressive strength design value of CFST. ξ denotes constraint effect coefficient. f and f_c are the compressive strength design values of steel and concrete, respectively. B and C denote the influence coefficients of the constraint effect.
CECS 159: 2004	$N = \varphi N_0$; $N_0 = f A_s + f_c A_c$	The meaning of each symbol is consistent with that in GB 50936-2014.
AISC/ANSI 360-16	when $\frac{P_{n0}}{P_e} \leq 2.25$, $P_n = P_{n0}\left(0.658^{\frac{P_{n0}}{P_e}}\right)$; when $\frac{P_{n0}}{P_e} > 2.25$, $P_n = 0.877 P_e$; $P_{n0} = f_y A_s + 0.85 f_c' A_c$; $P_e = \pi^2 (EI_{eff})/(KL)^2$	P_n denotes nominal compressive strength. P_{n0} denotes nominal compressive strength of a zero length, doubly symmetric, and axially loaded composite member. P_e denotes elastic critical buckling load. f_y denotes yield stress of steel. f_c' denotes specified compressive strength of concrete. EI_{eff} denotes effective stiffness of a composite section. K denotes effective length factor. L denotes the length of a member.
EC4	$\frac{N_{Ed}}{\chi N_{pl,Rd}} \leq 1.0$; $N_{pl,Rd} = A_s f_y + A_c f_c'$	N_{Ed} denotes the design value of compressive normal force. $N_{pl,Rd}$ denotes the design value of the plastic resistance of a composite section to compressive normal force. χ denotes the reduction factor for flexural buckling.
AS/NZS 2327: 2017	$N_{c,Rd} = \alpha_c N_{s,Rd} \leq N_{s,Rd}$; $N_{s,Rd} = \emptyset A_s f_y + \emptyset_c A_c f_c'$	$N_{c,Rd}$ denotes member resistance. $N_{s,Rd}$ denotes section resistance. α_c denotes compression member slenderness reduction factor. $\emptyset$ and $\emptyset_c$ denote capacity factor for steel and concrete, respectively, where $\emptyset = 0.9$, $\emptyset_c = 0.6$.

4.2. Analysis of calculation results

The ultimate bearing capacity (N_u) calculated based on different standards were compared with the test results (N_{ue}) presented in Table 6 and Fig. 13. It can be seen from the table that the five standards used were conservative. The difference between the predicted strengths of the HGMFSST members using GB 50936-2014 and the measured values were in the range of -0.4%–26%. The predicted strengths were lower than the measured values, except for that of member S-HGM3-4 (Table 6). The average ratio and standard deviation of N_u/N_e were 0.892 and 0.074, respectively. Using AISC/ANSI 360-16 and EC4, the member capacity was approximately 12%-25% lower than the measured ultimate strength, and the average N_u/N_e ratios were 1.017 and 0.968 with standard deviations of 0.048 and 0.042, respectively. The predicted strengths obtained using AS/NZS 2327:2017 were approximately 18%-32% lower than the measured values, and the average and standard deviation of N_u/N_e were 0.756 and 0.05, respectively. The predicted strengths obtained using CECS 159:2004 were approximately 2%-15% lower than the measured values, and the average and standard deviation of N_u/N_e were 0.931 and 0.043, respectively. As can be seen, in general, the predicted strengths of the HGMFSST members using the AS/NZS2327: 2017 standard had a minimum average of 0.756, which indicates that this standard was more conservative than the others. The combined analysis of Fig. 13 shows that the predicted values of CECS 159:2004 were closest to the measured values with minimum discreteness for a wide range of design parameter values.

Table 6
Summary table of calculation results

Specimen label	N_{ue}	GB50936-2014		AISC/ANSI 360-16		EC4		AS/NZS2327: 2017		CECS159: 2004	
		$N_{u,GB}$	$N_{u,GB}/N_{ue}$	$N_{u,AISC}$	$N_{u,AISC}/N_{ue}$	$N_{u,EC4}$	$N_{u,EC4}/N_{ue}$	$N_{u,AS}$	$N_{u,AS}/N_{ue}$	$N_{u,CECS}$	$N_{u,CECS}/N_{ue}$
S-HGM1-4	1295	1143	0.882	969	0.748	1045	0.807	888	0.685	1106	0.854
S-HGM2-4	1294	1242	0.959	993	0.767	1080	0.835	911	0.704	1181	0.912
S-HGM3-4	1554	1560	1.004	1253	0.806	1404	0.904	1153	0.742	1417	0.912
S-HGM1-6	1516	1204	0.794	1307	0.862	1337	0.882	1217	0.803	1459	0.963
S-HGM2-6	1587	1295	0.816	1328	0.837	1370	0.863	1240	0.781	1527	0.962
S-HGM3-6	1778	1597	0.898	1564	0.880	1657	0.932	1460	0.821	1743	0.980
Average			0.892		0.817		0.870		0.756		0.931
Standard deviation			0.074		0.048		0.042		0.050		0.043

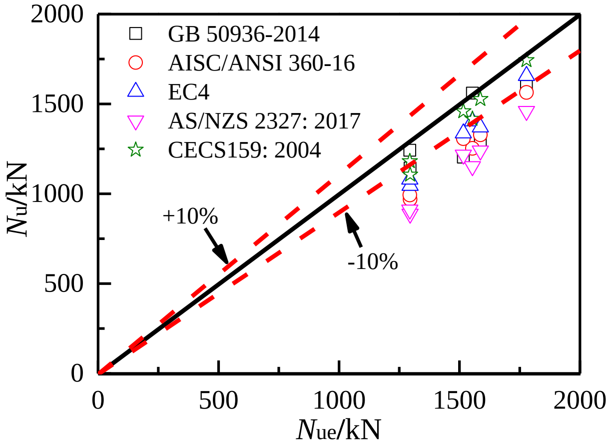

Fig. 13 Comparison of calculation results.

5. Conclusions

The following conclusions can be drawn from the axial compression test and correlation analysis:

(1) Testing of the cube blocks at different ages shows that the failure modes of the grouting materials HGM2 and HGM3 originated from vertical cracks and then developed into multiple small cylinders. These failure modes are different from those of ordinary concrete. In prismatic blocks, the failure modes occurred with the cracks penetrating through the upper and lower bearing surfaces along the diagonal of the blocks. In HGM3, the blocks remained undecomposed after fracture owing to the presence of steel fibers.

(2) The test results show that the members of Group I (t = 4 mm) failed due to both local buckling and overall buckling, whereas the members of Group II (t = 6 mm) failed due to overall buckling.

(3) For the HGMFSST members, the strength and ductility indices decreased with an increase in HGM strength. For the HST members, the strength index improved after HGM pouring because the inner HGM effectively delayed the local buckling of the steel tube.

(4) The load-strain relationships show that the inner HGM effectively delayed the local buckling of the steel tube, and the steel tube and inner HGM worked well in conjunction under axial compression. The HGM can be used as the inner filling material of the steel tube to form a composite member.

(5) Theoretical ultimate strengths of the HGMFSST members were calculated based on existing standards, which were conservative but acceptable. The results predicted with CECS 159: 2004 were the closest to the measured values, with minimum discreteness for a wide range of design parameter values.

Acknowledgements

This study was supported by Enterprise-commissioned Projects (No. HX2021-01).

References

[1] Mirza J, Mirza M S, Roy V, et al. Basic rheological and mechanical properties of high-volume fly ash grouts[J]. Construction & building materials. 2002, 16(6): 353-363.

[2] _ahmaran M, özkan N, Keskin S B, et al. Evaluation of natural zeolite as a viscosity-modifying agent for cement-based grouts[J]. Cement and Concrete Research. 2008, 38(7): 930-937.

[3] Sha F, Li S, Liu R, et al. Experimental study on performance of cement-based grouts admixed with fly ash, bentonite, superplasticizer and water glass[J]. Construction and Building Materials. 2018, 161: 282-291.

[4] Mohammed A, Mahmood W, Ghafor K. Shear stress limit, rheological properties and compressive strength of cement-based grout modified with polymers[J]. Journal of Building Pathology and Rehabilitation. 2020, 5(1).

[5] Zheng-Ming S, Jian-Qi Z, Chao-Ming Z, et al. Properties research on CGM high performance cement-based grout[J]. CONCRETE. 2007(11): 98-101. (in Chinese)

[6] Liao F, Han L, He S. Behavior of CFST short column and beam with initial concrete imperfection: Experiments[J]. Journal of Constructional Steel Research. 2011, 67(12): 1922-1935.

[7] Liao F, Han L, Tao Z. Behaviour of CFST stub columns with initial concrete imperfection: Analysis and calculations[J]. Thin-Walled Structures. 2013, 70: 57-69.

[8] Han L, Ye Y, Liao F. Effects of Core Concrete Initial Imperfection on Performance of Eccentrically Loaded CFST Columns[J]. Journal of Structural Engineering. 2016, 142(12): 1-13.

[9] Liao F Y, Li Y J. Experimental Behaviour of Concrete Filled Steel Tubes (CFST) with Initial Concrete Imperfection Subjected to Eccentric Compression[J]. Applied Mechanics and Materials. 2012, 174-177: 35-38.

[10] Guler S, Lale E, Aydogan M. BEHAVIOUR OF SFRC FILLED STEEL TUBE COLUMNS UNDER AXIAL LOAD[J]. ADVANCED STEEL CONSTRUCTION. 2013, 9(1): 14-25.

[11] Han L. The Influence of Concrete Compaction on the Strength of Concrete Filled Steel Tubes[J]. Advances in structural engineering. 2000, 3(2): 131-137.

[12] Han L, Yao G. Influence of concrete compaction on the strength of concrete-filled steel RHS columns[J]. Journal of Constructional Steel Research. 2003, 59(6): 751-767.

[13] Tao Z, Song T, Uy B, et al. Bond behavior in concrete-filled steel tubes[J]. Journal of Constructional Steel Research. 2016, 120: 81-93.

[14] Yu F, Yao C, Hu Y, et al. AXIAL COMPRESSIVE BEHAVIOR OF SELF-STRESSING STEEL SLAG AGGREGATE CONCRETE FILLED STEEL TUBULAR COLUMNS

WITH BOND-SLIP DAMAGE[J]. Advanced Steel Construction. 2020, 16(1): 13-19.

[15] Einea A, Yamane T, Tadros M K. Grout-Filled Pipe Splices for Precast Concrete Construction[J]. PCI Journal. 1995, 40(1): 82-93.

[16] Ling J H, Abd. Rahman A B, Ibrahim I S. Feasibility study of grouted splice connector under tensile load[J]. Construction and Building Materials. 2014, 50(1): 530-539.

[17] Ling J H, Abd. Rahman A B, Ibrahim I S, et al. Tensile capacity of grouted splice sleeves[J]. Engineering Structures. 2016, 111: 285-296.

[18] Hayashi Y, Nakatsuka T, Miwake I, et al. MECHANICAL PERFORMANCE OF GROUT-FILLED COUPLING STEELSLEEVES UNDER CYCLIC LOADS[J]. Journal of Structural & Construction Engineering. 1997, 496(496): 91-98.

[19] Lin F, Wu X. Mechanical Performance and Stress‑Strain Relationships for Grouted Splices Under Tensile and Cyclic Loadings[J]. International Journal of Concrete Structures and Materials. 2016, 10(4): 435-450.

[20] Qun Z, Xiao-Lin Z, Chao-Ming Z. CGM grouting material in gymnasium engineering of Beijing Institute of Technology[J]. Concrete. 2004, 179(9): 66-67, 80. (in Chinese)

[21] Yong-Xin Z, Mu-Xing S, Shu-Nan L, et al. The Application of High-strength Non-shrinkage Grouting Material of the Tail Pipe Steel Lining Replacement[J]. Northeast Electric Power Technology. 2015, 36(5): 8-10. (in Chinese)

[22] Du K. Construction of Two Times Concrete Pouring with High - strength Non - shrinkage Grouting instead of Steel Column Bottom[J]. Architectural Engineering Technology And Design. 2017(19): 1755-1756. (in Chinese)

[23] GB50936-2014, Technical Code for Concrete Filled Steel Tubular Structures[S]. Beijing, 2014.

[24] CECS 159: 2004, Technical specification for structures with Concrete-filled rectangular steel tube members[S]. Beijing, 2004.

[25] ANSI/AISC 360—16. Specification for Structural Steel Buildings[S]. Chicago, 2016.

[26] Eurocode 4. Design of composite steel and concrete structures - Part 1.1: General rules and rules for buildings[S]. Brussels, 2004.

[27] AS/NZS 2327: 2017. Composite structures—Composite steel-concrete construction in buildings[S]. AS/NZE, 2017.

[28] GB/T 50448-2015, Technical code for application of cementitious gout[S]. Beijing, 2015.

[29] GB/T50081-2019, Standard for test Methods of concrete physical and mechanical properties[S]. Beijing, 2019.

[30] Han L H. Concrete Filled Tubular Structures-theory and Practice[M]. Beijing: Science Press, 2004. (in Chinese)

[31] Yang Y, Han L. Compressive and flexural behaviour of recycled aggregate concrete filled steel tubes (RACFST) under short-term loadings[J]. Steel and Composite Structures. 2006, 6(3): 257-284.

[32] Han L H. Tests on stub columns of concrete-filled RHS sections[J]. Journal of Constructional Steel Research. 2002, 58(3): 353-372.

[33] Ge H, Usami T. Cyclic Tests of Concrete-Filled Steel Box Columns[J]. Journal of Structural Engineering. 1996, 122(10): 1169-1177.

[34] Zhao X, Hancock G. Tests to Determine Plate Slenderness Limits for Cold-Formed Rectangular Hollow Sections of Grade C450[J]. Steel Construction. 1991, 25(4).

[35] Han L. Tests on Concrete Filled Steel Tubular Columns with High Slenderness Ratio[J]. Advances in structural engineering. 2000, 3(4): 337-345.

[36] Wu Y, Yang X, Wang K, et al. Experimental study on the stress-strain curve of cementitious grout under uniaxial compression[J]. Industrial Construction. 2014, 151(s1): 909-913, 903. (in Chinese)